Wavelength Division Multiple Access in LiFi Networks

PhD Thesis

G. L. Martena

LiFi Research and Development Centre

Department

University of Strathclyde, Glasgow

February 7, 2025

Abstract

This thesis is focused on an indoor Light Fidelity (LiFi) network with a high amount of closely deployed Red-Green-Blue-Amber (RGBA) Access Point (AP)s and mobile users. The contributions made are threefold. Firstly, the impact of the Passband Shift (PS) effect is discussed in such a context, along with the challenges it entails. A generic system model is presented, including geometrical details, and the Probability Density Function (PDF) of the central wavelength of a shifted optical filter spectrum is presented, which is dependent on user mobility behaviour. Based on this, a new parameter (the Spectral Overlap (SO)) that can facilitate system design choices is formally introduced, and an investigation on the benefits of optimising the Optical Front-End (OFE) for networked Visible Light Communication (VLC) with RGBA densely deployed APs is carried out. Secondly, a novel resource allocation scheme based on **WD!** (**WD!**) that can be used in the context of LiFi, called adaptive Wavelength Division Multiple Access (WDMA), is proposed. It allocates resources in a way that adapts to users' mobility behaviours by leveraging the PS effect and spatial separation while maintaining underlying compatibility with smart lighting solutions. By means of custom-written simulations, this scheme is tested against a fixed benchmark, showing improved fairness in the allocation as well as lower Connection Loss (CL) probability. Thirdly, this scheme is evolved into its "adaptive Wavelength Division Multiple Access-Multiple Input Multiple Output (WDMA-MIMO)" version to achieve better utilisation of available network resources even in lowly crowded scenarios. It is then tested against a fixed benchmark in the context of increasing network crowdedness and considered in terms of handover rate. In terms of achievable data rate (both network and per-user), average Signal-to-Interference-plus-Noise Ratio (SINR) in active channels, and CL, the fixed benchmark is always outperformed by the proposed scheme.

Contents

List of Figures

List of Tables

List of Algorithms

List of Symbols

$\cdot$	Multiplication operator
Δ_λ	Spectral Half-Width-Half-Maximum
$\frac{d}{d}$	Single variable differential
γ^{SINR}	Signal-to-Interference-plus-Noise-Ratio
γ^{SIR}	Signal-to-Interference-Ratio
$\int$	Integration operator
Σ	Sum operator
$\mathbf{n}$	Unit vector
$\mathbf{R}$	Rotation matrix
erf()	Error function
Pr	Probability function
rect()	Rectangular function
$\triangleq$	is defined as
c	Speed of light in a vacuum
e	Napier's constant

List of Abbreviations

ACO-OFDM Asimmetrically Clipped Optical-Orthogonal Frequency Division Multiplexing

AoI Angle of Incidence

AP Access Point

APD Avalanche Photodiode

CDF Cumulative Distribution Function

CDMA Code Division Multiple Access

CL Connection Loss

CSI Channel State Information

CPC Compound Parabolic Concentrator

DCO-OFDM Direct Current Optical-Orthogonal Frequency Division Multiplexing

FEC Forward Error Correction

FOV Field Of View

FWHM Full Width at Half Maximum

HWHM Half Width at Half Maximum

IEEE Institute of Electrical and Electronics Engineers

IM/DD Intensity Modulation / Direct Detection

IoT Internet of Things

IR Infra-Red

LD Laser Diode

LDPC Low-Density Parity Check

LED Light Emitting Diode

LiFi Light Fidelity

LOS Line Of Sight

LTE Long Term Evolution

MAC Media Access Control address

MCS Modulation and Coding Scheme

MIMO Multiple-Input Multiple-Output

OFE Optical Front-End

OFDM Orthogonal Frequency Division Multiplexing

OFOV Out of Field Of View

OOK On-Off Keying

OWC Optical Wireless Communication

PAPR Peak-to-Average Power Ratio

PD Photo-Detector

PDF Probability Density Function

PHY Physical Layer

PS Passband Shift

QoS Quality of Service

RGB Red-Green-Blue

RGBA Red-Green-Blue-Amber

RF Radio-Frequency

SINR Signal-to-Interference-plus-Noise Ratio

SIR Signal-to-Interference Ratio

SO Spectral Overlap

TIA Trans-Impedance Amplifier

UE User Equipment

VLC Visible Light Communication

WDM Wavelength Division Multiplexing

WDMA Wavelength Division Multiple Access

WDMA-MIMO Wavelength Division Multiple Access-Multiple Input Multiple Output

WiFi Wireless Fidelity

Preface/Acknowledgements

I would like to acknowledge the contribution, help, and invaluable support received from Prof. Harald Haas, Dr. Rui Bian and Dr. Mohamed Islim, Janis Sperga, and all the team at pureLiFi Ltd. I am but a dwarf on the shoulders of these giants. I would also like to acknowledge the support of the European Union's Horizon 2020 research and innovation programme under the Marie Skłodowska-Curie grant agreement ENLIGHT'EM No. 814215 for the invaluable support. In fact, other than the generosity of its funding, its regularly organised events have resulted in both training and networking opportunities. Thanks to it, I have met colleagues and friends who will always have a place in my mind and heart.

Last but definitely not least, my family, and my amazing wife-to-be Viola, for the loving kindness and support.

Seriously, I wish everyone had a Viola in their life.

Chapter 1

Introduction

This chapter serves as an introduction to the thesis and the research presented throughout. Firstly, the motivations and the challenges of the Optical Wireless Communication (OWC) technology are briefly introduced. Secondly, this is further elaborated into an overview of the contributions made by the thesis. Lastly, the broader organisation of the dissertation is discussed. The chapter ends with a summary.

1.1 Motivations & Challenges

While browsing well known articles and papers in the field of OWC and Light Fidelity (LiFi), the interested reader can notice a very common trend of starting to acknowledge the problem of spectrum crunch in the Radio-Frequency (RF) realm. This is indeed the underlying motivation behind much of the research in this field: that of providing an alternative source to convey network traffic that is free and non-interfering with existing technologies. This is strengthened by the recent release of the 802.11bb standard amendment, which encompasses the addition of Media Access Control address (MAC) and Physical Layer (PHY) layer specifications for wireless light-based communications.

The Ericsson mobile data forecast projects a nearly 5-fold growth in monthly data traffic globally, reaching up to a whopping 237 EB per month in 2026, compared to 49 EB monthly at the end of 2020 [1]. As shown in Figure 1.1, the sheer number

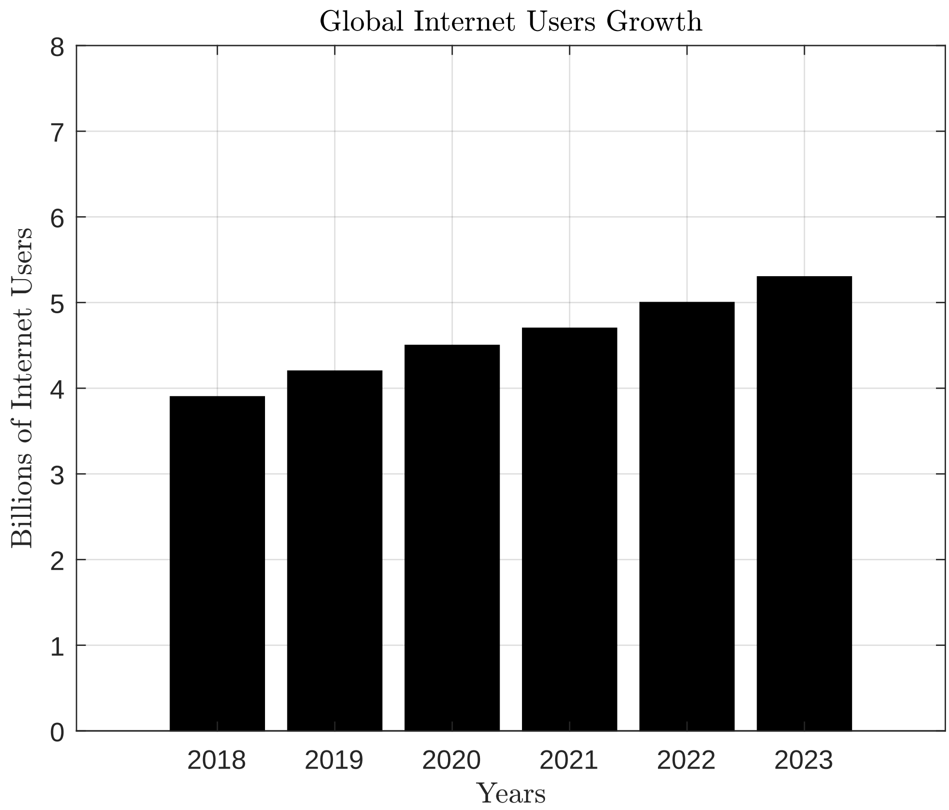

Figure 1.1: Global Internet users growth [5]. The estimated compound annual growth rate (CAGR) is 6 %.

of mobile users is increasing as well, expectedly exceeding 5.7 billion and generating up to 79% of the global data traffic [2]. Without a significant capacity increase, it will be difficult to provide all fixed and mobile devices, such as smartphones, tablets, wearables, and various wireless sensors, with a network connectivity that performs adequately [3]. Finally, in the evolutionary progression beyond fourth-generation (4G) and Long Term Evolution (LTE) wireless networks, the anticipated advancement in the fifth generation (5G) and subsequent cellular networks is characterized by an expected 1000-fold increase in capacity [4].

Within this, an increasingly important role is being played by Internet of Things (IoT) applications. In fact, it was forecast that 14.7 billion global machine-to-machine (M2M) connections will be established by 2023, and even if 5G is becoming the current standard for such applications, its future developments will also become incorporated within the IoT framework. Notably, it is also estimated that “more than 50% of the revenue of Internet service providers in the next decade will be driven by the enterprise IoT market segment" [6].

This results in an underlying congestion and limitation of the RF spectrum, leading to the challenging task of accommodating the ever-increasing bandwidth and high data throughput demand.

Technology has come a long way from when, in 1880, Alexander Graham Bell was able to transmit speech over a distance of 200 m with one of his inventions, the photophone [7]. The concept of using fast switching Light Emitting Diode (LED)s was first presented in 1999 [8] and further refined in Japan in the early 2000s by using white LEDs for communication and illumination at the same time [9]. Since then, OWC has been drawing significant attention from both academic and industrial spheres, primarily attributed to its capacity to operate within a free, extensive, and unregulated spectrum. This spectrum encompasses both Infra-Red (IR) and visible light frequencies, providing ample potential for wireless data transmission.

Nowadays, Visible Light Communication (VLC) is a technology falling under the OWC umbrella term that makes use of an emitter in the visible spectrum of light to transmit a signal by means of Intensity Modulation / Direct Detection (IM/DD) to an opportune Photo-Detector (PD), able to capture the radiation. Due to its advantages, VLC has raised the interest of many research groups around the world and is seen as a very promising technology for the future of OWC. Its spectrum is easily accessible, not subject to regulations, and is virtually free from interference with the existing and well-established RF technology.

On the emitter side, the current status of technology sees the use of fast-switching LEDs, Laser Diode (LD)s, and Vertical-Cavity Surface-Emitting Laser (VCSEL)s. The latter two are both types of lasers, where VCSELs emit a circular beam vertically from a substrate rather than from its edge (as it happens with LDs). All these can also be used as arrays to increase the output optical power, subject to limitations with respect to power consumption and eye safety considerations. This latter is particularly important: shorter wavelengths can induce more damage (i.e. visible light are potentially more damaging than Infra-Red (IR) sources), and commercially available devices employ various kinds of lenses and diffusers to avoid concentrating a high amount of optical power in a small spot.

Regarding the PD, a very common choice is to use P-type Intrinsic N-type (PIN) photodiodes which are semiconductor diodes that can convert light radiation into an electrical current. Its wide intrinsic region (which makes it different from a regular p-n semiconductor diode) can collect most of the photons that arrive on it, which then contribute to the generated photocurrent. Significantly higher gains can be achieved by Avalanche Photodiode (APD)s, in which an avalanche mechanism allows to increase the PD's sensitivity, at the cost of having excess noise which limits the Signal-to-Noise-Ratio (SNR) [10,11]. Arrays of Single Photon Avalanche Photo-Diode (SPAD)s are also being currently investigated, but their applicability seems to be limited by their sensitivity to ambient light [12]. For the purposes of LiFi, the PDs involved are usually put in an arrayed configuration. One particularly useful of such configurations has been termed "Matrix of Photodiodes" [13, 14], and it entails putting the photoreceiving devices (regardless of using PIN photodiodes or APDs) in series of N elements. These series are then connected in parallel between them, and this allows to increase the otherwise low generated photocurrent while countering the bandwidth reduction associated with a series of photodiodes.

For home and office data transmission applications, the wide availability and low required maintenance of LEDs, relatively low implementation complexity, and the possibility of using pre-existing lighting infrastructures makes this choice a more attractive one with respect to the use of LDs and VCSELs. In fact, with these two being more focused sources, they need higher complexity (such as the use of diffuser lenses or careful temperature management) which increase the cost even further, on top of LDs and VCSELs being generally more costly than LEDs.

As noted, the signal transmitted from a LED or LD is then picked up by a PD or APD making the VLC technology a point-to-point system without network capabilities. It has been demonstrated that it can achieve high data rate performance of up to 38 Gbps with LDs as transmitters [15], and up to 15.73 Gbps while using only off-the-shelf LEDs [16].

Within this framework, LiFi can be seen as a further step: with VLC providing a point-to-point physical layer foundation, LiFi encompasses a full duplex, multiuser, and multipoint wireless communication network in which each transmitter can be used as an Access Point (AP) in a dense deployment, providing connectivity to many users simultaneously [17]. Because of all these reasons, LiFi is deemed to be a potential solution to the spectrum crunch problem in RF as a complementary technology, capable to offload a part of the traffic and overcome some of the existing limitations [18].

As LiFi allows for very small cells and a very dense deployment, this is also referred to as an atto-cellular wireless network. In [19–21], a framework is established for the efficient design of atto-cell networks by outlining the most important parameters to take into account (such as cell radius, beam-shaping, and optimal cell deployment). Additionally, [19] offers a thorough analysis of the data rate and spectral efficiency performances of a LiFi network and a comparison with other small-cell RF systems, showing that the latter could be outperformed with a proper atto-cell network design. In [20], it is shown how LiFi and Wireless Fidelity (WiFi) networks can benefit from each other when used in a cooperative fashion to form a hybrid LiFi and WiFi system. As seen, this allows to offload some traffic from the RF network to LiFi, improving the achievable capacity while also removing some interference. For these reasons, the concept of a hybrid LiFi network is subject to a significant amount of interest in the research community [22–29].

More generally, and though on the verge of commercial implementation, many solutions are still being investigated in the literature under a plethora of different perspectives to further increase the performances and applicability of LiFi [30–53].

Furthermore, the IoT and its diverse applications demonstrate a congenial alignment with OWC and LiFi. [54–64]. The synergy is attributed to OWC and LiFi's speed, inherent security features, and the absence of hindering cables, which are particularly advantageous in large-scale deployments. Notably, OWC's utilization of visible light introduces a myriad of possibilities, wherein a network of lighting fixtures, serving as APs, can seamlessly integrate communication and illumination functionalities, exemplifying its multifaceted capabilities.

IoT is a communication framework that allows many everyday objects and devices, featuring various kinds of sensors, software, and other technologies, to become nodes of a network, with the purpose of gathering and sharing different kinds of data and communicating over the Internet. Every device is provided with a user ID and has the ability to transfer data over a network without the necessity of human-to-human or human-to-machine interaction [65, 66]. For these reasons, IoT is capable of bringing a wide range of smart functionalities to all objects that are part of the ecosystem. It drives both people and businesses to gain new insights into their lives and processes, as well as to improve control over these aspects.

One of the important features of an IoT smart environment is that it is related to smart lighting. It is defined as the ability, in a room or a building, to adaptively control the illumination activation, intensity, and colour temperature based on a wide variety of parameters. These include, but are not limited to: the time of day, external lighting, the user's presence and position, and the nature of tasks that are to be carried out in a specific area. For example, a high-precision manufacturing premise will need bright and directed light for operating machinery, while a study used for evening reading will have a warmer, slightly dimmed light. As seen in [67], smart lighting features are able to save power when the user is not present and forgets to switch the lighting off.

Another aspect of IoT that indirectly impacts the nature of this work is that "pretty much any physical object can be transformed into an IoT device if it can be connected to the internet to be controlled or communicate information." [68]. As a result, it is expected that the number of connection requests in a given time will be higher than those of a normal wireless network. Thus, a LiFi implementation for IoT needs to efficiently account for multiple access.

In this context, LiFi is seen as an enabler for the IoT [55–59]. However, this comes with a number of challenges, two of which consist of the random position and orientation that the users can take, along with their dense deployment. In fact, the random position and orientation of users can significantly lower the power of the received signal, while increased density of UEs and APs can strongly favour interference.

1.2 Objectives & Contributions

This thesis focuses on indoor LiFi systems using wavelength division to provide multiple access to a high number of clients while taking user mobility into account. Given the entity and complexity of the envisioned scenario, which would make experimental work costly and time-consuming, the contributions are primarily focused on custom simulations. The objectives to be pursued are as follows:

- Deepen the understanding of how the Passband Shift (PS) effect would impact wavelength division-based LiFi systems in the presence of mobile users, as in an everyday use case.
- Develop and propose a new network operation algorithm capable of improving network capacity and fairness while minimising connection disruption. The proposed approach should also not interfere with light dimming support and be compatible with smart lighting solutions.
- Simulate the achievable network performances in highly crowded indoor environments while taking mobile user behaviour into account. These results should also be compared with a suitable benchmark.

In the efforts to address these objectives, several contributions to existing knowledge have been generated.

- Firstly, a mathematical framework has been developed to investigate the impact of the PS in wavelength division-based systems. User mobility statistics have been considered together with the PS effect and the channel model, as well as prior studies, to derive the closed forms of the Probability Density Function (PDF) and Cumulative Distribution Function (CDF) of the shifted central wavelength of an optical filter mounted on the receiver of a mobile user. This knowledge is useful to further investigate system design choices, Optical Front-End (OFE) choices, attocell size, and network operation algorithms. In particular, it is here used to demonstrate that an adequate level of interference mitigation can still be achieved even in densely deployed environments and without the use of wavelength reuse patterns.

- Secondly, a novel allocation approach called "adaptive Wavelength Division Multiple Access (WDMA) is proposed and tested with custom simulations against a fixed allocation benchmark. This allocation scheme is based on adaptively maximising Signal-to-Interference-plus-Noise Ratio (SINR) for every user, and specifically designed to be compatible with smart lighting solutions and dimming support and to be independent of the modulation scheme. The comparison entails measuring the room coverage, aggregate average data rate, average data rate per user, and average connection loss probability while 4 users are in the network at the same time. Along with this, validation work on the simulation code used to generate the results is presented.

- Lastly, this allocation scheme is expanded in its Multiple-Input Multiple-Output (MIMO) version in order to tap into previously unutilised network resources and compared again with a fixed benchmark. This is done while progressively increasing the room crowdedness to investigate the network scalability potential and how the proposed scheme reacts to such high user- and AP- densities. As a further means of investigating the applicability of this scheme, the handover rate is also measured in four scenarios, designed after real-life situations.

Differently from what can be found in the literature concerning wavelength division-based systems, all simulation work is carried out with real optical filter spectra measured at increasing Angle of Incidence (AoI) in order to improve the accuracy of the results. In fact, such spectra can undergo significant transformations as the AoI gets further and further away from 0°.

1.3 Dissertation Layout

The remaining chapters of this dissertation are structured as follows:

- Chapter 2: A review of literature that discusses the current status of technological advancement in the fields of OWC and LiFi, modulation schemes and multiple access strategies, wavelength division, channel modelling, and network operation level.

- Chapter 3: Investigation of the effects of the PS effect on a wavelength division-based network while accounting for user mobility behaviour. A mathematical framework is presented to improve the understanding of how this effect can be mitigated and leveraged to improve network performances.
- Chapter 4: Introduces a novel resource allocation scheme for wavelength division-based multiuser LiFi systems with densely deployed APs. The proposed scheme is compared with a fixed scheme, employing a round-robin, first-come-first-served allocation, considering wavelength and spatial separation principles.
- Chapter 5: Introduces an adaptive Wavelength Division Multiple Access-Multiple Input Multiple Output (WDMA-MIMO) algorithm, building upon the adaptive WDMA discussed earlier. This aims to enhance network resource utilisation through a biphasic allocation process, prioritising fairness and minimising Connection Loss (CL). A fixed allocation scheme is established as a benchmark, utilising a round-robin approach based on SINR for channel determination.
- Chapter 6: Summarises the results obtained and explores further work that can be carried out in the future to improve understanding of technology and its applications in the field of LiFi.

1.4 Chapter Summary

The exponential increase in the sheer numbers of users accessing the Internet combined with the adoption of smart home and M2M innovations like the IoT is an emerging trend that is being highlighted by many credible sources. Because of it, it is envisioned that in the near future, RF technologies will struggle to provide every user with a strong, reliable, and ever-active connection. OWC and its networked version, LiFi, offer a possible solution to this problem, being able to exploit vast, free, and unregulated additional spectrum and being non-interfering with RF and mmWave technologies. This thesis is mainly focused on how the performances of indoor LiFi networks employing wavelength division paradigms in dense deployments can be improved. The problem is tackled from a network operation perspective after some useful considerations on the OFE (which still constitutes an influential part of the system). Firstly, a mathematical framework is developed and applied to deepen the understanding of how the PS effect impacts such systems populated with mobile users. Secondly, a novel allocation algorithm compatible with smart lighting solutions and independent of the employed modulation scheme is proposed and tested with a fixed benchmark. Lastly, this algorithm is extended to a MIMO version and tested within very crowded environments, and its handover rate is evaluated in simulation work mimicking real-life scenarios. All this is done by employing measured optical filter spectra, as their dependence on the AoI of the light can influence the end results significantly.

Chapter 2

Background

In this chapter, relevant literature in the fields of Light Fidelity (LiFi) and wavelength division will be reviewed and the outcomes presented in view of what is useful for this dissertation. The attention will especially be focused on the following topics: modulation schemes, channel characteristics, use of spatial domain, handover strategies, multiple access strategies, and atto-cell design.

2.1 Introduction

As mentioned earlier, a networked Optical Wireless Communication (OWC) (which includes Visible Light Communication (VLC)) system is known as LiFi. In LiFi, each luminaire can become a so-called "optical atto-cell" (in analogy with Radio-Frequency (RF) femto-cells), constituting an optical atto-cell network, that can achieve high communication performances due to its extremely dense spatial reuse [19]. An intuitive representation of a generic LiFi implementation is portrayed in Figure 2.1. As it is shown, multiple users are accessing the network through data that is wirelessly exchanged between the lighting fixtures and their User Equipment (UE)s. This is achieved via a technique called Intensity Modulation / Direct Detection (IM/DD), and its basic working principle has first been established in [69]; though much of this work refers specifically to wireless communication happening in the Infra-Red (IR) region of the light spectrum, and mostly referring to a point-to-point link, its principles can also

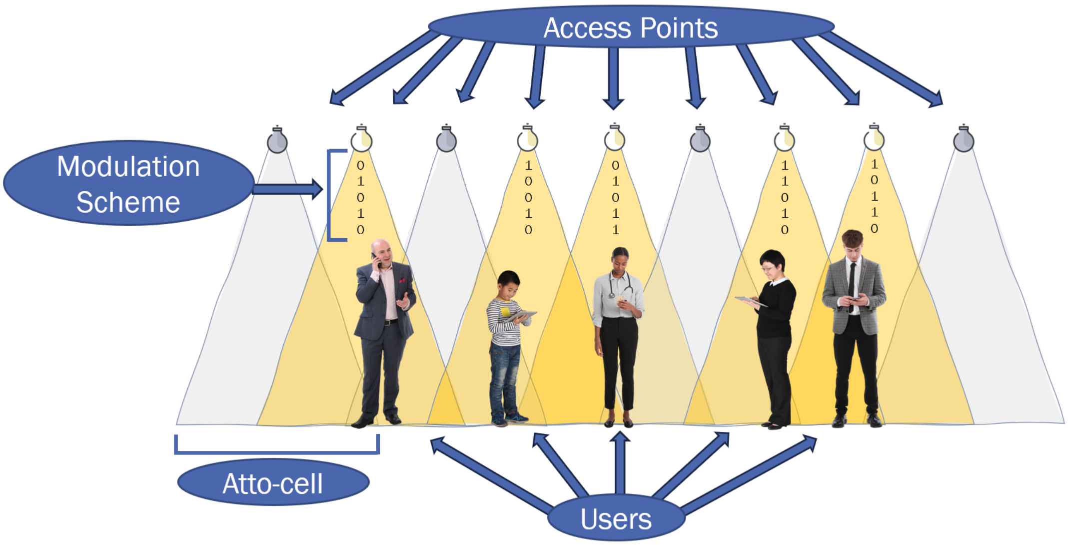

Figure 2.1: LiFi implementation diagram. A multitude of lighting fixtures provide networked access to multiple users at the same time, through direct modulation of light.

be applicable with visible light and in a networked fashion.

By zooming in to one of the links, as in Figure 2.2, one can appreciate the different components of a OWC link. As per the IM/DD, the transmitter is able to encode data in the intensity of the light via many different modulation schemes, the most important of which are presented in Section 2.2. The light then reaches the receiver of the UE by passing through the transmission medium; in the case of LiFi, this is the free space identified by the optical path between the transmitter and the receiver [69–71]. This attenuates the light by a certain amount, which will be further discussed in Section 2.4.

The light is then collected by the Photo-Detector (PD), which as discussed, can convert the optical power into a photocurrent following a wavelength-dependent curve called "responsivity". The shape of the responsivity is strongly correlated with the material of the PD. While a Silicon (Si) photodiode is more responsive in the visible region (400 - 700 nm), other materials like Indium Gallium Arsenide (InGaAS) or Germanium (Ge) are more responsive in the IR region. The -3 dB cutoff frequency of the PD, assuming a single PIN photodiode or Avalanche Photodiode (APD) is used, depends on the size of its active area [69]. A wider area will result in a lower bandwidth,

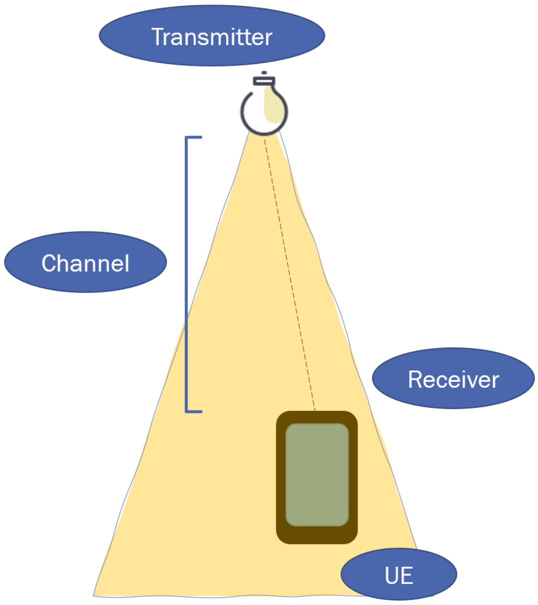

Figure 2.2: Single LiFi link diagram. A lighting fixture is the transmitter, which emits light in the free space (the channel). The light is picked up by a receiver (a PD) that is embedded onto a UE (such as a smartphone or wearable).

thus constituting one of the most important trade-offs with respect to receivers for OWC [69–71].

2.2 Modulation Schemes

A LiFi network can make use of many different modulation schemes, with their advantages and shortcomings, and in each system design phase, the choice has to be made carefully with respect to the application. In this context, it has to be noted that the Institute of Electrical and Electronics Engineers (IEEE) 802.15.7 standard [72] specifically focuses on OWC links with added support for dimming functionalities and reduced flickering effect. This is desirable for an indoor connectivity use case, and is oftentimes achieved through specific modulation techniques which will be discussed along with other options in the following sections.

2.2.1 Single Carrier Modulation

For Single Carrier Modulation (SCM), it is common to resort to schemes that have been widely studied in wireless communication [73] and tested or adapted to the optical domain: On-Off Keying (OOK), Pulse Amplitude Modulation (PAM), or Pulse Position Modulation (PPM). These all have in common that they encode the information in the switching of the light source between on and off states. On the power dissipation side, PPM is more energy-efficient than simple OOK but requires a higher bandwidth, so it has less applicability in contexts that require high-flexibility.

All these schemes have the great benefit of generally low power consumption and very low implementation and receiver complexity: this renders them interesting candidates in the scope of Internet of Things (IoT).

Differential PPM (DPPM) [74] is a modulation scheme that achieves a performance gain with respect to conventional PPM. However, its variable duration of symbols is not ideal for those applications that seek to jointly deliver lighting and communication functionalities. In fact, this could introduce unwanted illumination flickering. In [75], a solution is proposed to counter this effect. Moreover, another scheme called Variable PPM (VPPM) has been introduced in the IEEE 802.15.7 standard [72]. This is particularly relevant for indoor LiFi applications, as it includes dimming support with the pulse width and prevents the perceived effect of flickering lighting fixtures. Other interesting variations of PPM are proposed in [76, 77].

A carrier-less amplitude and phase modulation scheme [78] is also commonly used in LiFi, which is a variant of SCM Quadrature Amplitude Modulation (QAM). In the original scheme, the in-phase and quadrature components are carried by the real and imaginary parts of a complex signal. In its proposed LiFi version, these two components are instead sent with two distinct orthogonal signals as the transmitter is an intensity-modulated light source that can only transmit real, non-negative waveforms.

2.2.2 Spatial Modulation and Space-Shift Keying

Another scheme that is raising interest in the community is Spatial Modulation (SM) and Space Shift Keying (SSK) [67, 79–82]: each transmitter is treated as a spatial constellation point that is uniquely linked to a data symbol. Thus, only one transmitter is active at any given time. Consequently, the space dimension can be used to increase the spectral efficiency.

Additionally, another notable scheme that is called Flexible Light Emitting Diode (LED) Index Modulation (FLIM) [83] is proposed, which is capable of using the physical space even more efficiently.

2.2.3 Multicarrier Modulation

When the required data rates increase, the drawbacks of SCM schemes become too heavy, and there is a need to make use of multi-carrier modulation schemes. The most important of these is Orthogonal Frequency Division Multiplexing (OFDM), in which a stream of data is multiplexed on several narrowband and orthogonal subcarriers by means of an Inverse Discrete Fourier Transform (IDFT) (even though other transforms and approaches have also been investigated in [84–86]). This generates a bipolar and complex signal that can be rendered real-valued by imposing Hermitian symmetry. The two most widely used ways to make the signal unipolar and make it compatible with IM/DD are Direct Current Optical-Orthogonal Frequency Division Multiplexing (DCO-OFDM) and Asimmetrically Clipped Optical-Orthogonal Frequency Division Multiplexing (ACO-OFDM).

In DCO-OFDM [87], a positive direct-current bias is added to the time domain signal. This has the advantage of rendering it unipolar without losing spectral efficiency, but it also increases the Peak-to-Average Power Ratio (PAPR) and therefore raises the energy consumption. However, while this PAPR increase could be leveraged when illumination requirements are in place, it remains far from ideal for many applications (such as OWC uplink or IoT) in which power efficiency is crucial. A few groups have studied the optimisation of the biassing point [88–90], as a certain level of clipping noise is acceptable to tackle this problem. It has to be noted, though, that while DCO-OFDM is not the best solution in terms of power efficiency, it boasts the advantage of offering one of the best spectral efficiencies available in OWC.

In ACO-OFDM [91] the signal is clipped below zero, and only the positive (odd) subcarriers are considered to carry information. This has the advantage of yielding a lower PAPR and not increasing energy consumption, at the expense of the spectral efficiency which is halved with respect to DCO-OFDM. Another technique called Pulse-Amplitude-Modulated Discrete Multi-Tone (PAM-DMT) [92] uses only the imaginary component of the subcarriers. This only makes M-PAM applicable as a modulation scheme in this case, but in this way, anti-symmetry is achieved for the signal in the time domain, and since the clipping distortion would only affect the real part of the signal, it is possible to render it unipolar with tolerable noise.

The work in [93] has presented a simulation-based comparison of ACO-OFDM and DCO-OFDM with many different constellation sizes ranging from 4- to 1024-QAM. It concludes that ACO-OFDM performs better in terms of power efficiency only for lower constellation sizes, while the performance of DCO-OFDM is dependent on the bias. It also concludes that, because of optimization outcomes being the same for all constellation sizes, ACO-OFDM is better suited for adaptive systems.

Another interesting scheme called enhanced Unipolar OFDM (eU-OFDM) has been proposed in [33], which combines the advantages of both DCO-OFDM and ACO-OFDM, achieving a good balance of spectral efficiency and energy consumption.

Flipped OFDM (Flip-OFDM) [94] applies a similar concept. The OFDM frame is doubled, with the second half flipped. In this way, it can be rendered unipolar by zero-clipping without any loss of information. However, as it happens with the other aforementioned non-biassed schemes, the spectral efficiency is half that of DCO-OFDM. The interest in this research area is testified by many studies proposing efficient receiver designs for inherent unipolar OFDM techniques [95], [96–103].

In [104], Discrete Fourier Transform-Spread Orthogonal Frequency Division Multiplexing (DFT-s OFDM) is proposed. It entails performing a M-ary discrete Fourier Transform on the data symbols before putting them through the usual OFDM modulation, which helps in lowering the PAPR of the resulting waveform. It is even reported that, in most cases, it can unite the benefits of an OFDM-based multicarrier system with the lower PAPR of SCM modulation techniques.

Many other efforts have been made to explore the potential of OFDM in this field

[105–120], as the enhanced achievable data rates of this kind of modulation schemes have drawn the attention of the research community.

2.2.4 Colour-based Modulation Techniques

As every communication system has its own peculiarities, one must take them into account when designing a new system. For instance, LED arrays made up of elements of different colours can change the centre wavelength of the resulting beam by adjusting the intensity of the single-coloured elements. This is why, especially for VLC and LiFi applications, the property that a properly designed luminaire can introduce of changing the colour of the light beam has fostered research exploring this new degree of freedom. The Colour Shift Keying (CSK) is a modulation technique proposed in the IEEE standard 802.15.7 [72], in which the stream is encoded in a constellation made up of different colours from the chromatic CIE 1931 colour space [121]. The advantages in this regard are that colour-shifting is easy to implement and can occur while maintaining constant output optical power (a desirable feature in certain applications, as uniform illumination is equally important). Several studies [122–131] have proposed variations to this scheme, used both alone and in combination with other modulation techniques, demonstrating the active interest in this research area.

2.2.5 Multiple Access

As is intuitive, any wireless communication technology providing networking capabilities needs to adopt one or more multiple access protocols. This allows to counter interference between ongoing transmissions to multiple users, and most common techniques in RF can also be applied in LiFi. In this section, the most common multiple access techniques have been intuitively represented in Figure 2.3, and are explained and discussed as follows.

One of the most used multiple access techniques in LiFi is Orthogonal Frequency Division Multiple Access (OFDMA), which entails allocating one or more different subcarriers to each user [17, 132]. This is equivalent to regular OFDM, but different subcarriers are assigned to different users rather than parallel streams to the same

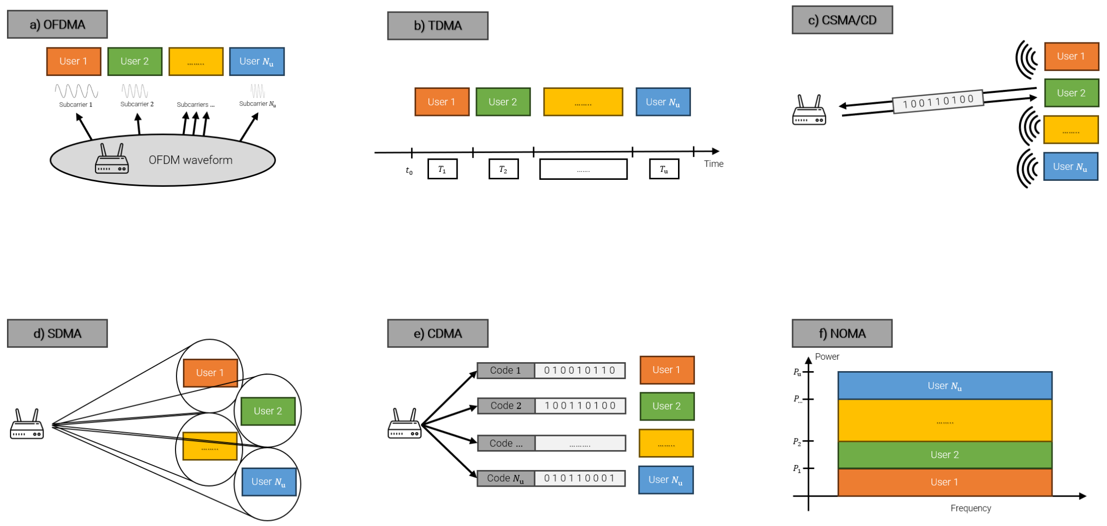

Figure 2.3: Common multiple access techniques in LiFi. In a) OFDMA, a regular OFDM waveform is used and each user is allocated a subset of subcarriers. In b) TDMA, each user can only receive incoming transmissions during an allocated time slot. In c) CSMA/CD, users can coordinate transmission to avoid collisions by means of continuous channel sensing. In d) SDMA, an angle-diversity transmitter can serve users separated in the spatial domain. In e) CDMA, each transmitter has a unique code that allows users to select which packets are destined to them. In f) NOMA, different power levels are allocated to each user.

single user to increase its throughput.

The commonly known Time Division Multiple Access (TDMA) can be applied to LiFi as well [133]. In fact, the Access Point (AP)s allocate time slots to different users to achieve multiple access, albeit losing spectral efficiency due to potentially very long waiting times as more and more users request access to the shared medium.

Continuous channel sensing allows the users in a network employing Carrier-Sense Multiple Access/Collision Detection (CSMA/CD) [134] to avoid collisions and achieve a relatively interference-free environment for many users at the same time. More specifically, idle users can sense when the channel is busy and consequently delay transmission until it becomes free again. On the other hand, the transmitting user can use CD to detect collisions and re-attempt transmission. While this technique could reduce the spectral efficiency loss of TDMA, it does not guarantee good performances especially with higher number of users.

In Space Division Multiple Access (SDMA) [135], an angle-diversity transmitter, composed by multiple transmitting elements, uses the space dimension to simultaneously serve users active in different positions. Though its RF version was already part of the IEEE 802.11ac standard [136], its OWC implementation requires designing a specific transmitter, which increases the complexity of the luminaires in an indoor application.

By exploiting optical orthogonal codes, a multiple access scheme called Code Division Multiple Access (CDMA) [137, 138] grants simultaneous multiuser network access. However, the presence of such codes requires to reserve communication overhead, leading to reduced performances.

A scheme called Non-Orthogonal Multiple Access (NOMA) [64, 139–141] assigns different power levels to multiple users, so that they can utilise the full time and spectrum resources at the same time; however, the differences in received power between users causes a reduction of Signal-to-Interference-plus-Noise Ratio (SINR) and consequent degradation in performances.

Another way of serving multiple users at the same time (that is specific to OWC and not applicable to RF) is that of employing Wavelength Division Multiple Access (WDMA), which has been thoroughly investigated in [56] and will be discussed in a separate section as it is relevant to the topic of this thesis.

In conclusion, it can be seen that many modulation schemes suitable for many different OWC applications are available in the literature. For example, in an application such as the IoT, one of the most appealing choices is OOK. This is because in IoT the nature of devices that are typically employed does not pertain to a single category. Simpler devices will introduce a complexity constraint on the receiving side of the communication system if the designed solution is to be usable on every IoT device. Other crucial benefits of this choice are that OOK is inherently ready to support digital dimming schemes and overall offers a good trade-off between implementation complexity, achievable transmission speed, and energy efficiency [17].

For what it is specifically concerned with this work, the choice of the modulation scheme does not constitute a strict requirement, and the proposed solutions can easily be implemented and verified with any of the presented schemes, both single- and multi-carrier.

The choice of the multiple access scheme, on the other hand, holds significant importance, and it will be discussed more in detail in the following section. As seen:

- OFDMA requires an increased transmitter and receiver complexity, which is seemingly not suitable for simpler devices normally found in the context of IoT.
- While very simple, TDMA does not have the capacity to account for very high number of users in a network: more users will significantly increase the time between successive time slots.
- CSMA/CD constitutes an improvement over TDMA, where users are able to detect collisions and only transmit whenever the channel is free. Nonetheless, the same concerns regarding the behaviour of the network in presence of very high number of users remain.
- Because of cost and size of the required angle-diversity transmitter, SDMA as proposed could struggle to guarantee a sufficient amount of separation in the spatial domain so that a higher number of users could be served.
- As discussed, the introduction of transmitter-specific codes in the transmission increases the required overhead and reduces network performance in Code Division Multiple Access (CDMA). Additionally, this degradation increases with the number of transmitters.
- Finally, the concept of allocating different power levels to different users naturally leads to substantial SINR degradation for those users that have a lower received power. This both limits the number of users that can be served at the same time, and the fairness of the resulting network.

For these reasons, an indoor LiFi network focused on user mobility, IoT and smart lighting capabilities would need a different, better suited approach.

2.3 Wavelength Division Paradigms

2.3.1 Wavelength Division Multiplexing

The concept of using colour as an additional degree of freedom is an interesting one because it would allow a good degree of separation over multiple channels (usually 3 or 4). This is achieved with the use of Red-Green-Blue (RGB), Red-Green-Blue-Amber (RGBA) or Red-Green-Blue-Yellow (RGBY) LEDs at the transmitter side and an equal number of PDs with matching coloured filters at the receiver side, potentially improving the network capacity. This approach is termed Wavelength Division Multiplexing (WDM), and it has been successfully implemented and demonstrated in several instances, such as [16, 142–147], with consistently good results in terms of achievable data rate. Another benefit of this paradigm is its independence from the modulation scheme employed. In fact, each colour can be seen as an individual, separate channel capable of delivering a virtually independent signal to a matched, colour-filtered receiver. It has to be noted, though, that spectral leakage can lead to severe cross-talk if the receiver design is not carefully considered, especially in terms of choosing the right filters [148–150].

2.3.2 Wavelength Division Multiple Access

WDMA employs a similar system to that of WDM, and its peculiarities have been explored and discussed in [151]. The key difference is that in WDMA each colour is meant to serve a different user, thus providing a trade-off between the number of serviceable users (which increases with the number of available channels) and the maximum achievable data rate for each user. As it is intuitive, though, the total network capacity remains the same. WDMA was first investigated in application to optical fibre communications [152] and has drawn the researcher's attention since then. [153] for instance, compare optical CDMA and WDMA in these settings and report that while the utilization of CDMA exceeds that of WDMA at high offered loads, the peak utilization of the WDMA system is still superior. Furthermore, in WDMA the communication medium (the free space optical path in this case) can be used at the same time by every wavelength at the transmitter side. This creates the potential of transmitting on as many parallel and independent channels as the number of wavelengths.

At receiver side, the signal is picked up by a receiver with an optical filter to exclude unwanted wavelengths. However, if a receiver is to be able to pick up any of the wavelenghts transmitted, it will need to have as many receivers, each with an optical filter. This severely limits the number of users that can be served with WDMA by each transmitter. Additionally, if more than one transmitter are close in space (as what happens with different luminaires in a room for example), there is a severe risk of cross-talk, as the transmitters would employ the same wavelengths.

To the best of the authors' knowledge, these limitations have not been tackled before in a LiFi environment with many users free to roam, and will be the focus of this dissertation.

2.4 Channel Model

A well-recognised work from J. Kahn and J. Barry [69] has summarised the various properties of a typical wireless line-of-sight "channel DC gain" for an OWC link where the transmitter is a Lambertian radiator. This case applies to all transmitters considered in this work, and such typical link is represented in Figure 2.4.

In their work, these authors described the channel DC gain $H(0)$ as following an inverse squared law with respect to the distance between the a-th transmitter and the u-th user's receiver. This introduces a severe attenuation of the received signal, which negatively affects the link budget and limits the achievable performance in OWC, both in single-point and networked configurations. In this regard, a bigger collection area at the receiver side, minimising the angle of emission of the transmitter and AoI of the receiver, all positively impact the received signal and can be used to contrast the effect of distance.

In later works, there is an effort to obtain the Channel Impulse Response (CIR) specific to a VLC system. This has been done in [154] by means of Monte Carlo ray-tracing simulations, with a method that can yield CIR for any given indoor environment by taking into account the effects of geometry, the objects in the environment,

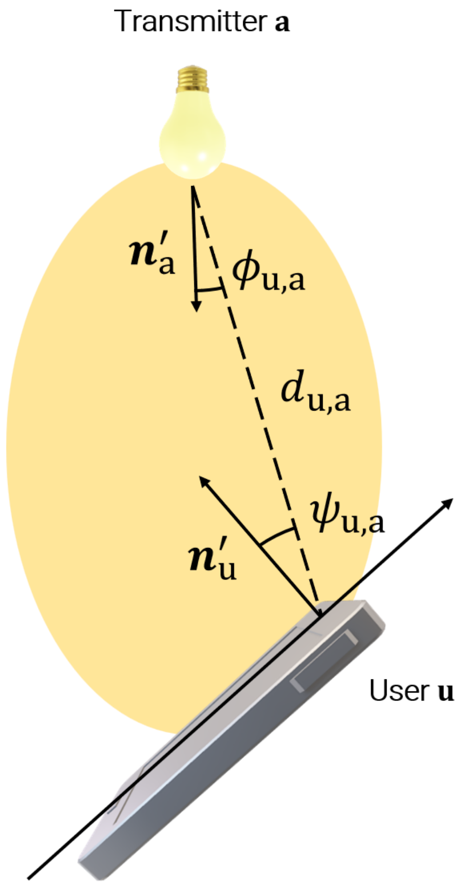

Figure 2.4: LOS optical path in a OWC link. Here, $\mathbf{n}'_{\mathrm{a}}$ is the direction of emission of the transmitter, $\phi_{\mathrm{u,a}}$ is the emission angle between the a-th transmitter and the u-th user's receiver, $d_{\mathrm{u,a}}$ is their Euclidean distance, $\mathbf{n}'_{\mathrm{u}}$ is the perpendicular direction to the u-th user's receiver, and $\psi_{\mathrm{u,a}}$ is the Angle of Incidence (AoI) of the light beam coming from the a-th transmitter to the u-th user's receiver

and their reflectance. Another interesting approach has been used to derive an analytical expression for the CIR in [155], with the advantage of lacking the need for time-consuming simulations. Finally, in [156] a comprehensive model is developed for obtaining the channel response of an indoor multi-wavelength system, which includes blockages and reflections. However, this interesting approach is very computationally demanding especially when a higher number of users imposes cumbersome calculations.

2.4.1 The Passband Shift Phenomenon

The Passband Shift (PS) phenomenon for thin-film optical filters has been described in detail in [157]. It consists of a shift towards shorter wavelengths of the relative transmission spectra of such optical filters, with a dependence on the AoI of the impinging light. The shifted wavelength of an optical filter characteristic, $\lambda_{\mathrm{OF}}(\psi)$, dependent on the AoI, is then given as:

$$\lambda_{\mathrm{OF}}(\psi) = \lambda_{\mathrm{OF},\psi=0}\sqrt{1 - \frac{\sin^2(\psi)}{n_{\mathrm{e}}^2}} \tag{2.1}$$

Where $\lambda_{\mathrm{OF},\psi=0}$ is the non-shifted wavelength of the considered transmission characteristic (namely, passband edges and central wavelength). Moreover, ψ is the AoI of the impinging light, and n_{e} is the effective refractive index of the specific optical filter employed. It can be verified that for the values that ψ will likely take in an everyday use case, as thoroughly investigated in [158–162], this phenomenon can become another important limitation to the channel separation capabilities of WDMA.

Additionally, to the best of the author's knowledge, the literature lacks a comprehensive study that investigates the performances of WDM and WDMA in the context of everyday use, where the users' random position and mobility are taken into account.

2.5 User Mobility

In networked indoor and outdoor environments involving the use of mobile devices (such as smartphones), accounting for the natural mobility of the users, which involves a degree of randomness in their movements, is of the utmost importance. Yet, because of the lack of an adequate model for device orientation, this aspect has often been overlooked in favour of fixed orientation with devices pointing upwards. A more comprehensive approach is only being considered relatively recently. A number of studies have considered the effect of device orientation [159–161, 163–165], but the first one that targets this issue from an experimental perspective provides a very interesting contribution. In fact, the authors in [158] have conducted a series of experimental measurements on 40 users, which show that the Probability Density Function (PDF) of the polar angle of the device (that is, the inclination at which the device is being held) can be modelled with a Laplace or a Gaussian distribution for static or walking users, respectively. In addition, they have derived a closed-form expression for the PDF of the cosine of the AoI.

Stemming from that work, in [159] the importance of device orientation is assessed in terms of the performance of a LiFi-based system.

Another important result is achieved in [160]. A correlation function-based model is proposed to measure channel variations coming from changes in the orientation and inclination of the receiver. The results show that a substantial change of $10°$-$20°$ in the receiver's inclination angle is required to produce a distinguishable change in the channel gain. Moreover, it is shown that repetitive measurements of the angles become uncorrelated after a few hundred milliseconds.

In [161], the authors propose an extended orientation-based random waypoint mobility model that combines findings of mobile device inclination and orientation angles with conventional user mobility models. This is considered both while users are walking and pausing in their trajectories.

In [165], the authors have analysed a hybrid LiFi-RF scenario, modelling the handover probability while using a RSSI-based handover algorithm.

2.6 User Localization

The problem of accessing information on a given user's position in time is relevant for many fields, and ethic concerns aside, optimising wireless communication (both in RF and OWC) certainly is one of such fields. For this reason, many technologies have been researched for this purpose.

A very common way of accessing the position of a device is through its Received Signal Strength (RSS) [166–171]. It is usually measured in dBm and its relative indicator, the Received Signal Strength Indicator (RSSI), can be calculated as:

$$\text{RSSI} = -10n\log_{10}(d) + A. \tag{2.2}$$

Here, n is the path loss exponent (which can assume many different values, e.g. 2 for free space), d is the distance between the transmitter and the receiver, and A is the calibrated RSSI at a reference distance. By reversing this formula as a function of the distance d, this latter can be estimated. However, this cannot be used for precise and reliable positioning especially in OWC, because it is not possible to derive the user's position from only knowing its distance from the transmitter. Furthermore, RSSI is insensitive to the contribution of cross-talk, which can be far from negligible in many cases, including when WDMA is employed.

Other common approaches include Time of Flight (ToF) or Time of Arrival (ToA) [172], Bluetooth Low Energy (BLE) [173] and Angle of Arrival (AoA) [174]. This latter specifically, is considered to be the most accurate for VLC [175,176]. However, all these methods impose an increase in receiver device complexity, which may not be feasible in IoT.

As the matter of precise user localization is still an open problem in OWC, this work will mainly rely on SINR measurements that are assumed to be carried out at a network level. SINR is a metric that not only includes the signal strength, but also the interference, rendering it more appealing for WDMA.

2.7 Smart Lighting

It is estimated that lighting expenditures account for 10-38% of total energy costs [177]. In a world striving for ever greener approaches to solving daily problems, smart lighting can introduce significant energy savings on account of being able to simply turn off artificial illumination sources when they are not needed. This is one of the reasons why it is envisioned that the market for smart lighting will account for 47 billion of dollars in the next 10 years [178].

Other than saving energy, smart lighting technologies can be used to achieve many purposes, such as enhancing carrying out specific tasks, achieving desirable aesthetic results, and improving user comfort. This is done with the help of IoT integrating together information coming from numerous sensors, such as motion, temperature, and luminous sensors installed throughout the environment. These can be used to automate artificial lighting power on, dimming level, and lighting temperature according to user-specified behaviours.

Lighting systems have to be designed with reliability in mind, other than the ability to separate functional “zones” in a home environment [179]. With smart lighting, this concept is extended to even more significant alterations to the mood of a room and the objects contained therein [180].

It comes as no surprise that research in this field is more active than ever to devise complex solutions that make lighting technologies even smarter. In the early stages of this development, authors in [181] have presented a comprehensive switch panel that allowed users to monitor and control all the lighting in a house with one single remote, saving the time and energy required to check every light source individually. The authors in [182] instead have shifted the focus on the lighting central control, proposing two decentralised algorithms that can experimentally achieve uniform lighting at the ground plane of an indoor environment. The approaches have been tested under a variety of adverse conditions, including cross-illumination and interference from external daylight, achieving encouraging results in terms of uniform illumination and saving energy. The work in [183] proposes a novel energy-efficient strategy for a smart lighting system by solving an optimisation problem that takes into account LED dimmability and the possibility of dimming external daylight with window shading systems. This can achieve energy savings on account of using indoor lighting to complement exactly the level of illumination coming into a building from natural sources. On the topic of providing dimming capabilities to indoor lighting fixtures, it has to be noted that the IEEE 802.15.7 standard [72] provides such capabilities in VLC systems. In fact, it presents several ways (compatible with different modulation schemes) to change the perceived brightness of the light sources while using them for wireless communication at the same time, by reducing the spectral efficiency in exchange.

In [184], smart lighting is achieved by using thermal sensors as a way of detecting human presence and turning on the illumination accordingly. In [185], a joint smart light and intrusion detection system based on the IoT and using Raspberry Pi is presented and prototyped.

In addition to this, there is also a growing interest in using IoT technologies in conjunction with OWC, and specifically VLC, often using the light to achieve both smart illumination and delivery of high-speed wireless communication at the same time. In [186], a power allocation algorithm is proposed to save energy while achieving uniform illumination and providing indoor VLC features at the same time. In [187], the authors leverage the IoT, LiFi, and the need for artificial lighting in agricultural contexts to envision a proof of concept for a precision greenhouse. Finally, the work in [188] further advances the technological synergy between LiFi and IoT (including smart lighting) by proposing a slicing scheme for AP resources. This is compatible with both technologies at the same time.

2.8 Network Operation Schemes

In an optical atto-cell network, co-channel interference (CCI) between adjacent optical atto-cells limits the performance. Multiple approaches have been investigated to tackle this problem. In [42], the sojourn time of users has been drafted analytically and considered with two handover criteria (Received Signal Strength, and RSS with threshold), suggesting that sojourn time could be a useful parameter to be used with prediction algorithms. In [43], Cheng et al. have proposed two Fractional Frequency Reuse (FFR) schemes in a DCO-OFDM-based optical atto-cell network and compared them with a full frequency reuse scheme. Results have shown that FFR schemes can effectively improve interference mitigation by using different frequency sub-bands for users according to their position in the centre or the edge of the cell. The improvement on the average SINR is between 2.07 and 10.3 dB with regard to the full frequency reuse. A novel Joint Transmission scheme is proposed in [47] that assigns the transmission type as a single point for users in the cell centre and a multi-point for users in the cell edges. By exploiting the fact that light signals superimpose constructively, this scheme is capable of improving median SINR by 16.4 dB in comparison to a full frequency reuse scheme and median system throughput by 67.6% when compared with a static resource partitioning scheme. Another cooperative reflection-based technique is investigated in [50]. By using the Reference Signal Received Power and its rate of change in [52], Wu shows that it is possible to skip certain unnecessary handovers and gain 26% higher throughput with respect to a conventional handover scheme. An interesting adaptive Multiple-Input Multiple-Output (MIMO) technique is presented in [53]. Based on a desired spectral efficiency and target error rate, the best technique is selected out of three possibilities: Repetition Coding (RC), Spatial Multiplexing (SMP), and Spatial Modulation. By operating the selection based on the lowest energy requirement, it is possible to minimise power consumption. In [189], the problem of lowering the PAPR is considered, with regard to different techniques that help tackle it.

Finally, in [190], a new cell-free architecture is proposed, and in [191], amorphous cells are introduced.These are particularly interesting approaches, as the concept of atto-cell is replaced by a user-centric perspective that opens a range of new possibilities, especially in terms of handover reduction, Quality of Service (QoS), and energy efficiency targets.

Concerning network algorithms targeting wavelength division-based systems, to the best of the author's knowledge, there is a considerable gap waiting to be filled as wavelength division paradigms present an underlying potential combining higher throughput with parallel channels and interference mitigation capabilities that would be useful in a densely deployed setting.

Conversely, much of the literature in this regard seems to be focused on wavelength reuse.In [192], the authors investigate the effects of the wavelength reuse pattern and cell size on the performance of a WDMA network employing OOK. They also propose design curves to facilitate the system design process. However, there is an inherent limitation introduced by the concept of wavelength reuse in a networked environment. Since it entails dividing the available wavelengths so that neighbouring cells do not interfere with each other, the wavelength reuse pattern can introduce variations in illumination temperature. Another limitation is that the achievable throughput is greatly limited because of wavelength reuse.

2.9 Chapter Summary

It is clear that, given the number of possibilities in terms of system design choices, one has to carefully choose all its aspects to work towards a common goal. For example, LiFi implementations in a highly industrialised complex, an office, a hospital, or a smart home environment will be all differently designed to accommodate the specific requirements of the application. This is why, given the context and the focus of this work, the following system design choices are made:

- Requirement: User Mobility and Density

  One of the device categories that the IoT encompasses is that of portable equipment. Smartphones, smartwatches, and other wearables, and even some more advanced tools, are not designed to be used in a fixed place and thus could pose a challenge in LiFi for IoT since the changing position and orientation could potentially decrease the received signal. Moreover, each user can have more than one of these User Equipments (UEs), dramatically increasing their number.

- Modulation Scheme: Independent

  Since the focus of this work is network-level operations, the system is independent of the modulation scheme and even retains the flexibility to implement higher-level algorithms to dynamically select the scheme employed.

  As mentioned at the end of Section 2.2.5, given the accent on IoT application, the OOK scheme could be chosen during the system design phase. This is motivated by two considerations: power efficiency and complexity. In fact, as seen in the literature, single-carrier modulation has the highest potential in terms of both power efficiency and complexity. The OOK scheme is one of the simplest modulations available both in RF and the OWC realms, and it would be easy to decode data sent this way even on the lower-complexity devices that can be found in an indoor IoT environment (such as home appliances or small portable devices that lack adequate processing power).

- Multiple Access Protocol: Wavelength Division Multiple Access

  Smart lighting is one of the applications of IoT, where a smart home has the capability of adaptively changing the illumination activation, intensity, and colour temperature based on parameters like the time of day, external lighting, the user's presence and position, and even the nature of tasks that are to be carried out in a specific area. With these premises, it is clear what advantage the ability to control colours individually will bring.

  Moreover, the wavelength selectivity introduces new degrees of freedom in the system that all concur to increase the network's achievable data rate.

Chapter 3

The Impact of Passband Shift

3.1 Introduction

The first technical chapter, which is based on the work published in [193], has the aim of determining the impact of the Passband Shift (PS) effect on a wavelength division-based Light Fidelity (LiFi) network. This is not only limited as to how and why the performances of such systems could be limited due to the presence of the PS effect, but also as to which opportunities would, from a system design perspective, allow to leverage this phenomenon.

As demonstrated in [15,16] among others, wavelength division is a useful framework for improving the performances of a Visible Light Communication (VLC) point-to-point link due to its ability to add a further degree of freedom by means of wavelength separation. As it is intuitive, this can also be extended to an entire LiFi network made up of multiple lighting fixtures each acting as an independent Access Point (AP).

Additionally, as the various Light Emitting Diode (LED)s composing a single AP are individually addressable (such as in the case of RGB, YRGB, or RGBA LEDs), their emitted power can be adjusted so that the entire system becomes compatible with the implementation of smart lighting strategies in a room or a building.

The contributions of this chapter can be listed as follows:

- A closed-form approximation of the Probability Density Function (PDF) of the central wavelength of an optical filter at its receiver, including the PS effect, is derived in the case of random Angle of Incidence (AoI). This is done by building on previous works that tackle user mobility behaviour and that contain a closed-form approximation of the cosine of the AoI of a portable device during walking activities with respect to a light source.

- Computer simulations using the Monte-Carlo method are designed and carried out with the aim of validating the aforementioned new approximation.
- A definition of the Spectral Overlap (SO) parameter, which takes both the AoI and PS into account, is formally introduced and derived. Then, its curve shape is discussed for a RGBA system.
- An extensive discussion is made on how this knowledge can be used in the system design phase for a wavelength division-based LiFi network with the aid of simulation work. Intra-AP and inter-AP interference are considered with respect to Optical Front-End (OFE) optimisation.

As shown in [157], one of the underlying characteristics of the PS effect is its dependence on the AoI of the light reaching the Photo-Detector (PD). In fact, when the light beam impinges perpendicularly, the central wavelength and shape of the optical filter's transmissivity curve does not show any variation with respect to its original design. This is the reason why, in the context of a wavelength division-based network, it is very important to consider the characteristics of user mobility. In this regard, this dissertation builds on the valuable premises regarding users' behaviour established by recent works, such as [158–161, 164].

In [158], two contributions are notable with respect to this chapter, both of which tackle one of the main shortcomings of the literature research up to that point. Firstly, the authors conducted an experiment involving 40 users with the aim of recording live data on the orientation of their portable devices under various usage conditions. An application for continuously recording acceleration and gyroscopic data on the devices was installed, and the users were asked to use such devices both in landscape mode and portrait mode to carry out various activities, both while sitting and while walking in a corridor (which was 1.5m wide and 40m long). These results are shown in Figure 3.1, which belongs to that work.

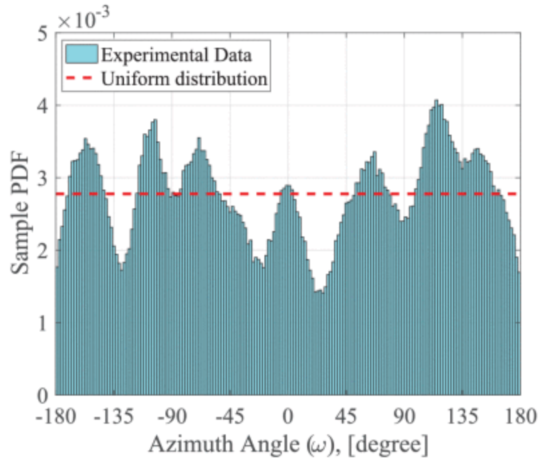

(a) Sitting activities

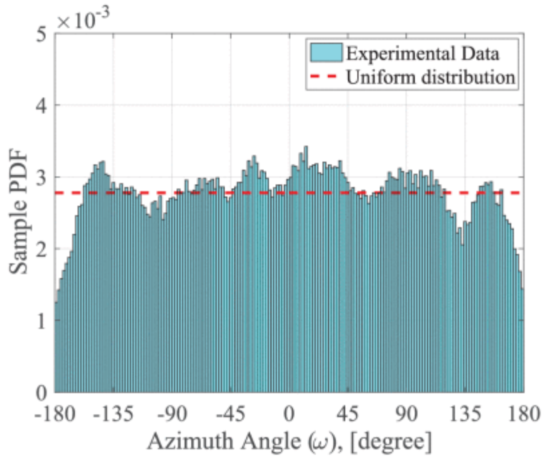

(b) Walking activities

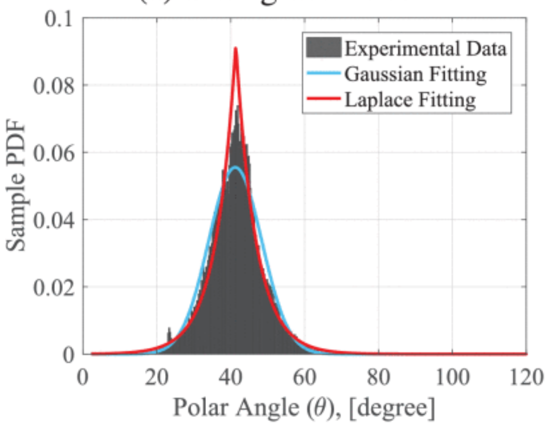

(c) Sitting activities

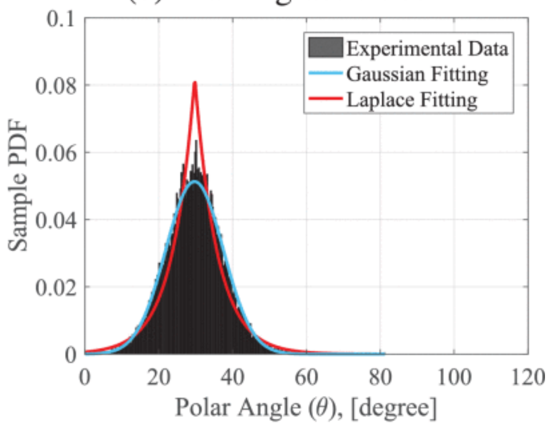

(d) Walking activities

Figure 3.1: Movement and rotation statistics. This figure, which belongs to the work in [158], shows experimental results for devices' position and orientation, both in sitting and walking activities, along with appropriate curve fitting. It can be seen that in the case of walking users, the position follows a uniform distribution and the orientation is best approximated by a Gaussian distribution.

Secondly, they derived the PDF of the inclination angle θ and of the optical path loss $H_{\text{LOS}}(0)$. They subsequently also derived a closed form expression for the PDF of the cosine of the AoI (denoted with ψ) conditioned on the user's orientation ω. These will be used as a basis to develop the work in this chapter.

3.2 System Model

3.2.1 Rotation Geometry

An important set of assumptions has to be made with respect to the rotation geometry, which is relevant not only to the present chapter but to the entire dissertation. It should be noted that in this context, the term "rotation geometry" is only referred to as the orientation in space that the *receiving devices* in a generic Optical Wireless Communication (OWC) link assume, as the transmitter side is usually thought to be well fixed in the ceiling.

The geometrical definition of the classic Euler angles is used throughout this work, and every rotation in the $\mathbb{R}^3$ space can be uniquely achieved by concatenating an ordinated set of three sub-rotations around the axes of a coordinate system. More specifically, two coordinate systems are considered here: one concerns device coordinates and is denoted with xyz, and the other concerns Earth coordinates, denoted with XYZ. Following this distinction, a rotation with respect to the device coordinates is called an "intrinsic rotation", while if the rotation is referred to in terms of the Earth's coordinates, it is termed "extrinsic rotation". Regarding intrinsic rotation specifically, the World Wide Web Consortium (W3C) has set the standard in the matter of rotation order regarding device orientation. This is $(z \rightarrow x' \rightarrow y'')$, where $x'y'z'$ and $x''y''z''$ are respectively the device coordinate systems after rotation around the z-axis and then after the x'-axis. The angles pertaining to each of the three sub-rotations (whose combination yields the final rotation), α, β, and γ, are respectively termed yaw, pitch, and roll. These are angles commonly recognised and easily accessible on modern mobile devices [194].

It is possible to define $\mathbf{n}_{\mathrm{u}} = [n_x, n_y, n_z]^{\mathrm{T}}$ as the unit vector normal to the device's receiver, and $\mathbf{n}'_{\mathrm{u}} = [n'_x, n'_y, n'_z]^{\mathrm{T}}$ as the same unit vector after the complete rotation has taken place. This latter can also be represented in spherical coordinates by using the polar angle θ and the azimuth angle ω, and these are respectively the inclination angle (which is dependent on human wrist movements) and the orientation angle (which describes which direction the user is facing). More specifically, θ is the angle between

$\mathbf{n}'_\mathrm{u}$ and the positive direction of the Z-axis, and ω is the angle between the vector made by the x and y components of $\mathbf{n}'_\mathrm{u}$ and the positive direction of the X-axis. Intuitively, when $\theta = 0$, the device is oriented directly towards the ceiling, and when $\omega = 0$, the user is facing in the north direction.

If $\mathbf{R}$ is the rotation matrix denoting the complete rotation, it can be written as $\mathbf{R} = \mathbf{R}_\alpha \mathbf{R}_\beta \mathbf{R}_\gamma$, which follows the aforementioned intrinsic rotation order standard. Assuming that the device is initially oriented towards the ceiling (as in $\mathbf{n}_\mathrm{u} = [0, 0, 1]^\mathrm{T}$), and that the Earth and device coordinate systems (xyz and XYZ respectively) coincide, the device's unit vector after rotation $\mathbf{n}'_\mathrm{u}$ can be calculated as:

$$\begin{aligned}\mathbf{n}'_\mathrm{u} &= \mathbf{R}_\alpha \mathbf{R}_\beta \mathbf{R}_\gamma \begin{bmatrix} 0 \\ 0 \\ 1 \end{bmatrix} \\ &= \begin{bmatrix} \cos\alpha & -\sin\alpha & 0 \\ \sin\alpha & \cos\alpha & 0 \\ 0 & 0 & 1 \end{bmatrix} \begin{bmatrix} 1 & 0 & 0 \\ 0 & \cos\beta & -\sin\beta \\ 0 & \sin\beta & \cos\beta \end{bmatrix} \begin{bmatrix} \cos\gamma & 0 & \sin\gamma \\ 0 & 1 & 0 \\ -\sin\gamma & 0 & \cos\gamma \end{bmatrix} \begin{bmatrix} 0 \\ 0 \\ 1 \end{bmatrix}.\end{aligned} \tag{3.1}$$

It can be seen that $\mathbf{n}'_\mathrm{u}$ is dependent on the yaw, pitch, and roll angles. From here, the polar angle θ is found as:

$$\theta = \cos^{-1}(\cos\beta \cos\gamma) \tag{3.2}$$

and the azimuth angle ω can be calculated as:

$$\omega = \tan^{-1}(\frac{n'_2}{n'_1}) = \tan^{-1}(\frac{\sin\alpha \sin\gamma - \cos\alpha \cos\gamma \sin\beta}{\cos\gamma \sin\alpha \sin\beta + \cos\alpha \sin\gamma}) \tag{3.3}$$

This model has been used in many works that tackle the problem of user mobility in LiFi [158–161,164], and this dissertation is based on such a mathematical framework for all concerning the rotation geometry and the relative position and orientation between a device and a source.

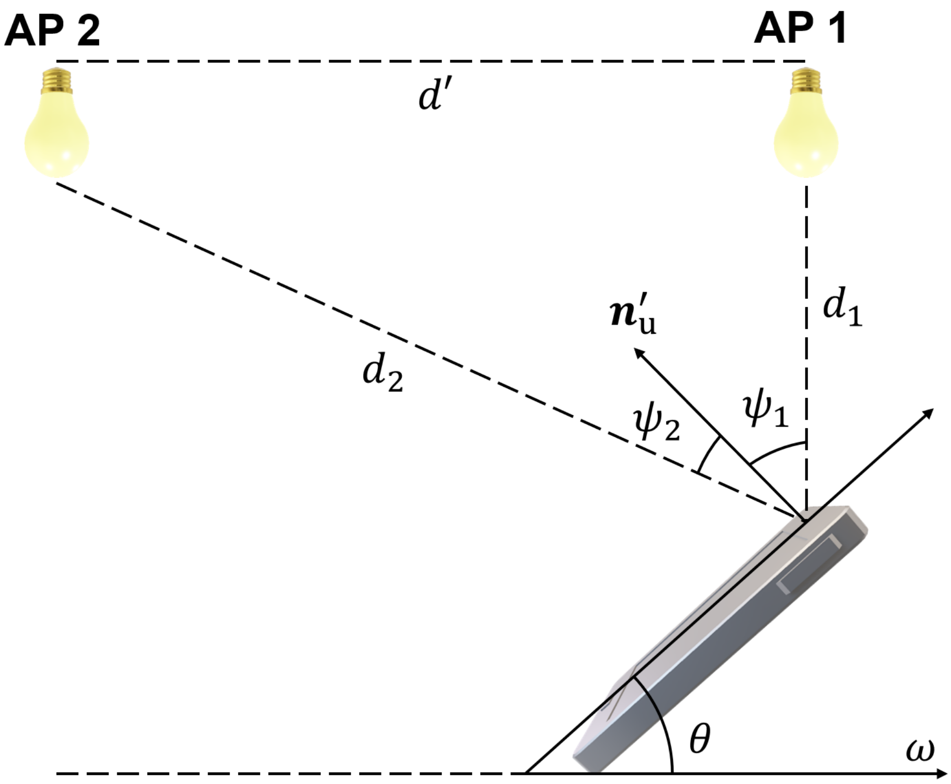

Figure 3.2: System geometry. The 2 APs are labelled as "AP 1" and "AP 2". The angles of incidence ψ for AP 1 and 2, and the polar angle θ, are shown. Note that in this work, the polar angle describes the inclination of the device when used in portrait mode.

3.2.2 Derivation of the PDF of the central wavelength

Figure 3.2 shows the system geometry that this chapter refers to. It depicts a room with two APs denoted as "AP 1" and "AP 2", and one user whose location is exactly below AP 1. As seen before, the inclination angle of the user's device (and thus, of the receiver, which is placed on the upper part of the screen) is denoted by θ. The unit vector perpendicular to the plane of the screen, whose origin coincides with the position of the receiver and positive direction goes from the screen itself towards the ceiling, is denoted with $\mathbf{n'}_{\mathrm{u}}$. The two angles of incidence with respect to AP 1 and AP 2 are denoted with ψ_1 and ψ_2, respectively, and as can be seen, they are directly related to the inclination angle of the device, θ. The distances between the user and the two APs are denoted by d_1 for AP 1 and d_2 for AP 2, while the distance between the two APs is denoted with d'. In order to avoid excessive complexity in the calculations, the user is assumed to have a fixed location and orientation. The user's orientation is opposite of the direction between AP 1 and AP 2 (intuitively described as looking away from AP 2). It can be seen that, as a result, the unit vector $\mathbf{n'}_{\mathrm{u}}$ is pointing towards AP 2. This is because the user is holding the device to comfortably look at its screen, and thus the user and the device itself are oriented in opposite directions.

In this chapter, the walking scenario is considered for users. Note that this does not refer to users changing their positions in the room but rather to the behaviour they adopt with respect to changing the polar angle as a result of their posture. Therefore, as modelled in [158], the cosine of the AoI ψ can be approximated with a truncated Gaussian distribution. Furthermore, an approximation of its PDF based on the first-order Taylor series ($\sin\theta \cong \theta'$ and $\cos\theta = 1$) is found in the same work as:

$$f_{\cos\psi}(\hat{\psi}) \approx \frac{\sqrt{2}e^{-\frac{1}{2}\left(\frac{\hat{t}-\hat{\mu}_\theta}{\hat{\sigma}_\theta}\right)^2}}{\hat{\sigma}_\theta\sqrt{\pi}\left[\operatorname{erf}\left(\frac{\hat{\tau}_{\max}-\hat{\mu}_\theta}{\sqrt{2}\hat{\sigma}_\theta}\right) - \operatorname{erf}\left(\frac{\hat{t}_{\min}-\hat{\mu}_\theta}{\sqrt{2}\hat{\sigma}_\theta}\right)\right]} \tag{3.4}$$

where $\hat{\tau}$ denotes the realisation of the random variable $\cos\psi$, $\hat{\tau}_{\max}$ and $\hat{\tau}_{\min} \leq \hat{\tau} \leq \hat{\tau}_{\max}$, since $\hat{\tau}_{\min}$ delimit the support range of $\hat{\tau}$ (and are not necessarily equal to 0 and 1, as it is shown in [158]). The mean and standard deviation of the distribution of the polar angle θ, respectively, are denoted with $\hat{\mu}_\theta$ and $\hat{\sigma}_\theta$. This equation shows that (as it is intuitive) the AoI ψ depends on the polar angle θ. The reason is that it represents an approximated analytical expression for the PDF of the cosine of ψ, conditioned on the position and orientation of the user.

Other fundamental contributions of the work in [158] are the closed-form approximation of the PDF and Cumulative Distribution Function (CDF) of the line-of-sight optical path loss, $H_{\mathrm{LOS}}(0)$. Those are respectively:

$$f_H(\bar{h}) \approx \frac{1}{h_{\mathrm{n}}} f_{\cos\psi}(\frac{\bar{h}}{h_{\mathrm{n}}}) + F_{\cos\psi}(\cos\Psi_{\mathrm{c}})\delta(\bar{h}) \tag{3.5}$$

$$F_H(\bar{h}) \approx F_{\cos\psi}(\frac{\bar{h}}{h_{\mathrm{n}}}) + F_{\cos\psi}(\cos\Psi_{\mathrm{c}})\mathcal{U}(\bar{h}) \tag{3.6}$$

where:

$$h_{\mathrm{n}} = \frac{(m+1)Ah^m}{2\pi d^{m+2}}$$

is a normalisation factor, Ψ_{c} is the half-Field Of View (FOV) angle of the receiver, and $F_{\cos\psi}(\cos\Psi_{\mathrm{c}})$ is the closed form expression for the approximated CDF of $\cos\psi$. Inside the expression h_{n}, m is the Lambertian emission order, A is the effective area of the PD, and d is the distance between the transmitter and the receiver. Lastly, $\delta(\bar{h})$ and $\mathcal{U}(\bar{h})$ respectively denote the delta Dirac function and the unit step function. The PDF and CDF of the line-of-sight optical path loss will not be used in the following derivation but will instead be useful as a means of validating the framework.

The derivation that is part of the contributions of this chapter begins with (3.4) and the exploitation of the fundamental relationship $\sin\psi = \sqrt{1-\cos\psi^2}$, which together lead to finding an expression of the CDF of the sine of the AoI, ψ:

$$F_{\sin\psi}(\hat{\eta}) = \Pr\{\sin\psi \leq \hat{\eta}\} = \Pr\{\sqrt{1-\cos\psi^2} \leq \hat{\eta}\} \tag{3.7}$$

$$F_{\sin\psi}(\hat{\eta}) = 1 - F_{\cos\psi}(\sqrt{1-\hat{\eta}^2}) \tag{3.8}$$

where $\hat{\eta}$ is the realisation of the random variable $\sin\psi$. This transformation is a fundamental and useful step because, as seen in (2.1), the shift of the central wavelength of an optical filter resulting from the PS effect, $\lambda_{\mathrm{OF}}(\psi)$, is dependent on the sine of the AoI. A further step can be made by noting that:

$$F_{\cos\psi}(\sqrt{1-\hat{\eta}^2}) = \int_0^{\sqrt{1-\hat{\eta}^2}} f_{\cos\psi}(t)\, dt \tag{3.9}$$

and solving the integral yields the closed form expression for the CDF of the sine of the AoI:

$$F_{\sin\psi}(\hat{\eta}) = 1 - \frac{1}{U}[\mathrm{erf}\,(\frac{\sqrt{1-\hat{\eta}^2}-\hat{\mu}_\theta}{\sqrt{2}\hat{\sigma}_\theta}) + \mathrm{erf}\,(\frac{\hat{\mu}_\theta}{\sqrt{2}\hat{\sigma}_\theta})], \tag{3.10}$$

where:

$$U = \mathrm{erf}\,[\frac{\hat{\tau}_{\max} - \hat{\mu}_\theta}{\sqrt{2}\hat{\sigma}_\theta}] - \mathrm{erf}\,[\frac{\hat{\tau}_{\min} - \hat{\mu}_\theta}{\sqrt{2}\hat{\sigma}_\theta}].$$

Lastly, differentiating (3.10) with respect to $\hat{\eta}$ yields:

$$f_{\sin\psi}(\hat{\eta}) = \frac{d}{d\hat{\eta}} F_{\sin\psi}(\hat{\eta}) = \frac{\sqrt{2}\hat{\eta} e^{-\frac{1}{2}\left(\frac{\sqrt{1-\hat{\eta}^2}-\hat{\mu}_\theta}{\hat{\sigma}_\theta}\right)^2}}{\sqrt{\pi}\hat{\sigma}_\theta U \sqrt{1-\hat{\eta}^2}} \tag{3.11}$$

which is a closed form expression for the PDF of the sine of the AoI, $\sin\psi$. With this, and manipulating (2.1) to be rewritten as:

$$\frac{\lambda_{\mathrm{OF}}(\psi)}{\lambda_{\mathrm{OF}}(\psi = 0)} = \sqrt{1 - \frac{\sin^2(\psi)}{n_{\mathrm{e}}^2}} \tag{3.12}$$

it is possible to write the following definition:

$$\rho(\psi) \triangleq \frac{\lambda_{\mathrm{OF}}(\psi)}{\lambda_{\mathrm{OF}}(\psi = 0)} = \sqrt{1 - \frac{\sin^2(\psi)}{n_{\mathrm{e}}^2}} \tag{3.13}$$

where $\rho(\psi)$ is hereby termed "spectral displacement". In fact, it is a factor that has to be multiplied by the starting central wavelength of the optical filter, $\lambda_{\mathrm{OF}}(\psi = 0)$, to obtain the shifted central wavelength, $\lambda_{\mathrm{OF}}(\psi)$ for a generic AoI. Its support range is $0 \le \rho(\psi) \le 1$, and it can be verified with (3.13) that if $\psi = 0$, then $\lambda_{\mathrm{OF}}(\psi) = \lambda_{\mathrm{OF}}(\psi = 0)$ and thus $\rho(\psi) = 1$. As a consequence, any starting central wavelength multiplied by the spectral displacement will result in no change. This is consistent with the AoI being $0°$, meaning that the light beam is impinging perpendicularly on the optical filter.

It is now possible to leverage 3.13 to define the CDF of the spectral displacement $\rho(\psi)$ as:

$$F_\rho(\hat{\rho}) = \Pr\{\rho(\psi) \le \hat{\rho}\} = \Pr\{\sqrt{1 - \frac{\sin^2(\psi)}{n_{\mathrm{e}}^2}} \le \hat{\rho}\} \tag{3.14}$$

where $\hat{\rho}$ denotes the realisation of the random variable $\rho(\psi)$. Note that this variable has a dependence on the AoI, ψ.

Now a closed form expression for the CDF of the spectral displacement $\rho(\psi)$ can be written as:

$$F_\rho(\hat{\rho}) = 1 - \frac{1}{U}[\mathrm{erf}\,(\frac{1-\hat{\mu}_\theta}{\sqrt{2}\hat{\sigma}_\theta}) - \mathrm{erf}\,(\frac{\sqrt{1-n_{\mathrm{OF}}^2(1-\hat{\rho}^2)}-\hat{\mu}_\theta}{\sqrt{2}\hat{\sigma}_\theta})], \tag{3.15}$$

which, after a differentiation with respect to the random variable $\hat{\rho}$, yields the PDF of the spectral displacement, $\rho(\psi)$:

$$f_\rho(\hat{\rho}) = \frac{\sqrt{2}n_{\mathrm{OF}}^2\hat{\rho}e^{-\frac{1}{2}(\frac{\sqrt{1-\hat{\eta}^2}-\hat{\mu}_\theta}{\hat{\sigma}_\theta})^2}}{\sqrt{\pi}\hat{\sigma}_\theta U\sqrt{1-n_{\mathrm{OF}}^2(1-\hat{\rho}^2)}}. \tag{3.16}$$

After noting that the definition of $\rho(\psi)$ provided in (3.13) is linear with respect to $\lambda_{\mathrm{OF}}(\psi)$, the next steps are as follows:

$$F_\lambda(\hat{\lambda}_{\mathrm{OF}}) = F_\rho(\frac{\hat{\lambda}_{\mathrm{OF}}}{\lambda_{\mathrm{OF}}(\psi=0)}) = \frac{1}{\lambda_{\mathrm{OF}}(\psi=0)}F_\rho(\hat{\rho}), \tag{3.17}$$

$$f_\lambda(\hat{\lambda}_{\mathrm{OF}}) = f_\rho(\frac{\hat{\lambda}_{\mathrm{OF}}}{\lambda_{\mathrm{OF}}(\psi=0)}) = \frac{1}{\lambda_{\mathrm{OF}}(\psi=0)}f_\rho(\hat{\rho}). \tag{3.18}$$

and finally explicit those in their extended forms:

$$F_\lambda(\hat{\lambda}_{\mathrm{OF}}) = \frac{1}{\lambda_{\mathrm{OF}}(\psi=0)}1 - \frac{1}{U}[\mathrm{erf}\,(\frac{1-\hat{\mu}_\theta}{\sqrt{2}\hat{\sigma}_\theta}) - \mathrm{erf}\,(\frac{\sqrt{1-n_{\mathrm{OF}}^2(1-\hat{\rho}^2)}-\hat{\mu}_\theta}{\sqrt{2}\hat{\sigma}_\theta})], \tag{3.19}$$

$$f_\lambda(\hat{\lambda}_{\mathrm{OF}}) = \frac{1}{\lambda_{\mathrm{OF}}(\psi=0)}\frac{\sqrt{2}n_{\mathrm{OF}}^2\hat{\rho}e^{-\frac{1}{2}(\frac{\sqrt{1-\hat{\eta}^2}-\hat{\mu}_\theta}{\hat{\sigma}_\theta})^2}}{\sqrt{\pi}\hat{\sigma}_\theta U\sqrt{1-n_{\mathrm{OF}}^2(1-\hat{\rho}^2)}}. \tag{3.20}$$

The equations in (3.19) and (3.20) are, respectively, the approximated closed form expressions of the CDF and PDF of the central wavelength of an optical filter. This concludes the derivation.

3.2.3 Spectral Overlap

The SO, $W(\psi)$, is defined as follows:

$$W(\psi) = \begin{cases} 0 & \text{if } \frac{|\lambda_{\mathrm{OF}}(\psi) - \lambda_{\mathrm{LED}}|}{\Delta\lambda_{\mathrm{OF}} + \Delta\lambda_{\mathrm{LED}}} > 1 \\ 1 - \frac{|\lambda_{\mathrm{OF}}(\psi) - \lambda_{\mathrm{LED}}|}{\Delta\lambda_{\mathrm{OF}} + \Delta\lambda_{\mathrm{LED}}} & \text{if } 0 \leq \frac{|\lambda_{\mathrm{OF}}(\psi) - \lambda_{\mathrm{LED}}|}{\Delta\lambda_{\mathrm{OF}} + \Delta\lambda_{\mathrm{LED}}} \leq 1 \end{cases} \tag{3.21}$$

and represents a measure of the overlap in the wavelength domain, given a certain AoI ψ, between a transmitter's emissivity and a receiver's transmissivity curves. The support range of the SO is $0 \leq W(\psi) \leq 1$. In fact, whenever these two curves occupy the same band in the spectrum (that is, if they have the same central wavelength and bandwidth), they overlap completely, and the SO will be equal to 1. Conversely, the farthest apart the central wavelength and bandwidths of the source and the optical filter are, the closer the resulting SO will be to 0. It can be noted that it has a dependency on ψ because of the PS effect, but it is also dependent on the starting central wavelength of the emissivity curve of the transmitter and the transmissivity curve of the optical filter. These two parameters are usually chosen during the system design phase of the OFE, and in order to maximise the performances, it is intuitive to choose them so that the SO is maximised. In some applications (such as laptops, desktop PCs, and home appliances) in which the receiver is usually kept fixed and can be oriented to have an AoI $\psi = 0°$ for prolonged periods of time, the ideal choice is to set the starting central wavelength of the optical filter transmissivity curve, $\lambda_{\mathrm{OF}}(\psi = 0)$, to be equal to its corresponding transmitter λ_{LED}. This can be done by means of adjustable receivers that have already been tested, and the SO can be reliably maximised.

However, in the case of indoor networks where users are free to roam and keep their devices at random orientations and inclination angles, this choice could become a very challenging one. Selecting a specific $\lambda_{\mathrm{OF}}(\psi)$ with the intent of optimising system performances regardless of users mobility could result in system performances being only occasionally optimised. This is because the AoI will not be fixed, and its distribution depends on users' movement in an analytically complex way. By using the closed form approximation (3.18) derived in this chapter, it is possible to find the most appropriate average value of ψ and evaluate how narrow or wide its distribution is around that value. This allows a better pairing of the two curves for the particular application. This means that in this case, based on the choice of the two central wavelengths $\lambda_{\mathrm{OF}}(\psi = 0)$

and λ_{LED}, the particular value of ψ for which the SO $W(\psi)$ is optimised will most likely be different than $0°$ as this latter corresponds to the receivers being kept facing exactly upwards. This particular value of ψ can be defined as $\psi' \geq 0°$ and $W(\psi') \rightarrow 1$.

At AoIs ψ higher than ψ', because of the PS effect, the transmissivity curve will shift its central wavelength towards shorter wavelengths, and its spectral shape will degrade. This will result in the SO $W(\psi)$ becoming progressively closer to 0 as ψ grows higher, meaning that $W(\psi)$ and ψ are inversely proportional.

The natural next step would be that of using the closed form PDF of the central wavelength of an optical filter derived in (3.18) in the definition of the SO, $W(\psi)$, to obtain an approximation of the PDF of the SO. However, despite attempts that have been made within this research, doing so results in an intractable equation that cannot undergo the integration required for the derivation method, even with computational means.

As seen, evaluating the SO can be useful in highlighting certain characteristics of the system design. A full system in a RGBA network will include four distinct PD on the receiver side, each with an optical filter for channel separation purposes. Intuitively, each optical filter will be impacted by the PS effect as a consequence of the random inclination of the device, and the implications of this have to be accounted for by considering the SO. A relevant example of this is shown in Figure 3.3, where the SO is evaluated for an entire RGBA receiver system with respect to increasing AoI. The central wavelength and Full Width at Half Maximum (FWHM) of the sources and OFs have been modelled after off-the-shelf components that have also been used in later chapters of this dissertation. More specifically, the sources are modelled after the emissivity of the RGBA LED LZ4-00MA08 from OSRAM Led Engin [195], while the OFs transmissivity is modelled after the FB450-40, FB550-40, FB590-10, and FB650-40 from Thorlabs [196–199]. Depending on the central wavelength of the sources and the OFs, it can be seen that the highest SO for each individual PD is not necessarily at $0°$.

To further highlight the impact that the PS has on such systems, Figure 3.4 shows a comparison, for each colour, of the SINR at increasing AoIs with and without the PS

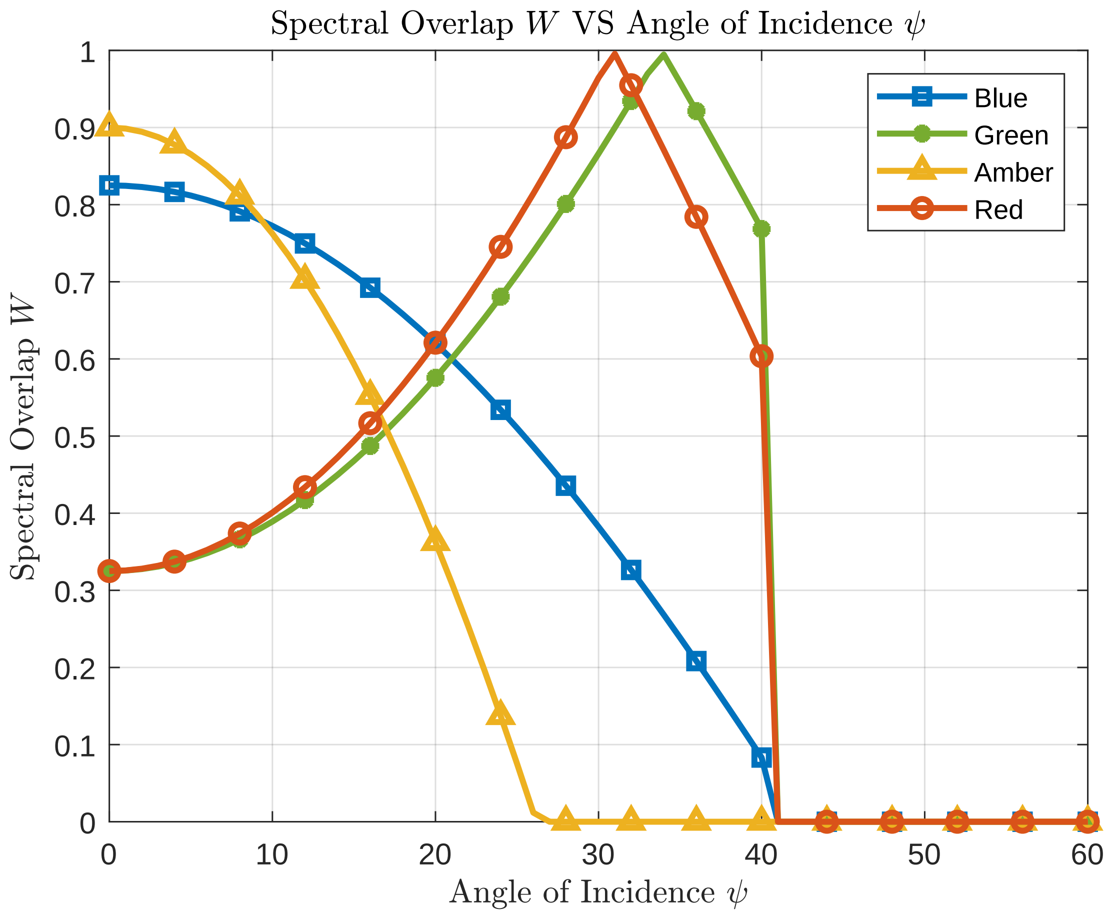

Figure 3.3: SO with increasing AoI in a RGBA system. Depending on the central wavelength of sources and optical filter, the optimal AoIs can be different for each individual PD.

effect. That means, when the AoI increases, in one case the PS effect is calculated and factored in as usual, while in the other the optical filter transmissivity does not shift, resulting in a curve that remains constant throughout the whole FOV. It should be noted that here, since a single AP with four colours is being considered, the interference for each colour is given by spectral leakage of the other three colours. This interference is termed "intra-AP interference" and refers only to other transmitters that make up the single AP (such as the case of RGB and RGBA fixtures).

In the case of the Amber optical filter, the PS is worsening the SINR from half FOV (20°) onwards. This happens because of its lower FWHM (10 nm, as opposed to 40 nm for every other colour), which makes it effectively more robust to the PS. However, it

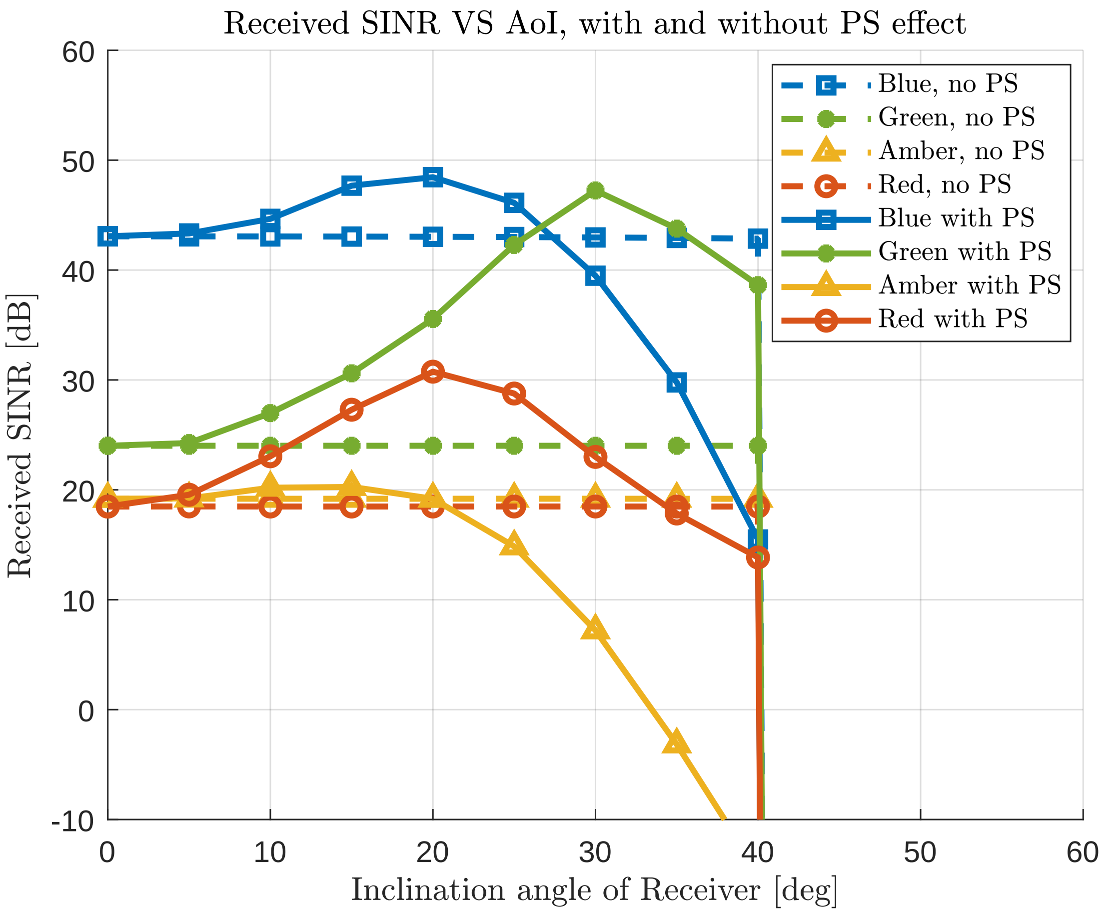

Figure 3.4: Signal-to-Interference-plus-Noise Ratio (SINR) with increasing AoI in a RGBA system, with and without the effect of the PS. At certain AoIs, the PS effect is improving the SINR.

can be seen from other colours that for these components, the presence of the PS effect does bring a benefit both in the average signal strength and channel separation, which translates into a better SINR for a large portion of the FOV. This demonstrates that the PS effect could be leveraged to improve the performances of the network; such a concept will also be investigated in a later section in the context of an entire network to evaluate the effects of inter-AP interference.

3.3 Analysis

3.3.1 Simulation Validation and Results

The simulation scenario used here is the same as the one shown in Section 3.2, and Figure 3.2 shows the geometry of the system. As mentioned previously, the only user that is present in this environment is located right below AP 1, and is facing the direction opposite to the horizontal component of the unit vector $\mathbf{n'}_{\mathrm{u}}$. Both its location and facing direction are fixed, but the polar angle at which the device is kept is variable and modelled with a truncated Gaussian distribution. The reason is that, as it was demonstrated in [158], this model approximates well the wrist movements when people use their mobile phones while walking.

For simplicity, only one colour is considered in these simulations, but this is done without loss of generality in the results, which are applicable to any other commonly employed options in the visible and IR spectra. This choice is made in this section in order to focus attention on the inter-AP interference, which is the interference provided by other channels employing the same wavelength in the source but that are spatially divided around the user. The transmitters are therefore considered to be single-colour LEDs, whose emissivity curve is here modelled with a rectangular function centred at $\lambda_{\mathrm{LED}} = 500$ nm, and the Half Width at Half Maximum (HWHM) is chosen as $\Delta\lambda_{\mathrm{LED}} = 25$ nm. This choice is actually arbitrary in this chapter and is made as such, as these are common values for off-the-shelf components. A similar function is also chosen to represent the optical filter transmissivity curve. As a consequence, the FWHM of the spectrum is 50 nm, which is also a common value for many off-the-shelf LEDs that are usually designed for illumination purposes. Moreover, it can be noted that in this case (which again, is an arbitrary one), $\lambda_{\mathrm{OF}}(\psi = 0) = \lambda_{\mathrm{LED}}$. This means that $\psi' = 0°$ and $W(\psi') = 1$. The effective refractive index of the optical filter is set as $n_{\mathrm{OF}} = 1.8$, similarly to what has been chosen in [157], as common values for real off-the-shelf components usually range between 1.6 and 2.0. This concludes the necessary set of system parameters that completely characterise a coloured link design, which are also listed in Table 3.1. The other parameters (such as Inter-AP distance, or Single detector area) that have not been discussed here come from the datasheets of off-the-shelf components that have been used throughout this entire dissertation.

Table 3.1: System parameters employed in computer simulations pertaining to this chapter.

System Parameters		
Symbol	**Description**	***Value***
N_{iter}	Number of realisations	10^6
d'	Inter-AP distance	1.2 m
A	Single detector area	9 mm^2
Ψ_{c}	Receiver half Field of View	40°
$\hat{\mu}_{\theta}$	Mean of polar angle	29.67°
$\hat{\sigma}_{\theta}$	Standard deviation of polar angle	7.78°
λ_{LED}	LED Central Wavelength	500 nm
n_{OF}	Effective Refractive Index of the optical filter	1.8
$\Delta\lambda_{\text{LED}}$	HWHM of LED emissivity	25 nm
$\Delta\lambda_{\text{OF}}$	HWHM of optical filter transmissivity	25 nm

The process for validating the equations found in the previous section is the following: first, $N_{\text{iter}} = 10^6$ realisations of the random variable θ (the polar angle) are generated according to the aforementioned truncated Gaussian distribution. Then, for each realisation of θ, the following parameters are calculated: ψ_1, ψ_2, $H_{\text{LOS},1}(0)$, $H_{\text{LOS},2}(0)$, $\lambda_{\text{OF}}(\psi)$, and $W(\psi)$. These are then compared with their corresponding analytical approximations, and the results are plotted against each other. This will allow to visually evaluate the closeness of the match between generated statistical data and its derived approximation.

Figure 3.5 shows the results for the optical channel gain. The comparison is made between the analytical approximation that was found in [158] and that was provided in (3.6). It can be seen that the optical channel gain is overall higher for AP 1, as the user is below that AP. Since the optical channel gain has an inverse square dependency on the distance between the user and the source, this is expected. In fact, as long as the source falls into the user's FOV (which is not always guaranteed in the case of random θ), a lower distance from the AP greatly impacts the optical channel gain.

Another important aspect that can be noticed in this result, though, is that the

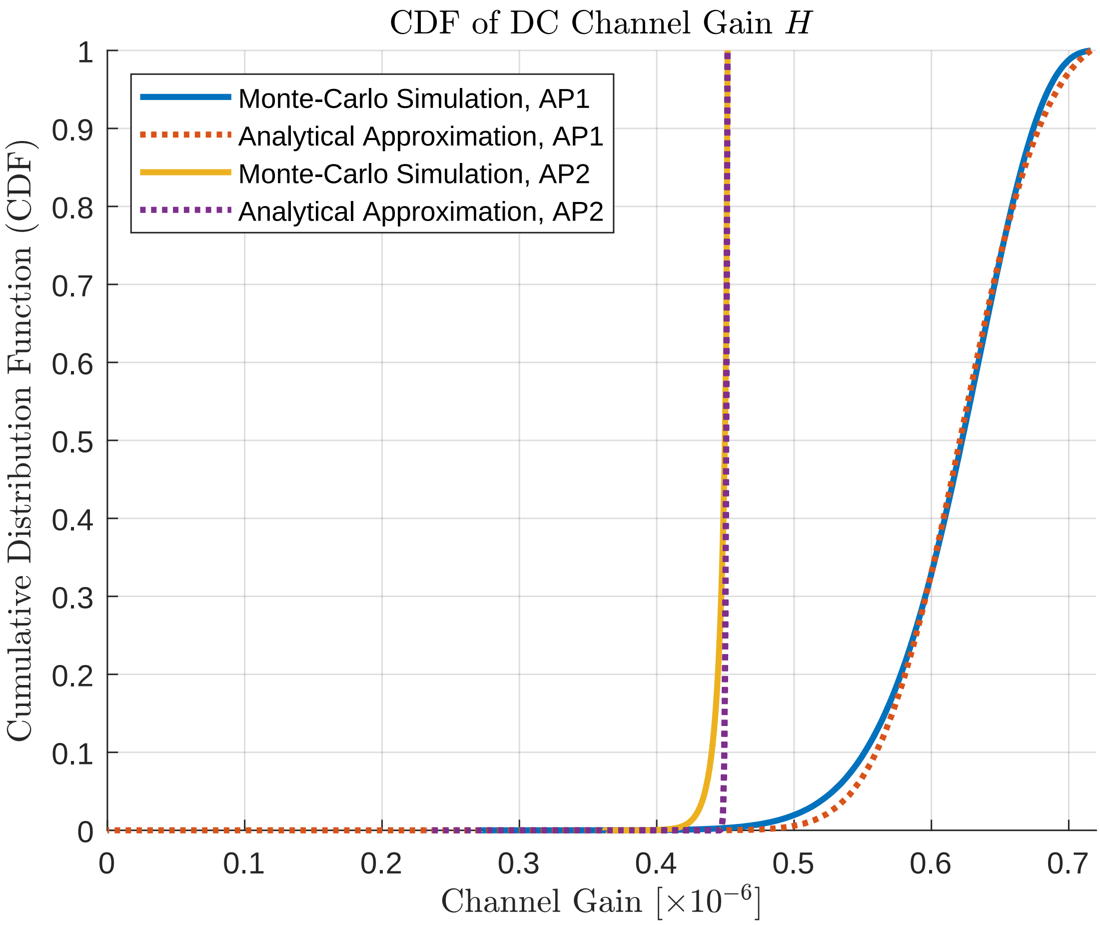

Figure 3.5: CDF of optical channel gain, for AP 1 and 2. Comparison between Monte-Carlo simulations and the analytical approximation. Optical path loss is more favourable when the user is directly below the AP (AP 1), but significantly less variable when displaced with respect to the AP (AP 2).

optical channel gain shows much lower variability for AP 2 than for AP 1. This means that in such a situation, even if the signal power coming from AP 2 might be lower, the sudden and continuous changes in the AoI generated by wrist movements would have a lesser impact on the signal strength, thus resulting in better reliability of the link. This is because the average AoI is close to $0°$ for AP 2.

Finally, as the analytical approximation closely matches the simulation results, this can be considered a validation of the simulation environment that has been built for this chapter and generated all the results shown thereafter.

Figure 3.6 shows the result of a comparison between Monte-Carlo simulations and

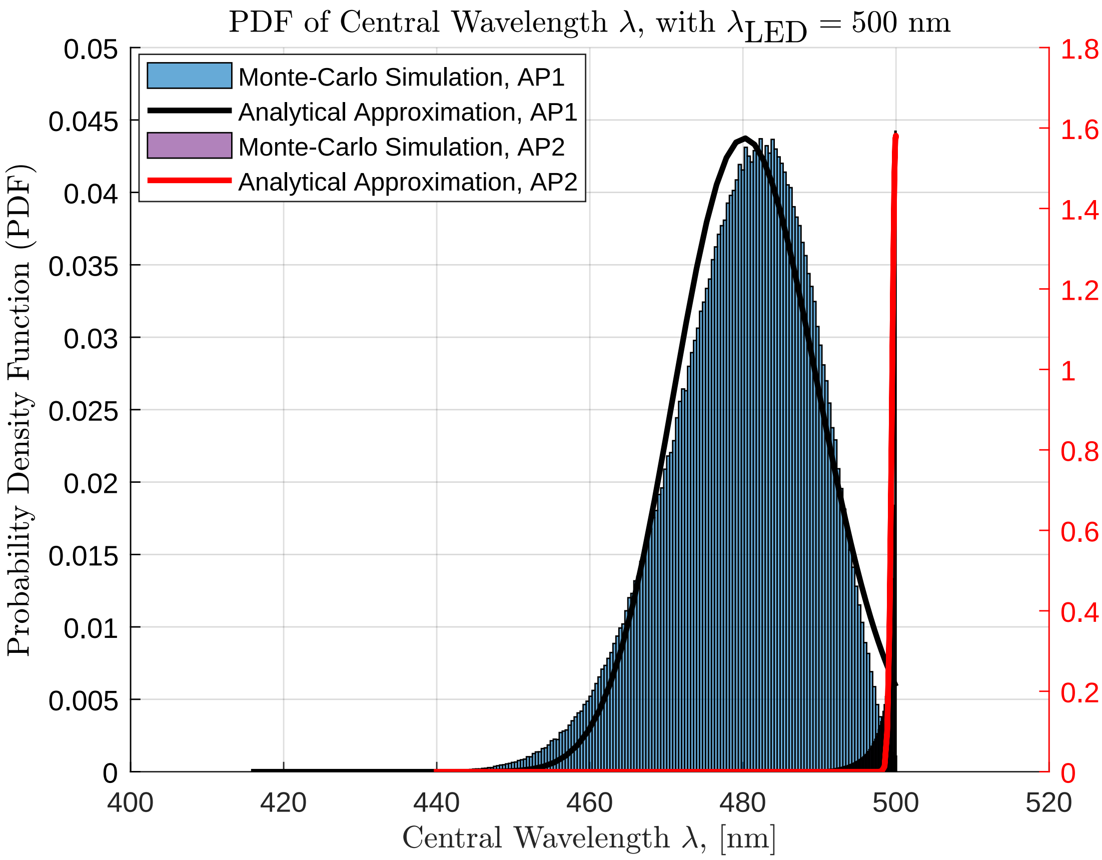

Figure 3.6: PDF of shifted central wavelength of the optical filter, for AP 1 and 2. Comparison between Monte-Carlo simulations and the analytical approximation. The central wavelength shift is much less prominent and variable for AP 2, suggesting that such a link would be more stable in these conditions.

the analytical approximation of the PDF of the central wavelength of an optical filter. Such an approximation is obtained using (3.20) that has been derived in Section 3.2.2. This is repeated for both APs, and the results are here plotted on different Y axes to improve readability. In the case of AP 2, the distribution's average is much closer to the original choice $\lambda_{\text{OF}}(\psi = 0) = 500$ nm because, due to how the user is positioned (and at which angle it holds the device, θ), the AoI is on average much closer to $0°$. This results in the PS effect having much less of an impact on signals coming from that AP, as opposed to AP 1. This particular result is location-specific, but it represents the wide variety of situations that can occur in a densely deployed grid of APs and users with a wide FOV. With regard to this latter, it is also important to notice that

Table 3.2: Results of Monte-Carlo simulations with central wavelength at 500 nm

$\lambda_{\mathbf{OF}}(\psi = 0) = 500$ **nm**	**AP 1**	**AP 2**
Mean DC Channel Gain	-62.45 dB	-63.49 dB
Mean Spectral Overlap	0.60	0.97
Resulting Overall Gain	-64.68 dB	-63.62 dB

using a smaller FOV is feasible to attain better selectivity and limit the interference from neighbouring APs. However, a wider FOV also provides higher and much needed flexibility in such a context, where mobile users' locations and orientations cannot be predicted.

Intuitively, the SO will also be higher for AP 2, and this is confirmed by the results. In a real system, the optical channel gain and the SO will interact together to determine the overall gain, which is consequently influenced by many parameters, many of which depend on system design choices and can be carefully tuned to obtain the desired results. A few examples of this include the area of the PD, the amplifying circuit, and the concentrator in front of the PD (as discussed in the earlier paragraph). On the other hand, there are many cases in which the relative location between the source and the receiver cannot be controlled because it depends on the users' intrinsic behaviours. This has profound effects both on the optical channel gain and on the SO, and this is why, in the field of LiFi, considering user mobility is paramount to establishing functional links.

The optical channel gain and the SO can be multiplied to determine which AP in the user's FOV will ensure the highest signal. By doing so for the two APs in the system, whose results are summarised in Tab. 3.2, it is possible to notice that the overall gain (resulting from both optical channel gain and optical filter transmissivity) is higher for AP 2, despite having a lower optical channel gain due to a higher distance from the user. This means that the received signal strength from AP 2 will be higher than the one received from AP 1.

3.3.2 Optimisation of the Optical Front-end

In the results presented earlier, and more specifically in Tab. 3.2, it can be noted that the overall gain is lower for AP 1 and that the lower SO (which measures the losses due to the optical filter transmissivity blocking part of the incoming light) is responsible for losing more than 2dB in the received signal. To avoid this, it could be possible to consider various options to optimise system performance. The most immediate possibility involves considering the OFE, and more specifically the optical filter, by choosing the central wavelength so that the SO, $W(\psi)$, is maximised. This approach can be written as follows:

$$\begin{aligned} &\text{maximise } W(\psi) \\ &\text{subject to } \lambda_{\mathrm{OF}}(\psi) = \lambda_{\mathrm{OF}}(\psi = 0)\sqrt{1 - \frac{\sin^2(\psi)}{n_{\mathrm{e}}^2}}. \end{aligned} \tag{3.22}$$

Since the objective function, $W(\psi)$, is a piece-wise defined function, it is possible to consider its definition in (3.21) to find a solution. More specifically, such a function depends on the central wavelength of the optical filter and is maximised when $\lambda_{\mathrm{OF}}(\psi) = \lambda_{\mathrm{LED}}$. However, as ψ is a random variable that changes continuously because of user mobility, it is convenient to approach the task of finding a solution to this problem by considering the average value assumed by the polar angle. In fact, since its distribution is Gaussian (or Laplacian, if the users are sitting), the average value of the polar angle can be interpreted as the inclination that the device will most commonly have. Thus, solving the problem for this particular value would still ensure a solution that is adequate with respect to the actual behaviour of the user.

By looking at the PDF of the central wavelength for AP 1 in Figure 3.6, it can be seen that its maximum corresponds to the mean of the distribution and that the central wavelength indicated in correspondence with that value is $\sim$ 480 nm. Observing the difference with respect to the starting central wavelength value, i.e., 500 nm, it can be concluded that the average central wavelength shift is 20 nm and that by choosing a central wavelength equal to 520 nm, the average AoI value will be compensated. As a further verification, it can be observed that because the user is right below AP 1,

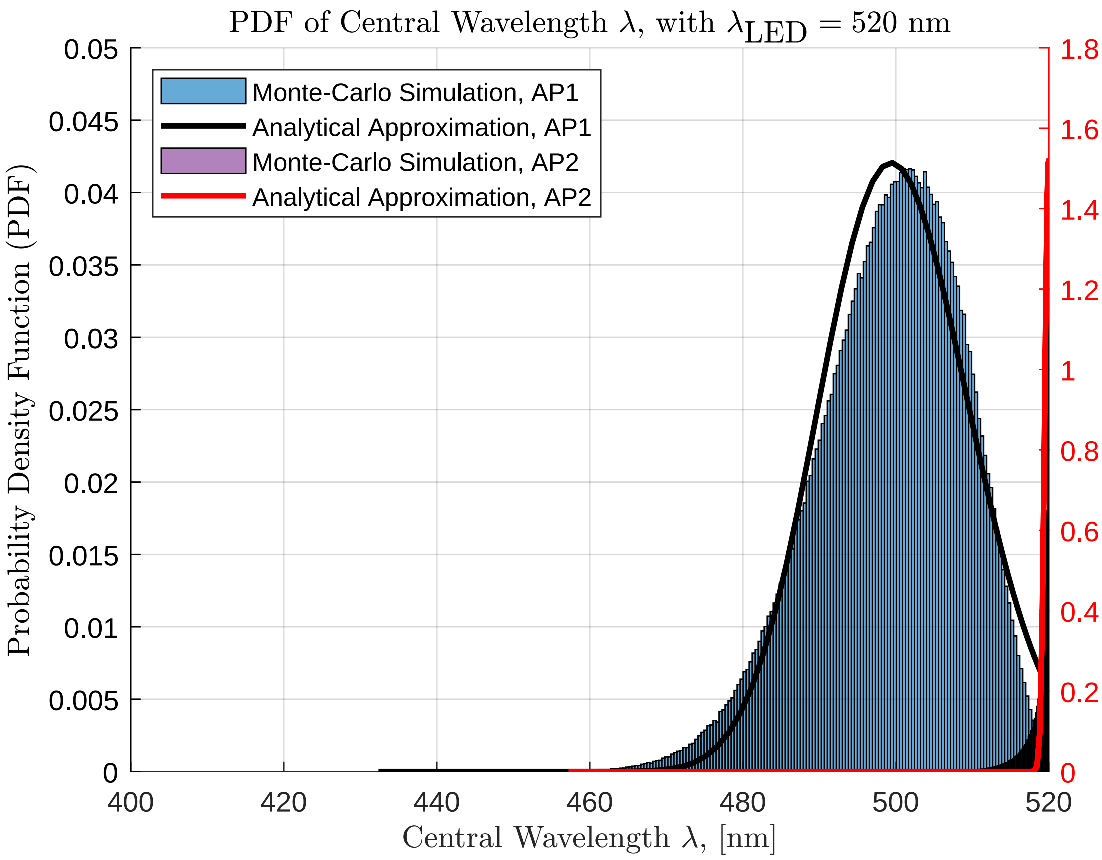

Figure 3.7: PDF of shifted central wavelength of the optical filter, for AP 1 and 2. Comparison between Monte-Carlo simulations and the analytical approximation. The chosen central wavelength compensates for the effect of the average AoI being higher than the 0° shift for AP 1. However, the link with AP 2 worsens as a result.

$\psi_1 = \theta$. Thus, the average AoI with respect to that AP will be the average inclination angle $\theta = 29.67°$. By substituting this value of ψ_1 into (2.1), it results:

$$\lambda_{\text{OF}}(\psi_1) = \lambda_{\text{OF}}(\psi = 0)\sqrt{1 - \frac{\sin^2(\psi_1)}{n_\text{e}^2}} \cong 480 \tag{3.23}$$

and similarly, if $\lambda_{\text{OF}}(\psi = 0) = 520$ nm was chosen as central wavelength of the optical filter, obtain:

$$\lambda_{\text{OF}}(\psi_1) = \lambda_{\text{OF}}(\psi = 0)\sqrt{1 - \frac{\sin^2(\psi_1)}{n_\text{e}^2}} \cong 500. \tag{3.24}$$

Then, to investigate this further, it is possible to perform another simulation to

Table 3.3: Results of Monte-Carlo simulations with central wavelength at 520 nm

$\lambda_{\mathbf{OF}}(\psi = 0) = 520$ **nm**	**AP 1**	**AP 2**
Mean DC Channel Gain	-62.45 dB	-63.49 dB
Mean Spectral Overlap	0.85	0.63
Resulting Overall Gain	-63.16 dB	-65.51 dB

obtain the PDF of the central wavelength and the overall channel gain as before, with respect to both APs. The sole difference being that the starting central wavelength of the optical filter is now chosen as $\lambda_{\mathrm{OF}}(\psi = 0) = 520$ nm while all other parameters remain the same. The result of this simulation is shown in Figure 3.7, and the compensation employed allows the central wavelength of the optical filter to be centred around 500 nm, maximising the SO for that configuration. On the other hand, it can be seen that the trade-off for such a change is that the link with AP 2 will worsen. This is also confirmed when observing the mean optical channel gain, SO, and overall gain in this configuration for both APs reported in Tab. 3.3.

3.3.3 Extension to a Complete Network

It is now necessary to extend all considerations made so far with respect to the impact of the PS effect to the case of a full indoor network, which is the focus of this dissertation. One of the main differences is that the user will usually have more than two APs in its FOV, and this introduces two problems. Firstly, assuming that only one AP per user will be responsible for transmitting the signal, it will be necessary to choose which AP to allocate to said user. Secondly, other APs are free to be allocated to other users and thus provide interference (inter-AP interference). It has to be noted that assuming all sources (transmitters) of all APs are transmitting at all times to serve other users, what is to be considered "signal" or "interference" depends entirely on the outcome of the resource allocation operations. In fact, when considering the simplest case, as seen before, with only two APs and one source per AP, only one of them will be providing a useful signal, and the other will be considered interference. In this case, the resource allocation could entail allocating the channel with the highest overall gain to the user

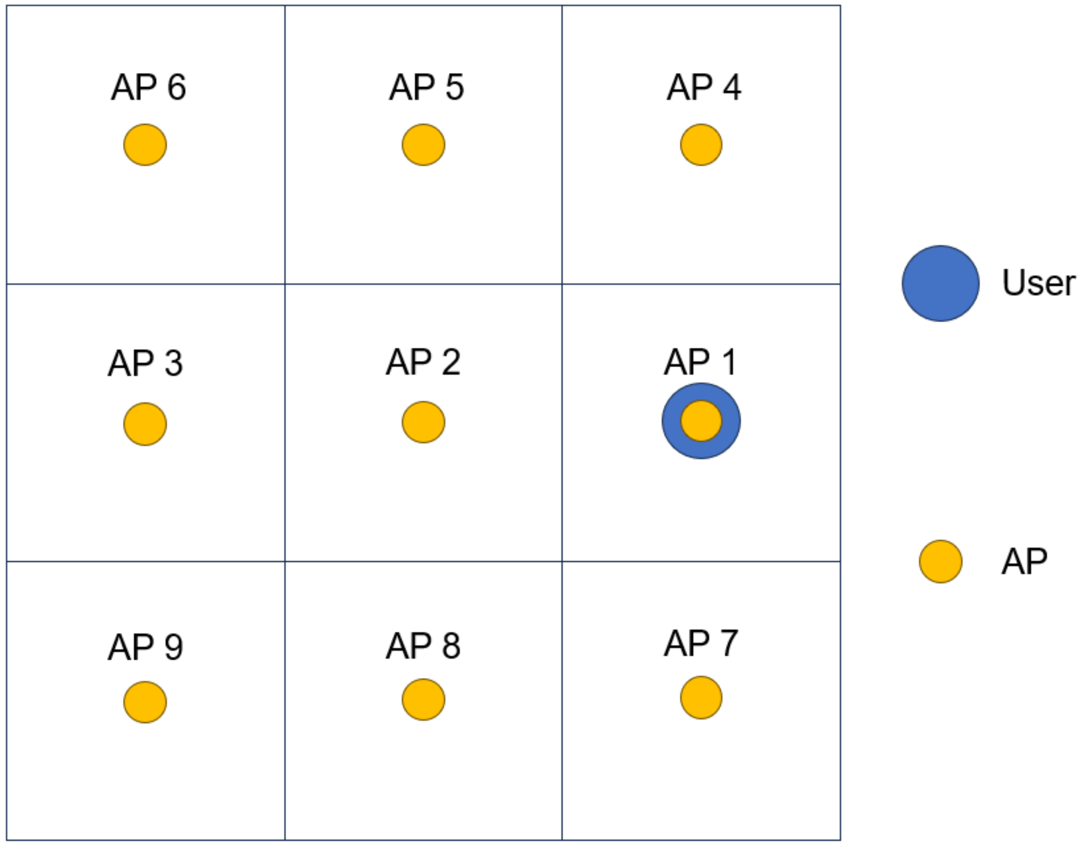

Figure 3.8: Network geometry. The user is below AP 1 as represented in the earlier system geometry used up to this point and is surrounded by other APs in a square lattice grid, as it would happen in a densely deployed indoor LiFi network.

so that the signal quality is the highest possible.

Location 1

In a bigger environment, with more users and APs, each with more than one transmitter, this interference could build up to the point of making the desired signal completely buried and non-recoverable. To better investigate such a situation, the simulation framework employed so far can be useful to consider a higher number of APs, which would also be positioned on the sides of the user if the ceiling of the room is fitted with a square lattice grid of APs. The user will be put again in a specific position, and the PDF of the central wavelength conditioned on the user's location will be calculated for all APs in the network. Then, the average central wavelength will be used to calculate

Table 3.4: Results of Monte-Carlo simulations with more APs, OFE comparison between $\lambda_{\mathrm{OF}}(\psi = 0) = 500$ nm (unoptimised) and $\lambda_{\mathrm{OF}}(\psi = 0) = 520$ nm (optimised). Location 1.

User below AP 1				
AP	Average optical gain	Average SO (unoptimised VS optimised)	Overall gain (unoptimised VS optimised)	Difference
1	−62.45 dB	0.60 / 0.85	−64.68 dB / − 63.17 dB	+1.51 dB
2	−63.49 dB	0.97 / 0.63	−63.62 dB / − 65.51 dB	−1.89 dB
3	−67.61 dB	0.79 / 0.80	−68.65 dB / − 68.59 dB	+0.06 dB
4	−68.99 dB	0.28 / 0.65	−74.53 dB / − 70.88 dB	+3.65 dB
5	−65.53 dB	0.65 / 0.95	−67.42 dB / − 65.73 dB	+1.69 dB
6	−68.90 dB	0.61 / 0.90	−71.05 dB / − 69.37 dB	+1.68 dB
7	−68.99 dB	0.28 / 0.65	−74.55 dB / − 70.88 dB	+3.67 dB
8	−65.53 dB	0.65 / 0.95	−67.42 dB / − 65.73 dB	+1.69 dB
9	−68.90 dB	0.61 / 0.90	−71.05 dB / − 69.37 dB	+1.68 dB

the SO and evaluate the impact of the PS on the user's received signal strength, while also considering the interference coming from neighbouring APs. An example of this is represented in Figure 3.8.

The original system geometry with only two APs has been expanded, and the user is now immersed in a full LiFi network with a higher number of APs in its FOV. Note that the user's position and orientation with respect to AP 1 and 2 have been kept similar, and further APs to the right of the figure have not been represented as they would fall out of the FOV for the majority of samples and thus do not contribute to the analysis in a substantial way.

The results for both $\lambda_{\mathrm{OF}}(\psi = 0) = 500$ nm and $\lambda_{\mathrm{OF}}(\psi = 0) = 520$ nm are summarised in Table 3.4 for a comparison. Firstly, it can be seen that APs 1-3 yield the highest overall gain in both cases; this is expected because of the user's position, as the distance from the receiver is lower on average. Moreover, since the user is oriented in a different direction for APs 4–9, the resulting average AoI will be higher, with a negative impact on both the path loss and the SO. This can also be verified in the results. Secondly, by looking at the last column, which summarises the gains and losses due to the different OFE design, it can be noted how the choice of $\lambda_{\mathrm{OF}}(\psi = 0) = 520$ nm (which is the optimised OFE design) results in an increment of the gains of every AP, with the only exception of AP n. 2, for the reasons seen in the earlier Section 3.3.2. It can also be seen that the SO of AP n. 3 seems to be robust to the change of central wavelength, as in, choosing the optimised or unoptimised design does not seem to have a noticeable effect on the SO; however, this is only a consequence of the particular position of the user. In fact, by calculating the average AoI for this particular case, it results in $\psi_3 = 20.62$. This corresponds to an average shift of 10 nm, and thus the two shifted central wavelength are:

$$\lambda_{\mathrm{OF}}(\psi_3) = \lambda_{\mathrm{OF,\,500}}(\psi = 0)\sqrt{1 - \frac{\sin^2(\psi_3)}{n_{\mathrm{e}}^2}} = 500\sqrt{1 - \frac{\sin^2(20.62)}{1.8^2}} \cong 490 \text{ nm}$$
$$\lambda_{\mathrm{OF}}(\psi_3) = \lambda_{\mathrm{OF,\,520}}(\psi = 0)\sqrt{1 - \frac{\sin^2(\psi_3)}{n_{\mathrm{e}}^2}} = 520\sqrt{1 - \frac{\sin^2(20.62)}{1.8^2}} \cong 510 \text{ nm}$$

and since the central wavelength of the source, $\lambda_{\mathrm{LED}} = 500$ nm, is exactly in between the two values, the resulting average SO will be similar for both OFE choices. This is a very particular case that is unlikely to happen consistently in practice and make a significant difference, as it is also tied to the spectra being modelled with rectangular functions.

Considering the entire network again, the higher gain for all APs can be a hindrance as the number of users populating the network grows. Assuming that only one AP provides the signal, all the others will be contributing to interference with an increased strength. This is easily verified by considering an allocation scheme that leverages Channel State Information (CSI) information and, based on the overall gains reported in Tab. 3.4, will assign one AP to the user while all others will be active to serve other users (thus contributing to interference). As it can be verified in Table 3.4, the AP allocation (based on highest overall gain) yields AP 2 when $\lambda_{\mathrm{OF}}(0) = 500$ nm, and AP 1 when $\lambda_{\mathrm{OF}}(0) = 520$ nm. For both these OFE design options, it is possible to calculate the signal and interference power received to evaluate the differences. Assuming that every AP emits an average optical power of $P_{\mathrm{AP}} = 1\mathrm{W}$, the required calculations can be carried out as such:

$$P_{\mathrm{sig}}^{\mathrm{rec}} = P_{\mathrm{AP}} H_{\mathrm{s}} W_{\mathrm{s}}$$
$$P_{\mathrm{int}}^{\mathrm{rec}} = P_{\mathrm{AP}} \sum_{i=1, i \neq i_{\mathrm{AP}}}^{N_{\mathrm{AP}}} H_{\mathrm{i}} W_{\mathrm{i}}$$

where $P_{\mathrm{sig}}^{\mathrm{rec}}$ is the power emitted by the AP allocated to the user after the free space attenuation and the optical filter attenuation (signal power), while $P_{\mathrm{int}}^{\mathrm{rec}}$ is the sum of the powers emitted by all other APs, equally considered after both the free space and optical filter attenuations (interference power). Then, to evaluate the impact of the interference in such a system, the Signal-to-Interference Ratio (SIR) can be considered for both OFE design options ($\gamma_1^{\mathrm{SIR}}(500)$ and $\gamma_1^{\mathrm{SIR}}(520)$ respectively):

$$\gamma_1^{\mathrm{SIR}}(500) = \frac{P_{\mathrm{sig},500}^{\mathrm{rec}}}{P_{\mathrm{int},500}^{\mathrm{rec}}} = 0.4$$
$$\gamma_1^{\mathrm{SIR}}(520) = \frac{P_{\mathrm{sig},520}^{\mathrm{rec}}}{P_{\mathrm{int},520}^{\mathrm{rec}}} = 0.36.$$

The $\gamma_1^{\mathrm{SIR}}(500)$ parameter is higher because all interference contributions have a lower gain, despite also having a slightly lower gain for the signal strength. It can be seen that, if an appropriate resource allocation scheme is in place in a LiFi network, choosing either of the OFE design options could yield good results regardless of the presence PS effect. Conversely, if the system does not have the ability of allocating the best AP to the user based on the received SIR, the goodness of the performances would be severely hindered by interference.

As it can be noted, these considerations are closely tied to the AoI between the sources and the user's device. This is not only dependent on the user's wrist movements but also on the location of the user. The entire framework presented so far is a statistical derivation conditioned on the location of the receiving device, and for this reason, it is important to extend this analysis to other user locations to verify that the conclusions drawn can be extended to the entire indoor space. The symmetric nature of a square grid is helpful and allows to carry out this verification by only considering a limited number of additional locations.

Locations 2 - 3

Figure 3.9 shows two additional locations in the network that cover the upper left quadrant of the square enclosing AP 1. It should also be noted that if the user was displaced by −0.3 m rather than +0.3 m with respect to the horizontal axis of the square for both new locations, the results would be the same because of the aforementioned symmetry.

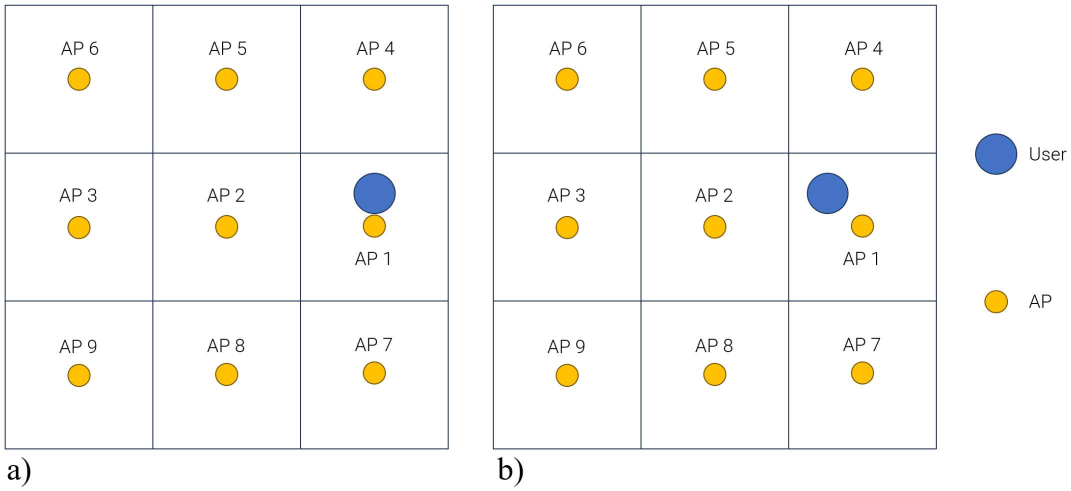

Figure 3.9: Network geometry with different user's locations. In a) the user is displaced vertically with respect to AP 1 by 0.3 m; in b) the user is displaced both horizontally and vertically with respect to AP 1 by 0.3 m.

In these two new locations, the user is getting closer to the edge of the square enclosing AP 1. In this dissertation, the concept of "cell" or "atto-cell" is not considered in its own right, as cell design trade-offs are a broad and complex topic that falls outside of the scope at hand; however, it is intuitive to notice that as the user is closer to the edge of a square, there will be a lower spatial separation between him and the surrounding APs. As a result, because of the relationship between the source-receiver distance and the path loss, the difference in strength between the signal and interference will be smaller, and the SIR will be overall lower.

The results concerning the second location of the user, which is vertically displaced by 0.3 m with respect to AP 1, are shown in Table 3.5.

The path losses between the user and APs 1–3 and 7–9 show a slightly lower gain

Table 3.5: Results of Monte-Carlo simulations with more APs, OFE comparison between $\lambda_{\mathrm{OF}}(\psi = 0) = 500$ nm (unoptimised) and $\lambda_{\mathrm{OF}}(\psi = 0) = 520$ nm (optimised). Location 2.

User displaced vertically by 0.3 **m**				
AP	Average optical gain	Average SO (unoptimised VS optimised)	Overall gain (unoptimised VS optimised)	Difference
1	-62.72 dB	0.57 / 0.85	-65.15 dB / -63.43 dB	$+1.72$ dB
2	-63.64 dB	0.95 / 0.65	-63.87 dB / -65.48 dB	-1.61 dB
3	-67.69 dB	0.77 / 0.81	-68.80 dB / -68.61 dB	$+0.19$ dB
4	-65.32 dB	0.39 / 0.77	-69.36 dB / -66.48 dB	$+2.88$ dB
5	-64.70 dB	0.77 / 0.84	-65.81 dB / -65.46 dB	$+0.35$ dB
6	-68.34 dB	0.68 / 0.87	-70.00 dB / -68.93 dB	$+1.07$ dB
7	-78.60 dB	0.16 / 0.52	-86.43 dB / -81.38 dB	$+5.05$ dB
8	-66.51 dB	0.52 / 0.90	-69.37 dB / -66.97 dB	$+2.40$ dB
9	-69.60 dB	0.53 / 0.89	-72.45 dB / -70.19 dB	$+2.26$ dB

with respect to the location investigated earlier because the new location induces an increase in both distance and AoI for those APs. On the other hand, and for the same reasons, APs 4–6 path losses have a higher gain: the user is closer and average AoIs are lower. The average SOs also reflect those changes, but only on account of the changes in AoI, because the distance has no effect on the SO. Furthermore, it should be noted that SOs in the case of unoptimised OFE are all generally low with the single exception of AP 2. This is an overall positive outcome because it will result in a better separation between signal and interference, both in the wavelength and spatial domains. The strongest gain for the user in the received signal comes from AP 2 in the case of $\lambda_{\mathrm{OF}}(\psi = 0) = 500$ nm, while in the case of $\lambda_{\mathrm{OF}}(\psi = 0) = 520$ nm, AP 1 remains the best choice. By computing the SIR for both cases and for this location, it results:

$$\gamma_2^{\mathrm{SIR}}(500) = \frac{P^{\mathrm{rec}}_{\mathrm{sig},500}}{P^{\mathrm{rec}}_{\mathrm{int},500}} = 0.37$$
$$\gamma_2^{\mathrm{SIR}}(520) = \frac{P^{\mathrm{rec}}_{\mathrm{sig},520}}{P^{\mathrm{rec}}_{\mathrm{int},520}} = 0.32.$$

Both SIRs are lower than their counterparts in the first location, and notably, the SIR of an unoptimised OFE in location 2 ($\gamma_2^{\mathrm{SIR}}(500)$) is comparable, but still slightly higher, than that of an optimised OFE in location 1 ($\gamma_1^{\mathrm{SIR}}(520)$). The aforementioned positive increase in signal and interference separation is partially countered by an increase, both in terms of distance and AoIs, between the AP providing signal and interfering APs. In other words, the location of the user does not provide enough interference mitigation.

The third location, whose results are summarised in Table 3.6, has the user displaced with respect to AP 1 by 0.3 m in the vertical direction and -0.3 m in the horizontal direction. This further movement towards AP 2 results in a noticeable difference between the path loss of this AP and all the others, which is also true for the SO when $\lambda_{\mathrm{OF}}(\psi = 0) = 500$ nm. Calculating the SIRs for this case yields:

$$\gamma_3^{\mathrm{SIR}}(500) = \frac{P_{\mathrm{sig},500}^{\mathrm{rec}}}{P_{\mathrm{int},500}^{\mathrm{rec}}} = 0.51$$
$$\gamma_3^{\mathrm{SIR}}(520) = \frac{P_{\mathrm{sig},520}^{\mathrm{rec}}}{P_{\mathrm{int},520}^{\mathrm{rec}}} = 0.26.$$

In the case of unoptimised OFE this SIR is the highest so far, while for an optimised OFE it is at its lowest because of the combined separation of path loss and SO. This location is a good example of why a dynamic channel allocation that takes the SO into account is a much preferable choice, especially when the network is fully populated: it can automatically select the best separation both in the spatial and wavelength domain between APs and available channels based on the instantaneous location of the user.

Locations 4 - 5

In this last section, two further locations will be evaluated in terms of AP allocation and received SIR as before. These locations have the peculiar characteristic of being exactly in between two APs (location 4) and in between four APs (location 5). This has the result of putting the user at exactly the same distance between two or more APs, reducing separation in the spatial domain. Furthermore, this reduced separation also interests the AoI of light beams coming from neighbouring APs, which also reduces separation in the wavelength domain, thus making it difficult to choose between two or more signal sources that feature the same signal strength. As a result, these can be

Table 3.6: Results of Monte-Carlo simulations with more APs, OFE comparison between $\lambda_{\mathrm{OF}}(\psi = 0) = 500$ nm (unoptimised) and $\lambda_{\mathrm{OF}}(\psi = 0) = 520$ nm (optimised). Location 3.

User displaced vertically by 0.3 **m and horizontally by** -0.3 **m**				
AP	Average optical gain	Average SO (unoptimised VS optimised)	Overall gain (unoptimised VS optimised)	Difference
1	-65.12 dB	0.36 / 0.72	-69.50 dB / -66.55 dB	$+2.95$ dB
2	-62.87 dB	0.93 / 0.67	-63.18 dB / -64.59 dB	-1.41 dB
3	-66.62 dB	0.83 / 0.76	-67.41 dB / -67.78 dB	-0.37 dB
4	-69.70 dB	0.23 / 0.58	-76.17 dB / -72.05 dB	$+4.12$ dB
5	-64.06 dB	0.74 / 0.87	-65.37 dB / -64.67 dB	$+0.70$ dB
6	-67.33 dB	0.72 / 0.86	-68.75 dB / -67.99 dB	$+0.76$ dB
7	-89.62 dB	0.07 / 0.38	-101.38 dB / -93.99 dB	$+7.39$ dB
8	-66.11 dB	0.47 / 0.84	-69.42 dB / -66.84 dB	$+2.58$ dB
9	-68.73 dB	0.54 / 0.91	-71.37 dB / -69.14 dB	$+2.23$ dB

considered worst-case scenarios from an allocation perspective.

Figure 3.10 shows the considered locations. Aside from all considerations regarding distance, further insight can be inferred about the AoI by looking at the shown configuration. In particular, it can be seen that since the device is not being held with the receiver pointing up but rather at an angle depending on the wrist movements of the user, θ, only two APs at the same time can hit the receiver with the exact same AoI. Furthermore, this is strongly dependent on the orientation of the user; in fact, two APs can have the same AoI only if the user is exactly in between them and facing exactly one of four precise orientations. These are aligned with the x and y axes and can be identified with the four cardinal directions in the case of a square grid: north, east, south, and west. In this particular case the user is facing the east direction, but the considerations made apply also to the other directions when the user is surrounded by APs, because of the grid's symmetry.

Table 3.7 summarises the results for location number 4. As expected, and due to the position of the user, APs 1–3 have the exact same path loss, SO, and overall gain of APs 4–6 for both OFE cases. Furthermore, AP number 7 now falls outside of the FOV of the user, and thus its path loss is $-$Inf. By comparing the average SOs between the

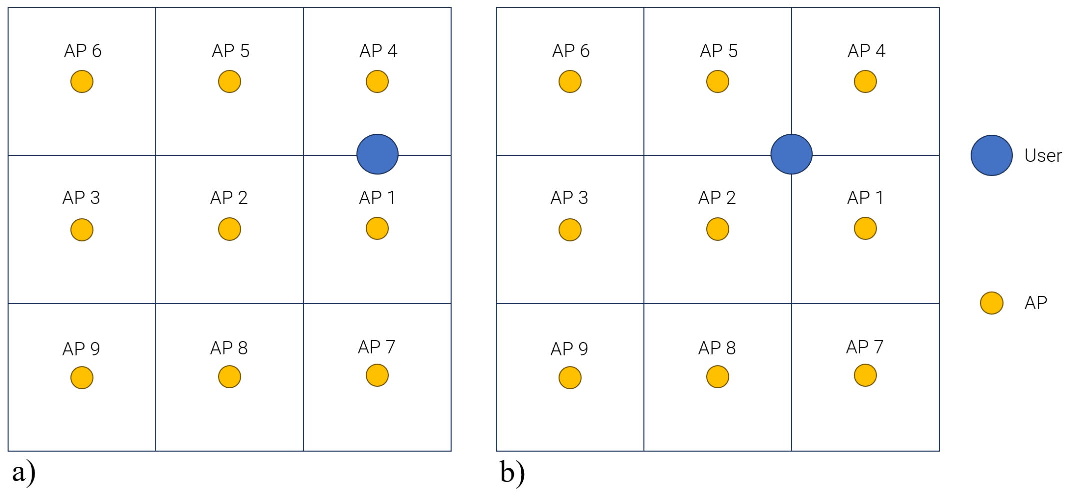

Figure 3.10: Network geometry with different user's locations. In a) the user is exactly in between AP 1 and 4; in b) the user is exactly in between APs 1, 2, 4, and 5.

two cases, it can be seen that for an optimised OFE, the SOs are consistently higher for all APs and much more concentrated in a short range (except for AP n. 7 because of an extreme AoI that makes the receiver fall out of the FOV). In terms of overall gains, APs 2 and 5 are equally good choices for a signal allocation while the user is using an unoptimised OFE ($\lambda_{\mathrm{OF}}(\psi = 0) = 500$ nm) because they have the exact same path loss and SO (which means that they are not separated in the spatial nor in the wavelength domain). If the user is alone in the network, choosing AP 2 or 5 as a signal source is perfectly indifferent with respect to the outcome. For this reason, the choice in this case will be AP 2. Similar reasoning and considerations in terms of overall gains and allocation can be made in the optimised OFE case, for which the user can be allocated either to AP 1 or 4; the choice will fall on AP 1 in this case. The SIRs for this location are calculated as follows for both optimised and unoptimised OFE:

$$\gamma_4^{\mathrm{SIR}}(500) = \frac{P^{\mathrm{rec}}_{\mathrm{sig},500}}{P^{\mathrm{rec}}_{\mathrm{int},500}} = 0.31$$
$$\gamma_4^{\mathrm{SIR}}(520) = \frac{P^{\mathrm{rec}}_{\mathrm{sig},520}}{P^{\mathrm{rec}}_{\mathrm{int},520}} = 0.26$$

and show that in this first worst-case scenario analysed here, the unoptimised OFE is still the best choice when the application entails a multi-user network connection rather

Table 3.7: Results of Monte-Carlo simulations with more APs, OFE comparison between $\lambda_{OF}(\psi = 0) = 500$ nm (unoptimised) and $\lambda_{OF}(\psi = 0) = 520$ nm (optimised). Location 4.

User exactly in between AP 1 and 4.				
AP	Average optical gain	Average SO (unoptimised VS optimised)	Overall gain (unoptimised VS optimised)	Difference
1	−63.58 dB	0.50 / 0.83	−66.60 dB / − 64.36 dB	+2.24 dB
2	−64.05 dB	0.88 / 0.73	−64.62 dB / − 65.43 dB	−0.81 dB
3	−67.93 dB	0.74 / 0.84	−69.25 dB / − 68.71 dB	+0.54 dB
4	−63.58 dB	0.50 / 0.83	−66.60 dB / − 64.36 dB	+2.24 dB
5	−64.05 dB	0.88 / 0.73	−64.62 dB / − 65.43 dB	−0.81 dB
6	−67.93 dB	0.74 / 0.84	−69.25 dB / − 68.71 dB	+0.54 dB
7	−Inf	0.07 / 0.41	−Inf / − Inf	N/A
8	−67.83 dB	0.39 / 0.76	−71.96 dB / − 69.00 dB	+2.96 dB
9	−70.82 dB	0.44 / 0.82	−74.37 dB / − 71.69 dB	+2.68 dB

than a point-to-point link. As with location number 3, the SIR in the optimised OFE case is at its lowest because many interference sources benefit from the optimisation as much as the single signal source.

In location number 5, the user is equidistant from APs 1, 2, 4, and 5. As aforementioned, it can be seen that despite this, there are 3 couples of APs providing the exact same overall gain: APs 1 and 4, APs 2 and 5, and APs 3 and 6. The reason why there are not 4 APs with the same gain is that spatial separation depends not only on the distance but also on the AoI. The results for this user location are summarised in Table 3.8, where it can be verified that due to the AoI, both average path losses and SOs are lower for AP 1 and 4. This excludes them as viable APs for allocation with respect to other options and contributes to keeping the interference coming from them low. In turn, and by looking at the resulting overall gains, the two viable choices in this case (and for both optimised and unoptimised OFEs) are AP 2 and 5. Again, the choice will be arbitrarily made to allocate the user to AP 2 for both cases, as more information would be needed on other users to influence the choice in one way or another (e.g., other users in the network that also need to use either AP 2 or 5 or both). It should be noted that after the allocation is made, e.g., with AP n. 2, it would be most beneficial to the network throughput if AP 5 is not allocated to any other user to greatly limit inter-AP interference. However, this aspect is not investigated here as all SIR calculations are made implying that the network is fully populated and thus the interference is at its possible maximum.

Table 3.8: Results of Monte-Carlo simulations with more APs, OFE comparison between $\lambda_{\mathrm{OF}}(\psi = 0) = 500$ nm (unoptimised) and $\lambda_{\mathrm{OF}}(\psi = 0) = 520$ nm (optimised). Location 5.

User exactly in between AP 1, 2, 4 and 5.				
AP	Average optical gain	Average SO (unoptimised VS optimised)	Overall gain (unoptimised VS optimised)	Difference
1	−72.77 dB	0.14 / 0.46	−81.38 dB / − 76.15 dB	+5.23 dB
2	−62.86 dB	0.78 / 0.81	−63.91 dB / − 63.74 dB	+0.17 dB
3	−65.88 dB	0.83 / 0.77	−66.67 dB / − 67.02 dB	−0.35 dB
4	−72.77 dB	0.14 / 0.46	−81.38 dB / − 76.15 dB	+5.23 dB
5	−62.86 dB	0.78 / 0.81	−63.91 dB / − 63.74 dB	+0.17 dB
6	−65.88 dB	0.83 / 0.77	−66.67 dB / − 67.02 dB	−0.35 dB
7	−Inf	0.00 / 0.17	−Inf / − Inf	N/A
8	−Inf	0.26 / 0.62	−Inf / − Inf	N/A
9	−69.03 dB	0.44 / 0.82	−72.59 dB / − 69.91 dB	+2.68 dB

By calculating the SIRs for this last worst-case location, it results:

$$\gamma_5^{\mathrm{SIR}}(500) = \frac{P^{\mathrm{rec}}_{\mathrm{sig},500}}{P^{\mathrm{rec}}_{\mathrm{int},500}} = 0.45$$
$$\gamma_5^{\mathrm{SIR}}(520) = \frac{P^{\mathrm{rec}}_{\mathrm{sig},520}}{P^{\mathrm{rec}}_{\mathrm{int},520}} = 0.43.$$

These are higher when compared with the previous location because there is one less interference source coming from AP 8. It can also be noted that there is a significantly lower difference between the two OFE cases, mostly due to the fact that SO for interfering APs in the optimised case are slightly lower than the ones for the unoptimised case. However, the conclusion is once again that the unoptimised OFE is preferable.

3.4 Chapter Summary

In this chapter, the impact of the PS effect on a full RGBA LiFi network has been studied by considering various aspects such as user behaviour, system design, and intra-AP and inter-AP induced interference.

The chapter has started with an analytical derivation of the PDF of the central wavelength of an optical filter mounted on the device of a human user, conditioned on the position and orientation of the latter in 3D space. The resulting expression makes it possible to see the distribution of the central wavelength of the optical filter after the PS effect while taking user behaviour into account. This expression has been later verified by means of Monte Carlo simulations, and results show that the derived expression matches such simulations closely.

Then, a formal definition of the SO has been provided, which allows to evaluate how well a source and optical filter spectral characteristics overlap. This definition also encompasses the effects of the PS, rendering it a useful tool to drive system design decisions in terms of planning the central wavelengths and FWHM of both source and receiver to achieve the best performances. However, it can be verified that optimising the central wavelengths of the OFs based on the central wavelength of the source and the expected AoI of the user (resulting from its behaviour) is not the most fruitful choice and leads to higher interference figures. Furthermore, by plotting the SO for each receiver and comparing it with the absence of the PS effect, it can be realised that this usually unwanted physical phenomenon can be leveraged to improve system performances by increasing channel separation. This limits both intra-AP and inter-AP interference and leads to improved SIR. This is also true when more APs are considered to be in the FOV of the user, such as in a common situation in an indoor network of densely deployed APs.

Lastly, the defined framework and the reasoning behind optimised and unoptimised central wavelength of the optical filter have been used in a complete LiFi network environment, investigating the outcomes of the allocation and the entity of the interference (via the SIR metric). This has been done by putting the user in five different locations while simulating a high number of realisations for the device inclination according to an experimental statistic of user behaviour. The conclusions that can be drawn from the results span the entirety of the square, thanks to the underlying symmetry of the proposed configuration. Results have shown that when more than two APs are in the FOV of the user, the unoptimised OFE is better at limiting the interference because of the separation introduced by the differences in AoI of light beams coming from all APs to the receiver of the user. Such differences improve separation both in terms of the path losses and of the SO (which is influenced by the PS effect, related to the AoI).

In summary, it is imperative to explore the potential benefits of harnessing the typically undesirable PS effect to enhance signal strength and channel separation within LiFi Wavelength Division Multiple Access (WDMA) networks. This warrants a comprehensive investigation. Throughout this chapter, a detailed analysis has been conducted, illuminating the significance of optimising the OFE for reception, especially in the context of point-to-point links employing Wavelength Division Multiplexing (WDM) or WDMA protocols.

However, further analysis has highlighted that this optimisation approach does not yield satisfying results in indoor environments characterised by the dense deployment of APs, which can introduce substantial interference, when compared with an unoptimised approach. This is primarily due to the fact that, in such scenarios, the sources of interference for each channel far outnumber the sources of the desired signal. Consequently, the impact of optimising the OFE is disproportionately skewed towards enhancing the gain of interference rather than signal quality.

In addressing this challenge, it becomes evident that an effective solution may lie in implementing alternative interference mitigation strategies at the network operation level rather than solely focusing on countering the PS effect at the physical layer. Hence, the subsequent chapter will delve into the exploration of dynamic resource allocation strategies specifically tailored for these complex indoor environments.

Chapter 4

Adaptive WDMA

4.1 Introduction

In the previous chapter, important results regarding the impact of the Passband Shift (PS) effect on a densely deployed indoor Wavelength Division Multiple Access (WDMA) Light Fidelity (LiFi) network have been presented and discussed. The main outcome of such discussion is that when multiple Access Point (AP)s (each with multiple coloured sources) are closely deployed together, such as in an indoor LiFi network, the problem of mitigating the interference cannot be tackled efficiently by simply optimising the Optical Front-End (OFE) with respect to the expected average Angle of Incidence (AoI) of the light beams on the receivers. This is because the optimisation will not only have an effect on the signal source but also on all interference sources, resulting in a lowered Signal-to-Interference Ratio (SIR) figure. For this reason, in the present chapter, the focus is shifted to how network resources can be efficiently allocated so that the system performances can be increased, leading to the formulation of a novel WDMA allocation scheme. To the best of the authors' knowledge, this is the first WDMA scheme proposed for LiFi. Additionally, noise sources and a simulation environment including off-the-shelf component parameters will be included.

The present chapter is based on the published work in [200]. However, the results presented therein are here expanded and revised in light of a different hardware arrangement, which reflects more faithfully the advances in the field. This chapter brings

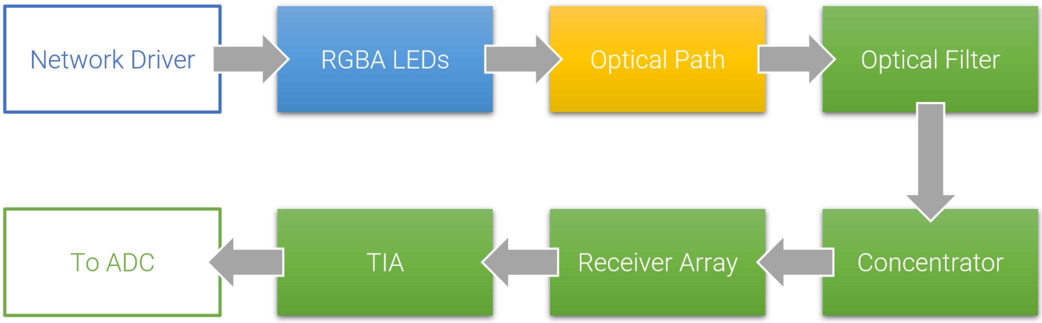

Figure 4.1: WDMA system block scheme. It describes the complete path of the signal from the digital domain at the network level up to its conversion and transmission in the optical domain before being captured and converted in the electrical domain and then back into the digital domain at the receiver side. Blocks in blue pertain to the transmitter, yellow block is the free space medium (air in this case), and green blocks belong to the receiver.

the following contributions:

- A novel adaptive WDMA dynamic allocation scheme is presented, which is capable of exploiting the effects of the PS along with the spatial diversity of the users for efficient wavelength reuse and lower interference.
- A set of simulations is carried out to demonstrate the effectiveness of this scheme in terms of network coverage. This is compared with a fixed allocation scheme, based on a round robin allocation approach.
- A second set of simulations is carried out to evaluate network performances. These include the user mobility behaviour statistics, meaning that both users' locations and device inclinations are randomly distributed.

4.2 System Model

Figure 4.1 shows a simple block scheme for the employed transmission system. Each AP consists of a RGBA Light Emitting Diode (LED) array, and thus it is capable of transmitting on four wavelengths with four LEDs. It is assumed that the network can route each signal to each channel allocated to each user and that it is possible to drive

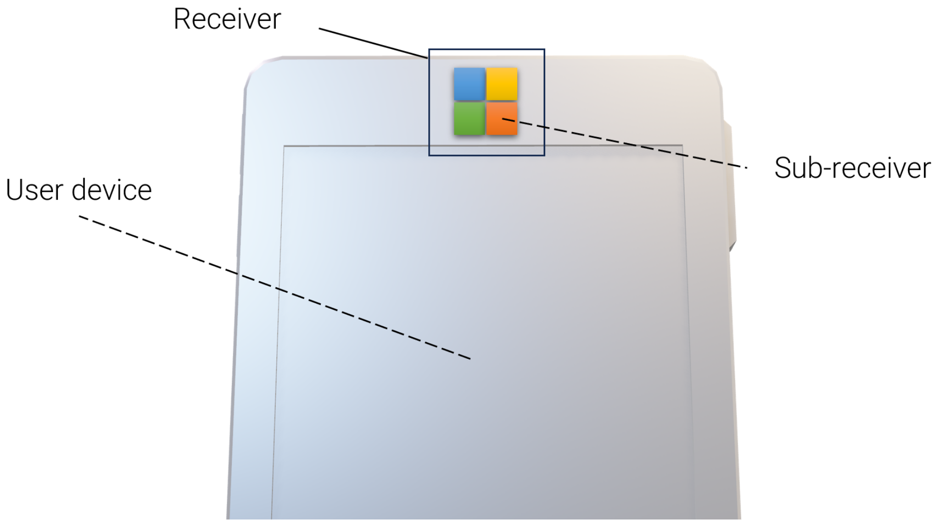

Figure 4.2: Structure of a user's receiver. It is divided into four independent elements, called sub-receivers, and each has an optical filter of a different colour mounted on top. This allows to process signals occupying different wavelengths independently.

the emitted optical power of each LED accordingly. Therefore, each LED can transmit an individual signal and they can be treated as parallel channels even if two users are being allocated to the same AP but different colours at the same time. Moreover, the transmission is independent of the modulation scheme, even allowing to choose a different scheme based on the status of the network (as it happens in current Institute of Electrical and Electronics Engineers (IEEE) standard [201]).

The so-emitted power in the optical domain will reach the interface of the receiver after covering the shortest optical path between the two, which is termed the Line Of Sight (LOS) path. This will introduce an attenuation of such optical power, which will be more formally detailed in Section 4.2.1. Even if it has been demonstrated that Optical Wireless Communication (OWC) links are still attainable without LOS [202–204], such techniques often introduce additional hardware and complexity which is not the target of this dissertation. For this reason, in this work, only the LOS component of the transmitted optical power will be considered, and thus the contribution of higher-order reflections (such as from walls and/or furniture) will be neglected.

The first element encountered by the optical power at the interface with the receiver is the optical filter. At this point, it is important to highlight that every user's receiver is assumed to be made of four sub-receivers, one for each wavelength, and each sub-receiver has an optical filter of a different colour. This configuration is shown in figure 4.2. While this ensures the required flexibility to tackle very dense environment, it has to be noted that this increased size of the receiving hardware may be an impediment for some classes of devices. This is one of the drawbacks of WDMA and for this reason, in this work the receiver has been carefully designed with specific size constraints in mind, in Section 4.2.2. That said, the following considerations equally apply to every optical filter in the visible spectrum. As intuitive, this is a crucial step in wavelength division-based systems because this component provides the required channel separation to successfully transmit parallel channels on different wavelengths. As seen in the earlier chapter, the emission spectrum of the emitted light radiation ($S_{\mathrm{LED}}(\lambda)$) and the AoI-dependent transmission spectrum of the optical filter ($S_{\mathrm{OF}}(\lambda, \psi)$) play an important role on this channel separation because their overlap will contribute to determining the overall attenuation, together with the LOS path, as described in Section 3.2.3. It is important to also highlight that even though modern optical filters can attain a very high transmittance ($> 80\%$), any filter will also induce an attenuation in its passed wavelength band. This constitutes an additional challenge in WDMA, because of the reduction in the link budget induced by the ever present optical filters.

After passing through the optical filter, the signal arrives at the optical concentrator. This particular component is a nonimaging lens that is commonly found on LiFi receivers and is used to increase the amount of light radiation collected on one end and concentrate it at a specific point on the other end without forming a complete image at its focal point (as opposed to imaging concentrators). This is needed to contrast the attenuation introduced by the optical path, which can severely impair the strength of the received signal.

The LOS- and optical filter-attenuated signal passes the optical concentrator and hits the active area of the sub-receiver placed right behind the concentrator itself. In this work, a sub-receiver is an array of $N_{\mathrm{PD}} = 4$ Avalanche Photodiode (APD)s, sufficient to guarantee a good signal level with respect to the noise floor. The sub-receiver converts the received power from the optical to the electrical domain, generating an electric current that is proportional to the optical power intensity. The wavelength-dependent power-current characteristic is called “responsivity” and is represented by $R(\lambda)$.

The small current generated in the earlier step reaches the Trans-Impedance Amplifier (TIA) stage, which converts and amplifies it into a much higher voltage, with a gain that in this work is assumed to be $G_{\mathrm{TIA}} = 2000$. This step adds non-negligible thermal noise to the overall Signal-to-Interference-plus-Noise Ratio (SINR) figure, but it is required so that the signal matches the dynamic range of typical ADC converters employed in such systems.

Finally, the ADC converter is responsible for converting the voltage back into a signal in the digital domain. This can then be fed into the device’s higher-level logic (such as a microcontroller or a processor) to be reconstructed, verified and transformed into usable data.

4.2.1 Optical path

As previously noted, as soon as the light radiation leaves the source, it is immersed in the free space medium and will reach the receiver by following not only the LOS optical path, but also through reflections coming from nearby surfaces (such as walls, furniture and other objects). In order to simplify the calculations and keep the simulation times manageable, only the LOS optical path has been considered throughout this whole dissertation, while all reflections have been neglected.

In terms of radiation pattern, the LEDs in this work can be modelled as Lambertian, with their emission order following the well-known equation:

$$m_{\mathrm{l}} = -\frac{\ln(2)}{\ln(\phi_{1/2})} \tag{4.1}$$

where $\phi_{1/2}$ represents the emission semiangle of the light source. All transmitters are assumed to share the same emission semiangle, and thus, their Lambertian emission order is the same. Moreover, since each transmitter occupies a different portion of the visible light spectrum, their emitted power will be a function of wavelength, given as follows:

$$P_{a,i}^{\mathrm{tr}}(\lambda) = \Phi_{a,i}^{\mathrm{tr}} S_{a,i}^{\mathrm{tr}}(\lambda) \tag{4.2}$$

where, considering the i-th transmitter in the a-th AP, $P_{a,i}^{\mathrm{tr}}(\lambda)$ is its spectral power (radiant flux per unit wavelength), $\Phi_{a,i}^{\mathrm{tr}}$ is its maximum radiant flux (as driven by the I_{peak} current, corresponding to the "High" state), and $S_{a,i}^{\mathrm{tr}}(\lambda)$ is its relative spectral distribution.

The LOS optical path between the transmitter and the receiver introduces an attenuation in the optical power, proportional to the square of the distance, which can be described as follows:

$$P_{a,i}^{\mathrm{fs}}(\lambda) = P_{a,i}^{\mathrm{tr}}(\lambda) H(0)_{u,a} \tag{4.3}$$

where $P_{a,i}^{\mathrm{fs}}(\lambda)$ is a continuous wavelength-dependent function describing the spectral power distribution of the i-th transmitter that reaches the interface of the device's receiver after the free space attenuation. In turn, $H(0)_{u,a}$ is the optical path loss. This has been described in [69] as "channel DC gain", and is given as follows:

$$H(0)_{u,a} = \begin{cases} \frac{(m_{\mathrm{l}}+1)A_{\mathrm{det}}}{2\pi d_{u,a}^2} \cos\phi_{u,a}{}^{m_{\mathrm{l}}} G_{\mathrm{OC}} \cos\psi_{u,a} & \text{if } 0 \leq \psi_{u,a} \leq \Psi_{\mathrm{c}} \\ 0 & \text{if } \psi_{u,a} > \Psi_{\mathrm{c}} \end{cases} \tag{4.4}$$

where A_{det} is the active area of the Photo-Detector (PD), $d_{u,a}$ is the module of the distance vector between the a-th AP and the u-th user, and $\phi_{u,a}$ is the transmitter emission angle (which is the angle between the distance vector $d_{u,a}$ and the unit vector $\bar{n}_{\mathrm{AP}}$), G_{OC} is the optical gain introduced by the lens in front of the receiver, and $\psi_{u,a}$ is the AoI of the light from the a-th AP impinging on the receiver of the u-th user (the angle between the distance vector $d_{u,a}$ and the unit vector $\bar{n}_{\mathrm{u}}$).

Notice that in equation 4.4 two parameters have been left out with respect to the expression reported in [69], namely the receiver responsivity ($R_{u,k}(\lambda)$) and the optical filter transmissivity ($S_{u,k,\psi}^{\mathrm{OF}}(\lambda)$). The first measures the ability of a photodetector to convert incident light power into a current [A/W], while the second expresses what fraction of power that hits the filter is able to pass through it (and it is typically expressed as a fraction or a percentage). In the literature, they are sometimes included in the channel DC gain; however, they are both dependent on the wavelength and given the focus on wavelength division, using their average would result in unacceptable errors. Thus, their contribution will be accounted for in more detail in a later section specifically focusing on the wavelength-dependent terms.

Finally, by inserting (4.2) into (4.3), it is possible to write:

$$P^{\mathrm{fs}}_{a,i}(\lambda) = \Phi^{\mathrm{tr}}_{a,i} H(0)_{u,a} S^{\mathrm{tr}}_{a,i}(\lambda). \tag{4.5}$$

The term $P^{\mathrm{fs}}_{a,i}(\lambda)$ represents the amount of optical power that impinges on the optical filter, after the freespace attenuation and the optical amplification of the concentrator lens.

The amount of optical power hitting the active surface of a sub-receiver is then further reduced, as in the following:

$$P^{\mathrm{rec}}_{u,k} = \int_{\alpha}^{\beta} P^{\mathrm{fs}}_{a,i}(\lambda) S^{\mathrm{OF}}_{u,k,\bar{\psi}}(\lambda) d\lambda \tag{4.6}$$

where $P^{\mathrm{fs}}_{a,i}(\lambda)$ has been defined in (4.3), α and β delimit the considered wavelength range (here, $\alpha = 400$ nm and $\beta = 700$ nm), and $S^{\mathrm{OF}}_{u,k,\bar{\psi}}(\lambda)$ is the transmission characteristic of the optical filter, considered at the specific AoI ($= \bar{\psi}_{u,a}$).

By inserting (4.5) in (4.6) and adding the contribution of the wavelenth-dependent responsivity curve of the PD inside the integral, it is possible to find the maximum current generated after the PD:

$$I^{\mathrm{rec}}_{u,k,a,i} = \Phi^{\mathrm{tr}}_{a,i} H(0)_{u,a} \int_{\alpha}^{\beta} S^{\mathrm{OF}}_{u,k,\bar{\psi}}(\lambda) S^{\mathrm{tr}}_{a,i}(\lambda) R_{u,k}(\lambda) d\lambda. \tag{4.7}$$

This relationship is a fundamental one, because once a resource allocation is available, it allows for the calculation of both signal and interference currents for every sub-receiver of every user. Assuming a vector containing the 0 and 1 symbol sequence is available for transmission on a certain channel, it can be represented with the symbol $S_{\bar{\mathrm{u}},\bar{\mathrm{k}},\bar{\mathrm{a}},\bar{\mathrm{i}}}$. This symbol sequence is uniquely identified and is destined to the u-th user on its k-th sub-receiver, transmitted by the a-th using the i-th coloured LED. Then the signal current vector, $I^{\text{sig}}_{\bar{\text{u}},\bar{\text{k}}}$, can be calculated as follows:

$$I^{\text{sig}}_{\bar{\text{u}},\bar{\text{k}}} = S_{\bar{\text{u}},\bar{\text{k}},\bar{\text{a}},\bar{\text{i}}} I^{\text{rec}}_{\bar{\text{u}},\bar{\text{k}},\bar{\text{a}},\bar{\text{i}}}. \tag{4.8}$$

It contains a sequence of sampled currents generated at the receiving sub-receiver resulting from picking up the light beam from this transmission, each element corresponding to the elements of $S_{\bar{\text{u}},\bar{\text{k}},\bar{\text{a}},\bar{\text{i}}}$. However, such a light beam will hit the other three sub-receivers of the user (generating intra-AP interference currents) and potentially also the receivers of other users (generating inter-AP interference currents). These two are represented by $I^{\text{int}}_{\bar{\text{u}},\bar{\text{k}},\bar{\text{a}},i\neq\bar{\text{i}}}$ and $I^{\text{int}}_{\bar{\text{u}},\bar{\text{k}},a\neq\bar{\text{a}},i}$, respectively, and can be calculated as:

$$I^{\text{int}}_{\bar{\text{u}},\bar{\text{k}},\bar{\text{a}},i\neq\bar{\text{i}}} = \sum_{i=1,i\neq\bar{\text{i}}}^{N_{\text{txcolour}}} S_{u,k,\bar{\text{a}},i} I^{\text{rec}}_{u,k,\bar{\text{a}},i} \tag{4.9}$$

$$I^{\text{int}}_{\bar{\text{u}},\bar{\text{k}},a\neq\bar{\text{a}},i} = \sum_{a=1,a\neq\bar{\text{a}}}^{N_{\text{AP}}} \sum_{i=1}^{N_{\text{txcolour}}} S_{u,k,a,i} I^{\text{rec}}_{u,k,a,i} \tag{4.10}$$

Then, for each sub-receiver of each user, the total interference can be calculated as follows:

$$I^{\text{int}}_{\bar{\text{u}},\bar{\text{k}}} = I^{\text{int}}_{\bar{\text{u}},\bar{\text{k}},\bar{\text{a}},i\neq\bar{\text{i}}} + I^{\text{int},i}_{\bar{\text{u}},\bar{\text{k}},a\neq\bar{\text{a}}}. \tag{4.11}$$

It is assumed that the noise variance is known for each sub-receiver:

$$\sigma^2_{\text{noise}} = \sigma^2_{\text{shot}} + \sigma^2_{\text{th}} \tag{4.12}$$

where σ^2_{shot} is the term coming from shot noise and σ^2_{th} from thermal noise generated by the circuitry.

It is then possible to consider that the expression in (4.8) contains the maximum signal current. This current can then be multiplied by G_{TIA} (the gain of the TIA) to obtain the maximum generated signal voltage:

$$V^{\text{sig}}_{\bar{\text{u}},\bar{\text{k}},\text{pp}} = I^{\text{sig}}_{\bar{\text{u}},\bar{\text{k}}} G_{\text{TIA}} \tag{4.13}$$

and note that it coincides with the peak-to-peak voltage, as it represents the generated signal voltage in the "High" state while in the "Low" state the transmitter is off. This term appears in the definition of the SINR for the k-th sub-receiver of the u-th user:

$$\gamma_{\bar{\mathrm{u}},\bar{\mathrm{k}}}^{\mathrm{SINR}}(t) = \frac{(V_{\bar{\mathrm{u}},\bar{\mathrm{k}},\mathrm{pp}}^{\mathrm{sig}})^2}{4[\sigma_{\mathrm{noise}}^2 G_{\mathrm{TIA}}^2 + \mathrm{var}(I_{\bar{\mathrm{u}},\bar{\mathrm{k}}}^{\mathrm{int}}) G_{\mathrm{TIA}}^2]}. \tag{4.14}$$

This expression assumes that at a time t a complete symbol sequence has been received (i.e. at a time $t+1$, an entirely new symbol sequence will be received and processed). It is based on the peak-to-peak voltage of a signal made by a symbol sequence transmitted with the On-Off Keying (OOK) NRZ protocol, which accounts for the errors in the received symbols due to the variances of both sub-receiver noise and interference.

4.2.2 Hardware

Transmitter

Similarly to Section 3.2.3, the transmitter is once again modelled after the RGBA LED, model LZ4-00MA08 sold and manufactured by OSRAM Led Engin [195]. This robust ceramic package is most suited for indoor lighting, rendering it a good choice for this thesis even though it is not strictly designed for OWC applications. In fact, as it is usual in OWC, the transmitter's rise and fall times limit the bandwidth, which in this case is set at $B_{\mathrm{mod}} = 30$ MHz. This has been calculated with the practical relationship presented in [205]:

$$B_{\mathrm{mod}} \approx \frac{0.35}{t_r} \tag{4.15}$$

where t_r is the device's rise time, and is set at $t_r = 9$ ns for the LEDs chosen in this work as part of the OFE design. Note that by this calculation, the modulation bandwidth could be as high as $B_{\mathrm{mod}} \approx 38$ MHz, but has been kept lower to accommodate for even slower devices.

According to [206], most indoor spaces (including general purpose offices) can be served with an illuminance level of 750 lx, which is taken as reference in this work.

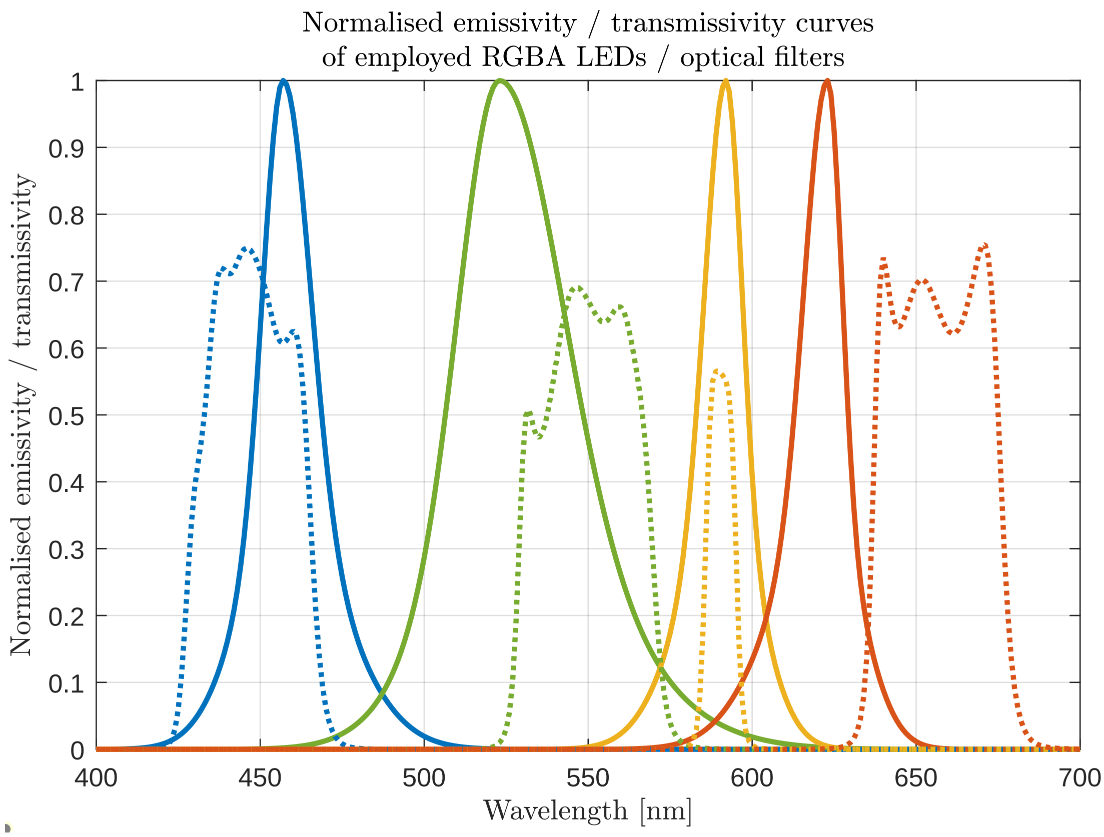

Figure 4.3: Normalised emissivity / transmissivity curves of RGBA LEDs / optical filters employed in this work. The LEDs' emission curves are well separated in terms of the occupied visible spectrum, which contributes to channel separation. The optical filters' transmissivities are only reported for a light beam impinging at an AoI of 0°, and thus their shifted spectra have to be computed and implemented with the well-known equation for all other AoIs.

In order to satisfy this illumination requirement, each AP is assumed to be made out of $N_\mathrm{i} = 4$ of the aforementioned RGBA LEDs. This is obtained by combining various illuminance and electrical parameters present on the datasheet and assuming a peak current of $I_\mathrm{peak} = 1000$ mA (which translates to an average current of $I_\mathrm{avg} =$ 500 mA when employing OOK) and a source efficacy of $\eta_\mathrm{LED} = 90$ lm/W. As a result, the illumination requirement is fulfilled in 98.03% of the room area. The resulting illuminance distribution in the room is shown in Figure 4.4. Even if out of the scope of this thesis, it has to be noted that such illuminance can be controlled by adjusting the emitted power of the APs (via I_peak modulation) to accommodate for different

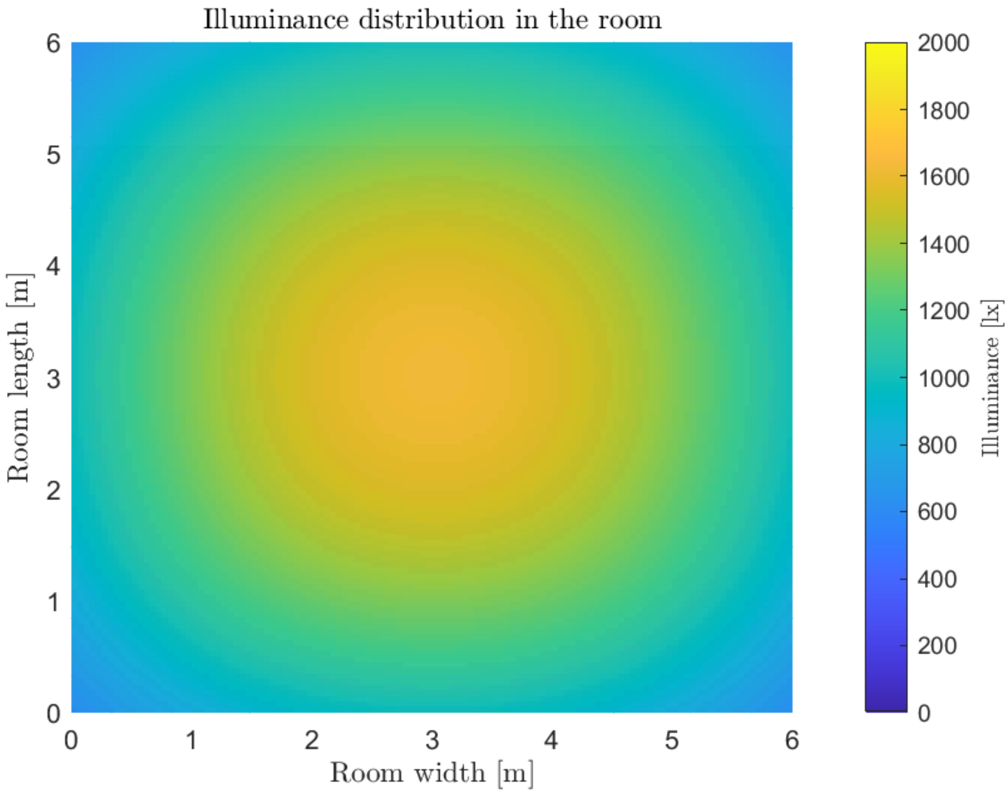

Figure 4.4: Illuminance distribution in the room for the fitted LEDs in the ceiling. The reference level for the illuminance is not achieved only in 1.97% of the room area, close to the walls.

light levels as required by the specific purpose of the room. In principle, it could also be possible to obtain a more uniform distribution by changing the emitted power of individual APs based on their location, although this would change the results obtained in this work in terms of SINR.

The central wavelengths of the Blue, Green, Amber, and Red LEDs are respectively 457, 523, 592, and 623 nm, and their normalised wavelength-dependent emissivity curves $S^{\mathrm{tr}}_{\mathrm{a,i}}(\lambda)$ are shown in Figure 4.3. When combined, their spectra result in a white light suitable for illumination. For this reason, every LED in the room is assumed to be on, even if not transmitting: whenever it is not allocated to a specific channel, an LED can be driven with a continuous I_{avg} current. This light component can be easily processed with a high-pass filter and will not increase the interference on other channels while still contributing to the overall illumination of the room. It also has to be noted that even though their contributions to the shot noise cannot be eliminated, this is a common problem of any receiver that functions in the presence of ambient light.

Receiver

As noted earlier, every user's receiver in this work is made up of $N_{\mathrm{k}} = 4$ sub-receivers, one for each wavelength (colour) in the system. Starting from the top of the sub-receiver, the first component that the light beam hits is the optical filter.

The only difference between sub-receivers is the optical filter that is placed in front of them, and similarly to section 3.2.3, they are modelled after the FB450-40, FB550-40, FB590-10, and FB650-40 from Thorlabs [196–199]. Their central wavelength and Full Width at Half Maximum (FWHM) are respectively 450/40, 550/40, 590/10, and 650/40 nm, and the corresponding transmissivity curves reported on their datasheets are depicted in Figure 4.3. It has to be noted that optical filter manufacturers usually report these spectra for a light beam impinging at an AoI of 0°. For this reason, the shifted spectra will be obtained in this work by applying a wavelength shift to them, that will be calculated with the PS effect equation 2.1. Additionally, the results discussed in this chapter have been generated both with datasheet spectra and measured spectra. Measured spectra have also been acquired for this work at AoIs different from 0°, and, as expected, they also account for the spectral degradation that is occurring as such. More information on this process, and the associated results and comparisons of spectra at different AoIs, are provided in Appendix B.

After passing the optical filter and before hitting a sub-receiver, the light beams encounter a concentrator, which is a lens with the critical function of increasing the optical power that the detectors can collect. This is usually done by effectively enlarging the collection area and design the lens in such a way that the vast majority of light rays hitting its input aperture get refracted and internally reflected onto the exit aperture.

Two types of concentrators are usually considered for OWC applications: hemispherical concentrators and CPCs [69]. The maximum attainable concentration of a lens is regulated by the law of Étendue and is given as [207]:

$$G_{\max} = \frac{n^2}{\sin^2(\psi_{\mathrm{FOV}})}. \tag{4.16}$$

This is a upper bound induced by the physics of the material, and is unlikely to be attainable in practice. Additionally, it can be seen that an hemispherical concentrator is a particular case in which $\psi_{\mathrm{FOV}} \approx \frac{\pi}{2}$ and as such, $G_{\max} \approx n^2$ [69, 208]. Observing the inverse relationship between the Field Of View (FOV) and the attainable gain, it can be seen that using a Compound Parabolic Concentrator (CPC) is more desirable in the context of this work. This is because of two reasons:

- As found throughout section 3.3.3, being able to select a specific FOV allows to strike a balance between the flexibility of having multiple APs in sight while limiting interference from those that would be too far to establish a high-quality link but whose interferences would add up to considerable amounts. This is even more relevant in an environment with high user mobility.
- By limiting their FOV by design, CPCs can attain higher gains than hemispherical lenses. This is important in the envisioned application, where the optical path loss and the optical filter transmissivity can lower the received optical power substantially.

To respect the desired form factor and fit into a mobile device, the CPC has to remain within set geometric and optic parameters. Though these have been arbitrarily chosen, they are deemed consistent with common commercial components that can be found at the time of writing. The aforementioned parameters are as follow:

- The exit aperture d_{CPC} should exactly match the diameter of a single APD, which is $d_{\mathrm{APD}} = 3$ mm.
- The input aperture D_{CPC} should not exceed 0.01 m, with a tolerance of ± 0.005 m. In this way, the surface area of the entire receiver will not exceed 0.04-by-0.02 m with a tolerance of ± 0.01-by-0.005 m.

- The total height H_{CPC} should not exceed 0.01 m, with a tolerance of ± 0.005 m. This allows to comply with strict requirements for the thickness of mobile devices.

- The CPC is assumed to be made of polymethyl methacrylate (PMMA), which has a refractive index $n_i = 1.49$ and a transmissivity index $T_{\text{CPC}} = 0.80$.

- The half FOV is set at $\theta_{\text{CPC}} = 40°$. Lower FOVs could be used to limit the amount of inter-AP interference but would also drastically reduce the amount of possible allocation combinations, which is a very important factor to consider when users have random locations, orientations, and device inclinations.

Assuming $d_{\text{CPC}} = 0.003$ m, $D_{\text{CPC}} = 0.01$ m, and $\theta_{\text{i,max}} = \theta_{\text{c}} = 40°$, the maximum geometrical gain of the CPC can be calculated as:

$$G_{\text{geom}} = \frac{D_{\text{CPC}}}{d_{\text{CPC}}} = 3.33. \tag{4.17}$$

It is then possible to calculate the angle at which the light beams leave the exit aperture (D_{CPC}) after being refracted and entering the CPC. This quantity has a relationship with the AoI of the incoming light rays, which can be set at $\theta_{\text{i}} \leq \psi_{\text{FOV}} = 40°$ as required by the design specifications:

$$\theta_{\text{r}} = \arcsin \frac{\sin \theta_{\text{i}}}{n_{\text{i}}} = 25.56°. \tag{4.18}$$

At this point, the resulting height of the CPC can be calculated with the following relationship:

$$H_{\text{CPC}} = (d_{\text{CPC}} + D_{\text{CPC}}) \cdot \cot(\theta_{\text{r}}) = 0.027 \text{ m}. \tag{4.19}$$

This CPC height would exceed the given requirement by more than 50%. To overcome this limitation, it is possible to use a truncated design for the CPC. In fact, as noted in [209], it is possible to reduce the height of the CPC by a factor of $\eta_{\text{height}} = 50\%$ while only losing $\eta_{\text{gain}} = 8\%$ of the original gain. In this way, it can be obtained:

$$H_{\text{CPC, tr}} = H_{\text{CPC}} \cdot \eta_{\text{height}} = 0.014 \text{ m} \tag{4.20}$$

which falls within the given requirements.
where G_{theo} is the theoretical gain of the CPC before the losses due to the truncation and the transmissivity of the material. These can be accounted for in the following way:

$$G_{\text{tr}} = G_{\text{geom}}(1 - \eta_{\text{gain}}) \tag{4.21}$$

$$G_{\text{OC}} = G_{\text{tr}} T_{\text{CPC}} \approx 2.25. \tag{4.22}$$

where G_{tr} is the gain after the truncation. Furthermore, by the effect of the truncation, the input aperture D_{CPC} will be even lower than the specified maximum requirement, further decreasing the size of the final OFE. These values in general satisfy the given requirements, and the CPC gain used to generate the simulation results, $G_{\text{OC}} = 2.25$, can be achieved and is a reasonable assumption for a practical setting.

Below the CPC, every sub-receiver is made up of a similar array of $N_{\text{PD}} = 2$ APDs, modeled after the off-the-shelf component S8664-30K Si APD [210] manufactured by Hamamatsu. Its wavelength-dependent responsivity curve is shown in Figure 4.5.

After being converted into a current proportional to the optical power that hits the sub-receiver by means of the APDs, the signal is converted again into a voltage, so that further processing is possible. This conversion is performed by a TIA, whose gain can be tuned by appropriately choosing its resistor. As mentioned, a TIA gain of $G_{\text{TIA}} = 2000$ V/A is assumed in this dissertation. After this, the voltage waveform is translated in the digital domain by an ADC. The devices' logic can then handle this waveform based on the employed scheme to turn it into usable data.

4.2.3 Indoor Scenario

The results that will be presented in Section 4.3 have been obtained by means of custom MATLAB code apt at defining a simulation scenario, carrying out the required calculations, and storing the related outcomes, which will be analysed to determine the performances. In this section, more details on such scenarios and the main performance

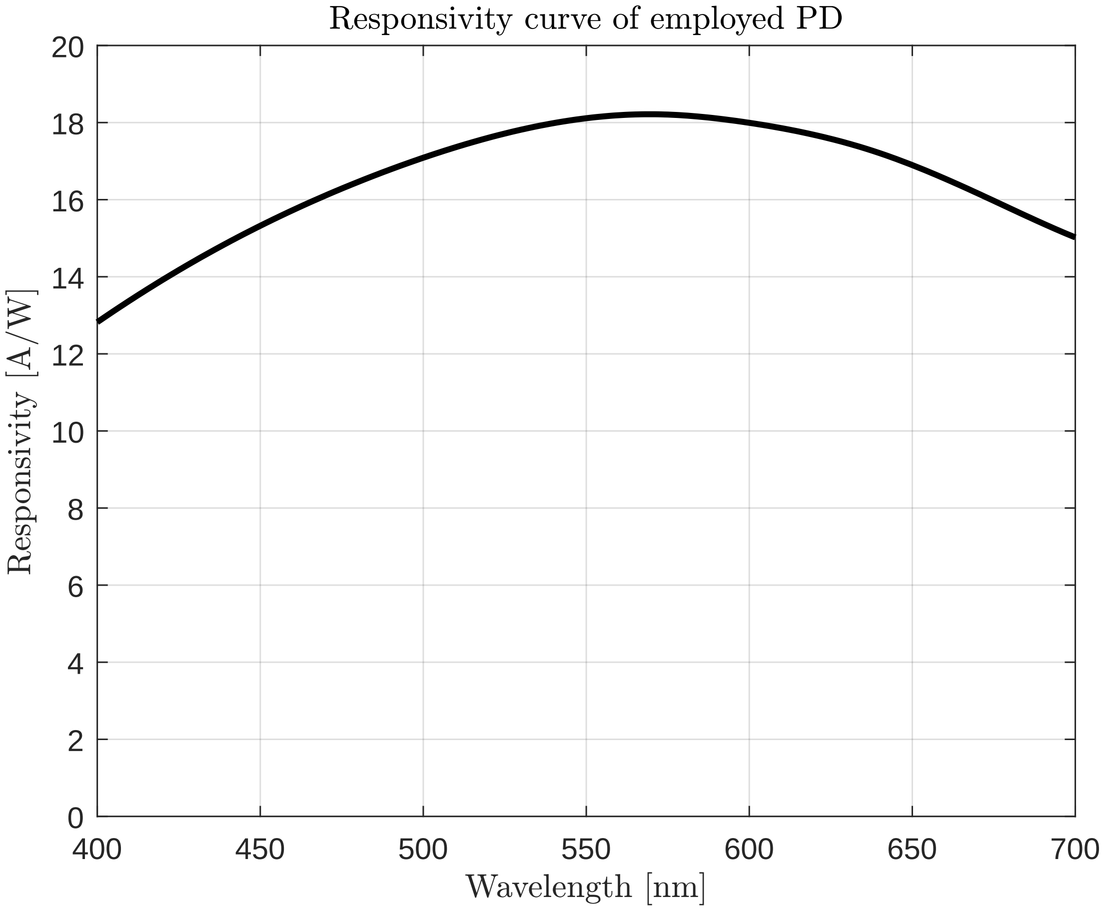

Figure 4.5: Responsivity curve of the APDs employed in this work, visually sampled from datasheets.

metrics will be provided.

Room

The room envisioned in this chapter's simulation scenarios is 6 m long, 6 m wide, and 3 m high. This is an arbitrary choice, that has been made by considering a reasonable size for an average common room or small office. The ceiling of the room is fitted with $N_{\mathrm{AP}} = 25$ RGBA LiFi APs, whose purpose is that of providing illumination along with wireless communication capabilities. The APs are arranged in a square lattice grid, made by $N_{\mathrm{y,AP}} = 5$ rows and $N_{\mathrm{x,AP}}$ columns. The distance between any AP and a neighbouring AP or wall is $d_{\mathrm{AP}} = 1.2$ m. The users are assumed to keep their devices at a height of $h_{\mathrm{u}} = 1$ m from the ground, and as a consequence, the transmitter and receiver planes are at a distance of $h = 2$ m. As mentioned, light reflections of any order coming from the walls are neglected in this work, and the room is assumed to be free from furniture. As a consequence, the entirety of the room size can be utilised by the users as there are no objects physically preventing them from moving freely.

User behaviour

It is assumed that users have the freedom to move around the room while using their devices in portrait mode as they walk. Consequently, their behavior is presumed to align with the statistical findings presented in 2 and 3.2, both of which reference the research conducted in [158].

Specifically, it is assumed that the users' inclination angles (θ_{u}) follow a Gaussian distribution characterized by a mean (μ_{u}) of 29.67° and a standard deviation (σ_{u}) of 7.78°. The users' facing directions (ω_{u}) follow a continuous uniform distribution within the range of $[0°, 360°)$. Similarly, the physical locations of the users within the room, denoted by $[x_{\mathrm{u}}, y_{\mathrm{u}}]$, follow a discrete uniform distribution within the room boundaries: $[x_{\mathrm{u}}, y_{\mathrm{u}}] \in [0\text{ m}, 6\text{ m}]$.

Simulation parameters

Two kinds of simulations have been carried out in this chapter, which are termed after the type of scenario they serve to investigate: coverage and network. All simulations in this chapter consist of up to $N_{\mathrm{u}} = 4$ concurrent users.

In coverage simulations, all users sweep every available position in the room, with their receivers pointing upwards. This is chosen as a method to fairly identify the amount of coverage provided by each AP in the room, since the random orientation would not provide comparable results across different locations.

Every iteration of the code is assumed to span for a time t in which, after performing the allocation, a symbol sequence can be sent to each user. In coverage simulations, in each iteration a different location is considered, and all users are assumed to occupy it at the same time; thus, the number of iterations N_{iter} is equal to the number of possible locations in the room. After calculating the necessary geometric parameters, a $N_{\mathrm{y,AP}}$-by-$N_{\mathrm{x,AP}}$-by-N_{u} matrix $H(0)_{\mathrm{u,a}}$ containing all the optical path losses between each AP and each user is generated, and (4.7) is used along with (4.8) and (4.11) to compute the received signal and interference currents of every sub-receiver of every user, coming from every transmitter of every AP. This means that the computation assumes the worst-case scenario, which is that every transmitter is active at any time, potentially providing considerable amounts of interference. The channel allocation is made with the fixed and adaptive schemes, and an individual signal sequence $S_{\bar{\mathrm{u}},\bar{\mathrm{k}},\bar{\mathrm{a}},\bar{\mathrm{i}}}$ is sent to every user. Note that in this sequence, specific values of $u = \bar{u}$, $k = \bar{k}$, $a = \bar{a}$, and $i = \bar{i}$ are considered since the allocation has now been performed and the system knows precisely which sequence has to be transmitted by which transmitter, which will be picked up by the desired user using the sub-receiver allocated to that channel. After this, the performance metrics according to Section 4.2.3 are computed and stored, based on which transmitters are actually active after the allocation.

Network simulations employ the Monte Carlo method. The Monte Carlo method comprises a broad class of computational algorithms that rely on repeated random sampling to obtain numerical results. These simulations differ from coverage simulations with respect to the users' behaviour: rather than sweeping every position in the room with receivers pointing up, users' location, orientation, and device inclination follow the statistical distributions described in Section 4.2.3. As a consequence, the number of iterations N_{iter} is not equal to the number of available room locations anymore, but it is fixed to $N_{\mathrm{iter}} = 1000$. Everything else, including the resource allocation method (both fixed and adaptive), is the same as in the coverage simulations.

Network performance metrics

Four metrics can be used to compare the performances of the network resulting from using either the fixed or adaptive scheme: average achievable data rate and connection loss rate, both total and per user. These will be discussed in this section while also showing how they are calculated within the simulations' code.

When a channel is assigned to a user, it effectively dedicates the sub-receiver of that colour for the purpose of signal reception. In the process, this sub-receiver not only captures the desired signal but also inadvertently and inevitably captures interference and background noise (which will add to the thermal noise generated in the elaborating circuit). Consequently, the SINR for this specific sub-receiver can be quantified using the formula presented in (4.14). This SINR value then plays a pivotal role when applying the widely recognized Shannon-Hartley capacity theorem [211] to approximate the attainable data transmission rate. The Shannon-Hartley capacity theorem, a fundamental concept in information theory, provides essential insights into the maximum data rate that can be reliably conveyed over a communication channel in the presence of noise and interference, offering valuable guidance for system optimization and capacity planning. In this case, it can be calculated as:

$$C_{\bar{\mathrm{u}},\bar{\mathrm{k}}}(t) = B_{\mathrm{mod}} \log_{10}[1 + \gamma_{\bar{\mathrm{u}},\bar{\mathrm{k}}}^{\mathrm{SINR}}(t)] \tag{4.23}$$

where B_{mod} is the modulation bandwidth of the channel (which in this work is constant for every channel and $B_{\mathrm{mod}} = 30$ MHz). Given that every sub-receiver is independent and capable of parallel reception, the total achievable data rate for each user in the t-th iteration is the sum of the achievable data rates of all its sub-receivers:

$$C_{\bar{\mathrm{u}}}(t) = \sum_{k=1}^{N_{\mathrm{k}}} C_{\bar{\mathrm{u}},k}(t). \tag{4.24}$$

Furthermore, the average achievable data rate for a single user can be calculated as the average across all iterations:

$$C_{\bar{\mathrm{u}}} = \frac{1}{N_{\mathrm{iter}}} \sum_{t=1}^{N_{\mathrm{iter}}} C_{\bar{\mathrm{u}}}(t) \tag{4.25}$$

whereas the total network average achievable data rate can be calculated as the sum of all per-user achievable data rates:

$$C_{\mathrm{tot}} = \sum_{u=1}^{N_{\mathrm{us}}} C_{\mathrm{u}}. \tag{4.26}$$

As a further step, the connection loss percentage for a single user can be defined. In fact, a successful allocation for the k-th sub-receiver of the u-th user will only be possible if the resulting SINR will exceed a set threshold which in this work, it is assumed $\gamma_{\text{th}}^{\text{SINR}} = -6$ dB. This specific choice is motivated by the limit for reliable communication while using Forward Error Correction (FEC), as it happens in modern telecommunication standards like 802.11ac (Wireless Fidelity (WiFi) 5), 802.11ax (WiFi 6 and 6E), and 802.11be (WiFi 7) [201]. This limit is, at the time of writing, commonly recognised between -6 dB and -10 dB when using Low-Density Parity Check (LDPC) codes at lower Modulation and Coding Scheme (MCS) levels in WiFi.

It is then possible to define $N_{\bar{\mathrm{u}}}^{\text{conn}}(t) = 1$ if, at the t-th allocation attempt, at least one sub-receiver of the user ū has a successful allocation, and 0 otherwise. Note that if $N_{\bar{\mathrm{u}}}^{\text{conn}}(t) = 0$, then $C_{\bar{\mathrm{u}}}(t) = 0$ Mbps, while if $N_{\bar{\mathrm{u}}}^{\text{conn}}(t) = 1$, then $C_{\bar{\mathrm{u}}}(t) > 0$ Mbps. It can also be noted that $N_{\bar{\mathrm{u}}}^{\text{conn}}$ is a vector of length N_{iter} which contains a sequence of 1 and 0 that identify in which iterations the user has not been able to connect.

At this point, the connection loss percentage for a particular user ū, $\chi_{\bar{\mathrm{u}}}^{\text{CL}}$, can be defined as follows:

$$\chi_{\bar{\mathrm{u}}}^{\text{CL}} = \frac{1}{N_{\text{iter}}} \sum_{t=1}^{N_{\text{iter}}} N_{\bar{\mathrm{u}}}^{\text{conn}}(t) \tag{4.27}$$

and results in a percentage indicating how many times the user has not been able to receive a useful signal over the course of the entire simulation.

4.2.4 Adaptive WDMA

In this section, the novel adaptive WDMA algorithm is presented. Its objective is to maximise the SINR of every user, prioritising a fair allocation among all users. Using the SINR as a target for the maximisation achieves three important results:

- It maximises the maximum achievable network capacity, which is proportional to the SINR.
- Allows the allocation process to indirectly take the Spectral Overlap (SO) into account, as the SINR depends on the overall gain (which in turn depends on both the LOS optical path attenuation and the SO).

- Inherently minimises the interference figure. Since the SINR is, by its nature, a measure of the strength of the signal in relation to that of the noise and interference, its maximisation represents an efficient strategy to increase both the user's and network's performances, as opposed to optimising the OFE.

The algorithm thus requires that Channel State Information (CSI) is collected, and therefore it is assumed that such information is available for the network. This knowledge makes it possible, even if two or more users are close in space, to implement smart wavelength reuse.

Algorithm 1: Adaptive WDMA algorithm.

Data: A $\gamma_{u,k,a,i}$ matrix with SINR values for each $\bar{u}, \bar{k}, \bar{a}, \bar{i}$ combination;
An empty Assignation List, L;
Result: An Allocation List, $A_{u,k,a,i}$
Initialization phase;
for $u = 1, 2, \ldots$ **do**
    if $\sum_{a=1}^{N_{AP}} H(0)_{\bar{u},a} > 0$ **then**
        Put $\bar{u}$ in L;
    end
end
Allocation phase;
while L *is not empty* **do**
    Find max in $\gamma_{u,k,a,i}$ and assign the corresponding $\bar{u}, \bar{k}, \bar{a}, \bar{i}$ combination in $A_{u,k,a,i}$;
    Set that $\bar{u}, \bar{k}, \bar{a}, \bar{i}$ combination $= 0$ in $\gamma_{u,k,a,i}$;
    Take $\bar{u}$ out of L;
end
L is now empty;
$A_{u,k,a,i}$ contains one $\bar{k}, \bar{a}, \bar{i}$ combination for every active user u;

The algorithm that performs an adaptive WDMA resource allocation is detailed as in Algorithm 1. At any time $t = \bar{\mathrm{t}}$, its main aim is that of using the CSI (in the form of a N_{k}-by-N_{AP}-by-N_{u} matrix $\gamma^{\mathrm{SINR}}(\bar{\mathrm{t}}) = \gamma_{u,k,a,i}$) and an assignation list (L). The assignation list is a vector of length N_{us} where each element is equal to 1 if the corresponding user is ready to be allocated a channel and 0 otherwise. At the start, this list is empty and thus all its elements are 0. Then, the algorithm outputs an allocation list in the form of a N_{k}-by-N_{AP}-by-N_{u} matrix $A(\bar{\mathrm{t}}) = A_{u,k,a,i}$. Here, every element is equal to 0 except those corresponding to the row (colour), column (AP), and page (user), which form the allocation. The population of this list starts with the initialisation phase, where the algorithm first checks which users have at least one AP in their FOV (that is, which pages of the SINR matrix have at least one element such that $> \gamma_{\mathrm{th}}^{\mathrm{SINR}}$). In fact, if a user is in a position where no APs are in its FOV and thus a LOS optical link is not possible, its page in the SINR matrix will only contain 0s.

The algorithm puts all the users that have at least one AP in their FOV in the assignation list $\Gamma(\bar{\mathrm{t}})$. Then, the allocation phase takes place by selecting one combination that maximises SINR for one channel and one user, and proceeds iteratively for the other users until the assignation list is empty, only considering pages of the $\gamma^{\mathrm{SINR}}(\bar{\mathrm{t}})$ whose corresponding users are present in such a list. To elaborate on how the actual allocation is performed, the algorithm first finds the maximum value of SINR that can be allocated across all pages of the SINR matrix. The corresponding element in the allocation list is set to 1 to record the allocation of that channel, whereas the SINR values of every other user corresponding to that allocation are put to 0. In this way, the same channel cannot be allocated to another user, which would cause the transmission to fail for both. Once this is complete, the element in the assignation list corresponding to the user is set to 0, and the allocation process is repeated with the next maximum SINR value in the matrix until all users are out of the assignation list.

As opposed to the adaptive WDMA allocation algorithm, the fixed algorithm is used as a benchmark and is more straight-forward. It does not require as much computation at the network level because it only entails that users are served with a different colour based on the order in which they have entered the network: user n. 1 will be served with blue, user n. 2 with green, user n. 3 with amber, and user n. 4 with red. If more than 4 users are present in the network, the 5th user is allocated the blue channel again, and so on. In this way, for more crowded scenarios, the fixed algorithm heavily relies on the spatial separation between users. However, in this chapter, only 4 users are considered to exclude this aspect while only focusing on highlighting the potential benefits and drawbacks of maximising the SINR.

4.2.5 Validation

The following subsection is dedicated to performing a validation of the presented system model. This will be done by calculating analytically three sample points of the Cumulative Distribution Function (CDF) of the datarate pertaining to a user immersed in a pre-defined scenario. These will then be compared with the empirical CDF resulting from a simulation, and a match between the analytical and empirical CDF will guarantee the sought reliability of the results presented in this chapter. The simulations for the empirical CDF will be executed with the same custom code used for the results discussed in the following section.

Given the user mobility considered in Section 4.2.3, the complete results of the CDF depend on the three independent probabilistic distributions concerning the user's location $(x_{\mathrm{u}}, y_{\mathrm{u}})$, orientation (ω_{u}), and device inclination (θ_{u}). This makes the analytical calculation difficult (alas, sometimes impossible) to perform by hand, and thus, simplifying the considered scenario is required for successfully conducting the validation. This can be achieved by imposing appropriate restrictions on user behaviour. More specifically, the changes with respect to the scenario in Section 4.2.3 are the following:

- Only two users are present in the room, and they are uniquely identified as u1 and u2.
- The location of u1 is fixed below AP 13 (that is, the AP exactly in the center of the room).
- The location of u2 still follows a discrete uniform distribution with the same boundaries, but the available locations are only selected amongst the locations of the APs. That is, in each iteration, u2 has an equal probability of being directly below one of the $N_{\mathrm{AP}} = 25$ APs in the room. As a result, the probability of u2 being exactly below one specific AP (whose location is $[\bar{x}_{\mathrm{AP}}, \bar{y}_{\mathrm{AP}}] \in [x_{\mathrm{AP1}}, y_{\mathrm{AP1}}; x_{\mathrm{AP2}}, y_{\mathrm{AP2}}; \ldots; x_{N_{\mathrm{AP}}}, y_{N_{\mathrm{AP}}}]$), can be calculated as:

$$P(x_{\mathrm{u2}} = \bar{x}_{\mathrm{AP}} \cup y_{\mathrm{u2}} = \bar{y}_{\mathrm{AP}}) = P(\bar{x}\bar{y}) = \frac{1}{N_{\mathrm{AP}}} = 0.04. \tag{4.28}$$

- The orientation of both users is fixed, and $\omega_{\mathrm{u1}} = \omega_{\mathrm{u2}} = 270°$. Given the rotation geometry employed in this dissertation, this implies that the users are facing towards the right wall of the room.

- The inclination angle of both users' devices is fixed, and $\theta_{\mathrm{u1}} = 0°$ while $\theta_{\mathrm{u2}} = \mu_{\mathrm{u}} = 29.67°$. This means that the device of u1 is pointing directly upwards (and towards AP 13), while u2 is keeping the device at the average of the distribution. Given the value of ω_{u2}, the device of u2 faces the left direction and is tilted by an angle of $90 - \theta_{\mathrm{u2}}$ with respect to the ground plane.

- Both users are only allowed to use the blue receiver allocated to the blue transmitter of the AP directly above them. This means that while only signals received by the blue receiver will be considered, every transmitter in the room can still contribute to the interference (because of spectral leakage). Furthermore, u1 is prioritised in the allocation process due to the round-robin allocation.

These changes simplify the analytical calculations, rendering them feasible while still providing good validation reliability between analytical and empirical CDF. Furthermore, considering that u1 has a fixed location and is prioritised in the allocation process, the objective is to calculate the analytical CDF for u2 while considering u1 as an interfering user.

Figure 4.6 shows the indoor environment considered, with the square grid of APs whose disposition simplifies the analytical calculations because of simmetry and because of the fact that u2 has a fixed orientation $\omega_{\mathrm{u2}} = 270°$. In fact, by drawing an imaginary line through APs 3, 8, 13, 18, and 23 acting as a symmetry axis, it can be found that all calculations made for the first two rows of APs will be equally valid for the fourth and fifth rows.

To pursue the set objective for the validation, it is useful to first recall the definition of a CDF. Given a random variable X, its CDF is given by [212]:

$$F_X(\bar{X}) = P(X \leq \bar{X}), \tag{4.29}$$

which can be interpreted as the probability that the random variable itself assumes a

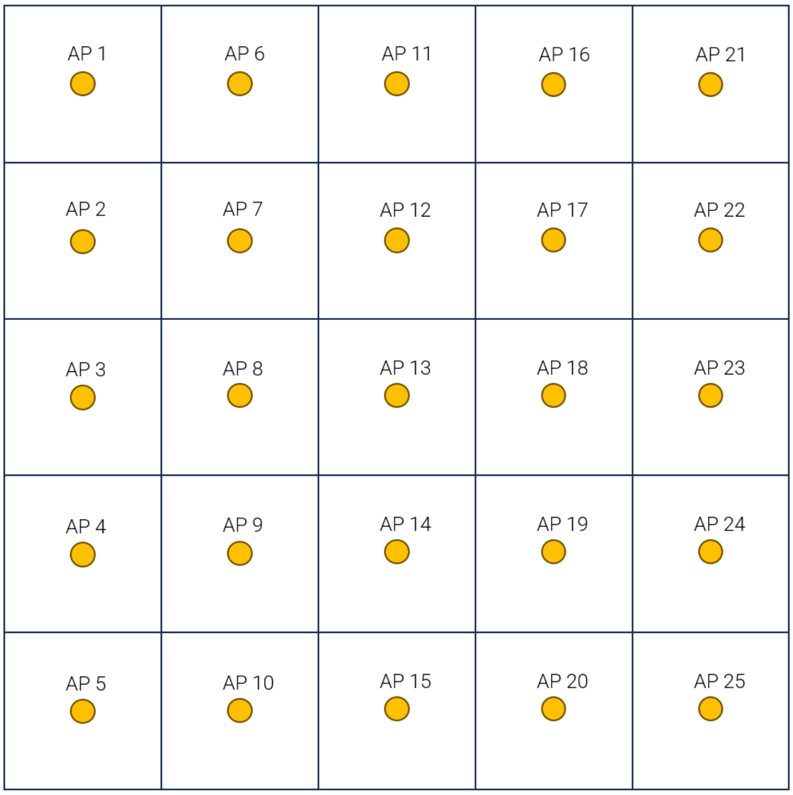

Figure 4.6: Room with square grid of APs. Each AP is numbered from 1 to N_{AP}. The square grid of APs allows to simplify analytical calculations thanks to its symmetry.

value that is equal to or less than another arbitrary value $\bar{X}$, defined in the supported range. With this in mind, it is possible to consider that if the random variable $X = C_{\mathrm{u2}}$ is the achievable channel capacity for u2 and $\bar{X} = X_{\mathrm{max}}$ is the maximum achievable data rate for u2, it holds that:

$$F_{C_{\mathrm{u2}}}(X_{\mathrm{max}}) = P(C_{\mathrm{u2}} \leq X_{\mathrm{max}}) = 1. \tag{4.30}$$

which coincides with the first point of the sought CDF. Thus, the next step is to calculate the value of X_{max}. This can be done by considering that the maximum data rate for u2 will be attained when there is no interference. Based on the presented model, and since u2 is exactly below one of the APs (for example, $\bar{a}$ is AP 1), the system parameters for this calculation are summarised in Table 4.1. All unlisted parameters are assumed to be equal to the ones reported in Section 4.2.

Table 4.1: Parameters of validation point 1.

1st Validation Parameters		
Symbol	*Description*	*Value*
m_{l}	lambertian emission order	1.7675
A_{det}	receiver effective area	1.4110^{-5}m
$d_{\mathrm{u2},\bar{a}}$	distance between source and receiver	2m
$\psi_{\mathrm{u2},\bar{a}}$	AoI of light beam	29.67°
$\phi_{\mathrm{u2},\bar{a}}$	source angle of emission	0°

Since $\psi_{\mathrm{u2},\bar{a}} < \Psi_{\mathrm{c}}$, (4.4) can be used to calculate the optical path loss for the transmitted signal:

$$H(0)_{\mathrm{u2},\bar{a}} = \frac{(m_{\mathrm{l}}+1)A_{\mathrm{det}}}{2\pi d^2_{\mathrm{u2},\bar{a}}} \cos\phi_{\mathrm{u2},\bar{a}}{}^{m_{\mathrm{l}}} G_{\mathrm{OC}} \cos\psi_{\mathrm{u2},\bar{a}} = 3.04 \cdot 10^{-6}. \tag{4.31}$$

Then, according to the analytical model, the maximum signal voltage can be calculated by inserting (4.8) into (4.13), as follows:

$$V^{\mathrm{sig}}_{\mathrm{u2},1} = G_{\mathrm{TIA}} \Phi^{\mathrm{tr}}_{\bar{a},1} H(0)_{\mathrm{u2},\bar{a}} \int_{\alpha}^{\beta} S^{\mathrm{OF}}_{\mathrm{u2},1,\bar{\psi}}(\lambda) S^{\mathrm{tr}}_{\bar{a},1}(\lambda) R_{\mathrm{u2},1}(\lambda) d\lambda = 0.043 \text{ V}. \tag{4.32}$$

It has to be noted that the term $\int_{\alpha}^{\beta} S^{\mathrm{OF}}_{\mathrm{u2},1,\bar{\psi}}(\lambda) S^{\mathrm{tr}}_{\bar{a},1}(\lambda) R_{\mathrm{u2},1}(\lambda) d\lambda$ includes the two spectra of the blue source and receiver, $S^{\mathrm{tr}}_{\bar{a},1}(\lambda)$ and $S^{\mathrm{OF}}_{\mathrm{u2},1,\bar{\psi}}(\lambda)$, which are not available in analytical explicit form. For this reason, only this specific term was attained with the MATLAB software by inputting the necessary code independently from the simulation environment that has been used to obtain the results. Further calculations will also entail calculating similar terms, and the method for obtaining them is the aforementioned.

As earlier noted, when $u2$ is immersed in the scenario that is being considered, the only real potential source of interference (that is, AP 13 that transmits to u1) is out of the user's FOV. However, as the lighting is assumed to be fully functioning, and for the purposes of calculating the correct noise variance, background lighting has to be taken into account. To this end, it is possible to calculate the intra-AP interference that will generate background noise by means of spectral leakage. The expression is similar to (4.32), except it entails calculating the sum of all contributions from other sources in the same AP (that is, in this case, green, amber, and red sources). It can be calculated as:

$$V_{\mathrm{u2},1}^{\mathrm{int}} = \sum_{a=1,a\neq\bar{a}}^{N_{\mathrm{AP}}} G_{\mathrm{TIA}} \Phi_{a,1}^{\mathrm{tr}} H(0)_{\mathrm{u2},a} \int_{\alpha}^{\beta} S_{\mathrm{u2},1,\bar{\psi}}^{\mathrm{OF}}(\lambda) S_{a,1}^{\mathrm{tr}}(\lambda) R_{\mathrm{u2},1}(\lambda) d\lambda = 2.22 \cdot 10^{-5}\ \mathrm{V}. \tag{4.33}$$

At this point, it is possible to calculate the variance of the noise, including the contributions of both shot noise coming from background illumination and thermal noise generated by the electrical circuit responsible for manipulating the signal (which has been discussed in Section 4.2.2). It can be done with (4.12), and it results:

$$\sigma_{\mathrm{noise}}^2 = 2qBI_{\mathrm{bg}} + \frac{4k_{\mathrm{B}}TB}{R_{\mathrm{l}}} = 2qB(\frac{V_{\mathrm{u2},1}^{\mathrm{sig}}}{2G_{\mathrm{TIA}}} + \frac{V_{\mathrm{u2},1}^{\mathrm{int}}}{2G_{\mathrm{TIA}}}) + \frac{4k_{\mathrm{B}}TB}{R_{\mathrm{l}}} = 7.85 \cdot 10^{-15} \tag{4.34}$$

and since u2 does not experience interference from other users, the SINR can be calculated with (4.14):

$$\gamma_{\mathrm{u2},1}^{\mathrm{SINR}}(\bar{t}) = \frac{[V_{\mathrm{u2},1}^{\mathrm{sig}}]^2}{4[\sigma_{\mathrm{noise,u2},1}^2 G_{\mathrm{TIA}}^2 + \mathrm{var}(I_{\mathrm{u},1}^{\mathrm{int}}) G_{\mathrm{TIA}}^2]} = 1.43 \cdot 10^4. \tag{4.35}$$

This SINR value can then be used in (4.26) to calculate X_{max} as:

$$X_{\mathrm{max}} = B \log_2[1 + \gamma_{\mathrm{u2},1}^{\mathrm{SINR}}(\bar{t})] = 30 \cdot 10^6 \cdot \log_2[1 + (1.43 \cdot 10^4)] = 414.11\ \mathrm{Mbps} \tag{4.36}$$

and completes the data regarding the first point of the validation.

The second point of the validation can be obtained by considering the user u2 in a different location than the earlier point, where some interference is present. One example of that is AP 22, and thus for the next calculations, $[x_{\mathrm{u2}}, y_{\mathrm{u2}}] = [x_{\mathrm{AP22}}, y_{\mathrm{AP22}}]$.

The resulting capacity X_{int} will be lower than X_{max} for this reason.

In this case, since the user's relative position with respect to the allocated transmitter is the same as the earlier point, the maximum signal voltage calculated in (4.32) is still usable.

The biggest difference, as earlier noted, is the presence of the interference coming from AP 13. The system parameters relative to u2 and this interfering AP are listed in Table 4.2.

Table 4.2: Parameters of validation point 2.

2nd Validation Parameters		
Symbol	*Description*	*Value*
$d_{\mathrm{u2,13}}$	distance between source 13 and receiver	3.34m
$\psi_{\mathrm{u2,13}}$	AoI of light beam	29.04°
$\phi_{\mathrm{u2,13}}$	source angle of emission	53.22°

The optical path loss is calculated as:

$$H(0)_{\mathrm{u2,13}} = \frac{(m_{\mathrm{l}}+1)A_{\mathrm{det}}}{2\pi d_{\mathrm{u2,13}}^2} \cos\phi_{\mathrm{u2,13}}{}^{m_{\mathrm{l}}} G_{\mathrm{OC}} \cos\psi_{\mathrm{u2,13}} = -63.55 \text{ dB}. \tag{4.37}$$

Subsequently, a similar approach as (4.32) can be used to calculate the maximum interference voltage generated at the blue receiver of u2 as a consequence of the signal coming from AP 13 to u1:

$$V_{\mathrm{u2,1}}^{\mathrm{int}} = G_{\mathrm{TIA}} \Phi_{13,1}^{\mathrm{tr}} H(0)_{\mathrm{u2,13}} \int_{\alpha}^{\beta} S_{\mathrm{u2,1},\bar{\psi}}^{\mathrm{OF}}(\lambda) S_{13,1}^{\mathrm{tr}}(\lambda) R_{\mathrm{u2,1}}(\lambda) d\lambda = 6.2 \cdot 10^{-3} \text{ V}. \tag{4.38}$$

As a next step, it is necessary to calculate the noise variance. In order to do this, it is necessary to again calculate the contribution to the interference coming from every single transmitter in the FOV of u2 (including, but not limited to, the current generated as a result of the interference calculated in the previous step). This will add to the received signal and constitute the background illumination. Similarly to (4.33), this can be calculated as:

$$V_{\mathrm{u2,1}}^{\mathrm{int,tot}} = \sum_{a=1,a\neq\bar{a}}^{N_{\mathrm{AP}}} G_{\mathrm{TIA}} \Phi_{a,1}^{\mathrm{tr}} H(0)_{\mathrm{u2},a} \int_{\alpha}^{\beta} S_{\mathrm{u2,1},\bar{\psi}}^{\mathrm{OF}}(\lambda) S_{a,1}^{\mathrm{tr}}(\lambda) R_{\mathrm{u2,1}}(\lambda) d\lambda = 0.22 \text{ V} \quad (4.39)$$

and thus, the noise variance is given by:

$$\sigma_{\mathrm{noise}}^2 = 2qBI_{\mathrm{bg}} + \frac{4k_{\mathrm{B}}TB}{R_{\mathrm{l}}} = 2qB(\frac{V_{\mathrm{u2,1}}^{\mathrm{sig}}}{2G_{\mathrm{TIA}}} + \frac{V_{\mathrm{u2,1}}^{\mathrm{int,tot}}}{2G_{\mathrm{TIA}}}) + \frac{4k_{\mathrm{B}}TB}{R_{\mathrm{l}}} = 7.87 \cdot 10^{-15}. \quad (4.40)$$

To calculate the SINR, it is necessary to know the variance of the interference current generated at the blue receiver of user u2. Note that other interference contributions from other transmitters in the user's FOV are not relevant to this calculation as they were for the background illumination: in fact, the only interfering AP that is actively transmitting (to user u1), other than illuminating, is AP 13. The needed maximum interference current is given by:

$$I_{\mathrm{u2,1}}^{\mathrm{sig}} = \frac{V_{\mathrm{u2,1}}^{\mathrm{sig}}}{G_{\mathrm{TIA}}} = 3.1 \cdot 10^{-6} \text{ A}. \quad (4.41)$$

At this point, to calculate its variance, it is sufficient to consider that an OOK signal is made of $n = 2$ equiprobable symbols, and consequently $p = 0.5$ [211]. Knowing this, the signal can be treated as a uniform discrete distribution $I \sim \mathrm{U}(a, b, n, p)$ where a and b coincide with the two possible values of the distribution. In this case, $a = 0$, $b = I_{\mathrm{u2,1}}^{\mathrm{sig}} = 3.1 \cdot 10^{-6}$ A, and calculating the variance can be done as given by [212]:

$$\mathrm{var}(I_{\mathrm{u2,1}}^{\mathrm{sig}}) = \mathbb{E}(I^2) - \mathbb{E}(I)^2 = \frac{b^2 - a^2}{2} - (\frac{b-a}{2})^2 = 2.4 \cdot 10^{-12} \quad (4.42)$$

Similarly to (4.35) and (4.36), the resulting SINR and channel capacity for this validation point can now be calculated, respectively, as:

$$\gamma_{\mathrm{u2,1}}^{\mathrm{SINR}}(\bar{t}) = \frac{[V_{\mathrm{u2,1}}^{\mathrm{sig}}]^2}{4[\sigma_{\mathrm{noise,u2,1}}^2 G_{\mathrm{TIA}}^2 + \mathrm{var}(I_{\mathrm{u,1}}^{\mathrm{int}}) G_{\mathrm{TIA}}^2]} = 16.70 \text{ dB}; \quad (4.43)$$

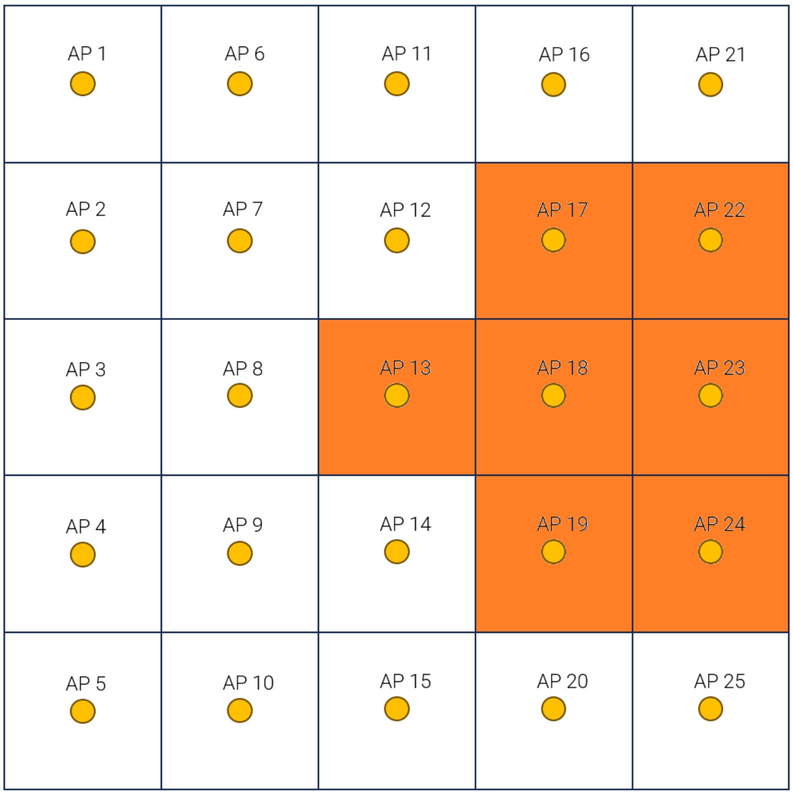

Figure 4.7: Room with square grid of APs. Highlighted in orange are the locations (below their relative APs) in which u2 experiences interference equal to or higher than that calculated for the 2$^{\text{nd}}$ validation point.

$$X_{\text{int}} = B\log_2[1 + \gamma^{\text{SINR}}_{\text{u2,1}}(\bar{t})] = 167.30 \text{ Mbps}. \tag{4.44}$$

It is now necessary to calculate the probability $P(X \leq X_{\text{int}})$ to completely characterise the CDF point associated with X_{int}. This can be done with the analytical framework by verifying that, in the specific case of blue transmitter of AP 13 allocated to u1 and blue transmitter of AP 22 allocated to u2, this latter experiences only a minimum quantity of interference with respect to the other locations that are closer to AP 13. Thanks to the aforementioned restriction on user movement possibilities and symmetry, this allows to select all the exact locations in the room in which u2 will experience interference that is equal to or higher than the value just found. The result of these considerations can be seen in Figure 4.7: the number of APs that are to be counted as "favourable cases" for calculating the sought probability is $N_{\text{AP, fav}} = 7$. The probability can then be calculated:

$$F_{C_{\text{u2}}}(X_{\text{int}}) = P(C_{\text{u2}} \leq X_{\text{int}}) = \frac{N_{\text{AP,fav}}}{N_{\text{AP}}} = 0.28. \tag{4.45}$$

This completes the data needed for the 2nd validation point to be compared with the empirical CDF.

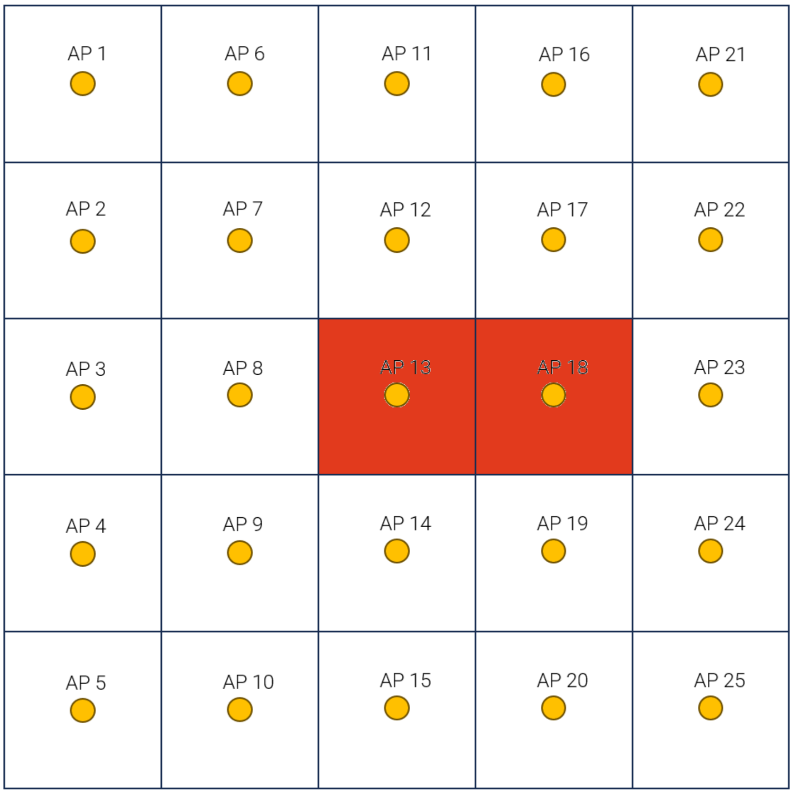

Figure 4.8: Room with square grid of APs. Highlighted in red are the locations (below their relative APs) in which u2 experiences a disconnection.

For the third and last point of the validation, it is convenient to investigate cases in which the network is unable to successfully allocate a channel to u2. This is equivalent to investigating in which cases the achievable capacity of u2 is $C_{\text{u2}} \leq X_{\text{CL}} = 0$ Mbps. It is intuitive to realise that this will happen whenever u2 is below AP 13, as the imposed restrictions and the priority of u1 in the allocation process will leave u2 without channels available.

The only other circumstance in which u2 will experience a disconnection is when the interference is too high with respect to the allocated signal, and by considering all other available locations in the room, the mathematical framework used so far can be employed to verify that this happens only when u2 is below AP 18. In fact, since the AoI between AP 13 and u2 is close to 0° in this circumstance, the PS effect would render this allocation better than that of AP 18. However, since AP 13 is already occupied by an allocation to u1, its transmitted signal causes very high interference for u2.

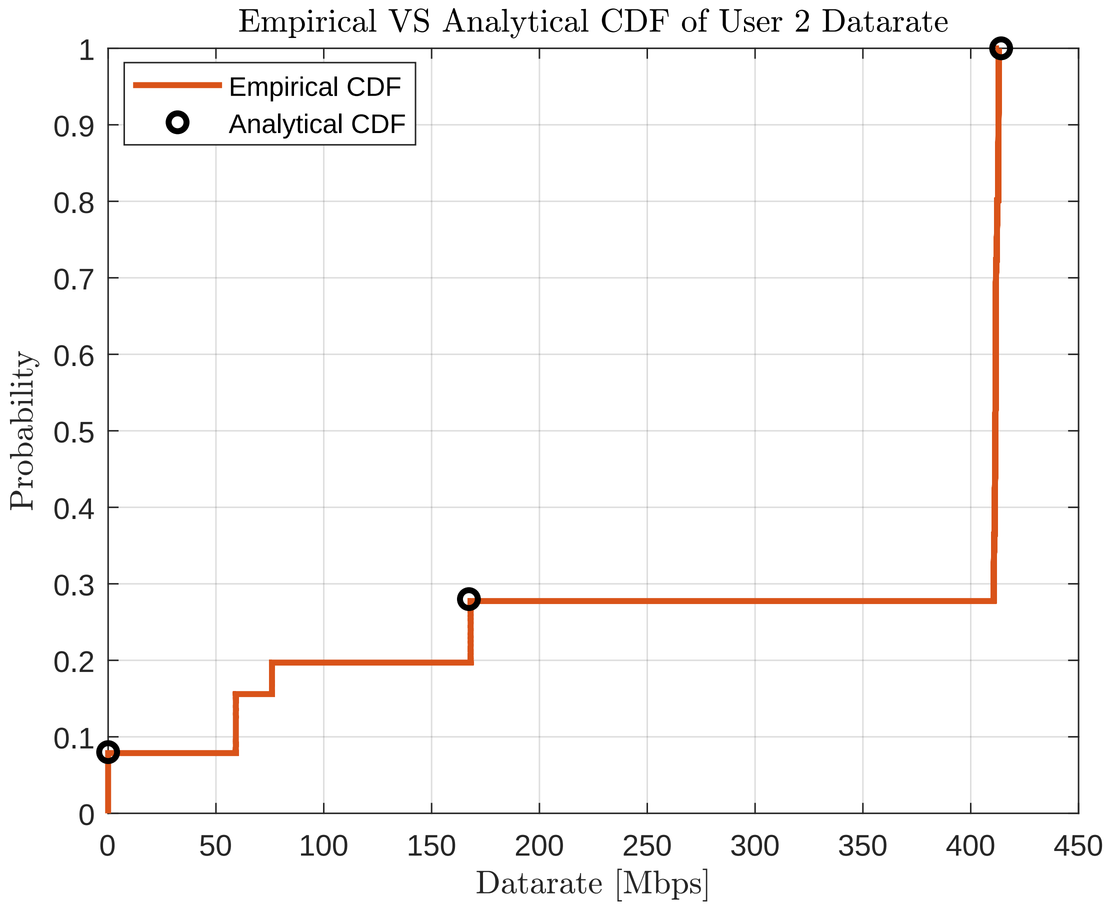

Figure 4.9: Validation by comparison of empirical versus analytical CDF of one user in the presence of a single interfering AP. Being CDFs, the X axis is the achieved data rate, while the Y axis represents the probability of achieving a data rate lower than X. The two CDFs have a good match, and the relative error is below 0.50%.

These two locations are reported in Figure 4.8, and from there, for the 3rd validation point, it can be inferred that $N_{\mathrm{AP,fav}} = 2$. The relative probability for this point is then given by:

$$F_{C_{\mathrm{u2}}}(X_{\mathrm{CL}}) = P(C_{\mathrm{u2}} \leq X_{\mathrm{CL}}) = \frac{N_{\mathrm{AP,fav}}}{N_{\mathrm{AP}}} = 0.08. \tag{4.46}$$

It is possible at this point to plot the simulated data in an empirical CDF for user u2 and overlap it with the three points that have been calculated analytically. The result can be seen in Figure 4.9.

As it can be seen, the visual match between the analytical validation points and the empirical CDF generated with the simulated data is good. The maximum relative error that is found is below $E_{\mathrm{rel}} < 0.50\%$.

4.3 Analysis

This section is focused on the analysis of the results obtained with the methodology described in earlier sections.

4.3.1 Coverage

Figure 4.10 shows the room coverage, represented as a spatial distribution of the achievable data rate, for each of the four users. The differences in spatial coverage and achievable data rate between users are clearly visible from comparing the various sub-figures, as they depend on the optical filter differences in terms of overlap between sources' emissivities and receivers' transmissivities.

According to the fixed allocation, user n. 1 is always assigned the blue channel, and by comparing the overlap between the continuous and dotted blue curves in Figure 4.3, it can be seen that the emissivity of the blue LEDs is concentrated in a relatively sharp spectrum that has a good SO with the corresponding optical filter. This latter also has a relatively wide transmissivity spectrum, which allows more blue light to pass while also being well separated from other wavelengths (especially green), which would introduce severe interference.

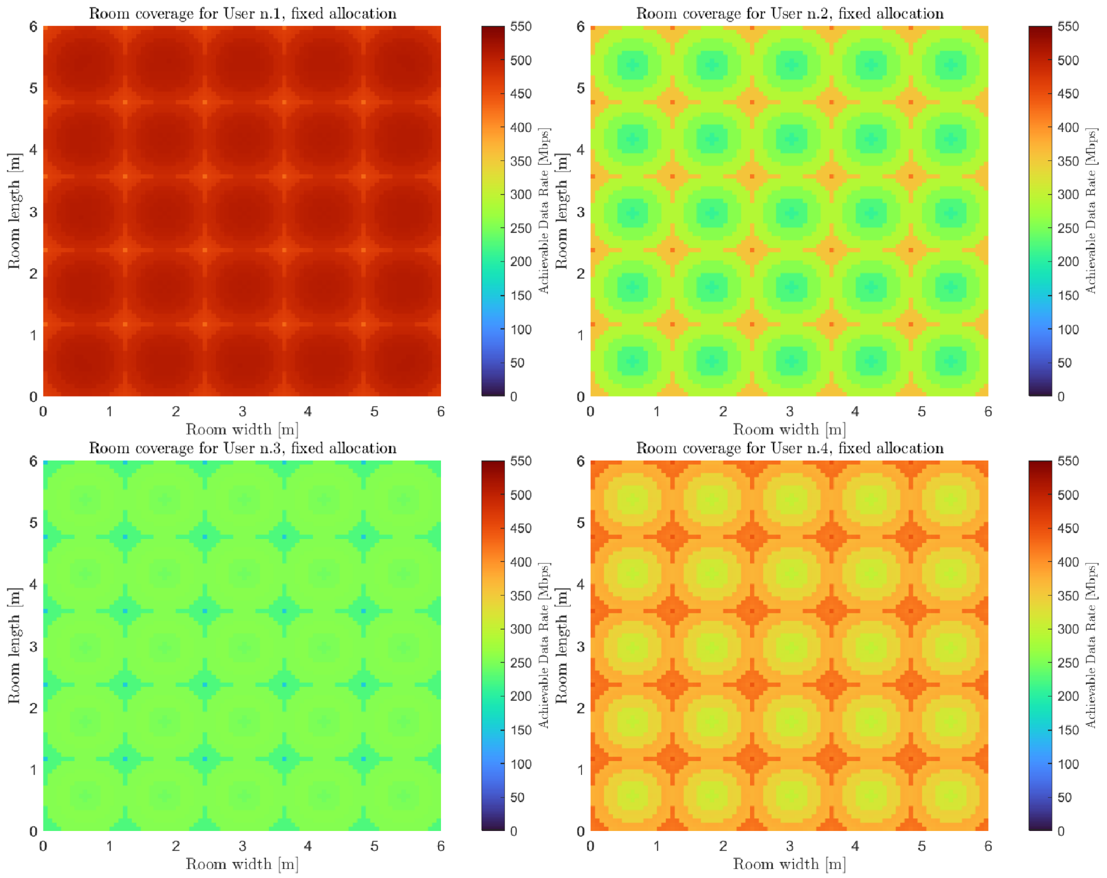

Figure 4.10: Room coverage for all four colours using the fixed allocation algorithm. The features of individual LED emissivity and optical filter transmissivity are clearly distinguishable.

According to the fixed allocation, user n. 2 is always assigned the Green channel, whose SO present some issues with respect to the Blue channel: the green LED emissivity is wider, but since the FWHM of the green optical filter is the same as the blue optical filter (40 nm), not as much green light has a chance to hit the green sub-receiver compared with the Blue channel case. Moreover, given the placement of the green optical filter transmissivity with respect to neighbouring LED emissivity spectra, it can be seen how the amount of interference could potentially be higher on average (especially because of the amber LED emissivity). This explains why Figure 4.10 shows higher achievable data rate when user n. 2 is on the edges of the coverage area of the AP: it is because of better SO, and lower interference.

According to the fixed allocation, user n. 3 is always assigned the Amber channel;

the most visible detail is that the FWHM of the amber optical filter is only 10 nm, and both emissivity and transmissivity spectra overlap very well when the AoI is 0°. This gives the Amber channel significant robustness to interference but also limits its adaptability to the PS effect. In fact, when the optical filter transmissivity starts to shift towards shorter wavelengths, its sharpness makes it difficult to capture an appreciable amount of amber light, whereas a wider spectrum would have made this a lot easier.

According to the fixed allocation, user n. 4 is always assigned the Red channel, whose SO conditions are comparable but slightly worse than those of the Blue channel: the central wavelength of the optical filter is higher than the central wavelength of the LED, and as a result, the link has a better SO at AoIs higher than 0°. This is also the reason why the coverage figure shows a higher achievable data rate near the edges of the area covered by the APs and lower in the centre.

Table 4.3: Per-user coverage performance employing the fixed allocation scheme and datasheet optical filter transmissivities.

Coverage performances, fixed, datasheet				
	User 1	**User 2**	**User 3**	**User 4**
Average Data Rate	492.95 Mbps	282.19 Mbps	249.08 Mbps	364.20 Mbps
Connection Loss	0.00 %	0.00 %	0.00 %	0.00 %
Network Data Rate	1.39 Gbps			

The performance spread of the users is also clearly visible by looking at the performance metrics calculated and reported in Table 4.3. It has to be noted that as mentioned in section 4.2.3, the average data rate is a theoretical upper bound of information that can be transmitted error-free, given by the Shannon-Hartley theorem, and based on a specified bandwidth (B_{mod} = 30 MHz in this case).

The differences between users have all been explained above while highlighting the overlaps in the emission and transmission spectra of each coupled LED and optical filter. Moreover, they relate to this particular aspect in the design of the OFE. In these conditions, the users experience no Connection Loss (CL), as the receivers are pointing directly upwards, and sufficient channel separation is easily ensured even if they are all under the same AP. These are particularly favourable yet very specific

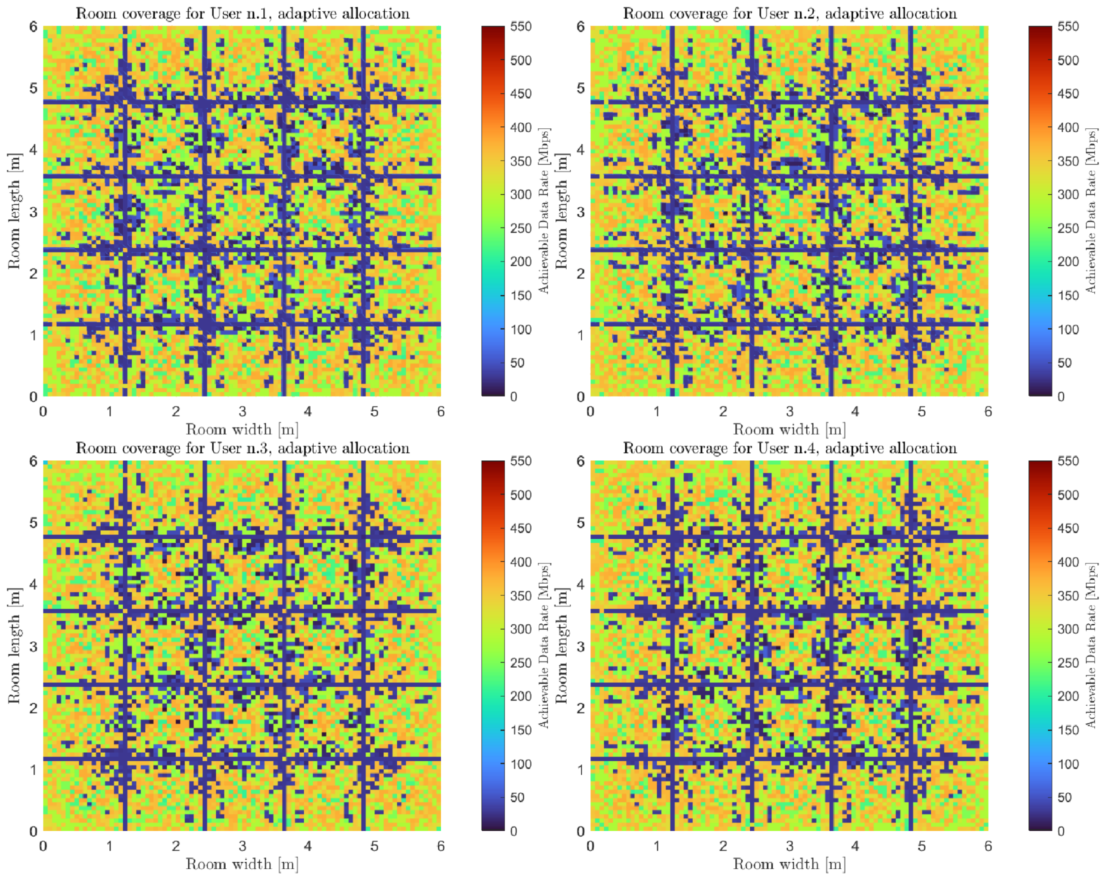

Figure 4.11: Room coverage for all four colours using the adaptive WDMA allocation algorithm. The reduced spatial separation between users does not make the adaptive WDMA algorithm perform as well as the fixed one in these conditions. Nonetheless, better fairness can be appreciated in the figure.

conditions (also with respect to the number of users) for a fixed allocation.

The results of the coverage simulation for the adaptive WDMA algorithm are shown in Figure 4.11. There are no noticeable differences between each user as opposed to when the fixed scheme was used, because the network adaptively allocates the most appropriate colour based not only on the user's conditions, but also on potential interference coming from other channels or APs.

Another spatial feature that is common among all users in the coverage analysis is a drop in the achievable data rate while near the edges of the coverage of any AP, except the in ones close to the room walls. This is explained by the interference coming from neighbouring APs (because the walls do not generate interference), coupled with the individual SO differences between channels, as discussed earlier in this section and more in detail in the previous chapter, Section 3.3.3. Neighbouring APs are not in use while using the fixed allocation, as every user is always allocated to the closest AP, and this is another advantage when $N_{\mathrm{us}} \leq 4$ because the 4 channels that are available per AP are sufficient to serve every user. In fact, in the case that $N_{\mathrm{us}} > 4$, from the 5-th user forward, the allocation would need to use neighbouring APs, which would cause a drop both in achievable data rate and total network data rate and an increase in CL. The investigation of a context in which the network is fully populated is left to the next chapter.

Table 4.4 sums up the results for the coverage analysis with the network using the adaptive allocation algorithm. Users can benefit from much higher fairness, as their achievable data rates are highly comparable, albeit at the expense of a lower network data rate. Moreover, they experience a slightly higher probability of losing the connection (as defined, CL) compared to the prior case. But rather than a real lack of network resources, this stems from an allocation error introduced by the fact that SINR values used for the maximisation cannot represent well the final AP activation, especially for a low number of users who tend to occupy the network to a lesser extent. As a result, the interference considered in the SINR calculation is at its achievable maximum. When this happens, and in certain users' spatial distribution conditions, it becomes challenging for the system to find a channel that yields a SINR lower than the set threshold, $\gamma_{\mathrm{th}}^{\mathrm{SINR}}$, and the allocation would fail. This also has an effect on the achieved SINR of the users, which is lower on average, and reflects on a lower achievable data rate as well. To summarise, for a low number of users (N_{us} ¡ N_{LED}) with low spatial separation, the proposed adaptive scheme promotes a better fairness between users but the fixed scheme offers slightly lower CL and higher achievable data rate.

This problem could be circumvented by implementing an algorithm that considers all allocation combinations and chooses the one with the highest network aggregate SINR, rather than considering one user's SINR at a time. However, the complexity of this approach scales with the number of users in the network; the required calculations could be feasible in an adequate amount of time when N_{us} is sufficiently low, but this case is not general in typical indoor environments. Furthermore, as highlighted in Chapter 2, the current trend is that of increasing the number of devices that each person uses, further increasing the necessity of accounting for a high number of users.

Table 4.4: Per-user coverage performance employing the adaptive allocation scheme and datasheet optical filter transmissivities.

Coverage performances, adaptive, datasheet				
	User 1	**User 2**	**User 3**	**User 4**
Average Data Rate	245.95 Mbps	245.10 Mbps	245.34 Mbps	244.34 Mbps
Connection Loss	0.08 %	0.08 %	1.80 %	0.07 %
Network Data Rate	0.98 Gbps			

Table 4.5: Per-user coverage performance employing the fixed allocation scheme and measured optical filter transmissivities.

Coverage performances, fixed, measured				
	User 1	**User 2**	**User 3**	**User 4**
Average Data Rate	456.10 Mbps	295.23 Mbps	243.34 Mbps	419.89 Mbps
Connection Loss	0.00 %	0.00 %	0.00 %	0.00 %
Network Data Rate	1.41 Gbps			

When using the results presented in Appendix B for measured optical filter transmissivity, however, the spectral degradation occurring at AoIs $> 0°$ introduces a fundamental difference. The deteriorating shape of the optical filter spectra can lower the received optical power dramatically, and this constitutes a penalty for the fixed allocation which lacks the required flexibility to tackle this circumstance. Figure 4.12 shows the coverage results for the fixed allocation scheme. It can be noted that performances can quickly degrade depending on AoIs and OFE system design. In general, if the LED and optical filter spectra of one colour are well overlapped when the AoI is $0°$ (such as in the case of the Amber colour), performances will be good at the centre of the cell and will degrade as the user moves towards the edge. Conversely, if the optical filter spectrum has a higher central wavelength than the spectrum of the corresponding

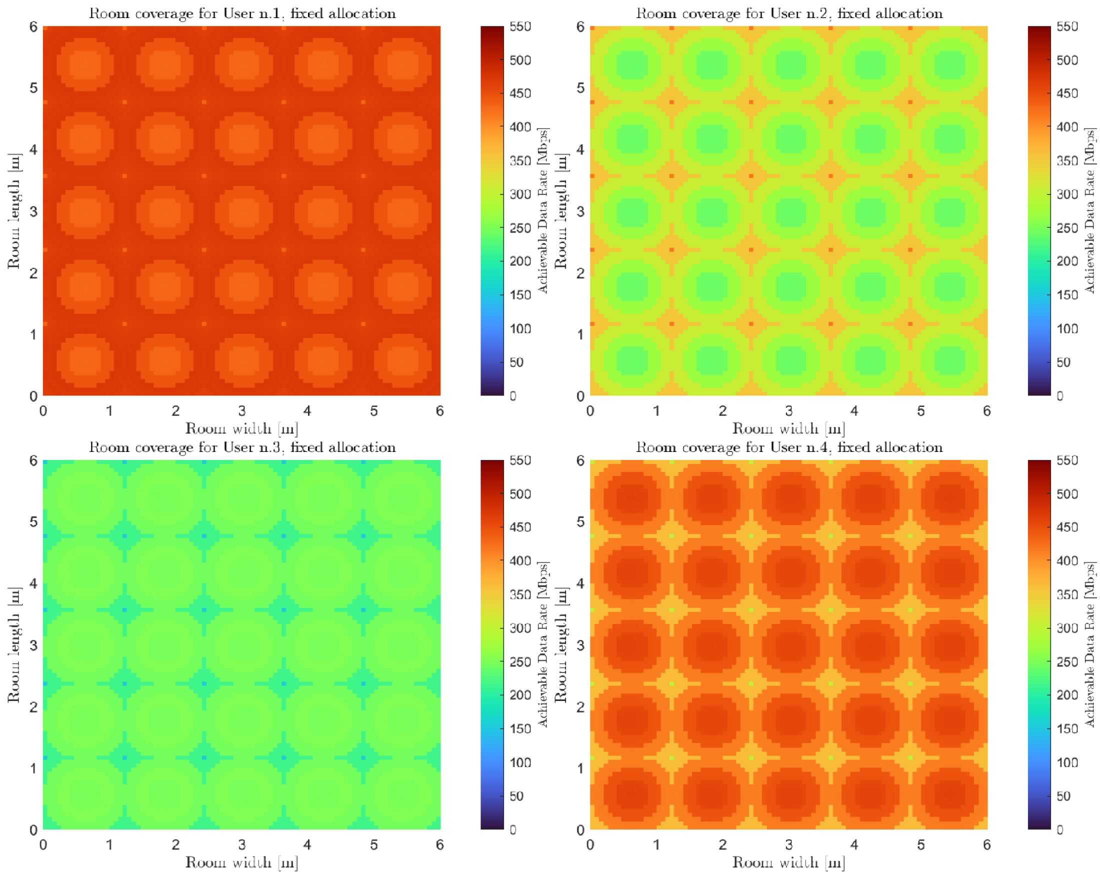

Figure 4.12: Room coverage for all four colours using the fixed allocation algorithm and measured optical filter transmissivities. The features of individual LED emissivity and optical filter transmissivity are clearly distinguishable.

LED (such as in the case of the Red colour), the user's performances will be better at the edges because the AoI shifts the spectrum of the optical filter thus improving the spectral overlap.

However, using the case of User n. 2 (Green colour) as an example, improved performances are not only seen because of the relationship between the transmissivity spectrum of the green optical filter and the emissivity of the corresponding green LED that has been discussed earlier. The shift of the spectrum towards shorter wavelengths also decreases the interference coming from the Amber channel, and is countered by the central wavelength of the optical filter being higher than that of the corresponding LED. The spectral degradation instead, is countered by the fact that at those AoIs the optical filter transmissivity has a better overlap with the peak of the LED emissivity.

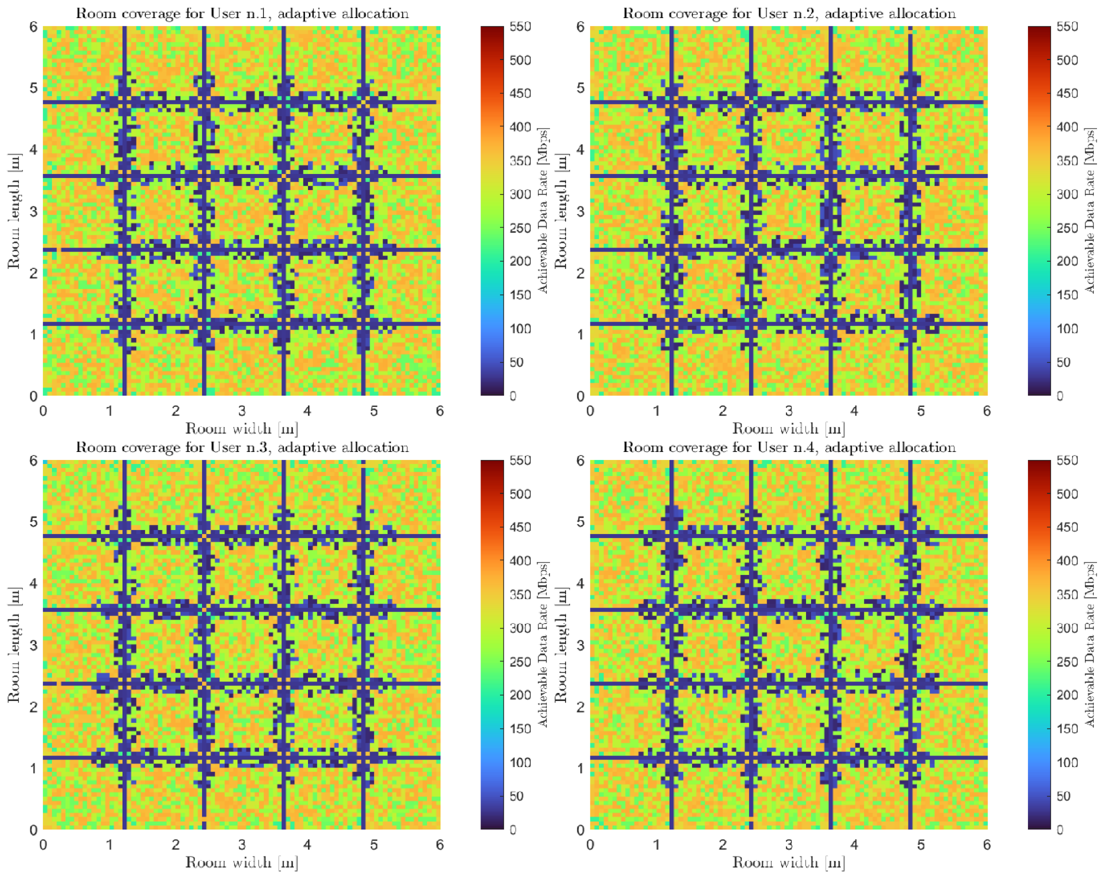

Figure 4.13: Room coverage for all four colours using the adaptive WDMA allocation algorithm and measured optical filter transmissivities. The spectral degradation at higher AoIs reduces interference overestimation in the allocation phase. Nonetheless, better fairness is still visible.

All this results in better achievable data rate in the edges of the AP coverage area. In terms of the other performance metrics, Table 4.5 reflects the differences between the datasheet and measured transmissivities when compared with earlier results in Table 4.3: average data rate and network data rate are slightly higher, while the CL is the same. However, there are still significant differences between the performances of the users, which strongly depend on the specific channel that is allocated to them.

On the other hand, by looking at Figure 4.13, it can be seen that using measured optical filter transmissivities rather than simply applying the PS formula in 2.1 to the transmissivity reported in the datasheet, changes the results. More specifically, use of the measured curves yields overall better performances than using curves from datasheets when the adaptive allocation scheme is employed. This is expected, as the overall effect of the addition of the spectral degradation is to reduce interference coming from neighbouring APs, especially those for which the link between the source LED and the user is impaired by a high AoI. In this way, a significant part of the interference contribution is levelled down, and the per-user SINR maximisation approach is more effective. As a result, Table 4.6 shows that not only users have a higher average data rate and network data rate is higher, but also the CL is lowered to 0.00%.

Table 4.6: Per-user coverage performance employing the adaptive allocation scheme and measured optical filter transmissivities.

Coverage performances, adaptive, measured				
	User 1	**User 2**	**User 3**	**User 4**
Average Data Rate	261.77 Mbps	261.68 Mbps	260.06 Mbps	259.51 Mbps
Connection Loss	0.00 %	0.00 %	0.00 %	0.00 %
Network Data Rate	1.04 Gbps			

This is an important result, as it highlights that adapting to the users' behaviour is very important in mobile multi-user networks, even when their receivers are pointing in an ideal direction, such as towards the ceiling where the APs are. Putting all the users in the same location is important in this analysis in removing the contribution of the spatial domain to the allocation's effectiveness while only concentrating on what happens in the wavelength domain.

4.3.2 Network

As previously discussed, in this section, the four users are modelled to follow the statistical behaviour in terms of location, orientation, and device inclination. As such, both the spatial and wavelength domains are included in this analysis because (due to their mobility) it is unlikely that users will all in the same location at the same time, and this analysis can thus be considered closer to what would happen in a real scenario.

Figure 4.14 reports the CDFs of the achievable datarates, comparing the fixed and the adaptive WDMA allocation schemes, on a per-user basis. Here, dotted lines show the results for the fixed allocation, while continuous lines show the results for the

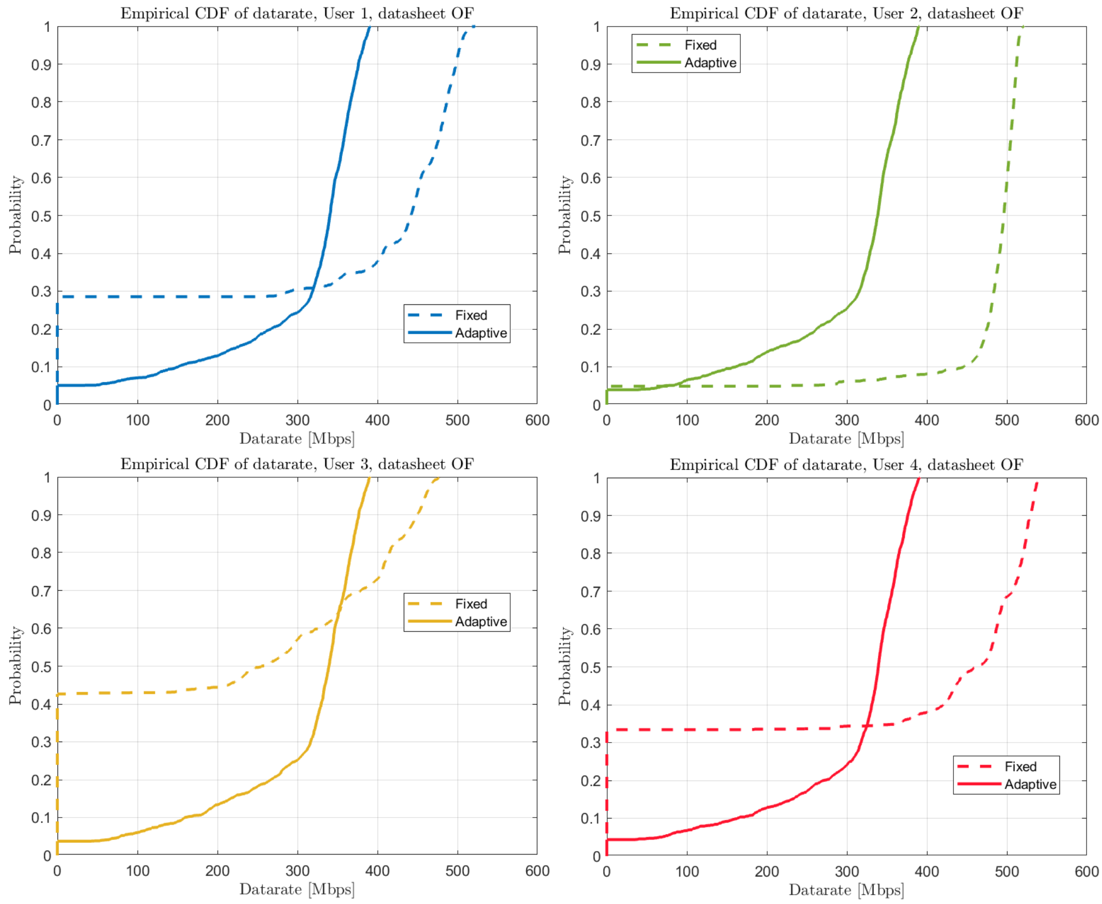

Figure 4.14: Network performances for users 1–4: comparison between the fixed and the adaptive allocation using datasheet optical filter transmissivities. Being CDFs, the X axis is the achieved data rate, while the Y axis represents the probability of achieving a data rate lower than X. The users show varying performances based on the specific allocated channel when using the fixed allocation. With adaptive allocation, these differences even out, resulting in higher fairness.

adaptive allocation. It should be noted that in the graphs, the line colours identify the colour of the channel assigned to the user only for the fixed allocation; in the case of adaptive allocation, for instance, user 1 could be allocated the green, amber, or red channels rather than blue if its position and orientation render it necessary or more fruitful (i.e., its SINR is maximised for another colour).

By looking at the figure, it is evident, and considerations made in the earlier section still hold true in this regard, that the fixed allocation consistently outperforms the adaptive one only for user 2. This is true for both the average achievable data rate and CL, and it is due to the green channel being the most robust because of the positioning of the emissivity and transmissivity spectra. In every other case, with the fixed allocation, users experience significantly higher average CL values, a higher maximum achievable data rate (depending on particularly favourable random positioning in some iterations), but considerably worse fairness. On the other hand, by visually comparing the continuous lines, their homogeneous shape suggests a much more desirable consistency of achieved performances across all users while using the adaptive WDMA allocation algorithm.

Table 4.7: Per-user mobility performances employing the fixed allocation scheme and datasheet optical filter transmissivities.

Network performances, fixed, datasheet				
	User 1	**User 2**	**User 3**	**User 4**
Average Data Rate	323.20 Mbps	464.31 Mbps	209.46 Mbps	322.84 Mbps
Connection Loss	28.55 %	04.90 %	42.65 %	33.40 %
Network Data Rate	1.32 Gbps			

Table 4.8: Per-user mobility performances employing the adaptive allocation scheme and datasheet optical filter transmissivities.

Network performances, adaptive, datasheet				
	User 1	**User 2**	**User 3**	**User 4**
Average Data Rate	304.51 Mbps	303.76 Mbps	305.56 Mbps	305.65 Mbps
Connection Loss	05.10 %	03.95 %	03.75 %	04.35 %
Network Data Rate	1.22 Gbps			

Tables 4.7 and 4.8 hold the numerical results calculated using the datasets generated with the methodology described earlier. The average data rates, calculated for each user individually as in 4.25, range between 209.46 Mbps and 464.31 Mbps in the case of the fixed allocation (with an overall mean of 329.95 Mbps across all users). When using adaptive WDMA, there are significantly less differences in the mean data rates of users, as these range between 304.51 Mbps and 305.65 Mbps and centered around an overall mean of 304.87 Mbps. This is lower than the overall mean in the fixed case,

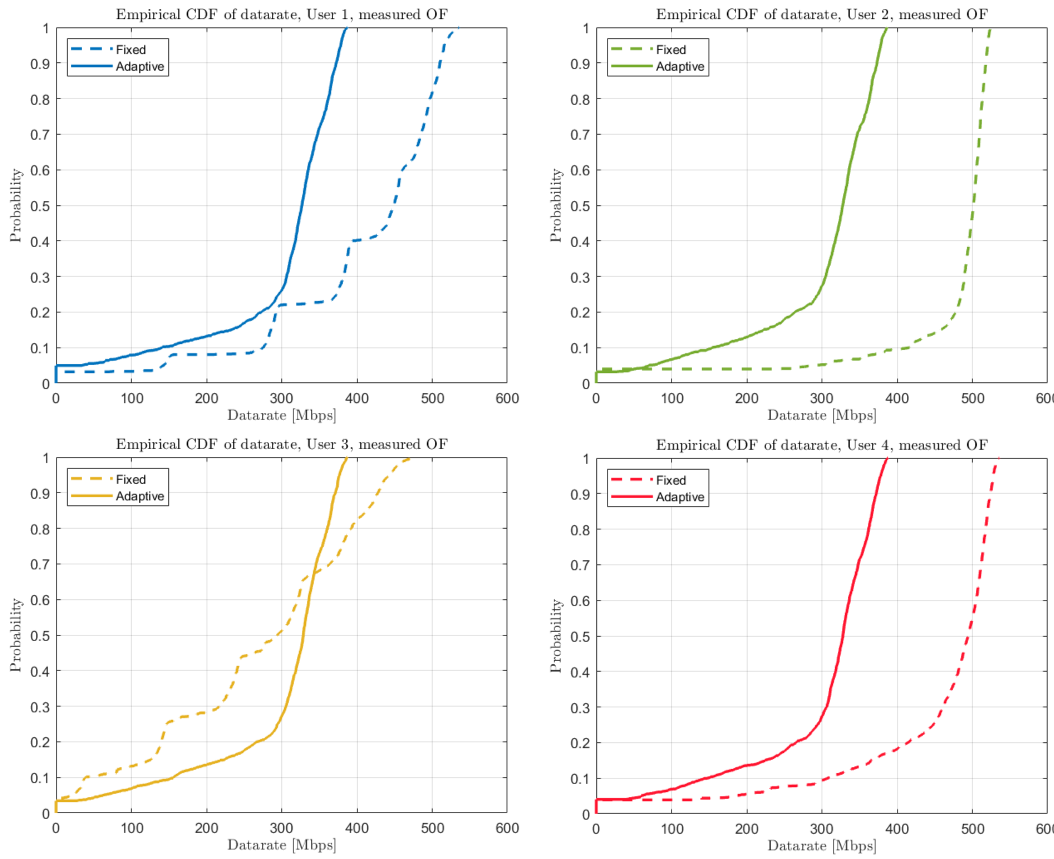

Figure 4.15: Network performances for users 1–4: comparison between the fixed and the adaptive allocation using measured optical filter transmissivities. Being CDFs, the X axis is the achieved data rate, while the Y axis represents the probability of achieving a data rate lower than X. Even though the overall performances are significantly lowered, the differences between fixed and adaptive allocations remain. In fact, with adaptive allocation, higher fairness can be obtained.

as it is the average network data rate: 1.32 Gbps against 1.22 Gbps. The reason for these differences is the problem outlined in Section 4.3.1: calculating the SINR before the allocation has taken place induces allocation errors as it is challenging to estimate the real interference before knowing which transmitters are active. This particular knowledge is difficult to acquire a priori because it depends not only on the actual number of users populating the network but also on the statistically identifiable, but ultimately unpredictable behaviour of each of these users. In other words, the adaptive WDMA cannot reliably estimate the interference that each user will incur after a certain allocation, which results in a sub-optimal allocation.

Other than much better fairness (at the expense of a slightly lower average data rate), the adaptive WDMA allocation scheme is also demonstrated to improve the reliability of the connection. This is apparent when analysing the CL results. These range between 04.90% and 42.65% with a mean of 25.87% when using a fixed allocation, while in the case of adaptive allocation, both their range and average are considerably lower at 03.75%, 05.10%, and 04.29%, respectively.

As a next step, and similarly to the coverage examination, the same analysis is then conducted by exploiting *measured* (and not datasheet-provided) AoI-dependent optical filter transmissivity spectra for all receivers. Figure 4.15 shows the results of this, and the visual inspection of the CDFs highlights a clear and significant improvement for the fixed scheme. As the main difference with the past analysis is the addition of the spectral degradation of the filters, it can be deduced that it is responsible for this improvement. More specifically, this is due to the fact that the spectral degradation renders the interference coming from neighbouring APs almost negligible, thinning out the differences between the adaptive and the fixed allocation schemes.

Table 4.9: Per-user mobility performances employing the fixed allocation scheme and measured optical filter transmissivities.

Network performances, fixed, measured				
	User 1	**User 2**	**User 3**	**User 4**
Average Data Rate	402.90 Mbps	469.07 Mbps	266.70 Mbps	448.44 Mbps
Connection Loss	03.20 %	04.00 %	04.20 %	03.90 %
Network Data Rate	1.59 Gbps			

Table 4.10: Per-user mobility performances employing the adaptive allocation scheme and measured optical filter transmissivities.

Network performances, adaptive, measured				
	User 1	**User 2**	**User 3**	**User 4**
Average Data Rate	296.86 Mbps	298.78 Mbps	297.84 Mbps	297.62 Mbps
Connection Loss	04.97 %	03.20 %	03.43 %	04.06 %
Network Data Rate	1.19 Gbps			

In fact, such differences only remain with respect to the higher fairness that can be achieved with the adaptive scheme, a consideration that still holds true. By comparing tables 4.9 and 4.10, which hold the numerical results for this analysis, this can be confirmed.

As highlighted, the adaptive WDMA scheme would excel at minimising interference in highly crowded network conditions. In order to verify this, it is possible to consider earlier network results, but under the assumption that all transmitters are occupied and thus contributing to interference. This mimics a situation in which many users are populating the network at once and will only be done for the case of measured optical filter transmissivity spectra because of the higher relevance with respect to a real scenario.

Table 4.11: Per-user mobility performances employing the fixed allocation scheme and measured optical filter transmissivities, with maximum interference.

Network performances, fixed, measured, max. interference				
	User 1	**User 2**	**User 3**	**User 4**
Average Data Rate	64.19 Mbps	56.73 Mbps	45.08 Mbps	45.53 Mbps
Connection Loss	03.20 %	04.00 %	03.35 %	03.90 %
Network Data Rate	0.21 Gbps			

Table 4.12: Per-user mobility performances employing the adaptive allocation scheme and measured optical filter transmissivities, with maximum interference.

Network performances, adaptive, measured, max. interference				
	User 1	**User 2**	**User 3**	**User 4**
Average Data Rate	102.35 Mbps	107.07 Mbps	106.35 Mbps	103.67 Mbps
Connection Loss	04.97 %	03.20 %	03.43 %	04.06 %
Network Data Rate	0.42 Gbps			

Figure 4.16 shows considerably lower network performances due to the added interference. However, this only affects the average per-user and network data rates, as can be seen from Tables 4.11 and 4.12. As it can be expected, a significantly higher amount of interference in the network lowers the average SINR that the users are able

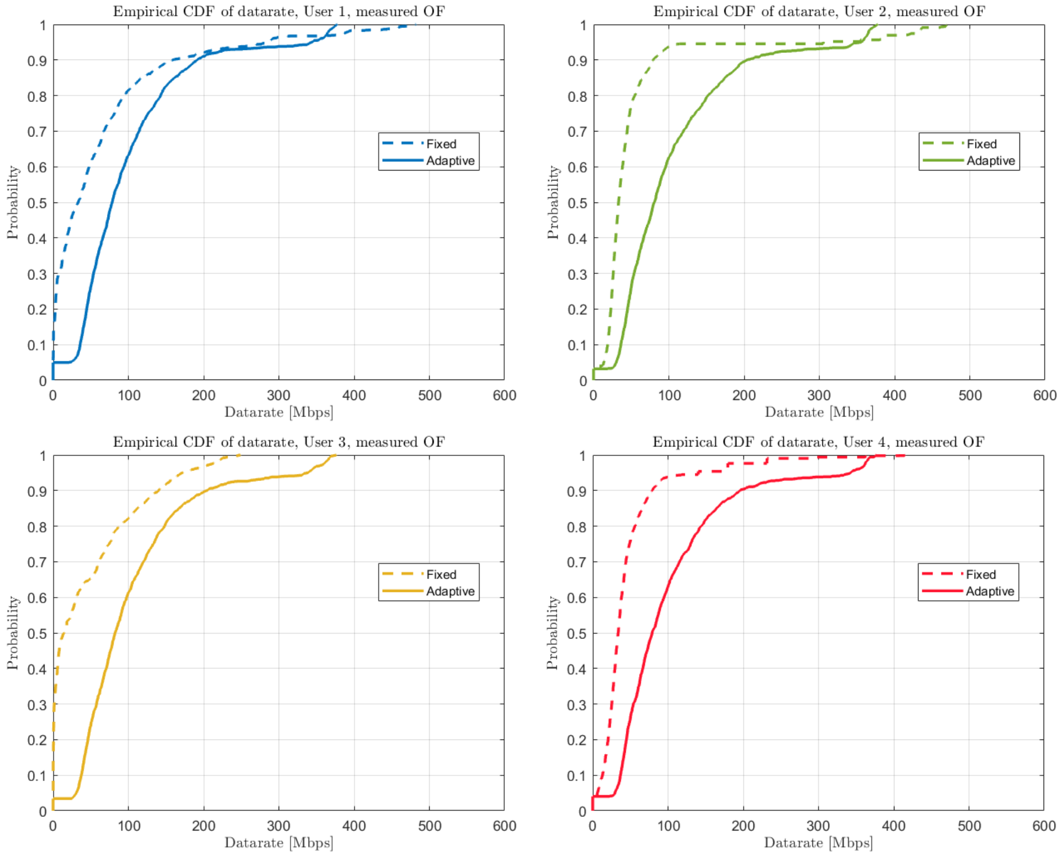

Figure 4.16: Network performances for users 1–4: comparison between the fixed and the adaptive allocation using measured optical filter transmissivities with maximum interference. Being CDFs, the X axis is the achieved data rate, while the Y axis represents the probability of achieving a data rate lower than X. The overall network performance is significantly lower because of considerable amounts of added interference. In this instance, the adaptive WDMA allocation scheme outperforms the fixed one.

to achieve, and a scheme that is based on SINR maximisation has the upper hand in these conditions. This is demonstrated by the aforementioned data rates, which, when compared, show the adaptive WDMA outperforming the fixed allocation in every regard other than the CL (which remains comparable). Most notably, the average network data rate is double when using the adaptive scheme with respect to the fixed one.

Those results confirm that the adaptive WDMA resource allocation scheme is more suitable to this scenario even with an overall low number of users populating the network, as its scheduling method allows all of them to be served fairly. Moreover, its increased flexibility in accommodating higher numbers of users could allow to optimise available resources and lower the average CL across all users.

4.4 Chapter Summary

In this chapter, a novel resource allocation scheme for wavelength division-based multiuser LiFi systems with densely deployed APs has been proposed and evaluated with respect to a fixed scheme based on a round-robin, first-come, first-served allocation. Both schemes are seen in light of the principles of wavelength and spatial separation of users, and their effectiveness is investigated in terms of coverage and indoor everyday use.

Firstly, a comprehensive system model has been presented. This includes the whole path that the signal follows, from its availability at the network level, where it needs to be properly routed, up to when it is received by the user in the optical domain and converted back into a current first, and then a voltage, ready for an additional conversion in the digital realm and further required manipulation. The indoor environment has been defined in terms of room dimensions, rotation geometry, user behaviour, and all equations governing the system. Then, the hardware of the network has been thoroughly discussed, both on the receiver and transmitter sides. This has led to precise design choices, subject to illumination requirements, performance constraints, and maximum user device dimensions. Furthermore, all components have been simulated based on real off-the-shelf ones that, at the time of writing, are available for purchase.

Secondly, the adaptive WDMA algorithm has been made explicit in pseudocode. It is based on allocating to each user the channel that provides the highest SINR, then removing that user from an assignation list, up to when this latter has been made empty. SINR maximisation is a method that inherently tends to minimise the interference and, for this reason, is anticipated to work well in situations where the network is particularly crowded.

In order to test all assumptions, a custom MATLAB simulation framework capable of implementing all hardware and software required (for both adaptive and fixed schemes) has then been built. By simulating a scenario in which the users sweep the room at the same time with the receivers pointing upwards, a coverage analysis of the room has been carried out. This has been done both for the fixed and adaptive schemes and repeated both when employing datasheets and measured optical filter transmissivity curves for all user receivers.

Lastly, by employing experimental user behaviour statistics available from prior literature, similar simulations have been conducted in an everyday use-case scenario. Here, users are free to move in the room and assume random orientations and inclinations with their devices. The Monte Carlo method is employed in this kind of simulation, which has been repeated in a similar fashion to the coverage ones for both schemes while employing both datasheets and measured optical filter transmissivity curves. In addition, they have also been repeated with measured optical filter curves for both schemes under the assumption that all transmitters in the network are active at the same time, providing the maximum amount of interference. This situation is closer to a scenario in which the network is particularly crowded.

In conclusion, and based on the results of the various analyses conducted, the adaptive WDMA allocation scheme seems more suitable for a densely deployed LiFi network employing wavelength division. This is because of the higher achievable fairness, an aspect that stays consistent throughout all the simulation-based tests and allows to even out the differences coming from the particular OFE design (especially in terms of central wavelength and Half Width at Half Maximum (HWHM) of optical filter and LED spectra). The cost is a slightly lower average per-user and network data rates achievable with the adaptive scheme with respect to the fixed scheme. There are two main reasons for this. Firstly, as the exact SINRs cannot be computed accurately before the allocation has taken place, allocation errors can occur. This is much more evident when the network is less crowded (which is the case in these simulations), as the real interference after the allocation is complete will be much lower and more variable. Secondly, there is an inherent difference between the two schemes: while in the fixed case each user is always assigned the same colour, in the adaptive scheme this is switched as needed based on users' locations, orientations, and device inclinations. As a result, and since only 4 concurrent users are being considered in this chapter, all 4 colours will be used at all times in the fixed scheme. The consequence is that in this case, there will be negligible cross-talk between users due to a very good colour separation. This is not the case for the adaptive scheme, for which allocating one colour or another is only related to the SINR achieved. Users can, in this way, ever so slightly interfere with each other due to selecting the same (or neighbouring) colours while not being sufficiently separated in space.

Additionally, it should be noted that higher maximum achievable data rates are not desirable in general, especially since these simulations are thought to span a long time and the maximum achievable data rate will only be achieved occasionally.

Finally, it is also worth noting that these results have been obtained while only considering 4 concurrent users, and more investigation is needed to understand the implications of using these schemes in a wider and more crowded network environment.

Chapter 5

Adaptive WDMA-MIMO

5.1 Introduction

After exploring a novel approach in the domain of dynamic resource allocation concerning a densely deployed Light Fidelity (LiFi) network using Wavelength Division Multiple Access (WDMA), this chapter is devoted to investigating and developing it even further. Section 4.2.2 has discussed the detailed architecture of every user's receiver. One of the underlying characteristics of such architecture is that it is formed of four identical Avalanche Photodiode (APD) arrays (or sub-receivers), each of them made by 4 elements and topped with an optical filter of a different colour. This allows every user to be equipped to receive a signal in any of the 4 wavelenghts employed by a transmitter, ensuring the required flexibility in terms of resource allocation: based on network conditions, and users' positions and orientations, they can be allocated any colour that yields a good Signal-to-Interference-plus-Noise Ratio (SINR). In terms of user capabilities, however, receiving a signal only on one wavelength at a time leads to a severe underutilisation of the available resources. As it is intuitive in fact, receiving up to 4 wavelengths at the same time (one for each sub-receiver) as parallel channel could lead to a substantial increase in performances with respect to the results presented in the earlier chapter. This is even more evident when also considering the presented transmitter architecture in Section 4.2.2: each Access Point (AP) is capable of transmitting four signal streams in parallel, which are well separated in the

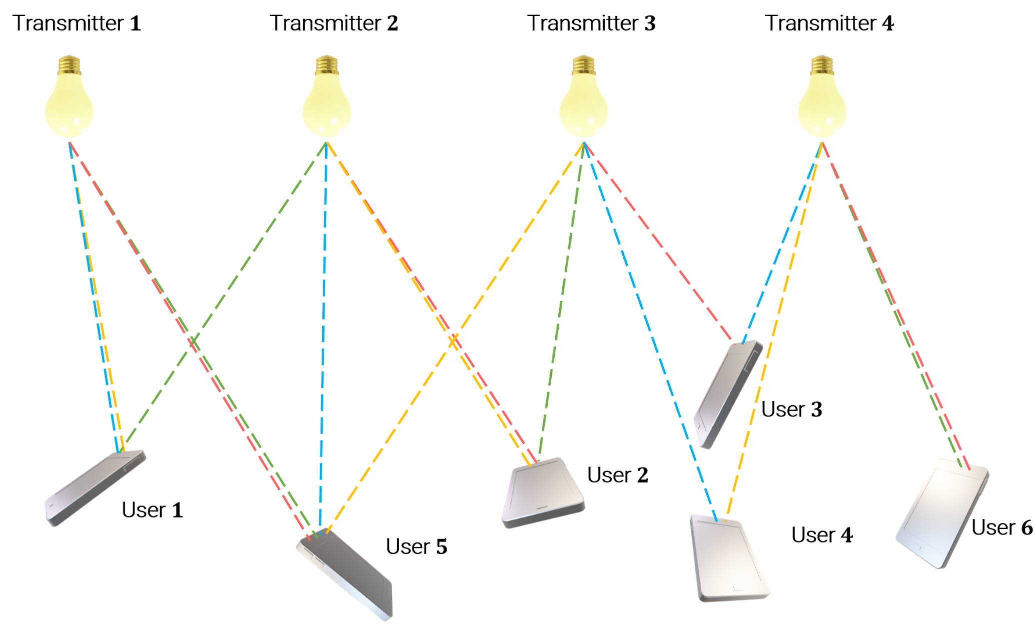

Figure 5.1: Diagram of Wavelength Division Multiple Access-Multiple Input Multiple Output (WDMA-MIMO). Multiple wavelengths can be allocated to each user, up to 4, and each transmitter and sub-receiver pair can compose a Multiple-Input Multiple-Output (MIMO) stream.

wavelength domain. This concept is represented in Figure 5.1.

The first part of this chapter's contribution is to develop the proposed scheme so that the network resources can be utilised in a better way, thus increasing the network's throughput and capacity in terms of served users.

After considering the basic adaptive WDMA scheme and comparing it with a fixed scheme in the previous chapter, the necessity has arisen to evaluate the network performances where more than 4 concurrent users are present in the network. Thus, another contribution of this chapter lies in conducting such an investigation. The developed adaptive WDMA-MIMO scheme will be compared with a fixed benchmark (which is also adjusted to be MIMO compatible to maintain comparison fairness) with an increasing number of concurrent users in the network.

In addition, having such a high number of possible combinations that are well contained in space (and thus subject to user movement) also raises the concern of considering the problem of handover and handover latency. In general terms, a handover occurs whenever the connection between a User Equipment (UE) and an AP becomes so unstable that it is necessary to switch the user to another AP to retain a good quality of service. The time it takes to the network to initiate, decide and execute the handover process (commonly referred to as "handover latency") may impact negatively the network performances, especially when a high number of users compete for the same resources.

Handover could be influenced not only by user movement (as it is intuitive and well investigated in literature [20, 52, 213]), but also by the Passband Shift (PS) effect as the users change their device's inclination even if their location does not change. In the second part of this chapter, handover rate is considered as a new metric while introducing a time dependency in the developed simulation framework, so that all the aforementioned aspects can be related to the PS effect.

With this in mind, the contributions of this chapter can be summarised as follows:

- After describing the approach and the differences with adaptive WDMA presented in the earlier chapter, an algorithm for the adaptive WDMA-MIMO dynamic allocation method is provided.
- A study based on custom-code simulations is conducted to investigate network performances in a densely deployed LiFi network with an increasing number of users. These simulations include parameters from datasheets of real off-the-shelf components. These performances are also compared with a fixed allocation scheme benchmark that is based on a simple round-robin, first-come, first-served assignation of the available channels with the highest SINR.
- Further simulation work is conducted to explore the downlink capabilities of a typical indoor LiFi network using the adaptive WDMA-MIMO resource allocation scheme with densely deployed APs. In these simulations, time dependency is considered to investigate results pertaining to handover, with users assuming a behaviour typical of various real-life-inspired scenarios in addition to the usual random locations.

The present chapter is based on two papers, which at the time of writing were submitted for publication to the Journal of Optical Communications and Networking ("An Adaptive Allocation Algorithm for Multiple Input Multiple Output Dense LiFi Networks Based on Wavelength Division") and to the Institute of Electrical and Electronics Engineers (IEEE) International Conference of Communications (ICC) 2024 ("Downlink Time-Dependent Performances of a WDMA-MIMO LiFi Network").

5.2 System Model

5.2.1 Algorithm WDMA-MIMO

The pseudo-code of the adaptive WDMA-MIMO algorithm is shown in Algorithm 2, and its functions are discussed in this section. After comparing it with Algorithm 1 contained in Section 4.2.4, it can be noted that its first part (up to line 13 included) is similar to the simpler adaptive WDMA algorithm.

Starting from line 14, the algorithm keeps assigning the $\bar{u}, \bar{a}, \bar{i}$ combinations that are still available in the $\gamma_{u,k,a,i}$ matrix and thus still seeks to maximise the SINR of the network. This outlines a separation in two distinct "phases": during the first, one channel per user is allocated, as in WDMA, while in the second, all remaining available channels are allocated. This approach is needed to overcome a specific limitation. In fact, a simple SINR maximisation approach would readily allocate the maximum number of available channels to users with a more favourable position in the spatial domain (that is, a better combination of location, orientation, and device inclination). As a result, other users with a less favourable position would have even less transmitters to choose from, at the evident expense of fairness. With this approach instead, the algorithm retains all the benefits investigated in Section 4.2.4 while substantially improving resource utilisation, at the cost of a higher complexity because of being split in two phases (which in turn increases the number of operations that have to be carried out). As in Section 4.2.4, Channel State Information (CSI) is assumed to be available at the network level, and uplink communication features are provided by either the LiFi technology on a different wavelength (i.e., in the IR range) or the Radio-Frequency (RF) technology (i.e., via Wireless Fidelity (WiFi)). Lastly, it has to be noted that this

Algorithm 2: Adaptive WDMA-MIMO algorithm.

Data: A $\gamma_{u,k,a,i}$ matrix with SINR values for each $\bar{u}, \bar{k}, \bar{a}, \bar{i}$ combination;
An empty Assignation List, L;
Result: An Allocation List, $A_{u,k,a,i}$

Initialization;
for $u = 1, 2, \ldots$ **do**
  if $\sum_{a=1}^{N_{AP}} H(0)_{\bar{u},a} > 0$ **then**
    Put $\bar{u}$ in L;
  end
end
while L *is not empty* **do**
  Find max in $\gamma_{u,k,a,i}$ and assign the corresponding $\bar{u}, \bar{k}, \bar{a}, \bar{i}$ combination in $A_{u,k,a,i}$;
  Set that $\bar{u}, \bar{k}, \bar{a}, \bar{i}$ combination $= 0$ in $\gamma_{u,k,a,i}$;
  Take $\bar{u}$ out of L;
end
L is now empty;
$A_{u,k,a,i}$ contains one $\bar{k}, \bar{a}, \bar{i}$ combination for every active user u;
for $\bar{u} = 1, 2, \ldots$ **do**
  if *$\bar{u}$ has at least 1 $\bar{u}, \bar{k}, \bar{a}, \bar{i}$ combination in $\gamma_{u,k,a,i}$ that is > 0* **then**
    Put $\bar{u}$ in L;
  end
end
while L *is not empty* **do**
  Find max in $\gamma_{u,k,a,i}$ and assign the corresponding $\bar{u}, \bar{k}, \bar{a}, \bar{i}$ combination in $A_{u,k,a,i}$;
  Set that $\bar{u}, \bar{k}, \bar{a}, \bar{i}$ combination $= 0$ in $\gamma_{u,k,a,i}$;
  if *$\bar{u}$ does not have at least 1 $\bar{u}, \bar{k}, \bar{a}, \bar{i}$ combination in $\gamma_{u,k,a,i}$ that is > 0* **then**
    Take $\bar{u}$ out of L;
  end
end
L is now empty;
$A_{u,k,a,i}$ contains all the $\bar{k}, \bar{a}, \bar{i}$ combinations for every active user u;

algorithm also retains its compatibility with modulation schemes other than the NRZ On-Off Keying (OOK) employed here and with the implementation of smart lighting protocols.

5.2.2 Fixed WDMA-MIMO

The fixed allocation scheme is used in this chapter as a benchmark against the adaptive WDMA-MIMO scheme. As well as this latter, the fixed scheme is an extension of the one presented in the foregoing Chapter 4 and is based on a first-come, first-served round-robin allocation in which each user is immediately allocated a central AP based on the highest SINR. This scheme is designed and adopted in the present chapter as a form of benchmark as, as explained in Chapter 2, the literature is lacking a proper WDMA and WDMA-MIMO allocation solution for LiFi while wavelength division does not have a direct correspondence with RF technology.

In the fixed WDMA-MIMO variant, users are tagged with a numbered label based on their time of arrival in the network, with the lowest value being assigned to the user that comes first and put into the allocation list. When the scheduling takes place, the user with the lowest time-of-arrival tag is picked, and each of its 4 receivers is allocated a transmission stream from the closest AP (if available). This is then repeated for the second user in the allocation list until all users have been served or the remaining users have no available channels that can be allocated to them.

As it is intuitive, in this way, if two users are below the same AP, one of them will potentially not have any available resources. In this regard the approach of dividing the adaptive WDMA-MIMO into two phases, so that every user has at least one channel allocated to them, allows to improve network scalability in more crowded environments.

5.2.3 Indoor Scenario

Room, hardware & users

While the underlying set of equations governing the work presented in this chapter remains similar to that discussed, successfully validated, and used in the earlier part of this dissertation, some differences related to other aspects of the environment have to be noted.

In terms of similarities with respect to the indoor scenario presented in Chapter 4, the room size, the number of APs in the ceiling of such room, and the hardware both at transmitter and receiver side (i.e. number of Light Emitting Diode (LED)s, APDs, optical filters) all remain the same. This means that, in terms of hardware costs, this will also be the same both for the fitting of the room and the per-user cost of the hardware. From the point of view of energy efficiency it should be noted that regardless of using the same hardware, employing a WDMA-MIMO scheme has a higher overall rate of transmitter activation: on average, users will be served with more than one transmitter (thus achieving MIMO communication and improving performances). As a direct consequence, the energy expenditure for running such a network will be higher when compared to employing a simple WDMA scheme. This is a trade off that has to be taken into account when designing a WDMA/WDMA-MIMO system.

In terms of differences, the first part of this chapter deals with the presence of a higher number of users in the network. More specifically, it investigates the network scalability within a very crowded indoor environment (like a conference room or an Internet of Things (IoT)-based domotic system). Such investigation is carried out by starting with the same number of users as in Chapter 4 so that results can also be compared between the WDMA and WDMA-MIMO schemes. Then, the simulation is repeated while constantly increasing the network population by 4 users at a time, until the maximum $N_{\mathrm{us}}^{\mathrm{max}} = 100$. It has to be noted that the choice of increasing network population by 4 users at a time is an arbitrary one and strikes a good balance between granularity in the data and overly extended simulation times.

As said, $N_{\mathrm{us}}^{\mathrm{max}} = 100$ is the chosen maximum network population. In fact, this is the theoretical limit of users that the network can serve at the same time, since $N_{\mathrm{AP}} = 25$ and $N_{\mathrm{i}} = 4$. This specific network, with this number of APs and transmitters, can thus potentially allocate up to $N_{\mathrm{AP}}N_{\mathrm{i}} = 100$ parallel channels. These channels are all separated in either the wavelength domain, spatial domain, or both: every AP has four LEDs that operate at four different wavelengths, and each LED of the same colour in the room, has its own location (since it is part of a different AP). However, it should be noted that the separation between transmitters of the same colour and from neighbouring APs is slim and introduces a substantial amount of interference for both the users allocated to them. This relationship is very difficult to express analytically as it involves considering many variables related to user movement, orientation, and inclination in complex equations, as seen in Chapters 3 and 4. Possible strategies that can be employed to reduce this drawback are joint transmission as presented in [47], where neighbouring transmitters on the same wavelength transmit the same stream so that SINR for a particular user is improved, or adopting a power loading scheme so that neighbouring transmitters on the same wavelength allocated to different users reduce their output power to provide less interference to neighbours (although this would also reduce signal power for their intended user). Nonetheless, these approaches are out of the present scope and would be an interesting direction for future studies that further refine the adaptive WDMA-MIMO scheme. In fact, they do not impair or hinder the successful application of the algorithm here presented.

Another important difference comes while investigating handover in such an environment, because this also introduces the necessity of further considering the time domain. The presented mathematical framework is comprehensive of network performances' evolution in time because SINR and channel capacity are both calculated at a specific time instant, and their averages are already dependent on time. In this regard, important results attained in [158] and further refined in [164] are to be noted with respect to the coherence time of the users' device inclination angle, θ. This is defined to be "in the order of a few hundreds of milliseconds" in these works, and it means that given usual network channel reallocation intervals (which fall in that same range), this θ angle can be treated as a stochastic random process as angle samples have the time to become uncorrelated.

Simulation method

For what is concerned with investigating a fully crowded network, the simulation methodology adopted in this chapter is similar to that described in Section 4.2.3 with regard to describing network simulations. This is true for all aspects and for both fixed and adaptive simulations, except the number of users in the network N_{us}, which, as described, is initially set so that $N_{\mathrm{us}} = 4$. The simulation is then repeated anew by increasing $N_{\mathrm{us}} = 8$, then $N_{\mathrm{us}} = 12$, and so on, until $N_{\mathrm{us}} = 100$. The results of each simulation are then stored and represented in the same figure, so that the evolution of network performances as a function of the number of users in the room can be appreciated.

With respect to the investigation of the handover rate, a slightly different approach is required. While the room geometry, APs, transmitters, and receivers configuration remain largely the same, in this case it is here arbitrarily assumed that the resource allocation is automatically updated by the network every 500 milliseconds. As mentioned in Section 5.2.3, this is a long enough time interval so that consecutive realisations of the stochastic random process θ are uncorrelated. The same time interval is assumed to pass between consecutive iterations, and as a consequence, $N_{\mathrm{iter}} = 1800$ corresponds to a continuous monitoring time of 15 minutes. This is the adopted monitoring duration for all simulation scenarios that will be described further.

Users are assumed to request access to the network in sessions, the duration of which is uniformly distributed between $T^{\mathrm{ses}}_{\mathrm{min}} = 20\mathrm{s}$ and $T^{\mathrm{ses}}_{\mathrm{max}} = 40\mathrm{s}$. A "session" is a variable period of time in which the user is either requesting service or standing by without using the network. The reason for this is to model a common power-saving strategy for IoT devices [59], which consists of intermittently accessing the network rather than being continuously connected. After each session's set time has expired, a user has a 50% chance to change its state from "Connected" to "Not Connected". When this happens, the user stops requesting services and exits the network for a certain amount of time. When the user tries to reconnect at the end of a pause session, it is once again included in the allocation schedule. Notice that there is a non-zero probability that the user's "Connected" time will outlast the duration of a single session; this is the case when, after the session, the state of the user does not change to "Not Connected". In this way, prolonged presence in the network (such as live-streaming of various content) is also adequately represented.

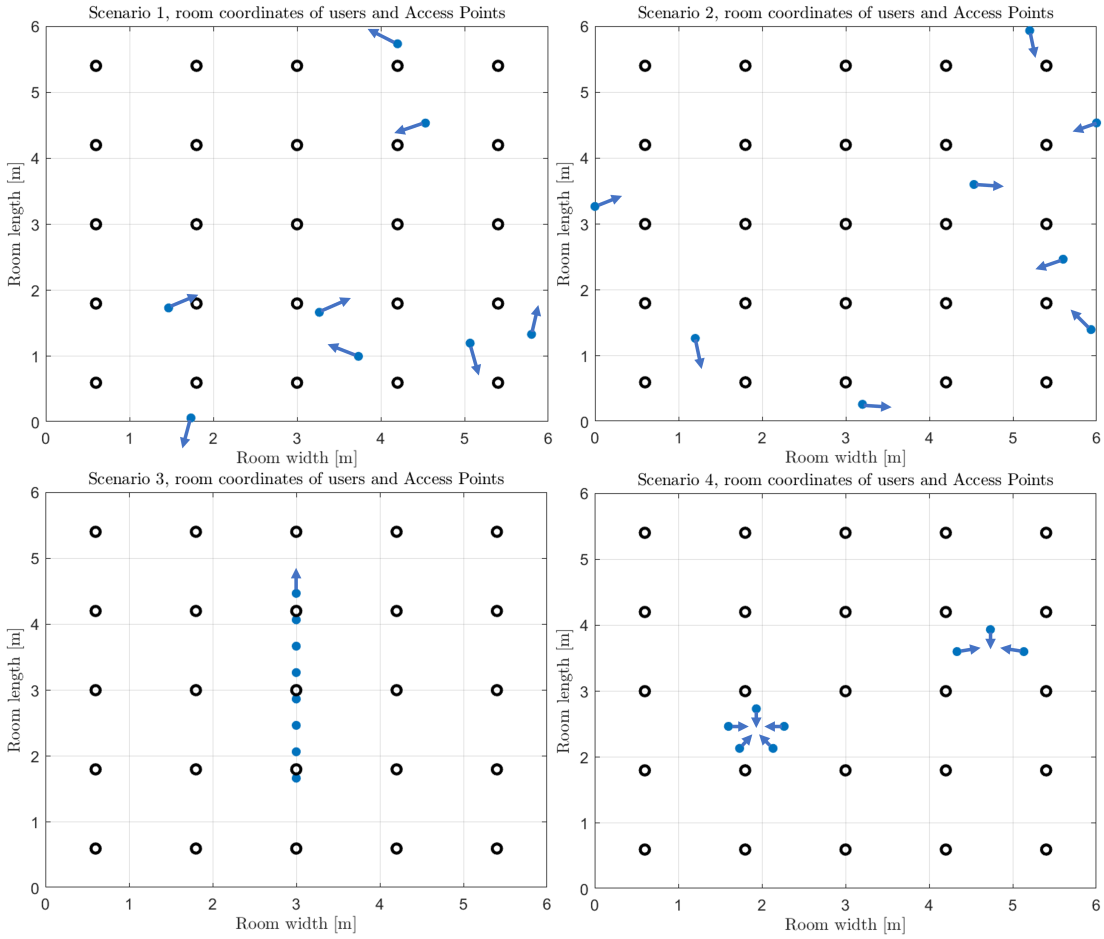

Figure 5.2: Four scenarios with eight users in different positions and orientations. In Scenario 1 and 2, users' positions and orientations have been generated according to a uniform distribution. In Scenario 3, users are placed in a typical queueing situation, as may be the case for a post office or a supermarket; their orientation is the same as they are all facing the destination of their queue. In Scenario 4, users are placed in an indoor home or office environment, gathered in groups, and socialising or discussing.

From the geometric point of view of the users' spatial distribution, four separate scenarios are investigated in this work. Each scenario has the users' locations and orientations fixed throughout the whole simulation, which encompasses a timeframe of 15 minutes. This duration is chosen to strike a balance between the statistical relevance of the data and simulation complexity. These scenarios are depicted in Figure 5.2, represented in the context of the room. The polar angle θ is modelled as a stochastic random process following a Gaussian distribution with a mean of 27.75° and a standard deviation of 7.67°. These parameters are representative of a user that walks while browsing content on a smartphone in portrait mode [158]. As for the users' locations and orientations, in scenarios 1 and 2, they have been generated randomly according to a uniform distribution. Note that their spread is not uniform, though, and this produces interesting results as it highlights once again the importance of spatial separation of users. In scenario 3, they are chosen to represent a queue as they use their devices when they wait in line at a bank or a post office. In scenario 4, a small group situation has been modelled to represent a home or office environment in which people are socialising and/or exchanging information.

5.2.4 Network performance metrics

Recalling all the metrics introduced in Section 4.2.3 and using them as a base to build upon, two more metrics will be discussed and used in this chapter.

As the number of users grows, the first new metric is much needed to gain further insight regarding possible failures of the allocation process for a given user due to an effective lack of resources, as opposed to when the combination of its position and orientation in space makes it impossible to connect regardless of the allocation scheme. In fact, a user may lose connectivity due to his movement behaviour, resulting in not having a single AP in its Field Of View (FOV). This case has to be separated from those in which there simply are not enough resources available to allocate every user to at least one channel, and this can be done with such a metric, termed "Out-of-FOV". It is hereby defined as a percentage of users not having any AP in their FOV throughout the entire simulation. By establishing:

$$N_{\bar{\mathrm{u}}}^{\mathrm{FOV}}(t) = \begin{cases} 1 & \text{if } \bar{\psi}_{\bar{\mathrm{u}},a} > \Psi_{\mathrm{c}} \text{ for every } a \in [1, N_{\mathrm{AP}}] \\ 0 & \text{otherwise} \end{cases} \tag{5.1}$$

it is subsequently possible to define the Out of Field Of View (OFOV) metric as:

$$\Omega_{\bar{\mathrm{u}}}^{\mathrm{FOV}} = \frac{\sum_{t=1}^{N_{\mathrm{iter}}} N_{\bar{\mathrm{u}}}^{\mathrm{FOV}}(t)}{N_{\mathrm{iter}}}. \tag{5.2}$$

However, as in this chapter, the number of users can be extremely high, it is also useful to consider the total average network OFOV, obtainable by averaging across all users in the network:

$$\Omega_{\mathrm{tot}}^{\mathrm{FOV}} = \frac{\sum_{u=1}^{N_{\mathrm{us}}} \Omega_{u}^{\mathrm{FOV}}}{N_{\mathrm{us}}}, \tag{5.3}$$

and the same can be done with the Connection Loss (CL) metric, $\chi_{\mathrm{tot}}^{\mathrm{CL}}$:

$$\chi_{\mathrm{tot}}^{\mathrm{CL}} = \frac{\sum_{u=1}^{N_{\mathrm{us}}} \chi_{u}^{\mathrm{CL}}}{N_{\mathrm{us}}}. \tag{5.4}$$

By considering these two equations and recalling their given definitions, it is intuitive to realise that when the OFOV metric equals the CL metric, $\Omega_{\mathrm{tot}}^{\mathrm{FOV}} = \chi_{\mathrm{tot}}^{\mathrm{CL}}$, it is an indication that every time a user is disconnected, it happens because of its movement behaviour and is not related to the network failing the allocation. Thus, when designing a network, it is desirable that the two metrics be as close as possible. Conversely, when $\Omega_{\mathrm{tot}}^{\mathrm{FOV}} < \chi_{\mathrm{tot}}^{\mathrm{CL}}$, the difference between the two represents a measure of how often a disconnection is due to a lack of resources as opposed to the user's spatial behaviour, and this occurrence would indicate that a network resource allocation scheme does not perform well in the test conditions. Finally, it can be seen that a situation in which $\Omega_{\mathrm{tot}}^{\mathrm{FOV}} > \chi_{\mathrm{tot}}^{\mathrm{CL}}$ is not possible by definition.

The second metric that will be introduced and used in this chapter is the handover rate. It is an important network Quality of Service (QoS)-related metric, which has been defined in the context of LiFi in [213] as follows:

$$\mathcal{H} = \frac{\sum_{i=1}^{N} N_{\mathrm{h},i}}{\sum_{i=1}^{N} T_{\mathrm{e},i}} \tag{5.5}$$

where $N_{\mathrm{h},i}$ is the number of handovers during the i-th elapsed time, $T_{\mathrm{e},i}$. It can be noted that the numerator and denominator are, respectively, the total number of handovers and the overall simulation time. A similar definition will be employed in this chapter, as implemented in the code, by having:

$$N_{\bar{\mathrm{u}}}^{\mathrm{HO}}(t) = \begin{cases} 1 & \text{if } \bar{u} \text{ is active and } A_{\bar{\mathrm{u}},k,a,i}(t) \neq A_{\bar{\mathrm{u}},k,a,i}(t-1) \text{ and } N_{\bar{\mathrm{u}}}^{\mathrm{CL}} \neq 0 \\ 0 & \text{otherwise} \end{cases} . \tag{5.6}$$

At this point, the definition of the handover rate for a user ū, $\mathcal{H}_{\bar{\mathrm{u}}}$, is given by:

$$\mathcal{H}_{\bar{\mathrm{u}}} = \frac{\sum_{t=1}^{N_{\mathrm{iter}}} N_{\bar{\mathrm{u}}}^{\mathrm{HO}}(t)}{N_{\mathrm{iter}}} \tag{5.7}$$

and the average handover rate of the whole network is given as an average across all users:

$$\mathcal{H}_{\mathrm{tot}} = \frac{\sum_{u=1}^{N_{\mathrm{us}}} \mathcal{H}_{\bar{\mathrm{u}}}}{N_{\mathrm{us}}}. \tag{5.8}$$

As it can be seen, this is equivalent to the definition given in the literature [213], which then constitutes a strong basis for the investigation conducted. However, note that based on this definition, each of the 4 employed wavelengths is treated as a single channel, and therefore, users can expect to have a handover rate that is about four times higher than single-channel solutions.

5.3 Analysis

In the coming section, the results of the simulations will be discussed in depth. The analysis will first focus on how network performances scale with the increasing number of users present in the room, and after that, it will shift its attention to considering the handover rate in four different 8-users scenarios with fixed positions and orientations

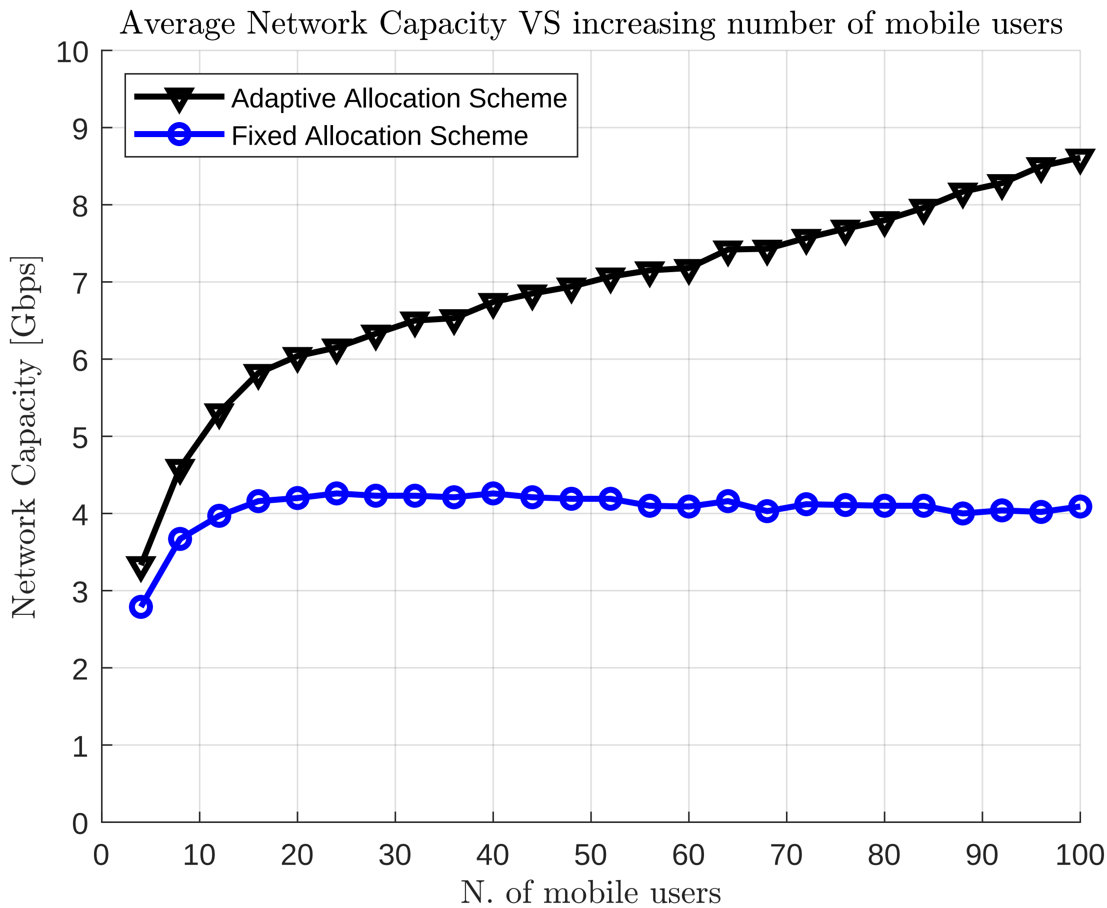

Figure 5.3: Average aggregate network capacity with an increasing number of users in the room. The adaptive WDMA-MIMO allocation scheme outperforms the fixed one consistently.

but varying device inclinations.

5.3.1 Densely populated network

The average aggregate network capacity for both fixed and adaptive WDMA-MIMO, with an increasing number of users, is shown in Figure 5.3. As can be seen by the difference between the two curves, the adaptive WDMA-MIMO scheme provides the network not only with better performances in general, but also a capability of increasing its output based on how many users are concurrently requesting service. Notably, by looking at the specific point $N_{\text{us}} = 4$, a comparison can be made with the network-concerning results presented in the foregoing chapter (Section 4.3.2). It can be seen that with respect to the WDMA case, adaptive WDMA-MIMO is more capable of optimising network performances as its focus on maximising SINR (and thus minimising interference with respect to signal) yields better results as the utilisation of the resources grows. In fact, with only 4 users in a RGBA LiFi network, a WDMA allocation scheme only pairs each user with 1 channel, while a WDMA-MIMO scheme can allocate up to $N_{\mathrm{k}} = 4$, with a tangible increase in interference (and the subsequently emerging need to mitigate it).

As user density grows, this competition for resources grows as well, and as anticipated, the adaptive WDMA-MIMO retains its ability to mitigate the interference generated by the higher transmitter activation (that is, a higher number of transmitters activated), while the fixed WDMA-MIMO caps its average throughput slightly above 4 Gbps with $N_{\mathrm{us}} = 40$ concurrent users present in the network, and after that, it starts dropping ever so slightly. This is precisely an effect of higher interference due to higher transmitter activation, as a consequence of a higher number of users requesting service.

Figure 5.4 reports, for the same amounts of users in the network, the average SINR per user. Despite both fixed and adaptive WDMA-MIMO being based on some form of SINR maximisation, it reflects the superior capability of the adaptive scheme to achieve better results. A higher SINR produces higher throughput, and adaptive WDMA-MIMO always grants SINR higher than 5 dB even in extremely crowded environments. The fixed scheme, on the other hand, can go as low as -5 dB of average SINR in order to provide connectivity.

In Figure 5.5, per-user average capacity and CL probability are reported. Before the room reaches a crowdedness of 20 users, the adaptive WDMA-MIMO scheme grants slightly higher per-user average capacity. After that point, the curve related to this scheme dips below the one related to the fixed scheme. However, by looking at the earlier SINR figure, a consistently higher performance of the adaptive scheme could be expected. This discrepancy comes from the fact that the adaptive scheme is designed to serve more users more fairly, even at the expense of per-user performances. Conversely, as the fixed scheme maximises the SINR one user at a time, it is certainly able to obtain higher maximum performances from a “single user” perspective. This is why,

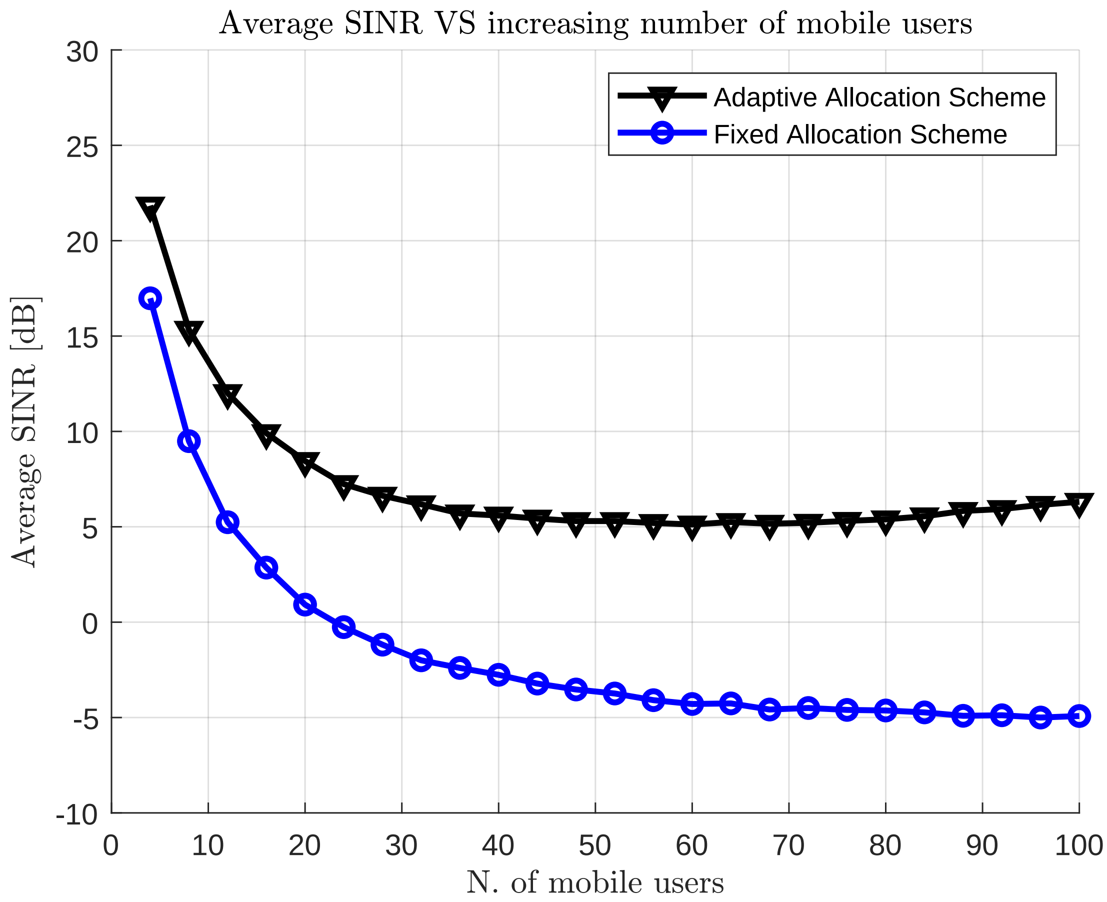

Figure 5.4: Average SINR with an increasing number of users in the room. As with the average aggregate network capacity, the adaptive WDMA-MIMO allocation scheme outperforms the fixed one consistently.

especially with a lower number of users in the room, its yielded performances may appear preferable. However, this comes at the expense of CL. This metric is always higher in the case of the fixed scheme, meaning that a higher percentage of users get disconnected on average. In fact, the CL curve for the fixed scheme is a convex function increasing monotonically that, even with only 4 users in the network, realises around 10% of disconnected users overall. At maximum crowdedness, it is over 75%. In the case of adaptive WDMA-MIMO, this metric remains consistently around 4% only increasing monotonically and in a concave fashion starting from 48 users in the network, reaching a maximum of less than 15% when room crowdedness is at its highest.

All of the aforementioned becomes clearer by looking at a comparison between CL

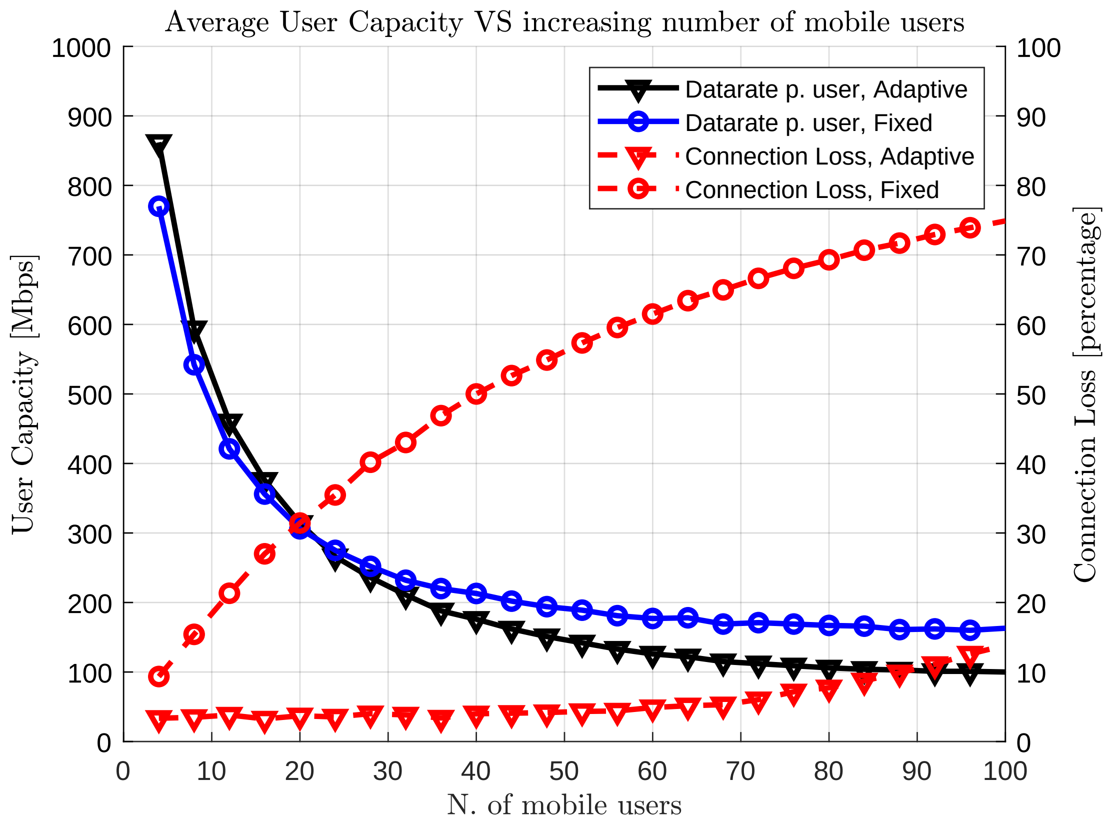

Figure 5.5: Per-user average capacity and connection loss probability. Up to a crowdedness of 20 users, the adaptive scheme yields slightly higher per-user performances, which then dip significantly. CL probability is consistently lower with the adaptive scheme, touching a maximum of less than 15% with 100 users in the room.

probability and the new OFOV probability metric, which is a measure of how many users' disconnections are caused by a lack of APs in the users' FOVs. As mentioned in Section 5.2.4, this is important to note because such disconnections are not due to a lack of network resources but rather to a peculiar combination of users' positions, orientations, and device inclinations. Figure 5.6 presents a comparison between CL and OFOV in the adaptive case. Recalling the definitions of these two metrics, it can be seen that being CL always higher than OFOV (stable at around 4%), the network consistently fails to provide a proper allocation. This becomes clear by considering that even in the case of only four users in the room, which should bring an abundance of network resources to be allocated, the CL is still prominent with respect to the OFOV.

In contrast, Figure 5.7 shows the same comparison in the adaptive WDMA-MIMO

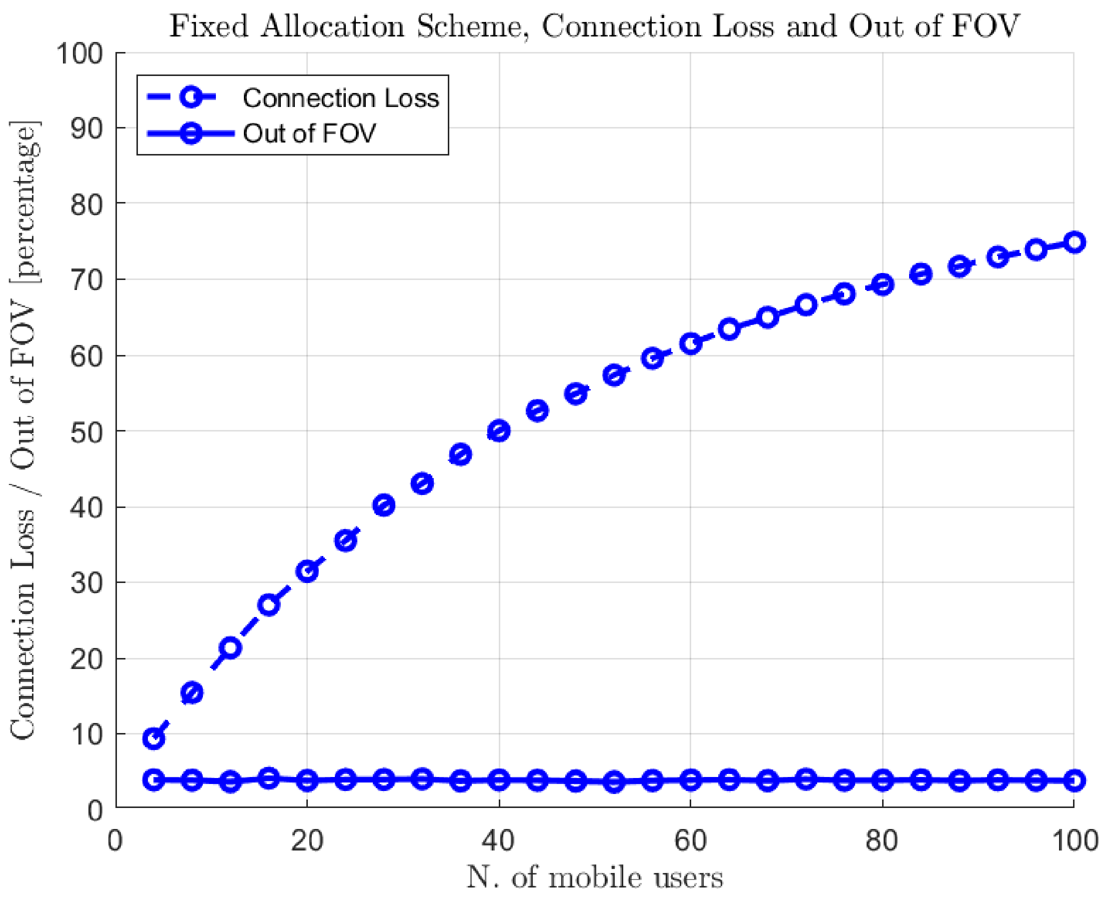

Figure 5.6: CL probability and OFOV VS increasing users, fixed scheme. CL probability is consistently higher than OFOV probability with the fixed WDMA-MIMO allocation scheme.

case, with an inset zooming on where the two curves start diverging. Up to this point, the two metrics always coincide, indicating that in these conditions, the adaptive scheme shows consistent efficiency in providing all users with at least a basic form of connectivity. However, as the number of users grows past 50% of the theoretical limit, the curves start diverging, indicating that in some instances, no resources are available for allocation. This is mostly related to the very high user density in the room, which dramatically reduces spatial diversity between users.

In Figure 5.8, the number of average active users is reported versus the total number of users in the room. These curves are closely related to the CL results, as they are directly influenced by them. Here, the term "active user" indicates a user that

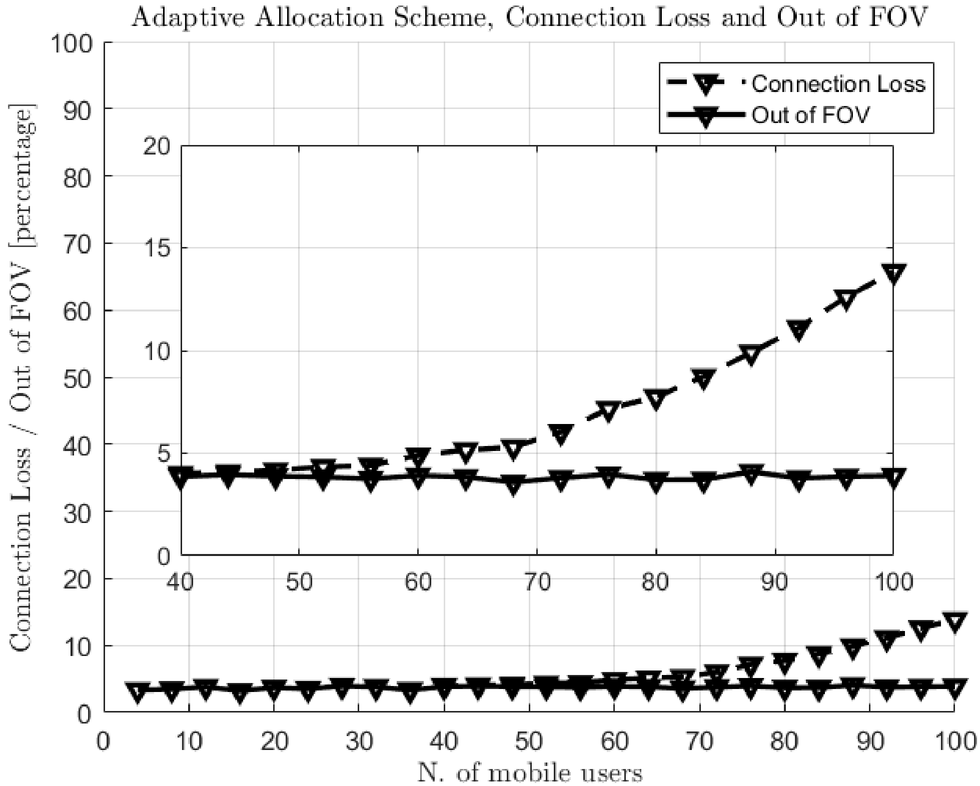

Figure 5.7: CL probability and OFOV VS increasing users, adaptive scheme. CL probability is equal to OFOV probability up to around 48 users in the room, where it starts diverging, indicating that all CL up to that point are due to OFOV.

has been successfully allocated network resources and can benefit from at least one allocated channel. Since the adaptive WDMA-MIMO scheme focuses on fairness, firstly allocating one channel to every user before trying to maximise resource utilisation, this outcome is expected. Nonetheless, despite showing remarkable adaptability to very limited spatial resources, the related curve becomes convex while approaching the theoretical limit of 100 users.

5.3.2 Time-dependent handover analysis

Table 5.1 reports the results for the 15-minutes long simulation in each of the 4 envisioned scenarios.

In terms of performance regarding aggregate network capacity, scenarios 1 and 2

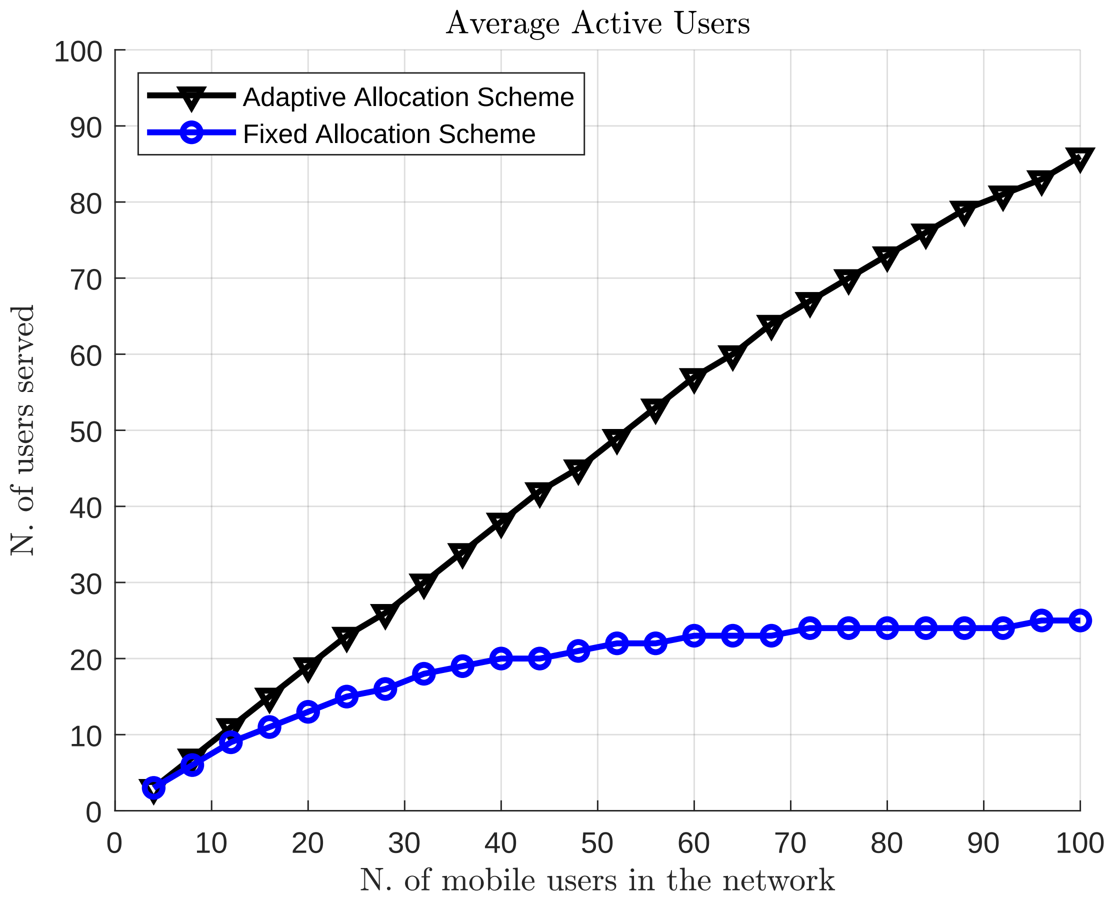

Figure 5.8: Average active users vs. increasing users in the room. As expected from CL performances, adaptive WDMA-MIMO yields better results than fixed WDMA-MIMO.

show comparable results (and the highest data rate is achieved in scenario 2). Slightly lower performances are yielded in Scenario 4, while the lowest average network data rate performance is attained in Scenario 3. The reason for this lies in the different spatial separation. In fact, by considering Figure 5.2 again, it can be seen that Scenario 2 features the best spatial diversity among the users. Scenario 1 follows, with a slightly more crowded area in the southern part of the room ($y_{\mathrm{u}} \in [0, 2]$). Scenario 4 has the user tightly grouped in two main locations, but given their orientation (facing each other), their devices will face a wider range of APs, providing better opportunity for the network to allocate channels to them. Finally, Scenario 3 shows the worst spatial diversity: the users are all close to each other, and since they are forming a queue, their orientation is not favourable for spatial diversity because only the 5 APs in the central

Table 5.1: Network performances in time-dependent indoor scenarios

Parameter	**Scenario 1**	**Scenario 2**	**Scenario 3**	**Scenario 4**
Avg. network data rate [Gbps]	2.75 Gbps	2.87 Gbps	1.59 Gbps	2.35 Gbps
Avg. data rate per user [Gbps]	0.70 Gbps	1.00 Gbps	0.39 Gbps	0.58 Gbps
Avg. SINR per channel [dB]	17.50 dB	25.46 dB	12.83 dB	15.52 dB
Connection loss [%]	0.00 %	27.69 %	0.00 %	0.00 %
Out of FOV [%]	0.00 %	27.69 %	0.00 %	0.00 %
Handover rate [1/s]	1.31 /s	1.32 /s	1.88 /s	1.79 /s
Percent handover rate [%]	16.40 %	16.51 %	23.49 %	22.42 %

column of the room ($x_{\mathrm{AP}} = 3$ m) are in a position of transmitting a clear signal to 8 users. In this regard, wavelength diversity holds crucial importance, as it allows 5 APs to serve 8 users without disruption. Conversely, in other scenarios, more APs can be employed at once due to spatial diversity, leading to less interference and a higher data rate. All this is also reflected in the average per-user data rate metric.

The CL probability is always 0.00% except in Scenario 2, where it can be seen from the users' spatial disposition that the network's inability to allocate channels to part of the users could be due to the fact that half of them have an unfavourable combination of position and orientation since they are located at the edges of the room and facing the centre. As a result, the screen of their devices will be pointing towards the walls, and it is possible that they will not have a single AP in their FOV since non-Line Of Sight (LOS) paths of light beams are not considered in this dissertation. The OFOV metric confirms exactly this hypothesis, as it is equal to Scenario 2 in this case (27.69%). This higher rate of disconnection in Scenario 2 also has another effect: in fact, if fewer users are being served, there is lower interference for all the other active channels.

As reported in the table, the average handover rates (calculated by averaging across all users in one scenario) are very similar in Scenarios 1 and 2, at 1.31/s and 1.32/s, respectively. These are the lowest, and this is for the same reasons discussed. Additionally, as the users' activities in requesting service and exiting the network unfold over time, there is a variable component in the interference and AP occupancy, which has a direct effect on the handover rate. In fact, there is a chance that users entering the network after an idle time could request service from an AP already allocated to

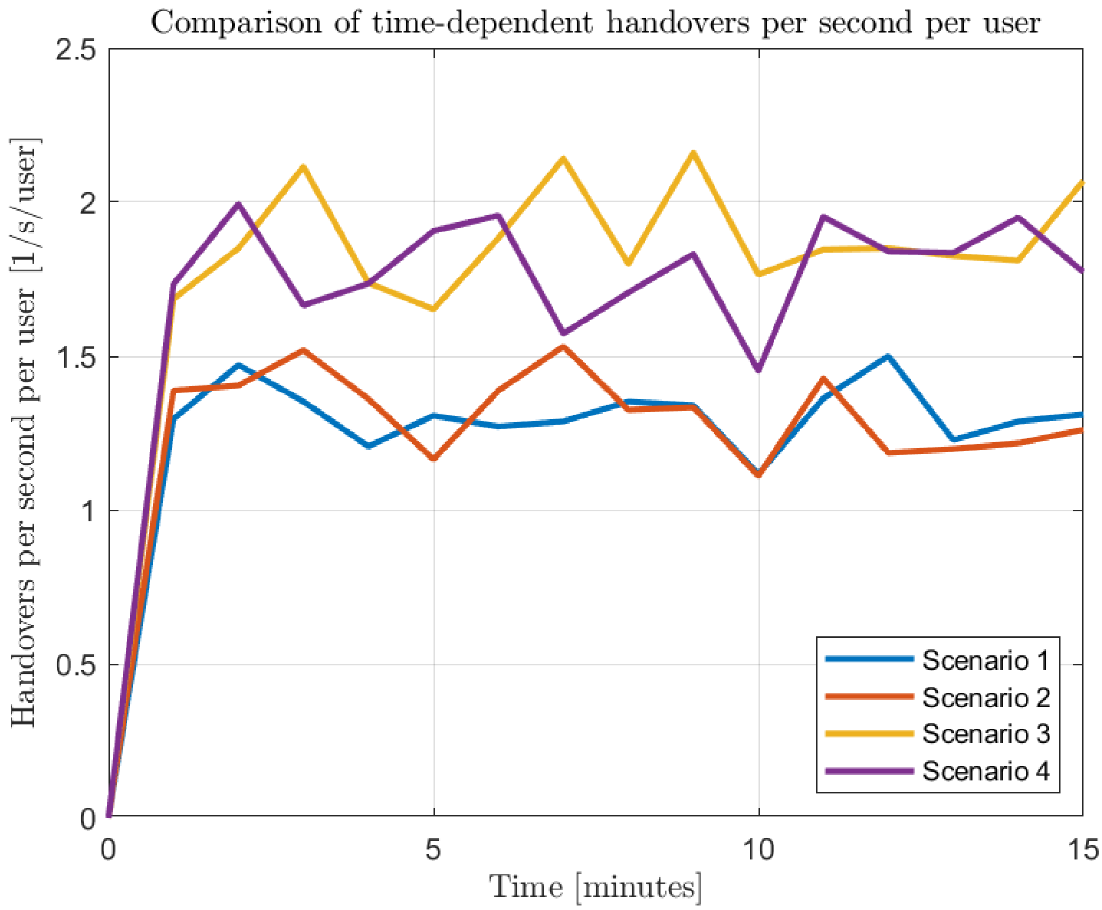

Figure 5.9: Time evolution of average handover rate in four scenarios. Scenario 3 and 4 exhibit a higher average and variability.

another user, and as a result, a handover will be forced on this latter. This can be seen in scenarios 3 and 4, in which users are less uniformly distributed in space and thus there is a higher level of competition for the same resources. Handover rates in these are 1.88/s and 1.79/s, respectively, which constitutes an increase with respect to the first two scenarios.

Figure 5.9 reports the time-dependent evolution of the average handover rate in all 4 scenarios. As it can be seen, apart from the higher average in Scenarios 3 and 4, the curves also show a higher variability of handover. It is expected that if users change their positions over time, other than their devices' inclinations, the handover rate will increase even more. Seen from this perspective, it could become necessary to modify the allocation scheme in order to accordingly reduce unnecessary handovers.

5.4 Chapter Summary

In this chapter, an adaptive WDMA-MIMO algorithm has been proposed. It is based on the simpler adaptive WDMA investigated in the foregoing part of the dissertation. Its biphasic approach to the allocation process allows every user to be provided with a connection, thus improving fairness and minimising CL.

The proposed adaptive WDMA algorithm has first been expanded into an adaptive WDMA-MIMO version, with the objective of ensuring better utilisation of the available network resources. In fact, these would conversely remain untapped. This has required us to adopt a biphasic approach to the allocation process so that in the first phase, every user is allocated one channel with the highest SINR, thus ensuring that a basic form of connectivity is provided to the highest number of clients. In the second phase, all remaining available channels are allocated to users with the same highest SINR method.

As a benchmark to test the performances yielded by such algorithm, a fixed allocation scheme has been devised for the lack of equivalent algorithms in the literature. It is based on a first-come, first-served round-robin allocation approach, still following the highest SINR method for determining the best channels.

The differences with the indoor scenario used in the previous chapter have been discussed in terms of the investigations that will be carried forward. Firstly, network scalability is investigated by incrementally increasing the user count up to a theoretical maximum of 100 clients concurrently requesting service. In fact, practical limitations would arise past this point due to the number of transmitters physically present in the envisioned room. It has to be noted that even though this theoretical limit of the network would entail an unlikely level of room crowdedness, it is important to test network scalability up to this point as the resulting curves' trends would only be completely exhausted once the theoretical limit has been hit.

The second part of the investigation deals with handovers, and as such, introduces a temporal dimension in the simulations. As seen, the coherence time of the inclination angle of the device is in the order of a few hundreds of milliseconds; such angle can then be treated as an uncorrelated stochastic random process even when sampling in the time domain (as opposed to a statistical evaluation with the Monte-Carlo method), with the condition of keeping the sampling time high enough that the angles have the time to become uncorrelated. As a consequence, it is possible to assume that the temporal changes in the devices' inclination angles are addressed by re-allocations of the network resources, based on the new angle, at regular intervals. Here it is emphasised the need to consider time-dependent factors for a comprehensive understanding of network performance evolution, as network stability over time is an important factor in the perceived quality from the perspective of a user.

In the examination of a fully crowded network, the simulation methodology mostly aligns with the approach outlined in the foregoing chapter in the network simulation part for both the fixed and adaptive schemes. The difference is that the number of concurrent users present in the room is progressively increased from 4 up to 100, which is the theoretical limit of the network's channel-forming capabilities. Each simulation result is then consolidated into a single figure to showcase the network's performance evolution concerning the number of users. Regarding the investigation of handover rates, a different approach is adopted. The room configuration remains consistent, and four scenarios are devised. In each scenario, the number of users is fixed, as is their position and orientation, while their inclination angle evolves with time as an uncorrelated Gaussian stochastic process. The resource allocation is assumed to update automatically after a set time interval (thus introducing the time dimension in the simulation). A continuous monitoring time of 15 minutes is established for each scenario. Users request network access in sessions, reflecting a power-saving strategy for both IoT and mobile devices. After each session, users can either exit the network or keep requesting service.

To help monitor these investigations, two new performance metrics have been introduced in this chapter: the OFOV and the handover rate. The first is a network-wide percentage expressing how many users, on average, have an unfavourable combination of position, orientation, and inclination, so that they do not have even a single AP in their FOV. Handover rate is as defined in the literature and adjusted for application in the case of wavelength division indoor LiFi networks.

Regarding the incremental users analysis, the showcased results highlight that adaptive WDMA-MIMO outperforms the fixed scheme with respect to average network capacity, average SINR per active channel, and CL probability. It is clear that the fixed scheme excels in achieving higher maximum performances for single users but incurs very high CL, reaching over 75% at maximum crowdedness, which means that less than 3/4 of the users experience connection outages. Conversely, the adaptive scheme maintains CL at less than 15% at maximum crowdedness. A comparison between CL and OFOV metrics highlights the adaptive scheme's consistent efficiency in providing basic connectivity to all users, while the fixed scheme struggles to allocate resources, particularly in high-density scenarios.

Regarding the time-dependent handover analysis, the evaluation of aggregate network capacity shows adaptive WDMA-MIMO exhibiting comparable results in scenarios 1 and 2, and achieving the highest data rate in scenario 2. In scenario 4, the algorithm shows slightly lower performance, while the lowest average network data rate is observed in scenario 3. This variation is attributed to lower spatial separation; in fact, scenario 2 features better spatial diversity, followed by scenario 1, which has a slightly more crowded area in the southern part of the room. Scenario 4, with users grouped in two locations facing each other, benefits from diverse AP orientations. Conversely, scenario 3, featuring closely positioned users in a queue, lacks favourable spatial diversity. In this context, wavelength diversity still provides manageable connection conditions for all users, enabling the network to serve all users without disruptions. The CL probability is consistently 0.00%, except in Scenario 2, where challenges arise in channel allocation due to unfavourable user positions. The OFOV metric confirms this, indicating disconnections due to users facing walls. Average handover rates are lowest in Scenarios 1 and 2, reflecting uniform user distribution. Higher rates in Scenarios 3 and 4, where users are less uniformly distributed, suggest increased competition for resources. The time-dependent evolution of handover rates highlights variability, especially in Scenarios 3 and 4, indicating potential modifications to the allocation scheme to reduce unnecessary handovers.

Chapter 6

Conclusions, Limitations, Future Work

6.1 Final Summary & Conclusions

In this thesis, the focus is on the challenges that an implementation of indoor wavelength division-based Light Fidelity (LiFi) networks with dense deployments of Access Point (AP)s presents. While the context calls for free mobility of users in terms of location, orientation, and device inclination, the Passband Shift (PS) effect imposed by the inherent physics of crucial components employed cannot be neglected in the link budget as it potentially introduces severe signal losses.

Firstly, the impact of the PS effect on a wavelength division-based system has been studied. A geometrical framework has been established to be used throughout the thesis, and the derivation of the Probability Density Function (PDF) of the central wavelength of an optical filter dependent on the user mobility behaviour has been carried out. Other than allowing to evaluate the importance of this effect, this has prompted the introduction of the Spectral Overlap (SO) parameter, which allows to visualise how well the spectrum of a source overlaps with that of an optical filter, taking user mobility into account. This tool has been used to evaluate the utility and performances of an Optical Front-End (OFE) optimisation in the wavelength domain in an indoor wavelength division-based LiFi network. Results have shown that such optimisation would even deteriorate the received Signal-to-Interference Ratio (SIR) with respect to an unoptimised OFE in which central wavelengths of Light Emitting Diode (LED)s and OFs coincide.

Prompted by these results, the focus has then been shifted to the network operation level to tackle the problem of mitigating interference in the indoor environment with a resource allocation approach. More specifically, channels can be allocated to users based on a Signal-to-Interference-plus-Noise Ratio (SINR)-maximisation method, which inherently takes random user mobility behaviour into account. After discussing various system design choices to be used in this setting and defining the underlying system model, a resource allocation scheme named “adaptive Wavelength Division Multiple Access (WDMA)” has been proposed. It is based on the aforementioned allocation method, and it has been compared with a fixed scheme, in which users are always assigned to the same colour based on their time of arrival. The comparison has included custom-made simulations to calculate coverage for both schemes as well as generating data with the Monte Carlo method for a real use case. In this latter case, four users would be free to roam in the room while requesting network access, according to their regular movement behaviour. The outcomes of these simulations have shown that the adaptive WDMA scheme seems more suitable for an indoor wavelength division-based LiFi network with densely deployed APs. More specifically, results have highlighted a trade-off between better fairness and lower Connection Loss (CL) probability, which come at the cost of a slightly lowered data rate, both averaged and per-user. This trade-off comes from the challenge of proper interference estimation to be fed to the SINR maximisation-based algorithm, which is a challenging task.

Lastly, the adaptive WDMA has been extended into an adaptive Wavelength Division Multiple Access-Multiple Input Multiple Output (WDMA-MIMO) algorithm. This allows to better exploit the network resources by trying to maximise the number of channels to be allocated to each user instead of limiting the process to one channel per user. The algorithm is divided into two distinct allocation phases (biphasic approach); this not only allows to retain adaptive WDMA’s characteristics of improved fairness but also to adaptively adjust to the network crowdedness, lowering the number of channels per user if in certain areas of the room the spatial separation between devices is too low. This new algorithm has been tested in conditions of increasing room crowdedness, up to its theoretical limit, and compared with a fixed Multiple-Input Multiple-Output (MIMO) allocation scheme. The method used to carry out the aforementioned is again using custom-made simulations, as building a physical testbed would be costly and time-consuming. Results have shown that the adaptive WDMA-MIMO has improved scalability and robustness with respect to the fixed scheme, and this has been demonstrated to be especially true as the number of user in the network increases. Network and per-user data rate, average SINR per active channel, and CL probability are higher in the adaptive WDMA-MIMO scheme, while the fixed WDMA-MIMO excels at maximising the data rate of the single users on a first-come, first-served basis. As a further investigation, the temporal dimension is introduced in the simulations by leveraging the coherence time of device inclination angles. It involves four scenarios in which 8 users randomly request or disconnect from service. The results highlight the potential to introduce further modifications to the allocation scheme so that unnecessary handovers can be avoided.

All the simulations have been carried out with measured optical filter spectra at increasing Angle of Incidence (AoI) of the incoming light, given substantial differences between the PS effects between datasheet and measured behaviour of optical filter that have been reported in Appendix B.

In the first instance, this work wanted to evaluate the feasibility of using the shifting spectra as a further dimension, that would allow to use a transmitter wavelength different from the central wavelength of the receiver's optical filter. For example, the blue transmitter of an AP would be paired to the green receiver, if its inclination made the optical filter's central wavelength shift in the blue region of the spectrum. This was demonstrated to be unfeasible because the central wavelength shift is accompanied by a severe spectral degradation, and even in conditions of extreme crowdedness these hybrid-coloured channels do not offer an increase in performances. Moreover, in densely deployed LiFi networks (where the number of APs is high), even if the AP that is closest to one user does not have any available channels, the other neighbouring APs offer plenty of solution for establishing a connection. Random orientation has been a concern in Optical Wireless Communication (OWC), and in densely deployed networks where interference could introduce additional potentially severe degradation in performances, this is an even more pressing matter. In that regard, the use of WD to address the problem may seem counterintuitive because of the spectral degradation and PS phenomenon that may further reduce the link budget; and in normal circumstances, it does. Yet, this work has demonstrated its feasibility and added interference-reducing capabilities even in extremely crowded environments, with the caveat that a smart resource allocation scheme must be implemented at the network operation level so that what seemed to be a drawback, can now be harnessed as a new and unexplored channel separation feature to improve network performances and provide multiuser access.

6.2 Limitations & Future Developments

The proposed adaptive WDMA and adaptive WDMA-MIMO schemes are demonstrated to provide improved fairness and network performances with respect to a fixed allocation benchmark. However, the SINR maximisation method on which they are based requires to consider the worst-case scenario, that is, while all transmitters are active at the same time. In this way, and especially when the network is populated with an overall lower number of users, the interference is overestimated. This can induce errors in the allocation, which then becomes suboptimal.

Throughout the entirety of the thesis, the presented results have been generated with Monte Carlo simulations. These feature a high number of iterations that look like “snapshots”, thus rendering the allocation system memory-less. An interesting future direction to pursue to overcome this limitation is to implement a random waypoint model so that the environment (and especially the user behaviour) is more faithfully represented in the time domain. In this way, not only would the handover rate investigation be more accurate, but from an algorithm-design perspective, it would be possible to store recent allocations and use them as a base for the reallocation in future time instants. This would take the real expected AP activation into account, thus making the allocation more robust than the simple memory-less SINR maximisation. Other possible approaches to tackle the problem of interference overestimation include:

- Using interference data to generalise an analytical expression so that more accurate SINR values can be used.
- Investigate reinforcement learning (and particularly the Q algorithm) to estimate the interference prior to the allocation, based on how many users are in the network and their location and orientation data, if available.

In this thesis, no path blockages due to the users' physical bodies are assumed. It appears reasonable to expect that an adaptive allocation scheme would be able to overcome this added system feature, while a benchmark fixed allocation method would yield worse results in terms of a lower achievable data rate and a higher CL figure (due to increased Out of Field Of View (OFOV)). However, all this cannot be guaranteed and needs to be confirmed with more accurate tests (either based on an experimental test-bed or on custom simulations).

One of the limitations encountered is that according to literature, the PS has two effects: one is the shift towards shorter wavelengths, and the other is the appearance of a spectrum degradation, which becomes more substantial as the AoI of the incident light increases. This second effect is closely tied to the internal structure of the OFs, and this makes it difficult to investigate and formalise for two main reasons:

- The quality and amount of spectral degradation can be inferred by knowing the composition of the internal layers of the optical filters. Since existing off-the-shelf components have been used throughout the study, this information is not available as it is part of the manufacturers' intellectual property.
- Devising a reliable and more general model for the spectrum degradation would involve measuring a vast array of optical filter of different qualities and manufacturers, which is a costly and time-consuming activity. The result of the spectrum degradation not only changes between different models and manufacturers of optical filter but also within each copy of the same optical filter model from the same manufacturer. Furthermore, as new materials and procedures are discovered and

implemented in the construction processes, such models could relatively quickly become outdated.

These are also the reasons for which the SO does not take into account such spectrum degradation. The spectra that have been measured and used in this thesis are more representative than the ones in datasheets on account of the PS effect. However, since they have been taken from specific physical copies of the OFs, they are specific to those optical filter models. Thus, since a generalised model for spectral degradation of the optical filters is not readily available, another interesting comparison would be similar to the one carried out for the OFE optimisation in a network setting, but using the spectra of real measured optical filter. It is anticipated that the spectral degradation would add to the channel separation even more, making the case in which $\lambda_{\mathrm{OF}}(0) = 500$ nm even more favourable with respect to the case in which $\lambda_{\mathrm{OF}}(0) = 520$ nm.

The ability to leverage the PS effect in the context of a WDMA LiFi indoor network could be further investigated as, in the author's opinion, it holds the potential to unlock a further step in the utilisation of LiFi on a larger scale. More specifically, it could be interesting to explore other system geometries (such as the exagonal shape) other than the square lattice used in this thesis. It would also be useful to explore how the adaptive WDMA and WDMA-MIMO algorithms can perform in different room conditions, such as in terms of distance between APs.

Appendix A

Validation of System Model

After defining an underlying system model as in Section 4.2, there is a need to conduct a validation in which the employed mathematical framework is compared to the results of an experimental acquisition made on a physical testbed specifically constructed to mimic, in a scaled-down capacity, what would happen in a real scenario. In terms of a meaningful validation, two main aspects have to be accounted for that bear a significant influence on the end results: the losses in the signal strength due to the optical path loss, $H_{\mathrm{LOS}}(0)$, and the ones introduced by the optical filter transmissivity curves. Regarding this latter, there is an interest in observing both the central wavelength shift of the OFs and the spectral degradations induced by the Passband Shift (PS) effect.

As a result, the validation process includes running an experiment with all four RGBA OFs chosen for the work to measure optical power as Angle of Incidence (AoI) goes up. These measured optical power values are subsequently compared with their analytically computed counterparts for validation.

Figure A.1 shows a reference of the test setup employed for the validation. From the left, the following components can be seen:

- A light source. In the figure, a blue micro Light Emitting Diode (LED) is depicted. However, for the experimental acquisition, this was substituted with a complete RGBA array of individually addressable LEDs. In this way, coloured sources can be activated one by one without touching the testbed. This is to avoid spectral leakage, as there is a slight overlap between sources' spectra.

Figure A.1: Reference to the test setup employed for the validation. On the left, the test setup is seen from the side. The black wall in the background is used to keep an opaque dark cover to avoid any background illumination interference. On the top right, a test setup close-up. On the bottom right, the test setup is seen from the top.

- A diffuser lens that is used to match the half-intensity angle of the blue micro LED to the one used in the simulation environment. Since the actual RGBA array has been used to generate the experimental results presented here, this diffuser lens has been removed for the acquisition.
- The blue optical filter. It is mounted on a rotation stage manufactured by Thorlabs, which features the possibility of fine-tuning the rotation angle. This is of crucial importance for this application.
- The power meter head.

As seen in the figure, in this setup, an RGBA LED optical source was positioned at a fixed distance from the power meter, with an optical filter (matched in colour to the LED source) interposed between them. The optical filter's orientation was adjusted as previously described, and received power measurements were obtained at various AoIs, including 0°, 10°, 20°, and 30°. These measurements, carried out in a light-controlled environment, were subsequently compared to the corresponding theoretical values.

This has proved a challenging endeavour for many reasons, but the most important one is the distinctive spectral degradation shown by every filter. In fact, complete validation has only been possible after measuring the optical filter transmission characteristics as in Appendix B and using them in computing the analytical results of the model.

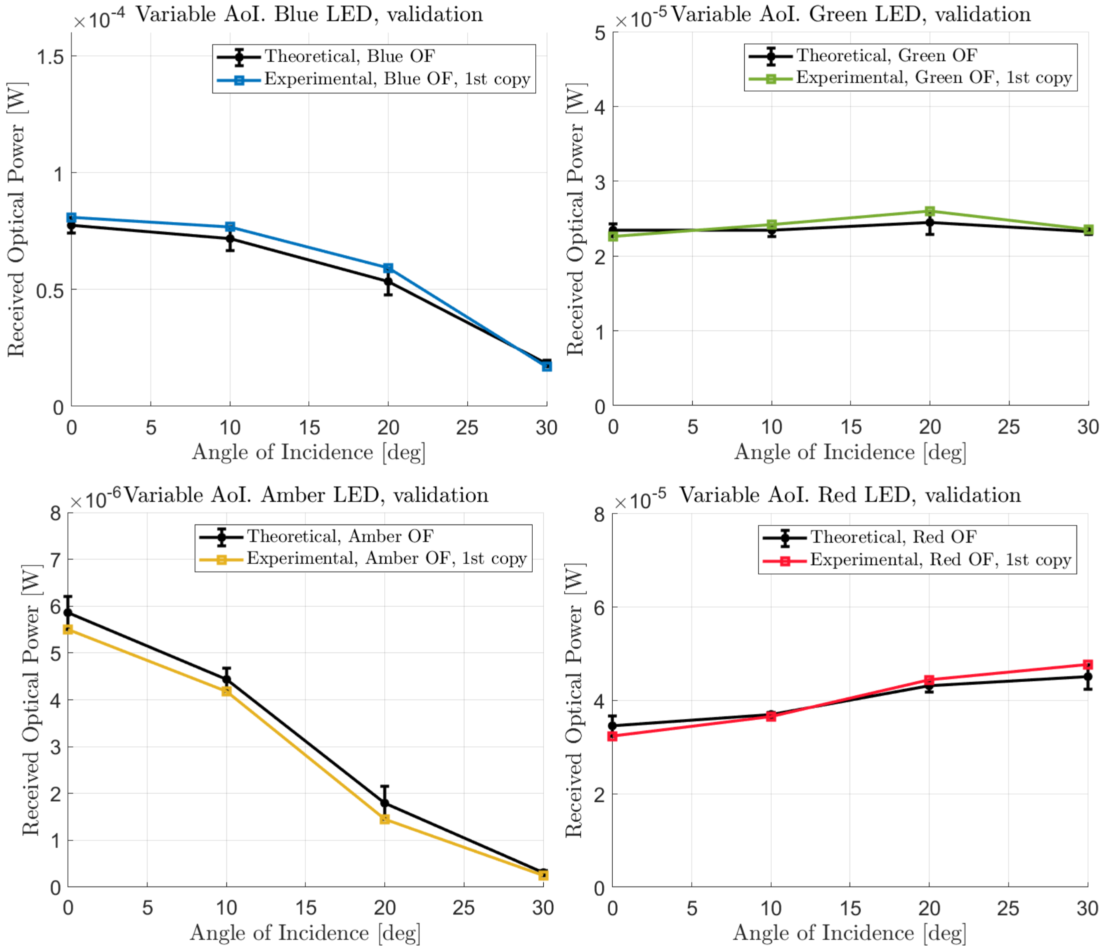

Figure A.2: Measured received power as obtained in the experimental setup versus theoretical, as calculated analytically. A close match between experimental and theoretical is obtained by using measured OFs spectra. These also account for the spectral degradation at higher AoIs.

Figure A.2 visually demonstrates a close alignment between experimental and theoretical data. It is worth emphasising that employing idealised or datasheet-based characteristics for OFs in earlier attempts has led to inaccurate results when compared to the outcomes achieved using actual optical filter devices.

Appendix B

Characterisation of OFs

Within this appendix, the results of an experimental characterisation of four OFs manufactured by Thorlabs are presented. These filters are the models used throughout the dissertation: blue (FB450-40 [196]), green (FB550-40 [197]), amber (FB590-10 [198]), and red (FB650-40 [199]). The primary objective of this analysis is to explore the transmission characteristics of these filters in relation to the AoI of the incident light. These AoI-dependent curves are essential components integrated into the simulation framework, as AoI variability is one of the main characteristics of the scenarios investigated in this dissertation. This is a very important step to ensure that the measured optical filter transmissivity spectral data reflect the actual behaviour of the spectral characteristics of the system and increase the confidence in all results obtained thereafter.

The acquisition of experimental data has been achieved by using a spectrometer, an instrument designed to capture the wavelength-dependent distribution of emitted power from an optical source, commonly referred to as its emissivity. Additionally, the emissivity measurements enable the derivation of the transmissivity of each optical filter placed between the source and the spectrometer. This is achieved through the application of a subtraction algorithm embedded within the spectrometer's internal software.

The spectral data collection took place in a controlled dark environment to prevent any interference from background illumination by using a test setup much similar to the one used in the validation process (with the only difference being the power meter head substituted with the spectrometer head). The AoI was varied incrementally, commencing from 0° and progressing up to 40° included, with measurements taken at 10° intervals. During this experiment, only the OFs were subjected to rotation while maintaining the power meter at a constant AoI of 0° and a fixed distance of 0.164m. As seen in Appendix A, this approach ensured that the optical path loss remained consistent throughout the entire experiment. In fact, by only rotating the optical filter with respect to the source but not the receiver, the AoI of the impinging light beam only generates the Passband Shift (PS) effect without impacting the optical path loss.

Figure B.1 visually represents the outcomes of this characterisation, juxtaposed with the relevant Light Emitting Diode (LED) normalised spectrum serving as a reference. Notably, at higher AoIs, discernible differences emerge in comparison to the idealized rectangular shape often assumed for OFs, as well as the curves typically found in datasheets. This discrepancy highlights the importance of conducting similar filter characterisations, even in simulation-based studies. Such an approach ensures that the simulation results align more closely with real-world scenarios.

Figure B.2 shows a comparison between the measured optical filter transmissivity of two physical copies of the same OFs at increasing AoI.

Appropriate modelling of OFs is still an open challenge. Past literature only provides precise indications regarding what is to be expected in terms of central wavelength shift. On the contrary, given any physical (and not simulated) optical filter component, it is not easy to foresee what the spectral degradation will be with respect to the AoI. This is because detailed information on the internal structure of each individual filter would be required. Obtaining such knowledge about OFs is a challenge for two reasons:

- The details of the optical filter construction (such as materials employed, number of layers, and their order) are typically regarded as proprietary information held by manufacturers, making access to this information challenging, if feasible at all.
- Any spectral degradation model developed in this manner would be specific to the particular optical filter model under consideration. Moreover, to account for variations between individual filter samples, extensive testing of multiple optical

filter copies would be required.

This highlights the complexity and limitations associated with accurate modelling of OFs accounting for AoI-dependent characteristics, which is the main motivation behind the choice of conducting this experiment to implement measured optical filter transmissivity spectra into the simulation work.

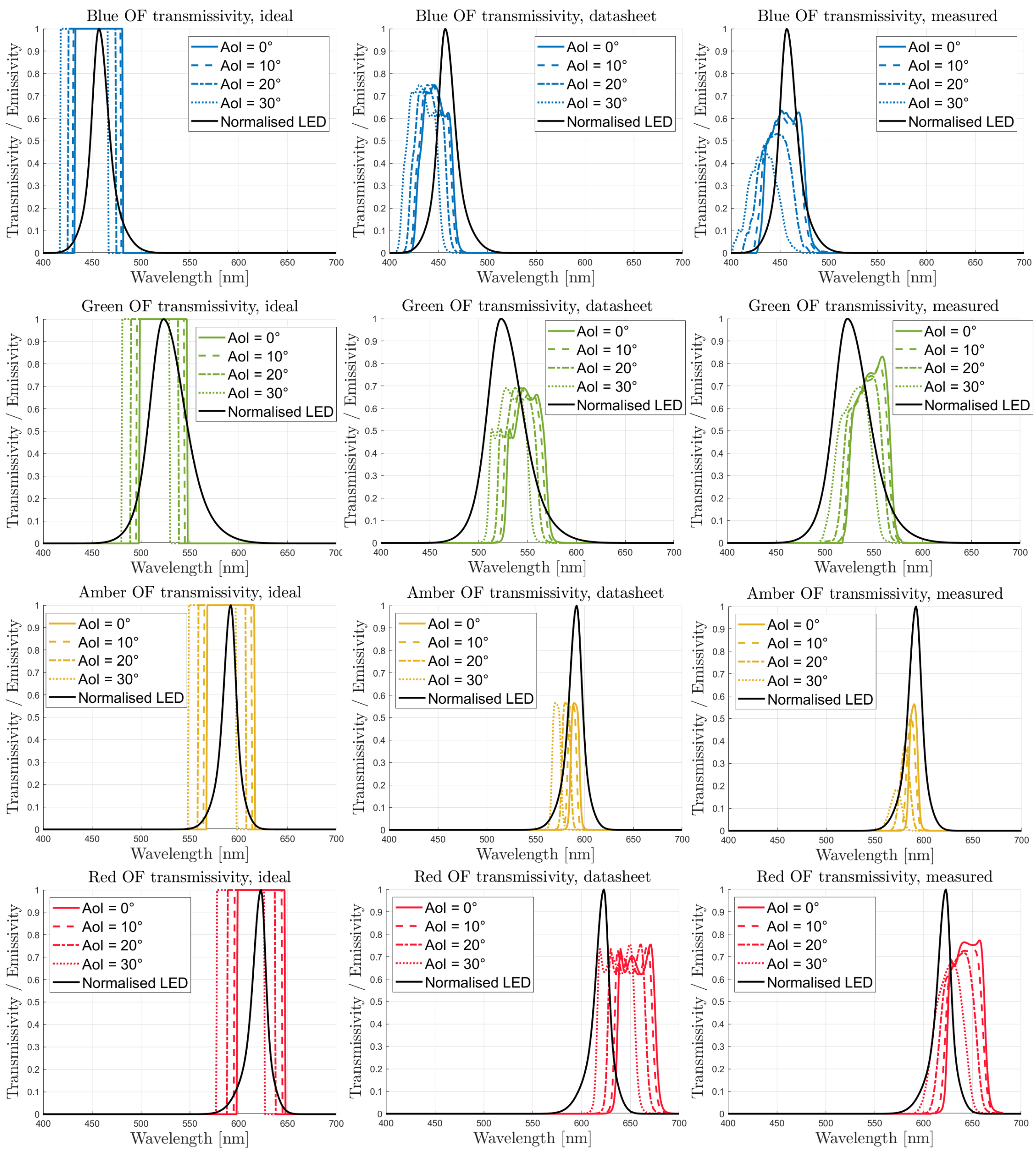

Figure B.1: Ideal versus datasheet versus measured optical filter transmissivity comparison. Each row contains ideal, datasheet, and measured spectra for each colour. At higher Angle of Incidence (AoI)s, the OFs' characteristics show a shift towards shorter wavelengths. However, only measured spectra report substantial spectral degradation. Conversely, ideal and datasheet curves have no reliable information on this effect.

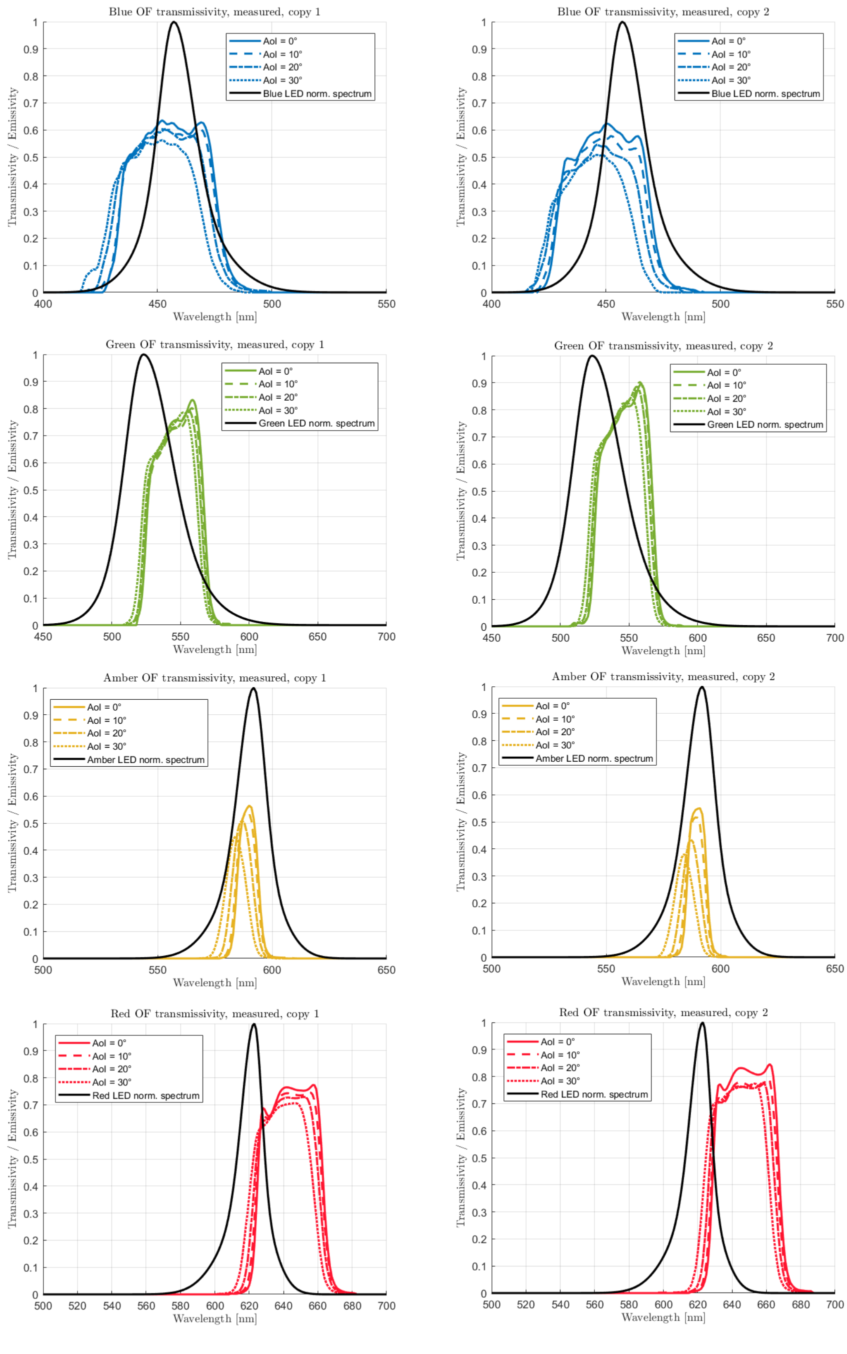

Figure B.2: Measured optical filter transmissivity comparison between two physical copies of the same OFs at increasing AoI. Other than showing substantial spectral degradation at higher AoIs, the significant variability between two physical copies of the same model of optical filter can be appreciated.

Appendix C

Published papers

C.1 Adaptive WDMA: improving the data rate of a densely deployed LiFi network (Internet of Lights 2021)

A novel adaptive Wavelength Division Multiple Access (WDMA) scheme is presented in this paper, capable of contrasting the effect of the Passband Shift (PS) phenomenon in an indoor densely deployed LiFi network. After an overview on WDMA in an indoor Internet of Things (IoT) setting, simulation work is defined and carried out. Results show how in such settings, the loss of connection is reduced to an average of 0.72 % compared to 31.25 % when using Adaptive WDMA. Additionally, the users are served with higher average speeds and better fairness.

C.2 Impact of Passband Shift in Optical Wireless Communication Systems based on Wavelength Division (ICC 2022)

In this paper we investigate the impact of the passband shift (PS) phenomenon on optical wireless communication (OWC) systems based on wavelength division (WD). We first introduce the associated challenges, then we discuss the mathematical framework needed to evaluate the performance of systems based on WD when the impact of the PS phenomenon is taken into account. We introduce the concept of spectral overlap

(SO) and discuss its role in the design of WD solutions. Results show that this design phase has to take the SO into account, and that its careful balance with the channel gain is essential when multiple colours are used for parallel communication in OWC.

C.3 A Simulation Tool for Interference Analysis in MIMO Wavelength Division LiFi Indoor Networks (ICC 2023)

In this paper we propose a novel simulation tool for indoor Light Fidelity (LiFi) networks based on Wavelength Division (WD) with real optical filters characteristics. Firstly we present the measured passband spectra of optical filters, along with a system model validation relying on such acquired spectra. Secondly, we propose a simulation tool developed to extend the work of adaptive wavelength division multiple access to the multiple-input multiple-output case, suitable for conducting Monte Carlo simulations. Then, we validate such tool by considering an example scenario with fixed positions and orientations, including increasing number of users in an indoor LiFi network using WD. In order to better clarify the interference contributions to the quality of service provided, we consider the first user as reference, and evaluate how the presence of progressively higher number of users in its vicinity impacts the interference that the main user is experiencing. We then analyse how the signal-to-interference-plus-noise ratio, interference-to-noise ratio and signal-to-interference ratio figures of the main user change depending on how many interfering users are included in the considered scenario.

Bibliography

[1] CISCO, “Vni mobile forecast highlights.” https://www.statista.com/statistics/471264/iot-number-of-connected-devices-worldwide/CISCO, 2017.

[2] V. Cisco, “Cisco visual networking index: Forecast and trends, 2017–2022,” *White paper*, vol. 1, no. 1, 2018.

[3] M. Cave *et al.*, “Review of radio spectrum management,” *An independent review for Department of Trade and Industry and HM Treasury (www. spectrumreview. radio. gov. uk)*, 2002.

[4] Q. C. Li, H. Niu, A. T. Papathanassiou, and G. Wu, “5g network capacity: Key elements and technologies,” *IEEE Vehicular Technology Magazine*, vol. 9, no. 1, pp. 71–78, 2014.

[5] “Cisco annual internet report (2018–2023) white paper.” https://www.cisco.com/c/en/us/solutions/collateral/executive-perspectives/annual-internet-report/white-paper-c11-741490.html#Trends, 2020.

[6] “Deliver 5g iot services faster white paper.” https://www.cisco.com/c/en/us/products/collateral/wireless/iot-mobility-services/5g-iot-services-wp.html, 2023.

[7] A. G. Bell, W. G. Adams, Tyndall, and W. H. Preece, “Discussion on ”the photophone and the conversion of radiant energy into sound”,” *Journal of the Society of Telegraph Engineers*, vol. 9, pp. 375–383, 1880.

[8] G. Pang, T. Kwan, C.-H. Chan, and H. Liu, "Led traffic light as a communications device," in *Proceedings 199 IEEE/IEEJ/JSAI International Conference on Intelligent Transportation Systems (Cat. No.99TH8383)*, pp. 788–793, 1999.

[9] Y. Tanaka, S. Haruyama, and M. Nakagawa, "Wireless optical transmissions with white colored led for wireless home links," in *11th IEEE International Symposium on Personal Indoor and Mobile Radio Communications. PIMRC 2000. Proceedings (Cat. No.00TH8525)*, vol. 2, pp. 1325–1329 vol.2, 2000.

[10] A. H. Azhar, T.-A. Tran, and D. O'Brien, "A gigabit/s indoor wireless transmission using mimo-ofdm visible-light communications," *IEEE Photonics Technology Letters*, vol. 25, no. 2, pp. 171–174, 2013.

[11] F. M. Wu, C. T. Lin, C. C. Wei, C. W. Chen, Z. Y. Chen, H. T. Huang, and S. Chi, "Performance comparison of ofdm signal and cap signal over high capacity rgb-led-based wdm visible light communication," *IEEE Photonics Journal*, vol. 5, no. 4, pp. 7901507–7901507, 2013.

[12] L. Zhang, D. Chitnis, H. Chun, S. Rajbhandari, G. Faulkner, D. O'Brien, and S. Collins, "A comparison of apd- and spad-based receivers for visible light communications," *Journal of Lightwave Technology*, vol. 36, no. 12, pp. 2435–2442, 2018.

[13] T. Koonen, K. A. Mekonnen, Z. Cao, F. Huijskens, N. Q. Pham, and E. Tangdiongga, "Beam-steered optical wireless communication for industry 4.0," *IEEE Journal of Selected Topics in Quantum Electronics*, vol. 27, no. 6, pp. 1–10, 2021.

[14] T. Koonen, K. Mekonnen, F. Huijskens, Z. Cao, and E. Tangdiongga, "Novel broadband owc receiver with large aperture and wide field-of-view," in *2020 European Conference on Optical Communications (ECOC)*, pp. 1–4, 2020.

[15] P. A. Loureiro, G. M. Fernandes, S. F. H. Correia, R. A. S. Ferreira, F. P. Guiomar, and P. P. Monteiro, "Multi-gigabit rgb-vlc transmission with jointly optimized lighting and communications," *Journal of Lightwave Technology*, vol. 42, no. 13, pp. 4425–4432, 2024.

[16] R. Bian, I. Tavakkolnia, and H. Haas, "15.73 gb/s visible light communication with off-the-shelf leds," *J. Lightw. Technol.*, vol. 37, no. 10, pp. 2418–2424, 2019.

[17] H. Haas, L. Yin, Y. Wang, and C. Chen, "What is LiFi?," *J. Lightw. Technol.*, vol. 34, no. 6, pp. 1533–1544, 2016.

[18] M. Jatau, M. David, and S. Zubair, "Lifi: The solution to radio frequency saturation," in *2020 International Conference in Mathematics, Computer Engineering and Computer Science (ICMCECS)*, pp. 1–6, 2020.

[19] C. Chen, D. A. Basnayaka, and H. Haas, "Downlink performance of optical attocell networks," *J. Lightw. Technol.*, vol. 34, no. 1, pp. 137–156, 2016.

[20] Y. Wang and H. Haas, "Dynamic load balancing with handover in hybrid li-fi and wi-fi networks," *J. Lightw. Technol.*, vol. 33, no. 22, pp. 4671–4682, 2015.

[21] C. Chen, D. Basnayaka, and H. Haas, "Downlink sinr statistics in ofdm-based optical attocell networks with a poisson point process network model," in *2015 IEEE Global Communications Conference (GLOBECOM)*, pp. 1–6, 2015.

[22] M. Ayyash, H. Elgala, A. Khreishah, V. Jungnickel, T. Little, S. Shao, M. Rahaim, D. Schulz, J. Hilt, and R. Freund, "Coexistence of wifi and lifi toward 5g: concepts, opportunities, and challenges," *IEEE Communications Magazine*, vol. 54, no. 2, pp. 64–71, 2016.

[23] J. Wang, C. Jiang, H. Zhang, X. Zhang, V. C. M. Leung, and L. Hanzo, "Learning-aided network association for hybrid indoor lifi-wifi systems," *IEEE Transactions on Vehicular Technology*, vol. 67, no. 4, pp. 3561–3574, 2018.

[24] J. Sanusi, S. Idris, A. M. Aibinu, S. Adeshina, and A. N. Obadiah, "Handover in hybrid lifi and wifi networks," in *2019 15th International Conference on Electronics, Computer and Computation (ICECCO)*, pp. 1–6, 2019.

[25] X. Wu and D. C. O'Brien, "A novel machine learning-based handover scheme for hybrid lifi and wifi networks," in *2020 IEEE Globecom Workshops (GC Wkshps*, pp. 1–5, 2020.

[26] R. Ahmad, M. D. Soltani, M. Safari, A. Srivastava, and A. Das, "Reinforcement learning based load balancing for hybrid lifi wifi networks," *IEEE Access*, vol. 8, pp. 132273–132284, 2020.

[27] B. Sukanya and V. Palliyembil, "Performance improvement of indoor lifi mobile users with random orientation using hybrid lifi and wifi networks (hlwnets)," in *2021 Sixth International Conference on Wireless Communications, Signal Processing and Networking (WiSPNET)*, pp. 390–394, 2021.

[28] S. Paramita, A. Srivastava, V. A. Bohara, A. Mitra, H. R. M, H. K. Atluri, and A. Paventhan, "Demo of hybrid lifi/wifi network for an indoor environment," in *2023 15th International Conference on COMmunication Systems & NETworkS (COMSNETS)*, pp. 213–215, 2023.

[29] D. Frometa Fonseca, B. Genoves Guzman, G. Luca Martena, R. Bian, H. Haas, and D. Giustiniano, "Prediction-model-assisted reinforcement learning algorithm for handover decision-making in hybrid lifi and wifi networks," *Journal of Optical Communications and Networking*, vol. 16, no. 2, pp. 159–170, 2024.

[30] D. Tsonev, S. Videv, and H. Haas, "Unlocking spectral efficiency in intensity modulation and direct detection systems," *IEEE Journal on Selected Areas in Communications*, vol. 33, no. 9, pp. 1758–1770, 2015.

[31] M. Kumari, "Performance evaluation of lifi-ocdma system using zcc code," in *2023 9th International Conference on Advanced Computing and Communication Systems (ICACCS)*, vol. 1, pp. 58–61, 2023.

[32] B. Pamukti, W. Vinsensius Sigit, A. Fahmi, N. M. Adriansyah, and N. Andini, "Water-filling random resource allocation (w-frra) using noma for downlink lifi system," in *2019 IEEE Asia Pacific Conference on Wireless and Mobile (APWiMob)*, pp. 13–18, 2019.

[33] D. Tsonev and H. Haas, "Avoiding spectral efficiency loss in unipolar ofdm for optical wireless communication," in *2014 IEEE International Conference on Communications (ICC)*, pp. 3336–3341, 2014.

[34] M. A. Dastgheib, H. Beyranvand, and J. A. Salehi, "Anticipatory approaches for resource allocation in lifi networks," in *2019 2nd West Asian Colloquium on Optical Wireless Communications (WACOWC)*, pp. 157–161, 2019.

[35] H. Liu, Y. Jiang, X. Zhu, and T. Wang, "Low-complexity and robust papr reduction and led nonlinearity mitigation for uaco-ofdm lifi systems," in *ICC 2019 - 2019 IEEE International Conference on Communications (ICC)*, pp. 1–6, 2019.

[36] Q. Wang, Y. Jiang, X. Zhu, and T. Wang, "Phase rotation based precoding for miso dco-ofdm lifi with highly correlated channels," in *2021 IEEE Wireless Communications and Networking Conference (WCNC)*, pp. 1–5, 2021.

[37] C. Chen, M. D. Soltani, M. Safari, A. A. Purwita, X. Wu, and H. Haas, "An omnidirectional user equipment configuration to support mobility in lifi networks," in *2019 IEEE International Conference on Communications Workshops (ICC Workshops)*, pp. 1–6, 2019.

[38] M. Mahbub, M. S. Islam, and B. Barua, "A study on the snr and sinr performance of a lifi transmission system: From the perspective of a smart classroom in bangladesh," in *2023 3rd Asian Conference on Innovation in Technology (ASIANCON)*, pp. 1–4, 2023.

[39] C. Chen, R. Bian, and H. Haas, "Omnidirectional transmitter and receiver design for wireless infrared uplink transmission in lifi," in *2018 IEEE International Conference on Communications Workshops (ICC Workshops)*, pp. 1–6, 2018.

[40] A. B. Ozyurt and W. O. Popoola, "Analysis of over-the-air time synchronization for industrial lifi networks," in *2023 IEEE Wireless Communications and Networking Conference (WCNC)*, pp. 1–5, 2023.

[41] M. A. Dastgheib, H. Beyranvand, E. Zolala, and J. A. Salehi, "Optimization of cellular lifi network deployment for gaussian mixture user distributions," in *2021 Iran Workshop on Communication and Information Theory (IWCIT)*, pp. 1–6, 2021.

[42] M. D. Soltani, Z. Zeng, H. Kazemi, C. Chen, H. Haas, and M. Safari, "A study of sojourn time for indoor lifi cellular networks," in *2019 IEEE 30th Annual International Symposium on Personal, Indoor and Mobile Radio Communications (PIMRC)*, pp. 1–6, 2019.

[43] C. Chen, S. Videv, D. Tsonev, and H. Haas, "Fractional frequency reuse in dco-ofdm-based optical attocell networks," *J. Lightw. Technol.*, vol. 33, no. 19, pp. 3986–4000, 2015.

[44] N. Lorrière, G. Chabriel, J. Barrère, M. Pasquinelli, G. Pic, N. Vannieuwenhuyse, L. Escoubas, and J.-J. Simon, "Lifi reception from organic photovoltaic modules subject to additional dc illuminations and shading effects," in *2019 Global LIFI Congress (GLC)*, pp. 1–5, 2019.

[45] S. Paramita, A. Bhattacharya, A. Srivastava, V. A. Bohara, K. Joshi, and D. Solanki, "Usage of p2p li-fi transceivers for establishing backhaul connectivity," in *2024 16th International Conference on COMmunication Systems & NETworkS (COMSNETS)*, pp. 333–335, 2024.

[46] M. Asif, T. A. Khan, N. Taleb, R. A. Said, S. Y. Siddiqui, and G. Batool, "A proposed architecture for traffic monitoring & control system via lifi technology in smart homes," in *2022 International Conference on Business Analytics for Technology and Security (ICBATS)*, pp. 1–3, 2022.

[47] C. Chen, D. Tsonev, and H. Haas, "Joint transmission in indoor visible light communication downlink cellular networks," in *2013 IEEE Globecom Workshops (GC Wkshps)*, pp. 1127–1132, 2013.

[48] S. Mohammadi Kouhini, S. Maravanchery Mana, P. Hellwig, J. Hilt, D. Schulz, A. Paraskevopoulos, R. Freund, and V. Jungnickel, "Performance of bidirectional lifi over plastic optical fiber (pof)," in *2020 12th International Symposium on Communication Systems, Networks and Digital Signal Processing (CSNDSP)*, pp. 1–6, 2020.

[49] A. B. Ozyurt and W. O. Popoola, "Comp-jt scheme for d2d communication in industrial lifi networks," *IEEE Access*, vol. 10, pp. 70760–70768, 2022.

[50] B. G. Guzmán, C. Chen, V. P. G. Jiménez, H. Haas, and L. Hanzo, "Reflection-based relaying techniques in visible light communications: Will it work?," *IEEE Access*, vol. 8, pp. 80922–80935, 2020.

[51] E. Ackermann, K. L. Bober, V. Jungnickel, and A. Lehmann, "Seka: Secretless key exchange and authentication in lifi networks," in *2024 IEEE 9th European Symposium on Security and Privacy (EuroS&P)*, pp. 633–657, 2024.

[52] X. Wu and H. Haas, "Handover skipping for lifi," *IEEE Access*, vol. 7, pp. 38369–38378, 2019.

[53] I. Tavakkolnia, C. Chen, R. Bian, and H. Haas, "Energy-efficient adaptive mimo-vlc technique for indoor lifi applications," in *2018 25th International Conference on Telecommunications (ICT)*, pp. 331–335, 2018.

[54] S. R. Teli, S. Zvanovec, and Z. Ghassemlooy, "Optical internet of things within 5g: Applications and challenges," in *Proc. of 2018 IEEE International Conference on Internet of Things and Intelligence System (IOTAIS)*, pp. 40–45, 2018.

[55] I. Demirkol, D. Camps-Mur, J. Paradells, M. Combalia, W. Popoola, and H. Haas, "Powering the internet of things through light communication," *IEEE Commun. Mag.*, vol. 57, no. 6, pp. 107–113, 2019.

[56] O. Alsulami, A. Alahmadi, S. Saeed, S. Mohamed, T. El-Gorashi, M. Alresheedi, and J. Elmirghani, "Optimum resource allocation in 6g optical wireless communication systems," 05 2020. © 2020 IEEE.

[57] B. Marr, "Will lifi take big data and the internet of things to a new level?." `https://www.forbes.com/sites/bernardmarr/2016/01/12/will-lifi-take-big-data-and-the-internet-of-things-to-a-new-level/`, 01 2016.

[58] S. R. Teli, S. Zvanovec, and Z. Ghassemlooy, "Optical internet of things within 5g: Applications and challenges," in *2018 IEEE International Conference on Internet of Things and Intelligence System (IOTAIS)*, pp. 40–45, 2018.

[59] A. Gupta and X. Fernando, "Exploring secure visible light communication in next-generation (6g) internet-of-things," in *2021 International Wireless Communications and Mobile Computing (IWCMC)*, pp. 2090–2097, 2021.

[60] M. Z. Chowdhury, M. K. Hasan, M. Shahjalal, M. T. Hossan, and Y. M. Jang, "Optical wireless hybrid networks: Trends, opportunities, challenges, and research directions," *IEEE Commun. Surveys Tut.*, vol. 22, no. 2, pp. 930–966, 2020.

[61] M. Asad and S. Qaisar, "Energy efficient qos-based access point selection in hybrid wifi and lifi iot networks," *IEEE Transactions on Green Communications and Networking*, vol. 6, no. 2, pp. 897–906, 2022.

[62] K. L. Bober, V. Jungnickel, M. Emmelmann, M. Riegel, E. Tangdiongga, A. M. J. Koonen, J.-P. Linnartz, D. Behnke, M. Müller, P.-B. Bök, S. V. Colonques, and M. M. Vazquez, "A flexible system concept for lifi in the internet of things," in *2020 22nd International Conference on Transparent Optical Networks (ICTON)*, pp. 1–4, 2020.

[63] J. Linnartz, C. Corrêa, T. Cunha, E. Tangdiongga, T. Koonen, X. Deng, M. Wendt, A. Abbo, P. Stobbelaar, M. Müller, D. Behnke, M. Vazquez, S. Colonques, M. Bech, T. Metin, M. Emmelmann, S. Kouhini, K. Bober, C. Kottke, and V. Jungnickel, "Eliot: New features in lifi for next-generation iot," in *2021 Joint European Conference on Networks and Communications & 6G Summit (EuCNC/6G Summit)*, pp. 148–153, 2021.

[64] C. Chen, S. Fu, X. Jian, M. Liu, X. Deng, and Z. Ding, "Noma for energy-efficient lifi-enabled bidirectional iot communication," *IEEE Transactions on Communications*, vol. 69, no. 3, pp. 1693–1706, 2021.

[65] "What is Internet of Things (IoT)?." https://internetofthingsagenda.techtarget.com/definition/Internet-of-Things-IoT. Accessed: 2021-09-10.

[66] "Internet of Things." https://en.wikipedia.org/wiki/Internet_of_things. Accessed: 2021-09-10.

[67] T. Fath, J. Klaue, and H. Haas, "Coded spatial modulation applied to optical wireless communications in indoor environments," in *2012 IEEE Wireless Communications and Networking Conference (WCNC)*, pp. 1000–1004, 2012.

[68] S. Ranger, "What is the iot? everything you need to know about the internet of things right now." https://www.zdnet.com/article/what-is-the-internet-of-things-everything-you-need-to-know-about-the-iot-right 2020.

[69] J. Kahn and J. Barry, "Wireless infrared communications," *Proc. of the IEEE*, vol. 85, no. 2, pp. 265–298, 1997.

[70] H. Haas, M. S. Islim, C. Chen, and H. Abumarshoud, *An Introduction to Optical Wireless Mobile Communications*. Artech House, 2021.

[71] S. R. Z. Ghassemlooy, W. Popoola, *Optical Wireless Communications, System and Channel Modelling with MATLAB®*. CRC Press, 2019.

[72] "Ieee standard for local and metropolitan area networks–part 15.7: Short-range wireless optical communication using visible light," *IEEE Std 802.15.7-2011*, pp. 1–309, 2011.

[73] B. Janjua, T. K. Ng, C. Zhao, H. M. Oubei, C. Shen, A. Prabaswara, M. S. Alias, A. A. Alhamoud, A. A. Alatawi, A. M. Albadri, A. Y. Alyamani, M. M. El-Desouki, and B. S. Ooi, "Ultrabroad linewidth orange-emitting nanowires led for high cri laser-based white lighting and gigahertz communications," *Opt. Express*, vol. 24, pp. 19228–19236, 08 2016.

[74] D.-S. Shiu and J. Kahn, "Differential pulse-position modulation for power-efficient optical communication," *IEEE Trans. on Commun.*, vol. 47, no. 8, pp. 1201–1210, 1999.

[75] F. Delgado, I. Quintana, J. Rufo, J. Rabadan, C. Quintana, and R. Perez-Jimenez, "Design and implementation of an ethernet-vlc interface for broadcast transmissions," *IEEE Commun. Letters*, vol. 14, no. 12, pp. 1089–1091, 2010.

[76] Y. Zeng, R. Green, and M. Leeson, "Multiple pulse amplitude and position modulation for the optical wireless channel," in *2008 10th Anniversary International Conference on Transparent Optical Networks*, vol. 4, pp. 193–196, 2008.

[77] S. H. Lee, S.-Y. Jung, and J. K. Kwon, "Modulation and coding for dimmable visible light communication," *IEEE Commun. Mag.*, vol. 53, no. 2, pp. 136–143, 2015.

[78] F.-M. Wu, C.-T. Lin, C.-C. Wei, C.-W. Chen, H.-T. Huang, and C.-H. Ho, "1.1-gb/s white-led-based visible light communication employing carrier-less amplitude and phase modulation," *IEEE Photonics Technology Letters*, vol. 24, no. 19, pp. 1730–1732, 2012.

[79] R. Mesleh, H. Haas, C. W. Ahn, and S. Yun, "Spatial modulation - a new low complexity spectral efficiency enhancing technique," in *2006 First International Conference on Communications and Networking in China*, pp. 1–5, 2006.

[80] Y. Chau and S.-H. Yu, "Space modulation on wireless fading channels," in *IEEE 54th Vehicular Technology Conference. VTC Fall 2001. Proc. (Cat. No.01CH37211)*, vol. 3, pp. 1668–1671 vol.3, 2001.

[81] J. Jeganathan, A. Ghrayeb, L. Szczecinski, and A. Ceron, "Space shift keying modulation for mimo channels," *IEEE Trans. on Wireless Commun.*, vol. 8, no. 7, pp. 3692–3703, 2009.

[82] J. Jeganathan, A. Ghrayeb, and L. Szczecinski, “Generalized space shift keying modulation for mimo channels,” in *2008 IEEE 19th International Symposium on Personal, Indoor and Mobile Radio Communications*, pp. 1–5, 2008.

[83] A. Yesilkaya, A. A. Purwita, E. Panayirci, H. V. Poor, and H. Haas, “Flexible led index modulation for mimo optical wireless communications,” in *GLOBECOM 2020 - 2020 IEEE Global Communications Conference*, pp. 1–7, 2020.

[84] M. Svaluto Moreolo, R. Munoz, and G. Junyent, “Novel power efficient optical ofdm based on hartley transform for intensity-modulated direct-detection systems,” *J. Lightw. Technol.*, vol. 28, no. 5, pp. 798–805, 2010.

[85] W. Huang, C. Gong, and Z. Xu, “System and waveform design for wavelet packet division multiplexing-based visible light communications,” *J. Lightw. Technol.*, vol. 33, no. 14, pp. 3041–3051, 2015.

[86] M. Noshad and M. Brandt-Pearce, “Hadamard-coded modulation for visible light communications,” *IEEE Trans. on Commun.*, vol. 64, no. 3, pp. 1167–1175, 2016.

[87] O. González, S. Rodríguez, R. Pérez-Jiménez, B. R. Mendoza, and F. Delgado, “Adaptive OFDM system for multi-user communications over the indoor wireless optical channel,” in *Photonic Materials, Devices, and Applications II* (A. Serpengüzel, G. Badenes, and G. C. Righini, eds.), vol. 6593 of *Society of Photo-Optical Instrumentation Engineers (SPIE) Conference Series*, p. 65931D, May 2007.

[88] S. Dimitrov and H. Haas, “Information rate of ofdm-based optical wireless communication systems with nonlinear distortion,” *J. Lightw. Technol.*, vol. 31, no. 6, pp. 918–929, 2013.

[89] X. Ling, J. Wang, X. Liang, Z. Ding, and C. Zhao, “Offset and power optimization for dco-ofdm in visible light communication systems,” *IEEE Trans. on Signal Processing*, vol. 64, no. 2, pp. 349–363, 2016.

[90] M. Zhang and Z. Zhang, "An optimum dc-biasing for dco-ofdm system," *IEEE Commun. Letters*, vol. 18, no. 8, pp. 1351–1354, 2014.

[91] J. Armstrong and A. Lowery, "Power efficient optical ofdm," *Electronics Letters*, vol. 42, pp. 370–372, 2006.

[92] S. C. J. Lee, S. Randel, F. Breyer, and A. M. J. Koonen, "Pam-dmt for intensity-modulated and direct-detection optical communication systems," *IEEE Photonics Technology Letters*, vol. 21, no. 23, pp. 1749–1751, 2009.

[93] J. Armstrong and B. J. Schmidt, "Comparison of asymmetrically clipped optical ofdm and dc-biased optical ofdm in awgn," *IEEE Communications Letters*, vol. 12, no. 5, pp. 343–345, 2008.

[94] N. Fernando, Y. Hong, and E. Viterbo, "Flip-ofdm for unipolar communication systems," *IEEE Trans. on Commun.*, vol. 60, no. 12, pp. 3726–3733, 2012.

[95] D. Tsonev, S. Sinanovic, and H. Haas, "Novel unipolar orthogonal frequency division multiplexing (u-ofdm) for optical wireless," in *2012 IEEE 75th Vehicular Technology Conference (VTC Spring)*, pp. 1–5, 2012.

[96] L. Chen, B. Krongold, and J. Evans, "Diversity combining for asymmetrically clipped optical ofdm in im/dd channels," in *GLOBECOM 2009 - 2009 IEEE Global Telecommunications Conference*, pp. 1–6, 2009.

[97] J. Dang, Z. Zhang, and L. Wu, "A novel receiver for aco-ofdm in visible light communication," *IEEE Commun. Letters*, vol. 17, no. 12, pp. 2320–2323, 2013.

[98] N. Huang, J.-B. Wang, C. Pan, J.-Y. Wang, Y. Pan, and M. Chen, "Iterative receiver for flip-ofdm in optical wireless communication," *IEEE Photonics Technology Letters*, vol. 27, no. 16, pp. 1729–1732, 2015.

[99] Y. Zheng, Z. Zhang, J. Dang, and L. Wu, "A novel receiver for filp-ofdm in optical wireless communication," in *2015 IEEE 16th International Conference on Communication Technology (ICCT)*, pp. 620–625, 2015.

[100] J. Dang, Z. Zhang, and L. Wu, "Frequency-domain diversity combining receiver for aco-ofdm system," *IEEE Photonics Journal*, vol. 7, no. 6, pp. 1–10, 2015.

[101] J. Xu, W. Xu, H. Zhang, and X. You, "Asymmetrically reconstructed optical ofdm for visible light communications," *IEEE Photonics Journal*, vol. 8, no. 1, pp. 1–18, 2016.

[102] N. Huang, J.-B. Wang, J. Wang, C. Pan, H. Wang, and M. Chen, "Receiver design for pam-dmt in indoor optical wireless links," *IEEE Photonics Technology Letters*, vol. 27, no. 2, pp. 161–164, 2015.

[103] N. Xiang, Z. Zhang, J. Dang, and L. Wu, "A novel receiver design for pam-dmt in optical wireless communication systems," *IEEE Photonics Technology Letters*, vol. 27, no. 18, pp. 1919–1922, 2015.

[104] C. Wu, H. Zhang, and W. Xu, "On visible light communication using led array with dft-spread ofdm," in *2014 IEEE International Conference on Communications (ICC)*, pp. 3325–3330, 2014.

[105] M. S. A. Mossaad, S. Hranilovic, and L. Lampe, "Visible light communications using ofdm and multiple leds," *IEEE Trans. on Commun.*, vol. 63, no. 11, pp. 4304–4313, 2015.

[106] H. Elgala and T. D. C. Little, "Reverse polarity optical-ofdm (rpo-ofdm): dimming compatible ofdm for gigabit vlc links," *Optics Express*, vol. 21, no. 20, pp. 24288–24299, 2013.

[107] S. D. Dissanayake, K. Panta, and J. Armstrong, "A novel technique to simultaneously transmit aco-ofdm and dco-ofdm in im/dd systems," in *2011 IEEE GLOBECOM Workshops (GC Wkshps)*, pp. 782–786, 2011.

[108] S. D. Dissanayake and J. Armstrong, "Comparison of aco-ofdm, dco-ofdm and ado-ofdm in im/dd systems," *J. Lightw. Technol.*, vol. 31, no. 7, pp. 1063–1072, 2013.

[109] B. Ranjha and M. Kavehrad, "Hybrid asymmetrically clipped ofdm-based im/dd optical wireless system," *IEEE/OSA Journal of Optical Communications and Networking*, vol. 6, no. 4, pp. 387–396, 2014.

[110] Q. Wang, Z. Wang, and L. Dai, "Iterative receiver for hybrid asymmetrically clipped optical ofdm," *J. Lightw. Technol.*, vol. 32, no. 22, pp. 4471–4477, 2014.

[111] H. Elgala and T. D. C. Little, "P-ofdm: Spectrally efficient unipolar ofdm," in *OFC 2014*, pp. 1–3, 2014.

[112] H. Elgala and T. D. Little, "Polar-based ofdm and sc-fde links toward energy-efficient gbps transmission under im-dd optical system constraints [invited]," *IEEE/OSA Journal of Optical Communications and Networking*, vol. 7, no. 2, pp. A277–A284, 2015.

[113] N. Wu and Y. Bar-Ness, "A novel power-efficient scheme asymmetrically and symmetrically clipping optical (asco)-ofdm for im/dd optical systems," *EURASIP J. Adv. Signal Process.*, vol. 2015, no. 1, pp. 1–10, 2015.

[114] K. Asadzadeh, A. A. Farid, and S. Hranilovic, "Spectrally factorized optical ofdm," in *2011 12th Canadian Workshop on Information Theory*, pp. 102–105, 2011.

[115] T. Mao, C. Qian, Q. Wang, J. Quan, and Z. Wang, "Pm-dco-ofdm for papr reduction in visible light communications," in *2015 Opto-Electronics and Communications Conference (OECC)*, pp. 1–3, 2015.

[116] M. S. Islim, D. Tsonev, and H. Haas, "A generalized solution to the spectral efficiency loss in unipolar optical ofdm-based systems," in *2015 IEEE International Conference on Communications (ICC)*, pp. 5126–5131, 2015.

[117] M. S. Islim, D. Tsonev, and H. Haas, "Spectrally enhanced pam-dmt for im/dd optical wireless communications," in *2015 IEEE 26th Annual International Symposium on Personal, Indoor, and Mobile Radio Communications (PIMRC)*, pp. 877–882, 2015.

[118] M. S. Islim, D. Tsonev, and H. Haas, "On the superposition modulation for ofdm-based optical wireless communication," in *2015 IEEE Global Conference on Signal and Information Processing (GlobalSIP)*, pp. 1022–1026, 2015.

[119] H. Elgala and T. D. C. Little, "See-ofdm: Spectral and energy efficient ofdm for optical im/dd systems," in *2014 IEEE 25th Annual International Symposium on Personal, Indoor, and Mobile Radio Communication (PIMRC)*, pp. 851–855, 2014.

[120] Q. Wang, C. Qian, X. Guo, Z. Wang, D. G. Cunningham, and I. H. White, "Layered aco-ofdm for intensity-modulated direct-detection optical wireless transmission," *Opt. Express*, vol. 23, pp. 12382–12393, 05 2015.

[121] The International Commission on Illumination (CIE), "Cie 1931 standard colorimetric observer." `www.cie.co.at`, 08 2008.

[122] R. J. Drost and B. M. Sadler, "Constellation design for color-shift keying using billiards algorithms," in *2010 IEEE Globecom Workshops*, pp. 980–984, 2010.

[123] E. Monteiro and S. Hranilovic, "Design and implementation of color-shift keying for visible light communications," *J. Lightw. Technol.*, vol. 32, no. 10, pp. 2053–2060, 2014.

[124] R. Singh, T. O'Farrell, and J. P. R. David, "An enhanced color shift keying modulation scheme for high-speed wireless visible light communications," *J. Lightw. Technol.*, vol. 32, no. 14, pp. 2582–2592, 2014.

[125] J. Jiang, R. Zhang, and L. Hanzo, "Analysis and design of three-stage concatenated color-shift keying," *IEEE Trans. on Vehicular Technology*, vol. 64, no. 11, pp. 5126–5136, 2015.

[126] N. Murata, H. Shimamoto, Y. Kozawa, and Y. Umeda, "Performance evaluation of digital colour shift keying for visible light communications," in *2015 IEEE International Conference on Communication Workshop (ICCW)*, pp. 1374–1379, 2015.

[127] K.-I. Ahn and J. K. Kwon, "Color intensity modulation for multicolored visible light communications," *IEEE Photonics Technology Letters*, vol. 24, no. 24, pp. 2254–2257, 2012.

[128] P. M. Butala, J. C. Chau, and T. D. C. Little, "Metameric modulation for diffuse visible light communications with constant ambient lighting," in *2012 International Workshop on Optical Wireless Communications (IWOW)*, pp. 1–3, 2012.

[129] J. Luna-Rivera, R. Perez-Jimenez, V. Guerra-Yañez, C. Suarez-Rodriguez, and F. Delgado-Rajo, "Combined csk and pulse position modulation scheme for indoor visible light communications," *Electronics Letters*, vol. 50, no. 10, pp. 762–764, 2014.

[130] S. Pergoloni, M. Biagi, S. Colonnese, R. Cusani, and G. Scarano, "Merging color shift keying and complementary pulse position modulation for visible light illumination and communication," in *2014 Euro Med Telco Conference (EMTC)*, pp. 1–6, 2014.

[131] F. A. Delgado Rajó, V. Guerra, J. A. Rabadán Borges, J. R. Torres, and R. Pérez-Jiménez, "Color shift keying communication system with a modified ppm synchronization scheme," *IEEE Photonics Technology Letters*, vol. 26, no. 18, pp. 1851–1854, 2014.

[132] S. S. Wijesinghe and R. P. Thilakumara, "Multiuser access in lifi using ofdma," in *2018 4th International Conference for Convergence in Technology (I2CT)*, pp. 1–5, 2018.

[133] Q. Mao, P. Yue, M. Xu, Y. Ji, and Z. Cui, "Octmac: A vlc based mac protocol combining optical cdma with tdma for vanets," in *2017 International Conference on Computer, Information and Telecommunication Systems (CITS)*, pp. 234–238, 2017.

[134] S. K. Nobar, K. A. Mehr, and J. M. Niya, "Comprehensive performance analysis of ieee 802.15.7 csma/ca mechanism for saturated traffic," *Journal of Optical Communications and Networking*, vol. 7, no. 2, pp. 62–73, 2015.

[135] Z. Chen and H. Haas, "Space division multiple access in visible light communications," in *2015 IEEE International Conference on Communications (ICC)*, pp. 5115–5119, 2015.

[136] "Iso/iec/ieee international standard - information technology – telecommunications and information exchange between systems – local and metropolitan area networks – specific requirements – part 11: Wireless lan medium access control (mac) and physical layer (phy) specifications amendment 4," *ISO/IEC/IEEE 8802-11:2012/Amd.4:2015(E) (Adoption of IEEE Std 802.11ac-2013)*, pp. 1–430, 2015.

[137] M. H. Shoreh, A. Fallahpour, and J. A. Salehi, "Design concepts and performance analysis of multicarrier cdma for indoor visible light communications," *Journal of Optical Communications and Networking*, vol. 7, no. 6, pp. 554–562, 2015.

[138] H. Qian, S. C. Dai, S. Zhao, S. Z. Cai, and H. Zhang, "A robust cdma vlc system against front-end nonlinearity," *IEEE Photonics Journal*, vol. 7, no. 5, pp. 1–9, 2015.

[139] A. Benjebbour, Y. Saito, Y. Kishiyama, A. Li, A. Harada, and T. Nakamura, "Concept and practical considerations of non-orthogonal multiple access (noma) for future radio access," in *2013 International Symposium on Intelligent Signal Processing and Communication Systems*, pp. 770–774, 2013.

[140] Z. Ding, Z. Yang, P. Fan, and H. V. Poor, "On the performance of non-orthogonal multiple access in 5g systems with randomly deployed users," *IEEE Signal Processing Letters*, vol. 21, no. 12, pp. 1501–1505, 2014.

[141] H. Marshoud, V. M. Kapinas, G. K. Karagiannidis, and S. Muhaidat, "Non-orthogonal multiple access for visible light communications," *IEEE Photonics Technology Letters*, vol. 28, no. 1, pp. 51–54, 2016.

[142] X. Zhu, F. Wang, M. Shi, N. Chi, J. Liu, and F. Jiang, "10.72gb/s visible light communication system based on single packaged rgbyc led utilizing qam-dmt

modulation with hardware pre-equalization," in *2018 Optical Fiber Communications Conference and Exposition (OFC)*, pp. 1–3, 2018.

[143] Y. Wang, L. Tao, X. Huang, J. Shi, and N. Chi, "Enhanced performance of a high-speed wdm cap64 vlc system employing volterra series-based nonlinear equalizer," *IEEE Photonics Journal*, vol. 7, no. 3, pp. 1–7, 2015.

[144] F.-M. Wu, C.-T. Lin, C.-C. Wei, C.-W. Chen, Z.-Y. Chen, and H.-T. Huang, "3.22-gb/s wdm visible light communication of a single rgb led employing carrier-less amplitude and phase modulation," in *2013 Optical Fiber Communication Conference and Exposition and the National Fiber Optic Engineers Conference (OFC/NFOEC)*, pp. 1–3, 2013.

[145] Y. Wang, L. Tao, X. Huang, J. Shi, and N. Chi, "8-gb/s rgby led-based wdm vlc system employing high-order cap modulation and hybrid post equalizer," *IEEE Photonics Journal*, vol. 7, no. 6, pp. 1–7, 2015.

[146] H. Chun, S. Rajbhandari, G. Faulkner, D. Tsonev, E. Xie, J. J. D. McKendry, E. Gu, M. D. Dawson, D. C. O'Brien, and H. Haas, "Led based wavelength division multiplexed 10 gb/s visible light communications," *J. Lightw. Technol.*, vol. 34, no. 13, pp. 3047–3052, 2016.

[147] O. Z. Alsulami, M. K. A. Aljohani, S. O. M. Saeed, S. H. Mohamed, T. E. H. El-Gorashi, M. T. Alresheedi, and J. M. H. Elmirghani, "Impact of room size on wdm optical wireless links with multiple access points and angle diversity receivers," in *2020 22nd International Conference on Transparent Optical Networks (ICTON)*, pp. 1–6, 2020.

[148] P. Ge, X. Liang, J. Wang, C. Zhao, X. Gao, and Z. Ding, "Optical filter designs for multi-color visible light communication," *IEEE Trans. on Commun.*, vol. 67, no. 3, pp. 2173–2187, 2019.

[149] P. Ge, X. Ling, J. Wang, X. Liang, R. Zhang, and C. Zhao, "Optical filter bank for multi-color visible light communications," in *2019 IEEE Global Communications Conference (GLOBECOM)*, pp. 1–6, 2019.

[150] P. Ge, X. Ling, J. Wang, X. Liang, S. Li, and C. Zhao, "Optical filter bank modeling and design for multi-color visible light communications," *IEEE Photonics Journal*, vol. 13, no. 1, pp. 1–19, 2021.

[151] L. Cui, Y. Tang, H. Jia, J. Luo, and B. Gnade, "Analysis of the multichannel wdm-vlc communication system," *Journal of Lightwave Technology*, vol. 34, no. 24, pp. 5627–5634, 2016.

[152] J. Senior, S. Cusworth, and A. Ryley, "Wavelength division multiple access in fibre optic lans," in *IEE Colloquium on Fibre Optic LANS and Techniques for the Local Loop*, pp. 5/1–5/4, 1989.

[153] A. Stok and E. Sargent, "System performance comparison of optical cdma and wdma in a broadcast local area network," *IEEE Commun. Letters*, vol. 6, no. 9, pp. 409–411, 2002.

[154] F. Miramirkhani and M. Uysal, "Channel modeling and characterization for visible light communications," *IEEE Photonics Journal*, vol. 7, no. 6, pp. 1–16, 2015.

[155] C. Chen, D. Basnayaka, and H. Haas, "Non-line-of-sight channel impulse response characterisation in visible light communications," in *2016 IEEE International Conference on Communications (ICC)*, pp. 1–6, 2016.

[156] A. Ramirez-Aguilera, J. Luna-Rivera, V. Guerra, J. Rabadan, R. Perez-Jimenez, and F. Lopez-Hernandez, "Multi-wavelength modelling for vlc indoor channels using montecarlo simulation," in *2016 10th International Symposium on Communication Systems, Networks and Digital Signal Processing (CSNDSP)*, pp. 1–6, 2016.

[157] J. R. Barry and J. M. Kahn, "Link design for nondirected wireless infrared communications," *Appl. Opt.*, vol. 34, pp. 3764–3776, 07 1995.

[158] M. D. Soltani, A. A. Purwita, Z. Zeng, H. Haas, and M. Safari, "Modeling the random orientation of mobile devices: Measurement, analysis and lifi use case," *IEEE Trans. on Commun.*, vol. 67, no. 3, pp. 2157–2172, 2019.

[159] M. Dehghani Soltani, A. A. Purwita, I. Tavakkolnia, H. Haas, and M. Safari, "Impact of device orientation on error performance of lifi systems," *IEEE Access*, vol. 7, pp. 41690–41701, 2019.

[160] J. Chen, I. Tavakkolnia, C. Chen, Z. Wang, and H. Haas, "The movement-rotation (mr) correlation function and coherence distance of vlc channels," *J. Lightw. Technol.*, vol. 38, no. 24, pp. 6759–6770, 2020.

[161] M. Dehghani Soltani, A. A. Purwita, Z. Zeng, C. Chen, H. Haas, and M. Safari, "An orientation-based random waypoint model for user mobility in wireless networks," pp. 1–6, 2020.

[162] M. A. Arfaoui, M. D. Soltani, I. Tavakkolnia, A. Ghrayeb, C. M. Assi, M. Safari, and H. Haas, "Measurements-based channel models for indoor lifi systems," *IEEE Trans. on Wireless Commun.*, vol. 20, no. 2, pp. 827–842, 2021.

[163] M. Dehghani Soltani, X. Wu, M. Safari, and H. Haas, "Access point selection in li-fi cellular networks with arbitrary receiver orientation," in *2016 IEEE 27th Annual International Symposium on Personal, Indoor, and Mobile Radio Communications (PIMRC)*, pp. 1–6, 2016.

[164] A. A. Purwita, M. D. Soltani, M. Safari, and H. Haas, "Terminal orientation in ofdm-based lifi systems," *IEEE Transactions on Wireless Communications*, vol. 18, no. 8, pp. 4003–4016, 2019.

[165] A. A. Purwita, M. D. Soltani, M. Safari, and H. Haas, "Handover probability of hybrid lifi/rf-based networks with randomly-oriented devices," in *2018 IEEE 87th Vehicular Technology Conference (VTC Spring)*, pp. 1–5, 2018.

[166] Z. Yang, Z. Zhou, and Y. Liu, "From rssi to csi: Indoor localization via channel response," *ACM Comput. Surv.*, vol. 46, Dec. 2013.

[167] P. Castro, P. Chiu, T. Kremenek, and R. R. Muntz, "A probabilistic room location service for wireless networked environments," in *Proceedings of the 3rd International Conference on Ubiquitous Computing*, UbiComp '01, (Berlin, Heidelberg), p. 18–34, Springer-Verlag, 2001.

[168] A. Haeberlen, E. Flannery, A. M. Ladd, A. Rudys, D. S. Wallach, and L. E. Kavraki, "Practical robust localization over large-scale 802.11 wireless networks," in *Proceedings of the 10th Annual International Conference on Mobile Computing and Networking*, MobiCom '04, (New York, NY, USA), p. 70–84, Association for Computing Machinery, 2004.

[169] P. Krishnan, A. Krishnakumar, W.-H. Ju, C. Mallows, and S. Gamt, "A system for lease: Location estimation assisted by stationary emitters for indoor rf wireless networks," in *IEEE INFOCOM 2004*, vol. 2, pp. 1001–1011 vol.2, 2004.

[170] A. M. Ladd, K. E. Bekris, A. Rudys, G. Marceau, L. E. Kavraki, and D. S. Wallach, "Robotics-based location sensing using wireless ethernet," in *Proceedings of the 8th Annual International Conference on Mobile Computing and Networking*, MobiCom '02, (New York, NY, USA), p. 227–238, Association for Computing Machinery, 2002.

[171] P. Kumar, L. Reddy, and S. Varma, "Distance measurement and error estimation scheme for rssi based localization in wireless sensor networks," in *2009 Fifth International Conference on Wireless Communication and Sensor Networks (WCSN)*, pp. 1–4, 2009.

[172] C. P. W. Dargie, *Localization*, ch. 10, pp. 249–266. John Wiley & Sons, Ltd, 2010.

[173] F. Zafari, I. Papapanagiotou, and K. Christidis, "Microlocation for internet-of-things-equipped smart buildings," *IEEE Internet of Things Journal*, vol. 3, no. 1, pp. 96–112, 2016.

[174] S. Kumar, S. Gil, D. Katabi, and D. Rus, "Accurate indoor localization with zero start-up cost," in *Proceedings of the 20th Annual International Conference*

on Mobile Computing and Networking, MobiCom '14, (New York, NY, USA), p. 483–494, Association for Computing Machinery, 2014.

[175] Y.-S. Kuo, P. Pannuto, K.-J. Hsiao, and P. Dutta, "Luxapose: indoor positioning with mobile phones and visible light," in *Proceedings of the 20th Annual International Conference on Mobile Computing and Networking*, MobiCom '14, (New York, NY, USA), p. 447–458, Association for Computing Machinery, 2014.

[176] J. Armstrong, Y. A. Sekercioglu, and A. Neild, "Visible light positioning: a roadmap for international standardization," *IEEE Communications Magazine*, vol. 51, no. 12, pp. 68–73, 2013.

[177] D. Devi, A. Kumar, P. Scholar, and M. Tech, "Design and implementation of cpld based solar power saving system for street lights and automatic traffic controller," 07 2018.

[178] "Smart lighting: A global strategic business report," tech. rep., Global Industry Analysts Inc., 2015.

[179] R. Leslie and K. Conway, *The Lighting Pattern Book for Homes.* McGraw-Hill Inc., 1996.

[180] D. Phillips, *Planning Your Lighting.* A Design Centre Book, 1996.

[181] M. Hassan, M. Mustafa, and I. A. A. Jalal, "Lighting management system," in *Proceedings. Student Conference on Research and Development, 2003. SCORED 2003.*, pp. 309–312, 2003.

[182] M. T. Koroglu and K. M. Passino, "Illumination balancing algorithm for smart lights," *IEEE Transactions on Control Systems Technology*, vol. 22, no. 2, pp. 557–567, 2014.

[183] M. Petkovic, D. Bajovic, D. Vukobratovic, G. McCutcheon, L. Stankovic, and V. Stankovic, "Effect of external daylight in smart dimmable led lighting systems," in *2019 28th Wireless and Optical Communications Conference (WOCC)*, pp. 1–5, 2019.

[184] M. V. Rafliana Roostandi, T. A. Nathaniel, D. Qinthara, and S. S. Boby, "Smart light control using thermal sensor as human presence detection," in *2021 4th International Conference on Information and Communications Technology (ICOIACT)*, pp. 75–79, 2021.

[185] P. Netinant, M. Rukhiran, and P. Rattanakorn, "Development of smart light control and intruder detection with voice and motion based on internet of things using raspberry pi," in *2022 6th International Conference on Business and Information Management (ICBIM)*, pp. 190–195, 2022.

[186] Shashikant and P. Garg, "Smart led with power allocation algorithm for indoor visible light communication system," in *2018 7th International Conference on Reliability, Infocom Technologies and Optimization (Trends and Future Directions) (ICRITO)*, pp. 834–839, 2018.

[187] B. G. Guzman, J. Talavante, D. F. Fonseca, M. S. Mir, D. Giustiniano, K. Obraczka, M. E. Loik, S. Childress, and D. G. Wong, "Toward sustainable greenhouses using battery-free lifi-enabled internet of things," *IEEE Communications Magazine*, vol. 61, no. 5, pp. 129–135, 2023.

[188] H. Alshaer, H. Haas, and O. Y. Kolawole, "An optimal networked lifi access point slicing scheme for internet-of-things," in *2021 IEEE International Conference on Communications Workshops (ICC Workshops)*, pp. 1–6, 2021.

[189] B. Genovés Guzmán, V. Gil Jiménez, and R. Pérez, *Peak-to-Average Power Ratio Reduction Techniques*, pp. 1–32. 10 2019.

[190] J. Beysens, Q. Wang, A. Galisteo, D. Giustiniano, and S. Pollin, "A cell-free networking system with visible light," *IEEE/ACM Transactions on Networking*, vol. 28, no. 2, pp. 461–476, 2020.

[191] R. Zhang, H. Claussen, H. Haas, and L. Hanzo, "Energy efficient visible light communications relying on amorphous cells," *IEEE Journal on Selected Areas in Communications*, vol. 34, no. 4, pp. 894–906, 2016.

[192] R. A. Elsayed, Y. A. Diab, A. E. A. Farahat, K. F. A. Hussein, and A. A. Hamdi, "Effect of the wavelength reuse pattern and cell size on the performance of indoor cellular visible light communication," in *2023 International Telecommunications Conference (ITC-Egypt)*, pp. 629–636, 2023.

[193] G. L. Martena, R. Bian, and H. Haas, "Impact of passband shift in optical wireless communication systems based on wavelength division," in *ICC 2022 - IEEE International Conference on Communications*, pp. 3820–3825, 2022.

[194] C. Barthold, K. Pathapati Subbu, and R. Dantu, "Evaluation of gyroscope-embedded mobile phones," in *2011 IEEE International Conference on Systems, Man, and Cybernetics*, pp. 1632–1638, 2011.

[195] OSRAM Led Engin, LZ4-00MA08, *RGBA LED datasheet*. `https://ams-osram.com/products/leds/multi-leds/osram-led-engin-luxigen-lz4-00ma08` (accessed: 21.08.2023).

[196] Thorlabs Gmbh, FB450-40, *Thin Film Bandpass Filter datasheet*. `https://www.thorlabs.com/thorproduct.cfm?partnumber=FB450-40` (accessed: 21.08.2023).

[197] Thorlabs Gmbh, FB550-40, *Thin Film Bandpass Filter datasheet*. `https://www.thorlabs.com/thorproduct.cfm?partnumber=FB550-40` (accessed: 21.08.2023).

[198] Thorlabs Gmbh, FB590-10, *Thin Film Bandpass Filter datasheet*. `https://www.thorlabs.com/thorproduct.cfm?partnumber=FB590-10` (accessed: 21.08.2023).

[199] Thorlabs Gmbh, FB650-40, *Thin Film Bandpass Filter datasheet*. `https://www.thorlabs.com/thorproduct.cfm?partnumber=FB650-40` (accessed: 21.08.2023).

[200] G. L. Martena, R. Bian, and H. Haas, "Adaptive wdma: Improving the data rate of a densely deployed lifi network," in *Proc. of the Workshop on Internet*

of Lights, IoL '21, (New York, NY, USA), p. 7–12, Association for Computing Machinery, 2021.

[201] IEEE Standards Association, "802.11be-2024 standard." https://standards.ieee.org/ieee/802.11be/7516/, 2024. accessed: 18-11-2024.

[202] X. Zhang, Z. Cao, J. Li, D. Ge, Z. Chen, I. M. Vellekoop, and A. M. J. Koonen, "Wide-coverage beam-steered 40-gbit/s non-line-of-sight optical wireless connectivity for industry 4.0," *Journal of Lightwave Technology*, vol. 38, no. 24, pp. 6801–6806, 2020.

[203] W. Fang, W. Chen, Q. Wu, K. Wang, S. Zhang, Q. Liu, and J. Li, "Reconfigurable intelligent surface assisted free space optical information and power transfer," *IEEE Internet of Things Journal*, vol. 11, no. 18, pp. 30260–30277, 2024.

[204] F. Feng, I. H. White, and T. D. Wilkinson, "Free space communications with beam steering a two-electrode tapered laser diode using liquid-crystal slm," *Journal of Lightwave Technology*, vol. 31, no. 12, pp. 2001–2007, 2013.

[205] M. Buzuayene, "Rise time vs. bandwidth and applications." https://interferencetechnology.com/rise-time-vs-bandwidth-and-applications/. accessed: 18-11-2024.

[206] Mount Lighting Ltd., "Recommended lighting levels." `https://mountlighting.co.uk/technical/cibse-recommended-lighting-levels/`. accessed: 05-09-2023.

[207] J. Chaves, *Introduction to Nonimaging Optics.* Taylor & Francis, CRC Press, 2016.

[208] M. E. Marhic, M. D. Kotzin, and A. P. van den Heuvel, "Reflectors and immersion lenses for detectors of diffuse radiation," *J. Opt. Soc. Am.*, vol. 72, pp. 352–355, Mar 1982.

[209] F. Masood, P. A.-L. Nallagownden, I. Elamvazuthi, J. Akhter, M. A. Alam, and M. Yusuf, "Design and parametric analysis of compound parabolic concentrator

for photovoltaic applications," in *2020 8th International Conference on Intelligent and Advanced Systems (ICIAS)*, pp. 1–6, 2021.

[210] Hamamatsu Photonics K.K., S8664-30, *Silicon APD datasheet.* `https://www.hamamatsu.com/content/dam/hamamatsu-photonics/sites/documents/99_SALES_LIBRARY/ssd/s8664_series_kapd1012e.pdf` (accessed: 04-09-2023).

[211] Proakis, *Digital Communications 5th Edition.* McGraw Hill, 2007.

[212] K. I. Park, *Fundamentals of Probability and Stochastic Processes with Applications to Communications.* Springer Cham, 2017.

[213] M. D. Soltani, H. Kazemi, M. Safari, and H. Haas, "Handover modeling for indoor li-fi cellular networks: The effects of receiver mobility and rotation," in *2017 IEEE Wireless Communications and Networking Conference (WCNC)*, pp. 1–6, 2017.